UNIVERSIDAD MIGUEL HERNÁNDEZ DE ELCHE

Programa de Doctorado
Tecnologías Industriales y de Telecomunicación

Analysis of multipactor effect in partially dielectric-loaded rectangular waveguides

Andrés Berenguer Alonso

Thesis Advisor:
Dra. Ángela Coves Soler

A Thesis submitted in partial fulfilment of the requirements for the degree of

Doctor of Philosophy

Elche, November 21, 2020

Esta tesis se presenta en formato convencional y como indicio de calidad se presenta con trabajos previamente publicados.

Revistas

- A. Berenguer, A. Coves, B. Gimeno, E. Bronchalo and V. E. Boria, "Experimental Study of the Multipactor Effect in a Partially Dielectric-Loaded Rectangular Waveguide", *IEEE Microwave and Wireless Components Letters*, vol. 29, no. 9, pp. 595–597, Sep. 2019, DOI: 10.1109/LMWC.2019.2929488.
- A. Berenguer, A. Coves, F. Mesa, E. Bronchalo and B. Gimeno, "Analysis of Multipactor Effect in a Partially Dielectric-Loaded Rectangular Waveguide", *IEEE Transactions on Plasma Science*, vol. 47, no. 1, pp. 259–265, Jan. 2019, DOI: 10.1109/TPS.2018.2880652.

UNIVERSITAS
Miguel Hernández

Dña. Ángela Coves Soler, Licenciada y Doctora en Ciencias Físicas, profesora de la Universidad Miguel Hernández de Elche,

CERTIFICA

que la tesis titulada "Analysis of multipactor effect in partially dielectric-loaded rectangular waveguides", de la que es autor el doctorando D. Andrés Berenguer Alonso, ha sido realizada bajo su dirección.

Considerando que se trata de un trabajo original de investigación que reúne los requisitos establecidos en la legislación vigente, autoriza su presentación. Y para que así conste, firma el presente certificado.

En Elche, a 6 de diciembre de 2020.

COVES SOLER ANGELA MARIA - 33497781Y

Firmado digitalmente por COVES SOLER ANGELA MARIA - 33497781Y
Fecha: 2020.12.06 17:54:07 +01'00'

Fdo. Dña. Ángela Coves Soler.

UNIVERSITAS
Miguel Hernández

D. Óscar Reinoso García, coordinador del programa de doctorado de "Tecnologías Industriales y de Telecomunicación", profesor de la Universidad Miguel Hernández de Elche,

INFORMA

favorablemente que la tesis titulada "Analysis of multipactor effect in partially dielectric-loaded rectangular waveguides" de la que es autor el doctorando D. Andrés Berenguer Alonso, y dirigida por la doctora Dña. Ángela Coves Soler, tiene la conformidad de la Comisión Académica del Programa de Doctorado para que sea depositada y presentada para su exposición pública, ya que cumple los requisitos en cuanto a forma y contenido.

En Elche, a 6 de diciembre de 2020.

OSCAR| REINOSO| GARCIA

Firmado digitalmente por OSCAR|REINOSO| GARCIA
Fecha: 2020.12.07 08:39:18 +01'00'

Fdo. D. Óscar Reinoso García.

Esta tesis se la dedico a
mi madre y hermano
por su apoyo incondional en todo momento
y a mi padre
allá donde nos esté mirando

Agradecimientos

Y llegó el momento. Llegó el momento de escribir mis últimas palabras de esta tesis, de este largo camino que he tratado de disfrutar desde el primer día. Llegó el momento de mirar hacia atrás y acordarse de todas esas personas que de una forma u otra me han acompañado durante esta etapa de mi vida que está llegando a su fin. Espero no olvidarme de nadie.

En primer lugar, y por su puesto como no puede ser de otra manera, mi mayor agradecimiento es para **Ángela Coves**, mi directora de tesis. Sin lugar a dudas, esta tesis no hubiese sido posible sin tu apoyo en todo momento. Agradecerte el tiempo y esfuerzo que me has dedicado siempre que he necesitado de tu ayuda. Cientos de correos, reuniones, llamadas,... y siempre con una actitud inmejorable. Gracias también por tu paciencia conmigo, y el haber sabido entender perfectamente mi situación a la hora de embarcarme en este trabajo juntos. Seguro que esto es un punto y seguido. Gracias.

De forma muy especial, el segundo de mis agradecimientos es para una persona excepcional en todos los sentidos, **Enrique Bronchalo**. Tu ayuda y consejos, han sido igualmente fundamentales para conseguir esta meta. Cuando no veíamos muy clara la solución, ahí estabas para echar una mano, para aportar tu enorme conocimiento. Con tu implicación y dedicación en esta tesis, el camino ha sido mucho más fácil. Gracias.

No puedo olvidarme de agradecerle su ayuda desde la distancia a **Benito Gimeno**. Gracias Benito por haber sabido marcarnos la dirección correcta en muchos momentos. Y gracias al fabuloso grupo de Valencia que te acompaña, en especial a **Vicente Boria** y la gente de **Val Space Consortium**. Una tesis necesita sus medidas experimentales, y ahí habéis estado vosotros para ayudarnos, entre otras muchas. Gracias.

A veces hay gente que te hace sentir cómodo desde el primer momento que la conoces. En mi caso, en el desarrollo de mi tesis, esa gente la encontré en Sevilla. En concreto en el laboratorio del Dpto. de Física Aplicada I

de la Universidad de Sevilla, y más particularmente, en la figura de **Paco Mesa**. Por su puesto, una parte importante de esta tesis te la debo a ti Paco, y a tu inmensa sabiduría. Gracias.

Finalmente, mi último pero no menos importante agradecimiento está dedicado **a mi familia**. En especial **a mi madre** y **a mi hermano**. Vosotros mejor que nadie sabéis el esfuerzo que hay detrás de esto. Sé que os sentís tan felices y orgullosos como yo. Gracias por vuestro apoyo, gracias por todo.

Andrés Berenguer Alonso

Abstract

The multipactor effect is a physical phenomenon that is triggered when free electrons, which may be generated in space-borne equipment by cosmic radiation, are subject to electromagnetic fields strong enough to lift electrons from the surface walls of physical devices. Given vacuum conditions, the free electrons can be accelerated rapidly from a surface wall of the device to another because there are no gas particles for the electrons to collide with and be slowed down. Depending on their energy, angle of impact, and the secondary emission characteristics of the wall surface, these impacting electrons can cause secondary electrons to be emitted from the wall. If the radio-frequency field changes phase at the time of collision, it can accelerate these secondary electrons towards the opposite device wall, generating more secondary electrons and enabling exponential growth in the electron population. This build-up, known as a radio-frequency discharge, or the multipactor effect, can be sufficiently large to reflect the incident power, and even damage the device or system involved.

The multipactor phenomenon has been studied within several fields in the past. Thus, particle physicists have studied the phenomenon in relation to plasma science and particle beam dynamics, while engineers have used the phenomenon to amplify signals in vacuum tubes and klystrons. Therefore, depending on the situation, the multipactor phenomenon can be viewed either as a valuable tool or an undesirable effect. The current research work focuses on the effects of multipactor breakdown in radio-frequency devices on board space vehicles (e.g. satellites), where it is viewed as an undesirable phenomenon because it can cause irreparable damage to these devices, rendering them unusable. In the context of this research, typical radio-frequency devices used in space applications include waveguides, filters, and multiplexers. While the power handling of these devices has increased in recent years, so has their geometric complexity. Because most

multipactor models make some simplifying assumptions, not least about the geometries involved, current models of multipactor are becoming increasingly inaccurate and inefficient as devices become more complex.

In the first part of this thesis, a rigorous study of the multipactor effect in a partially dielectric-loaded rectangular waveguide is presented. An efficient multipactor model is developed that could, eventually, analyse the increasingly complex structures used in the space industry. To produce the simulations presented in this thesis, a detailed analysis of the electron dynamics inside this form of waveguide has been performed, taking into account the radio-frequency electromagnetic fields propagating in the waveguide and the electrostatic field that appears because of the charging of the dielectric layer therein. The characterization of this electrostatic field is obtained by computing the electric potential produced by an arbitrary charge distribution on the dielectric layer in a dielectric-loaded waveguide; by numerically solving the equations of motion, the electron trajectories are obtained.

Another important element of the electron emission process is the secondary emission yield; defined as the number of secondary electrons emitted per incident electron and being material-specific, it is one of the main drivers of the multipactor effect. A number of different alternatives for modelling the secondary emission yield have also been studied in this thesis.

The second part of the thesis has involved detailed numerical simulations of multipactor discharges inside several configurations of rectangular waveguide containing dielectric materials. These simulations have been carried out using bespoke code specifically developed for the purpose in the course of the research work presented here. The results obtained have been validated with real measurements, carried out in the laboratory, on devices manufactured for this purpose.

Resumen

El efecto multipactor es un fenómeno físico que se desencadena cuando electrones libres, que pueden generarse en los equipos espaciales debido a la radiación cósmica, están sujetos a campos electromagnéticos lo suficientemente intensos como para desprender electrones de la superficie de las paredes de los dispositivos físicos. En condiciones de vacío, los electrones libres pueden acelerarse rápidamente desde la superficie de una pared del dispositivo a otra ya que no existen partículas de gas con las que los electrones colisionen y disminuyan su velocidad. Dependiendo de su energía, ángulo de impacto y las características de emisión secundaria de la superficie de la pared, los electrones impactantes pueden provocar que se emitan nuevos electrones secundarios. Si el campo de radiofrecuencia cambia de fase en el momento de la colisión, puede acelerar los electrones secundarios hacia la pared opuesta del dispositivo, generando más electrones secundarios y permitiendo un crecimiento exponencial en la población de electrones. Esta acumulación, conocida como descarga de radiofrecuencia o efecto multipactor, puede ser lo suficientemente grande como para reflejar la potencia incidente e incluso dañar el dispositivo o sistema involucrado.

El fenómeno multipactor se ha estudiado en varios campos en el pasado. Así, los físicos de partículas han estudiado el fenómeno en relación con la ciencia del plasma y la dinámica del haz de partículas, mientras que los ingenieros han utilizado el fenómeno para amplificar señales en tubos de vacío y klistrones. Por tanto, dependiendo de la situación, el efecto multipactor puede verse como una fenómeno beneficioso o como un efecto indeseable. El trabajo de investigación actual se centra en los efectos de la ruptura por multipactor en dispositivos de radiofrecuencia a bordo de vehículos espaciales (por ejemplo, satélites), donde éste se considera un fenómeno indeseable ya que puede causar daños irreparables en estos dispositivos, dejándolos inutilizables. En el contexto de esta investigación,

los dispositivos de radiofrecuencia típicos utilizados en aplicaciones espaciales incluyen guías de ondas, filtros y multiplexores. Si bien el manejo de potencia de estos dispositivos ha aumentado en los últimos años, también lo ha hecho su complejidad geométrica. Debido a que la mayoría de los modelos de multipactor hacen algunas suposiciones para simplificar el problema, sobre todo en las geometrías involucradas, los modelos actuales de multipactor se vuelven cada vez más inexactos e ineficientes a medida que los dispositivos se vuelven más complejos.

En la primera parte de esta tesis se presenta un estudio riguroso del efecto multipactor en una guía de ondas rectangular parcialmente cargada con dieléctrico. Se desarrolla un modelo multipactor eficiente que podría, eventualmente, analizar las estructuras cada vez más complejas utilizadas en la industria espacial. Para producir las simulaciones presentadas en esta tesis, se ha realizado un análisis detallado de la dinámica del electrón dentro de esta forma de guía de ondas, teniendo en cuenta los campos electromagnéticos de radiofrecuencia que se propagan en la guía de ondas y el campo electrostático que aparece debido a la carga depositada sobre la capa dieléctrica de la misma. La caracterización de este campo electrostático se obtiene calculando el potencial eléctrico producido por una distribución de carga arbitraria en la capa dieléctrica en una guía de ondas cargada con dieléctrico; resolviendo numéricamente las ecuaciones de movimiento, se obtienen las trayectorias de los electrones.

Otro concepto importante del proceso de emisión de electrones es el conocido como *secondary emission yield*; definido como el número de electrones secundarios emitidos por electrón incidente, y siendo específico del material, es uno de los principales impulsores del efecto multipactor. En esta tesis se han estudiado varias alternativas diferentes para modelar el *secondary emission yield*.

La segunda parte de la tesis ha involucrado simulaciones numéricas detalladas de descargas multipactor dentro de varias configuraciones de guías de ondas rectangulares que contienen materiales dieléctricos. Estas simulaciones se han llevado a cabo utilizando un código a medida desarrollado específicamente para este trabajo de investigación. Los resultados obtenidos han sido validados con medidas reales realizadas en laboratorio sobre dispositivos fabricados para tal fin.

Resum

L'efecte multipactor és un fenomen físic que es desencadena quan electrons lliures, que poden generar-se en els equips espacials a causa de la radiació còsmica, estan subjectes a camps electromagnètics prou intensos com per a desprendre electrons de la superfície de les parets dels dispositius físics. En condicions de buit, els electrons lliures poden accelerar-se ràpidament des de la superfície d'una paret del dispositiu a una altra ja que no hi ha partícules de gas amb què els electrons col · lidisquen i disminuïsquen la seua velocitat. Depenent del seu Energia, angle d'impacte i les característiques d'emissió secundària de la superfície de la paret, els electrons impactants poden provocar que s'emeten nous electrons secundaris. Si el camp de radiofreqüència canvia de fase en el moment de la col · lisió, pot accelerar els electrons secundaris cap a la paret oposada del dispositiu, generant més electrons secundaris i permetent un creixement exponencial en la població d'electrons. Esta acumulació, coneguda com a descàrrega de radiofreqüència o efecte multipactor, pot ser prou gran com per a reflectir la potència incident i inclús danyar el dispositiu o sistema involucrat.

El fenomen multipactor s'ha estudiat en uns quants camps en el passat. Així, els físics de partícules han estudiat el fenomen en relació amb la ciència del plasma i la dinàmica del feix de partícules, mentres que els enginyers han utilitzat el fenomen per a amplificar senyals en tubs de buit i klistrones. Per tant, depenent de la situació, l'efecte multipactor pot veure's com una fenomen beneficiós o com un efecte indesitjable. El treball d'investigació actual se centra en els efectes de la ruptura per multipactor en dispositius de radiofreqüència a bord de vehicles espacials (per exemple, satèl · lits) , on este es considera un fenomen indesitjable ja que pot causar danys irreparables en estos dispositius, deixant-los inutilitzables. En el context d'esta investigació, els dispositius de radiofreqüència típics utilitzats en aplicacions espacials inclouen guies d'ones, filtres i multiplexors. Si bé el maneig de potència d'estos dispositius ha augmentat en els

últims anys, també ho ha fet la seua complexitat geomètrica. Pel fet que la majoria dels models de multipactor fan algunes suposicions per a simplificar el problema, sobretot en les geometries involucrades, els models actuals de multipactor es tornen cada vegada més inexactes i ineficients a mesura que els dispositius es tornen més complexos.

En la primera part d'esta tesi es presenta un estudi rigorós de l'efecte multipactor en una guia d'ones rectangular parcialment carregada amb dielèctric. Es desenrotlla un model multipactor eficient que podria, eventualment, analitzar les estructures cada vegada més complexes utilitzades en la indústria espacial. Per a produir les simulacions presentades en esta tesi, s'ha realitzat una anàlisi detallat de la dinàmica de l'electró dins d'esta manera de guia d'ones, tenint en compte els camps electromagnètics de radiofreqüència que es propaguen en la guia d'ones i el camp electrostàtic que apareix a causa de la càrrega depositada sobre la capa dielèctrica de la mateixa. La caracterització d'este camp electrostàtic s'obté calculant el potencial elèctric produït per una distribució de càrrega arbitrària en la capa dielèctrica en una guia d'ones carregada amb dielèctric; resolent numèricament les equacions de moviment, s'obtenen les trajectòries dels electrons.

Un altre concepte important del procés d'emissió d'electrons és el conegut com *secondary emission yield*; definit com el nombre d'electrons secundaris emesos per electró incident, i sent específic del material, és un dels principals impulsors de l'efecte multipactor. En esta tesi s'han estudiat diverses alternatives diferents per a modelar el *secondary emission yield*.

La segona part de la tesi ha involucrat simulacions numèriques detallades de descàrregues multipactor dins de diverses configuracions de guies d'ones rectangulars que contenen materials dielèctrics. Estes simulacions s'han dut a terme utilitzant un codi a mesura desenrotllat específicament per a este treball d'investigació. Els resultats obtinguts han sigut validats amb mesures reals realitzades en laboratori sobre dispositius fabricats per a tal fi.

Contents

List of Tables

List of Figures

Listings

List of Acronyms

1D One-Dimensional.

2D Two-Dimensional.

3D Three-Dimensional.

CAD Computer-Aided Design.

DC Direct Current.

EEM Effective Electron Model.

EM Electromagnetic.

ESA European Space Agency.

FEP Fluorinated Ethylene Propylene.

HFSS High-Frequency Structure Simulator.

LSE Longitudinal Section Electric.

LSM Longitudinal Section Magnetic.

MDM Molecular Dynamics Method.

MoM Method of Moments.

MSSA Multichannel Singular Spectrum Analysis.

RF Radio Frequency.

SEE Secondary Electron Emission.

SEY Secondary Emission Yield.

SSA Singular Spectrum Analysis.

SVD Singular Value Decomposition.

TE Transverse Electric.

TEM Transverse Electromagnetic.

TM Transverse Magnetic.

VSC Val Space Consortium.

Chapter 1

Introduction

1.1 Background

The multipactor effect is a high-power resonant electron discharge frequently observed in microwave and millimetre-wave subsystems operating under the vacuum conditions present in a wide range of different scenarios, such as passive components of satellite communication payloads, travelling wave tubes or particle accelerators.

A scheme of the multipactor effect can be seen in Figure 1.1. In an ultra-high vac-

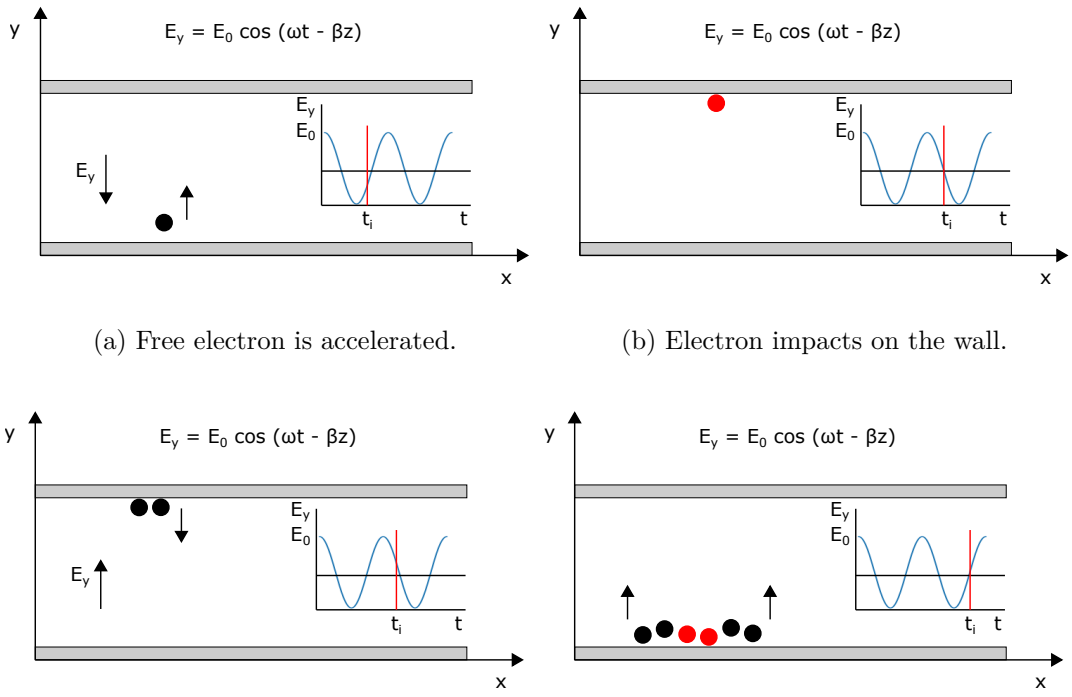

(a) Free electron is accelerated.

(b) Electron impacts on the wall.

(c) Secondary particles are emitted.

(d) Formation of electron cloud over time.

Figure 1.1: Multipactor build-up.

uum environment, free electrons inside a microwave device are accelerated by radio-frequency (RF) electromagnetic fields (Figure 1.1(a)) and impact against its metallic walls (Figure 1.1(b)). If an electron's impact energy is high enough, one or more secondary electrons might be released from the surface (Figure 1.1(c)). When certain resonance conditions are satisfied, secondary electrons become synchronized with the RF fields, and the electron population inside the device then grows exponentially, leading to a multipactor discharge (Figure 1.1(d)). As referenced in [5], experimental results show that this exponential discharge does not continue to grow indefinitely but eventually reaches saturation [6]. Several theories have been presented in the literature to explain the cause of this, but most agree that the underlying cause is that of the space-charge effect, also known as the electron-cloud effect [7]. This will be discussed in later chapters.

This multipactor discharge has some negative effects that degrade device performance: increase of signal noise and reflected power, heating of the device walls, outgassing, detuning of resonant cavities, and even the partial or total destruction of the component. Several lines of multipactor research have aimed to study and characterize the phenomenon, and predict under what conditions it will appear [8, 9, 10, 11]. Many works [12, 13] take advantage of susceptibility charts, calculated with analytical models, in empty parallel-plate waveguides [14], and they are directly used to predict multipactor breakdown in the component under study, which will happen at the point of highest field intensity. Thus, they aim to determine the region of highest field intensity, which is, in general, the smallest device gap. However, such susceptibility diagrams do not take into account important effects such as the so-called elastic and inelastic electrons, the 3D character of the motion of the electrons inside the waveguide, or the non-uniform nature of the electromagnetic fields in some particular cases.

Some RF devices, such as filters, multiplexers, and RF satellite payloads, include dielectric materials, commonly used as resonators and supporting elements. Kishek [15] presents a review of multipactor discharge on metals and dielectric windows that takes into account the dependence on surface materials, and the effects of space charge and cavity loading. The multipactor effect has been widely investigated in particle accelerators, including the use of dielectric materials in a single-surface multipactor regime; for instance, in ceramic RF windows [16, 17] and in alumina-based dielectric-loaded acceleration structures [18]. In contrast, there are very few contributions in relation to multipactor breakdown of dielectrics in the scenario of RF systems for space applications [19, 20, 21], and most of these rely on the parallel-plate waveguide

approximation. However, multipactor inside an empty rectangular waveguide has also been studied [22, 4], where conventional resonance theory gives correct predictions for the multipactor threshold if the height of the waveguide is very small and first-order resonance multipactor dominates. When the waveguide height exceeds a certain critical value, which depends on the waveguide width, an accurate prediction of the multipactor threshold requires consideration of the RF fields inside the waveguide without approximations. Therefore, an accurate prediction of the electron discharge in devices involving partially dielectric-loaded rectangular waveguides needs to be achieved.

1.2 Motivation and scope

The multipactor effect restricts the attainment of the optimum power limits of the devices used in space missions, a sufficient reason for the ESA and other research centres to invest time and resources in its suppression, or at least to diminish the secondary emission of electrons and, as a result, the detrimental consequences of multipactor [23].

As already noted, dielectrics in multipactor analysis have been, mainly, investigated within the framework of particle accelerators for the cases of ceramic RF windows [16, 24, 25, 26, 27, 28, 29] and dielectric-loaded accelerating (DLA) structures [30, 31, 32]. However, little is known about multipactor discharges on dielectric surfaces in the context of space applications. Some works have dealt numerically with multipactor discharge inside a parallel-plate waveguide partially loaded with a dielectric slab [19, 20]. Simulation results revealed an interesting self-extinguishing mechanism that acts within the long-term evolution of the phenomenon. However, these studies were based on the critical simplification of neglecting the charges induced on the metallic walls due to the surface charge on the dielectric material. It has been reported that such induced charges can significantly affect the steady state of the multipactor discharge [33], which provides a strong motivation to study the problem by including the effect of these induced charges [34].

1.3 Thesis contributions

A deep study of the multipactor effect in a partially dielectric-loaded rectangular waveguide has been carried out in this thesis. Consideration has been given to the RF electromagnetic fields, obtained with a very efficient vectorial modal method, and

the DC field caused by the appearance of a charge distribution in the dielectric layer. The solution of the electrostatic problem has required the use of different numerical integration techniques and interpolation methods. The electron trajectory has been numerically solved by using the velocity Verlet algorithm that provides sufficient accuracy and good efficiency. The multipactor prediction results for an empty and a partially dielectric-loaded rectangular waveguide have been obtained for validation. In both cases, the multipactor effect has been theoretically analysed (with and without dielectric material) and compared with multipactor measurements, and has shown excellent agreement between the theoretical model and the experimental data.

1.4 Thesis outline

The research work presented in this thesis is organized and structured in the form of six chapters, which are briefly described below:

- **Chapter 1** gives a relatively brief description of the theoretical background in relation to the research topic. For the purposes of clarity and understanding, this chapter is written as simply as possible to accommodate readers without a strong background in this topic. However, the reader is expected to have a basic knowledge of the underlying physics.

- **Chapter 2** provides a comprehensive review of the electromagnetic theory of rectangular waveguides. In order to accurately describe the trajectory of the electrons inside a rectangular waveguide, it is necessary to obtain the expressions of the electromagnetic fields within it. In particular, the case of a rectangular waveguide partially filled with dielectric material is rigorously analysed, it being the main subject of this thesis.

- **Chapter 3** presents the new model of the multipactor effect in rectangular waveguides partially filled with dielectric material that is developed in this research work. The chapter describes both the dynamics of the electrons inside the waveguide, and the underlying physics of the process of secondary electron emission that gives rise to the multipactor effect.

- **Chapter 4** presents the results of the simulation of the multipactor effect in different configurations of rectangular waveguides, both empty and partially filled with dielectric material. To conduct these simulations, the simulation

tool developed in this thesis is presented, in relation to which different methods and approximations of the calculations are compared.

- **Chapter 5** validates the theoretical model of the multipactor effect presented here. To meet this objective, the results of the simulations carried out with the software developed in-house are compared with those obtained with simulation tools from third-party providers. Moreover, experimental measurements carried out within the framework of this thesis are used to corroborate the validity of the new multipactor model in rectangular waveguides partially filled with dielectric material.

- **Chapter 6** concludes the thesis with a review of its findings and remarks about the present research work. The scope for future work is also discussed.

1.5 List of publications

The findings of this thesis have been presented in several journal publications, international conferences and Spanish national conferences. The active participation of the author in various lines of research offered the opportunity to develop fruitful collaborations with other entities in the wider context of this thesis, specifically the Department of Applied Physics and Electromagnetism-ICMUV at the University of Valencia, the Department of Applied Physics I at the University of Seville, the Department of Communications at the Polytechnic University of Valencia, and the Val Space Consortium.

A complete list of publications and dissemination activities, together with their associated contributions, are listed below.

Journals

- A. Berenguer, A. Coves, B. Gimeno, E. Bronchalo and V. E. Boria, "Experimental Study of the Multipactor Effect in a Partially Dielectric-Loaded Rectangular Waveguide", *IEEE Microwave and Wireless Components Letters*, vol. 29, no. 9, pp. 595–597, Sep. 2019, DOI: 10.1109/LMWC.2019.2929488.

- A. Berenguer, A. Coves, F. Mesa, E. Bronchalo and B. Gimeno, "Analysis of Multipactor Effect in a Partially Dielectric-Loaded Rectangular Waveguide", *IEEE Transactions on Plasma Science*, vol. 47, no. 1, pp. 259–265, Jan. 2019, DOI: 10.1109/TPS.2018.2880652.

Conferences

- A. Berenguer, A. Coves, E. Bronchalo, F. Mesa and B. Gimeno, "Técnicas numéricas avanzadas para el cálculo del campo electrostático en guías de onda rectangulares con dieléctrico", *XXXIV Simposium Nacional de la Unión Científica Internacional de Radio (URSI19)*, Sevilla, Spain, Sep. 2019.

- A. Berenguer, A. Coves, F. Mesa, E. Bronchalo and B. Gimeno, "Nuevo modelo del efecto multipactor para guías rectangulares parcialmente rellenas de dieléctrico", *XXXIV Simposium Nacional de la Unión Científica Internacional de Radio (URSI19)*, Sevilla, Spain, Sep. 2019.

- A. Berenguer, A. Coves and E. Bronchalo, "Comparative Study of Multipactor Effect in Rectangular and Parallel-plate Waveguides Partially Loaded with Dielectric", *Photonics & Electromagnetics Research Symposium (PIERS19)*, Rome, Italy, Jun. 2019, DOI: 10.1109/PIERS-Spring46901.2019.9017302.

- A. Berenguer, A. Coves, E. Bronchalo and F. Mesa, "Analysis of Mathematical Techniques for the Calculation of the Electrostatic Field in a Dielectric-loaded Waveguide", *Photonics & Electromagnetics Research Symposium (PIERS19)*, Rome, Italy, Jun. 2019, DOI: 10.1109/PIERS-Spring46901.2019.9017715.

- A. Berenguer, A. Coves, F. Mesa, E. Bronchalo and B. Gimeno, "A New Multipactor Effect Model for Dielectric-Loaded Rectangular Waveguides", *2019 IEEE MTT-S International Conference on Numerical Electromagnetic and Multiphysics Modeling and Optimization (NEMO19)*, Boston, MA, USA, May 2019, pp. 1-4, DOI: 10.1109/NEMO.2019.8853708.

- A. Berenguer, A. Coves, F. Mesa, E. Bronchalo, B. Gimeno and V. Boria, "Analysis of the electrostatic field generated by a charge distribution on a dielectric layer loading a rectangular waveguide", *XXXI Simposium Nacional de la Unión Científica Internacional de Radio (URSI16)*, Madrid, Spain, Sep. 2016.

- A. Berenguer, A. Coves, F. Mesa, E. Bronchalo, B. Gimeno and V. Boria, "Calculation of the electrostatic field in a dielectric-loaded waveguide due to an arbitrary charge distribution on the dielectric layer", *Progress In Electromagnetics Research Symposium (PIERS16)*, Shanghai, China, Aug. 2016, DOI: 10.1109/PIERS.2016.7735274.

- A. Berenguer, A. Coves, E. Bronchalo, B. Gimeno and V. Boria, "Comparison of multipactor effect in parallel-plate and rectangular waveguides: 1D and 2D-3D models", *XXX Simposium Nacional de la Unión Científica Internacional de Radio (URSI15)*, Pamplona, Spain, Sep. 2015.

- A. Berenguer, A. Coves, E. Bronchalo, B. Gimeno and V. Boria, "Analysis of multipactor effect in parallel-plate and rectangular waveguides", *Progress In Electromagnetics Research Symposium (PIERS15)*, Praga, Czech Republic, Jul. 2015.

Other journal publications related to this thesis

- A. Berenguer, L. Gandarias and A. Arévalo, "Singular spectrum analysis for modelling the hard-to-model risk factors", *Risk Management*, vol. 22, no. 3, pp. 178–191, Sep. 2020, DOI:10.1057/s41283-020-00060-5.

Chapter 2

Electromagnetic analysis of dielectric-loaded rectangular waveguides

2.1 Introduction

Waveguides are transmission media commonly used in electronics, especially at microwave frequencies. Some common guiding structures are the coaxial cable, hollow conducting waveguides, two-wire and microstrip transmission lines and optical fibers. These devices are used to transfer electromagnetic power efficiently from one point in space to another. The choice of structure is determined by the desired operating frequency band, the amount of power to be transferred, and the level of transmission losses that can be tolerated. In this chapter, we focus on the rectangular waveguide, a structure widely used in space communications engineering for its power handling capability and its low losses.

In Section 2.2, the electromagnetic analysis of an empty rectangular waveguide is performed, and the equations that describe the movement of electrons inside the waveguide in both relativistic terms and under a non-relativistic approach are derived.

The case of a rectangular waveguide that is partially filled with dielectric material is examined in Section 2.3. This form of waveguide greatly interests the space industry because, among other characteristics, it allows the range of input power and working frequencies in which the multipactor effect occurs to be changed. In these structures, design flexibility is increased by introducing variables such as the height and physical characteristics of the dielectric material. To date, the multipactor effect in these waveguides has not been widely studied, and it is to this that the work carried out in this thesis pays special attention. In this section, the methods used to calculate the

electromagnetic fields inside the guide are shown, using both numerical and analytical methods. Finally, in Section 2.4, the equations for the electrostatic field that is generated during the movement of an electron inside the waveguide because of its multiple impacts with the dielectric layer are determined.

2.2 Empty rectangular waveguide

Rectangular waveguides were one of the earliest transmission media used to transport microwave signals, and they are still used for many applications. A large variety of components, such as attenuators, power detectors, couplers, isolators, and slotted lines, are commercially available for various standard waveguide bands from 1 GHz to 220 GHz. There is still a need for waveguides in a variety of uses, including high-power systems, satellite systems, millimetre-wave applications, and some precision-testing applications [35]. In Figure 2.1, some standard rectangular waveguide components available in industry are shown.

Figure 2.1: Several examples of rectangular waveguide straight sections. Image downloaded from QuinStar Technology, Inc. website in May 2020.

We start by studying the movement of a free electron in the case of a rectangular hollow waveguide with conducting walls. The waveguide is typically filled with air, but any other dielectric material (of permittivity ϵ_r) may be assumed. Figure 2.2 shows the transverse section of an empty rectangular waveguide, air-filled (ϵ_0), of width a and height b. Without loss of generality, we may assume that the lengths a, b of the inner sides satisfy $b \ll a$. The RF electromagnetic field is assumed to propagate

along the positive direction of the z-axis. The electron located at $\mathbf{r} = (x, y, z)$ can move within the air-filled region of the rectangular waveguide.

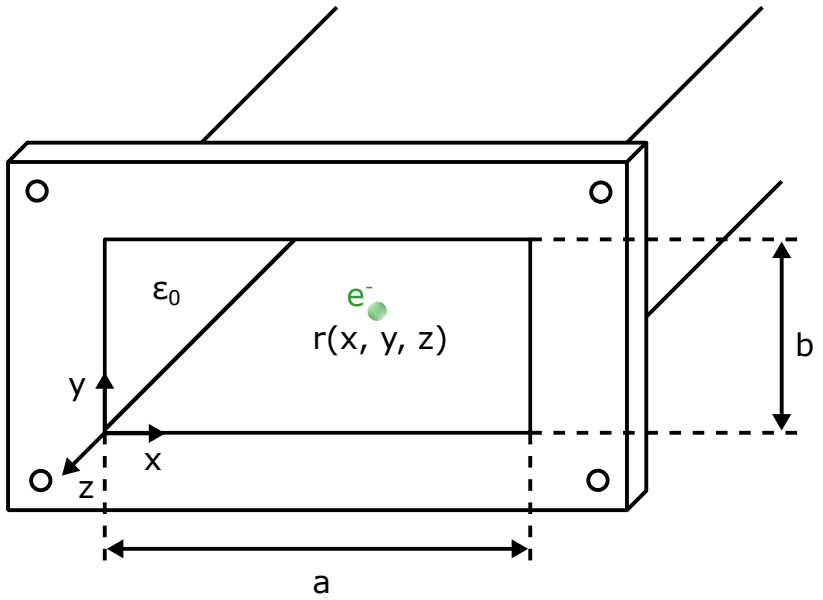

Figure 2.2: Transverse section of an empty rectangular waveguide, air-filled (ϵ_0), of width a and height b.

A highly efficient vectorial modal method developed in [36] for obtaining the modes of an inhomogeneously dielectric-filled waveguide can be employed to find the propagation constant and all of the electric and magnetic field components of the p-th waveguide mode (β_p, $\mathbf{e}_p$, $\mathbf{h}_p$). This method becomes relevant for partially dielectric-loaded waveguides, in which case the electromagnetic fields $\mathbf{E}_{\mathrm{RF}}$ and $\mathbf{H}_{\mathrm{RF}}$ have to be numerically computed, given that in general there is no analytical solution for the propagation modes in this case. This will be explained in more detail later. However, given that an analytical solution exists in the case of an empty rectangular waveguide, we have directly used this solution in this instance.

The normalized $\mathrm{TE}_{\mathrm{mn}}$ and $\mathrm{TM}_{\mathrm{mn}}$ modes in an empty rectangular waveguide are given by [37]:

$$\tilde{\mathbf{e}}_p^{\mathrm{TE}} = -N_p^{\mathrm{TE}} \left(k_{yn} \cos\left(k_{xm}x\right) \sin\left(k_{yn}y\right) \hat{\mathbf{x}} - k_{xm} \sin\left(k_{xm}x\right) \cos\left(k_{yn}y\right) \hat{\mathbf{y}}\right) , \tag{2.1a}$$

$$\tilde{\mathbf{h}}_p^{\mathrm{TE}} = -N_p^{\mathrm{TE}} \left(k_{xm} \sin\left(k_{xm}x\right) \cos\left(k_{yn}y\right) \hat{\mathbf{x}} - k_{yn} \cos\left(k_{xm}x\right) \sin\left(k_{yn}y\right) \hat{\mathbf{y}}\right) , \tag{2.1b}$$

$$\tilde{\mathbf{e}}_p^{\mathrm{TM}} = N_p^{\mathrm{TM}} \left(k_{xm} \cos\left(k_{xm}x\right) \sin\left(k_{yn}y\right) \hat{\mathbf{x}} + k_{yn} \sin\left(k_{xm}x\right) \cos\left(k_{yn}y\right) \hat{\mathbf{y}}\right) , \tag{2.1c}$$

$$\tilde{\mathbf{h}}_p^{\mathrm{TM}} = -N_p^{\mathrm{TM}} \left(k_{yn} \sin\left(k_{xm}x\right) \cos\left(k_{yn}y\right) \hat{\mathbf{x}} + k_{xm} \cos\left(k_{xm}x\right) \sin\left(k_{yn}y\right) \hat{\mathbf{y}}\right) , \tag{2.1d}$$

which refer to a coordinate system origin located at the bottom-left waveguide corner (Figure 2.2), and where the normalization constants N_p^{TE} and N_p^{TM} for both the $\mathrm{TE_{mn}}$ and $\mathrm{TM_{mn}}$ modes are defined as:

$$N_p^{\mathrm{TE}} = \sqrt{\frac{\epsilon_m \epsilon_n}{ab}} \frac{1}{\sqrt{k_{xm}^2 + k_{yn}^2}}\,, \tag{2.2a}$$

$$N_p^{\mathrm{TM}} = \frac{2}{\sqrt{ab}} \frac{1}{\sqrt{k_{xm}^2 + k_{yn}^2}}\,, \tag{2.2b}$$

and $k_{xm} = m\pi/a$, $k_{yn} = n\pi/b$ are the wave-numbers along the x- and y-axes respectively for the $\mathrm{TE_{mn}}$ and $\mathrm{TM_{mn}}$ modes. The p-th mode has associated the pair of indices m and n, which can take the following values for each family of modes: $\{\mathrm{TE_{mn}} : m, n \in \mathbb{W} \setminus m = n = 0\}$[1] and $\{\mathrm{TM_{mn}} : m, n \in \mathbb{N}\}$.

The cut-off wave-number $(k_c)_{mn}$ of these modes takes on the quantized value:

$$(k_c)_{mn} = \sqrt{k_{xm}^2 + k_{yn}^2} = \sqrt{\left(\frac{m\pi}{a}\right)^2 + \left(\frac{n\pi}{b}\right)^2}\,, \tag{2.3}$$

where the cut-off frequencies $(f_c)_{mn}$ and wavelengths $(\lambda_c)_{mn}$ are:

$$(f_c)_{mn} = \frac{1}{2\sqrt{\epsilon\mu}} \sqrt{\left(\frac{m}{a}\right)^2 + \left(\frac{n}{b}\right)^2}\,, \tag{2.4a}$$

$$(\lambda_c)_{mn} = \frac{2}{\sqrt{\left(\frac{m}{a}\right)^2 + \left(\frac{n}{b}\right)^2}}\,. \tag{2.4b}$$

The simplest and dominant propagation mode is the $\mathrm{TE_{10}}$ mode, which depends only on the x-coordinate (of the longest side.) We have restricted our study to this single-mode regime of the waveguide at the working frequency ($p = 1$, and thus $\beta_1 = \beta$, $\mathbf{e}_1 = \mathbf{e}$, and $\mathbf{h}_1 = \mathbf{h}$).

The instantaneous electric and magnetic field vectors inside the waveguide interacting with the electron are given by:

$$\mathbf{E}_{\mathrm{RF}}(x, y, z, t) = E_0 \,\mathrm{Re}\left(\mathbf{e}(x, y) e^{j(\omega t - \beta z + \phi_0)}\right)\,, \tag{2.5a}$$

$$\mathbf{H}_{\mathrm{RF}}(x, y, z, t) = H_0 \,\mathrm{Re}\left(\mathbf{h}(x, y) e^{j(\omega t - \beta z + \phi_0)}\right)\,, \tag{2.5b}$$

where ϕ_0 is the initial phase, and E_0, H_0 constants relate to the transmitted power in the waveguide. These expressions can be directly extended if higher-order modes must be taken into account (e.g. in waveguide discontinuities) by using the mode-matching technique.

[1] $\mathbb{W}$ refers to the set of whole numbers, i.e. the set of natural numbers $\mathbb{N}$ including 0.

2.2.1 Relativistic movement of an electron in the field of a linearly polarized plane wave

Before analysing the trajectory of the electrons in an empty waveguide, we will here describe the movement of an electron in the field of a linearly polarized plane wave with electric field $E_y = E_0 \cos(\omega t - \beta z)$ polarized along the y-axis in the most general case, including the relativistic terms, that has an analytical solution [38]. The equations of motion are obtained as:

$$x = 0\,, \tag{2.6a}$$

$$y = -\frac{eE_0 c}{\gamma\omega^2}\cos(\eta)\,, \tag{2.6b}$$

$$z = -\frac{e^2 E_0^2 c}{8\gamma^2\omega^3}\sin(2\eta)\,, \tag{2.6c}$$

$$t = \frac{\eta}{\omega} + \frac{z(\eta)}{c}\,, \tag{2.6d}$$

where

$$\gamma^2 = m^2c^2 + \frac{e^2E_0^2}{2\omega^2}\,, \tag{2.7}$$

and the parameter η ranges from 0 to 2π, having a periodic movement.

The above equations make reference to a system in which the charged particle is at rest, on average, describing a figure-of-8-shaped periodic movement. At non-relativistic speeds, and for typical frequencies and fields ($f \sim 10\,\mathrm{GHz}$, $E_0 \sim 1000\,\mathrm{V\,m^{-1}}$), Equation (2.7) can be approximated as:

$$\gamma \cong mc\,, \tag{2.8}$$

and the equations of motion are given by:

$$x = 0\,, \tag{2.9a}$$

$$y = -\frac{eE_0}{m\omega^2}\cos(\eta)\,, \tag{2.9b}$$

$$z = -\frac{e^2E_0^2}{8m^2c\,\omega^3}\sin(2\eta)\,, \tag{2.9c}$$

$$t = \frac{\eta}{\omega} + \frac{z(\eta)}{c}\,. \tag{2.9d}$$

The ratio of the amplitudes of the movement along the y- and z-axes is $\frac{8mc\omega}{eE_0}$. Therefore, for ordinary frequencies and fields, this ratio is of the order of 10^6. Thus, in the circumstances described, the movement of an electron on the z-axis due to the action of the wave is irrelevant, in terms of the reference system in which the electron is, on a time average, at rest.

2.2.2 Non-relativistic movement of an electron in an empty rectangular waveguide in a single-mode regime

In contrast with the previous case, in the empty rectangular waveguide the equation of motion of an electron, even in a single-mode regime when only the fundamental TE_{10} mode propagates, has no analytical solution. However, for energies lower than 100 eV, in which case the electron velocity is lower than $0.02c$, the magnetic field component of the Lorentz force is not very relevant. Under these conditions, the only force on the electron is due to the electric field, which can be expressed as:

$$E_y(x,z,t) = E_0 \cos\left(\frac{\pi x}{d}\right) \cos(\omega t - \beta z + \phi_0)\,, \tag{2.10}$$

where ϕ_0 is the field phase at $z = 0$ and $t = 0$. Note that, for simpler notation, the width dimension a of the rectangular waveguide has been substituted by d to avoid confusion with the acceleration term of the electron.

Next, we will show that the electron equations of motion can be solved analytically. To start with, consider the initial conditions for the movement of the electron at $t = t_0$ to be:

$$\mathbf{r}(t_0) = (x_0, y_0, z_0)\,, \tag{2.11a}$$

$$\mathbf{v}(t_0) = (v_{0x}, v_{0y}, v_{0z})\,. \tag{2.11b}$$

The evolution of the electron's position, based on the previous assumption, is given by:

$$x(t) = x_0 + v_{0x}(t - t_0)\,, \tag{2.12a}$$

$$z(t) = z_0 + v_{0z}(t - t_0)\,, \tag{2.12b}$$

$$\begin{aligned} y(t) = {} & y_0 + v_{0y}(t - t_0) - \frac{a_0(t - t_0)}{2}\left(\frac{\sin(\omega_- t_0 + \phi_-)}{\omega_-} + \frac{\sin(\omega_+ t_0 + \phi_+)}{\omega_+}\right) \\ & - \frac{a_0}{2}\left(\frac{\cos(\omega_- t + \phi_-) - \cos(\omega_- t_0 + \phi_-)}{\omega_-^2} + \frac{\cos(\omega_+ t + \phi_+) - \cos(\omega_+ t_0 + \phi_+)}{\omega_+^2}\right)\,, \end{aligned} \tag{2.12c}$$

and its velocity is:

$$v_x(t) = v_{0x}\,, \tag{2.13a}$$

$$v_z(t) = v_{0z}\,, \tag{2.13b}$$

$$\begin{aligned} v_y(t) = {} & v_{0y} \\ & + \frac{a_0}{2}\left(\frac{\sin(\omega_- t + \phi_-) - \sin(\omega_- t_0 + \phi_-)}{\omega_-} + \frac{\sin(\omega_+ t + \phi_+) - \sin(\omega_+ t_0 + \phi_+)}{\omega_+}\right)\,, \end{aligned} \tag{2.13c}$$

where

$$a_0 = \frac{-eE_0}{m}\,, \tag{2.14}$$

$$\omega_- \equiv \omega - \beta v_{0z} - \frac{\pi}{d} v_{0x}\,, \tag{2.15a}$$

$$\omega_- \equiv \omega - \beta v_{0z} + \frac{\pi}{d} v_{0x}\,, \tag{2.15b}$$

$$\phi_- \equiv \beta(v_{0zt_0 - z_0}) + \phi_0 - \frac{\pi}{d}(x_0 - v_{0x}t_0)\,, \tag{2.16a}$$

$$\phi_+ \equiv \beta(v_{0zt_0 - z_0}) + \phi_0 + \frac{\pi}{d}(x_0 - v_{0x}t_0)\,. \tag{2.16b}$$

Such equations of motion for an electron inside an empty rectangular waveguide will be used in Chapter 3, along with the most general case in which all field components of the fundamental mode are taken into account, in order to assess the validity of the approximations that have been applied.

Finally, for the case that considers the magnetic force at non-relativistic speeds, the electromagnetic fields of the fundamental mode are given by:

$$E_y = -E_0 \cos\left(\frac{\pi x}{d}\right) \cos(\omega t - \beta z)\,, \tag{2.17a}$$

$$B_x = \frac{E_0}{c}\sqrt{1 - \left(\frac{\omega_c}{\omega}\right)^2} \cos\left(\frac{\pi x}{d}\right) \cos(\omega t - \beta z)\,, \tag{2.17b}$$

$$B_z = \frac{E_0}{c}\frac{\omega_c}{\omega} \sin\left(\frac{\pi x}{d}\right) \sin(\omega t - \beta z)\,, \tag{2.17c}$$

and the non-relativistic equations for electron movement are:

$$a_x = \frac{-e}{m} v_y B_z\,, \tag{2.18a}$$

$$a_y = \frac{-e}{m}(E_y - v_x B_z + v_z B_x)\,, \tag{2.18b}$$

$$a_z = \frac{-e}{m}(-v_y B_x)\,. \tag{2.18c}$$

In Equation (2.18b), the magnetic force due to B_x is negligible compared to the electric force at ordinary speeds (B_x and E_y vary in the same way along the x-coordinate), so it can be discounted.

The magnetic force due to B_z is equal in amplitude to that due to E_y when:

$$\frac{v_x}{c}\frac{\omega_c}{\omega} = \cot\left(\frac{\pi x}{d}\right)\,. \tag{2.19}$$

On the side walls ($x = \pm d/2$), the cotangent function is zero. The electric field in $x = \pm d/2$ is null, and therefore the magnetic force becomes greater than the electric force for any non-zero velocity.

The higher the velocity v_x, the more the lines in which both forces are equalized move toward the centre. For a speed of $0.05c$ (electron energy of the order of 250 eV), and assuming a working frequency of 1.5 times that of cut-off frequency:

$$\tan\left(\frac{\pi x}{d}\right) = 30\,, \tag{2.20}$$

$$x = d\,\frac{\arctan(30)}{\pi} = 0.489d\,. \tag{2.21}$$

Therefore, for ordinary energies the line in which the magnetic force is equal to the electric one is practically next to the side walls. In the vast majority of the interval $-d/2 < x < d/2$, the y-component of the force due to the z-component of the magnetic field B_z is also negligible. The two terms that have been omitted are the same as those ignored by Semenov et al. [22]. Thus, defining $a_0 \equiv eE_0/m$, the equations of motion are then:

$$a_x = -a_0\frac{v_y}{\omega}\frac{\pi}{d}\sin\left(\frac{\pi x}{d}\sin(\omega t - \beta z)\right)\,, \tag{2.22a}$$

$$a_y = a_0\cos\left(\frac{\pi x}{d}\cos(\omega t - \beta z)\right)\,, \tag{2.22b}$$

$$a_z = a_0\frac{v_y}{v_f}\cos\left(\frac{\pi x}{d}\cos(\omega t - \beta z)\right)\,, \tag{2.22c}$$

where v_f is the phase velocity of the guided wave. Because there is no explicit dependency on the y-component in any of the equations, we can use v_y instead of y as the dependent variable. Using Equation (2.22b), Equation (2.22c) can then be expressed in the form:

$$a_z = \frac{v_y}{v_f}a_y = \frac{1}{2v_f}\frac{\mathrm{d}v_y^2}{\mathrm{d}t}\,. \tag{2.23}$$

Integrating with respect to time we obtain:

$$v_z = v_{0z} + \frac{v_y^2 - v_{0y}^2}{2v_f}\,, \tag{2.24}$$

where the zero subscripts indicate value at $t = 0$.

Next, consider the relationship between the variation in kinetic energy and the work done by the forces on the electron, bearing in mind that magnetic forces do not do work:

$$\frac{m}{2}\frac{\mathrm{d}}{\mathrm{d}t}\left(v_x^2 + v_y^2 + v_z^2\right) = \mathbf{F}\mathbf{v} = -eE_y v_y = m\dot{v_y}v_y\,, \tag{2.25}$$

thus:

$$v_x \dot{v_x} + v_z \dot{v_z} = 0 \implies v_x^2 + v_z^2 = v_{0x}^2 + v_{0z}^2 \,. \tag{2.26}$$

From Equations (2.24) and (2.27), the velocity v_x can be expressed as a function of v_y:

$$v_x^2 = v_{x0}^2 - \left(\left(\frac{v_{z0}}{v_f} - \frac{v_{0y}^2}{2v_f^2} \right) (v_y^2 - v_{0y}^2) + \frac{1}{4v_f^2}(v_y^4 - v_{0y}^4) \right) . \tag{2.27}$$

Defining $u \equiv v_y$, the equations of motion can then be expressed as:

$$\dot{x} = \left[v_{x0}^2 - \left(\left(\frac{v_{z0}}{v_f} - \frac{v_{0y}^2}{2v_f^2} \right) (u^2 - v_{0y}^2) + \frac{1}{4v_f^2}(u^4 - v_{0y}^4) \right) \right]^{1/2} , \tag{2.28a}$$

$$\dot{z} = v_{0z} + \frac{1}{2v_f}(u^2 - v_{0y}^2) \,, \tag{2.28b}$$

$$\dot{u} = a_0 \cos\left(\frac{\pi x}{d}\right) \cos(\omega t - \beta z) \,, \tag{2.28c}$$

resulting in a system of first-order differential equations (neither linear nor autonomous), there being an explicit dependency on t. These equations have no analytical solution so the velocity Verlet numerical method will be used to solve the equations for an electron path in the empty rectangular waveguide, without approximations.

2.3 Dielectric-loaded rectangular waveguide

The previous results apply to an empty waveguide, but in some cases of practical interest a waveguide is used with a partial dielectric filling. In such cases, an additional set of boundary conditions are introduced at the material interface, requiring a fresh analysis.

Partially dielectric-loaded waveguides have received considerable attention in recent decades because of their application to a variety of waveguide-based components. The modes of propagation of such waveguides are not, in general, TM or TE modes, but hybrid modes. In addition, in certain symmetrical situations, such as a dielectric layer with the same waveguide width, the so-called longitudinal-section modes are obtained [39]. There is an analogy between the way transverse (TE and TM) modes are arrived at and the definition of longitudinal-section (Longitudinal Section Electric (LSE) and Longitudinal Section Magnetic (LSM), also known as TE^{y} and TM^{y}) modes.

As explained by Zhang and Li in [40], when determining whether a structure can support a particular TE mode, one sets the electric field in the z-direction (the

longitudinal direction of the waveguide) to zero and then solves Maxwell's equations for the boundary conditions set by the physical structure of the waveguide. One can just as easily set the electric field in the x-direction to zero and ask what modes that gives rise to. Such modes are designated $\mathrm{LSE}^{\mathrm{x}}$ modes. Similarly, there can be $\mathrm{LSE}^{\mathrm{y}}$ modes and, analogously for the magnetic field, $\mathrm{LSM}^{\mathrm{x}}$ and $\mathrm{LSM}^{\mathrm{y}}$ modes.

When dealing with longitudinal-section modes, the TE and TM modes are sometimes written as $\mathrm{LSE}^{\mathrm{z}}$ and $\mathrm{LSM}^{\mathrm{z}}$, respectively, to produce a consistent set of notations and to reflect the analogous way in which they are defined. Both LSE and LSM modes are a linear superposition of the corresponding TE and TM modes (that is, the modes with the same suffix numbers). Thus, in general, the LSE and LSM modes have a longitudinal component of both electric and magnetic fields. Likewise, the LSM modes are found by setting one of the transverse components of the magnetic field to zero, with analogous results .

Several configurations of inhomogeneously filled waveguides have been studied in the literature, such as the image waveguide. As explained by Monsoriu in [41], complex modes in lossless waveguides are guided waves with complex propagation constants. Because of the lossless nature of the structure supporting such modes, they always exist in pairs with complex conjugate propagation constants of opposite sign, so that both have the same attenuation constant. Each one of these complex modes has a total power flow equal to zero, with one sign inside the dielectric region and the opposite sign outside. For the corresponding conjugate mode, these signs are the opposite ones. Investigations have shown that complex waves have to be included in the field expansion used in field-matching procedures for the analysis of discontinuity problems in waveguide structures; their omission leads to erroneous results. Because complex waves make up an unavoidable part of the spectrum of the operator describing electromagnetic field propagation in inhomogeneously dielectric-filled waveguides, it is important to have a robust method of analysis in order to deal with these modes and ensure accurate and efficient computational modelling. However, the characterization of complex modes with conventional methods presents some difficulties (e.g. the nature of complex modes makes their detection difficult, while other propagating modes could mask them).

The rigorous and computationally efficient method to determine the electromagnetic field in a dielectric-loaded rectangular waveguide proposed by Silvestre et al. in [42] has been used in this thesis. As they explain in their work, it is a straightforward and spurious-mode-free method that can derive the complex modal spectrum in inhomogeneously filled waveguides with lossy dielectrics of arbitrary profile. Starting

with the differential equations governing the propagation of the transverse electric and magnetic fields, a pair of linear non-self-adjoint operators is identified, whose eigenvectors satisfy a bi-orthogonality relationship. The key element of the approach is to transform the system of differential equations into a linear matrix eigenvalue problem using the Galerkin method, using the eigenvectors of an auxiliary problem. From a computational point of view, this method is very efficient because the integrals involved in the matrix elements are, in principle, frequency-independent, so they have to be evaluated only once to obtain the dispersion curves, thus generating robust and efficient code.

Figure 2.3 shows the transverse section of a partially dielectric-loaded rectangular waveguide of width a and height b, and whose dielectric material has relative permittivity ϵ_r. In the problem under study, a dielectric slab of thickness h and width a is placed over the bottom waveguide wall, d being the empty waveguide height wherein the electrons travel.

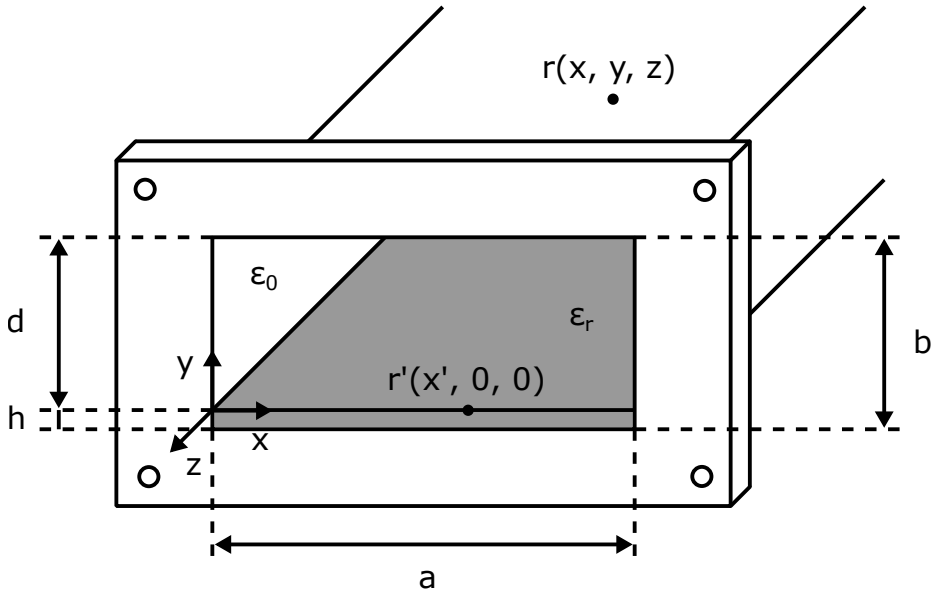

Figure 2.3: Partially dielectric-loaded rectangular waveguide with a dielectric layer on the bottom wall.

The auxiliary system chosen for this problem is a homogeneous rectangular waveguide filled with air, of the same dimensions as the dielectric-loaded waveguide under study. It also meets the same boundary conditions at the walls of the waveguide satisfied by the real problem. Due to the boundary conditions imposed by the discontinuity in the y-axis of the dielectric material, the families of TE^y and TM^y modes of the homogeneous rectangular waveguide, which are transverse modes to the direction of the y-axis and therefore also meet the boundary conditions of the real system,

have been considered. These modes, once normalized to fulfil the bi-orthogonality relationship, are given by:

$$\tilde{\mathbf{e}}_p^{\mathrm{TE}} = \cos(k_{xm}x)\sin(k_{yn}y)\hat{\mathbf{x}}\,, \tag{2.29a}$$

$$\tilde{\mathbf{h}}_p^{\mathrm{TE}} = -\frac{k_{xm}k_{yn}}{-k_{yn}^2}\sin(k_{xm}x)\cos(k_{yn}y)\hat{\mathbf{x}} + \cos(k_{xm}x)\sin(k_{yn}y)\hat{\mathbf{y}}\,, \tag{2.29b}$$

$$\tilde{\mathbf{e}}_p^{\mathrm{TM}} = N_p^{\mathrm{TM}}\left(k_{xm}\cos\left(k_{xm}x\right)\sin\left(k_{yn}y\right)\hat{\mathbf{x}} + k_{yn}\sin\left(k_{xm}x\right)\cos\left(k_{yn}y\right)\hat{\mathbf{y}}\right)\,, \tag{2.29c}$$

$$\tilde{\mathbf{h}}_p^{\mathrm{TM}} = \sin(k_{xm}x)\cos(k_{yn}y)\hat{\mathbf{x}}\,, \tag{2.29d}$$

where the p-th mode has the pair of indexes m and n associated with it, which can take the following values for each family of modes: $\mathrm{TE}^y : m = 0, 1, 2, ...\ n = 1, 2, 3, ...$; $\mathrm{TM}^y : m = 1, 2, 3, ...\ n = 0, 1, 2, ...$.

2.3.1 Analytical approach for the fundamental mode of a rectangular waveguide with a dielectric layer on the bottom wall

Let us consider a rectangular waveguide loaded with a dielectric layer of height h on the bottom wall with relative permittivity ϵ_r. Figure 2.3 shows the transverse section of the waveguide. The modes in this waveguide are hybrid modes, with z-components in the magnetic and electric fields. If the height h of the dielectric layer is much smaller than b, the fundamental mode should resemble the TE_{10} mode of the empty waveguide. The corresponding hybrid mode is the TM_{10}^y, with no magnetic field in the y-component.

The electric field components for the TE_{10} mode in a vacuum are:

$$E_x = \frac{1}{j\beta}\frac{\partial^2 F}{\partial x \partial y}\,, \tag{2.30a}$$

$$E_y = \frac{1}{j\beta}\frac{\partial^2 F}{\partial y^2} + \beta^2 F\,, \tag{2.30b}$$

$$E_z = \frac{1}{j\beta}\frac{\partial^2 F}{\partial z \partial y}\,, \tag{2.30c}$$

and the magnetic field components are:

$$H_x = -\frac{1}{\mu_0}\frac{\partial F}{\partial z}\,, \tag{2.31a}$$

$$H_y = 0\,, \tag{2.31b}$$

$$H_z = \frac{1}{\mu_0}\frac{\partial F}{\partial x}\,, \tag{2.31c}$$

where $F(x, y, z)$ is the potential function, defined as:

$$F = F_0 \sin(\beta_x x) \cos(\beta_y (b - y + h)) e^{-j\beta_z z}\,, \tag{2.32}$$

where $\beta_x = \pi/a$ and β_y meets the condition:

$$\beta_x^2 + \beta_y^2 + \beta_z^2 \equiv \beta^2 = \frac{\omega}{2c}^2\,. \tag{2.33}$$

Substituting Equation (2.32) into Equations (2.30) and (2.31) yields:

$$E_x = F_0 \frac{\beta_y \beta_z}{j\beta} \cos(\beta_x x) \sin(\beta_y (b - y + h)) e^{-j\beta_z z}\,, \tag{2.34a}$$

$$E_y = F_0 \frac{\beta_x^2 + \beta_z^2}{j\beta} \sin(\beta_x x) \cos(\beta_y (b - y + h)) e^{-j\beta_z z}\,, \tag{2.34b}$$

$$E_z = -F_0 \frac{\beta_z \beta_y}{\beta} \sin(\beta_x x) \sin(\beta_y (b - y + h)) e^{-j\beta_z z}\,, \tag{2.34c}$$

and

$$H_x = F_0 \frac{j\beta_z}{j\mu_0} \sin(\beta_x x) \cos(\beta_y (b - y + h)) e^{-j\beta_z z}\,, \tag{2.35a}$$

$$H_y = 0\,, \tag{2.35b}$$

$$H_z = F_0 \frac{\beta_x}{\mu_0} \cos(\beta_x x) \cos(\beta_y (b - y + h)) e^{-j\beta_z z}\,. \tag{2.35c}$$

The value of β_y can be obtained by forcing β_z to take the same value on both sides of the boundary, i.e. phase adjustment. This condition leads to:

$$\epsilon_r \beta_y \tan(\beta_y (b - h)) + \sqrt{\left(\frac{\omega}{c}\right)^2 (\epsilon_r - 1) + \beta_y^2} \tan\left(h \sqrt{\left(\frac{\omega}{c}\right)^2 (\epsilon_r - 1) + \beta_y^2}\right) = 0\,. \tag{2.36}$$

In terms of the TE_{10} mode of the empty rectangular waveguide, it must be quite similar to the TM_{10}^y in the presence of dielectric when $h \ll b$:

$$\left(\frac{\pi}{a}\right)^2 + \beta_z^2 = \left(\frac{\omega}{c}\right)^2\,. \tag{2.37}$$

Thus β_y must be much smaller than ω/c when $h \ll b$ and it is reasonable to make the approximation:

$$\tan(\beta_y (b - h)) \cong \beta_y (b - h)\,. \tag{2.38}$$

Moreover, because h is smaller than a and ω/c is the same order of magnitude as π/a, it transpires that:

$$\tan\left(h \sqrt{\left(\frac{\omega}{c}\right)^2 (\epsilon_r - 1) + \beta_y^2}\right) \cong h \sqrt{\left(\frac{\omega}{c}\right)^2 (\epsilon_r - 1) + \beta_y^2}\,. \tag{2.39}$$

Thus, the approximate equation yields:

$$\beta_y^2(\epsilon_r(b-h)+h)+\left(\frac{\omega}{c}\right)^2(\epsilon_r-1)\,, \tag{2.40}$$

which gives rise to a straightforward solution:

$$\beta_y = j\frac{\omega}{c}\sqrt{\frac{(\epsilon_r-1)h}{\epsilon_r(b-h)+h}}\,. \tag{2.41}$$

The imaginary result indicates that the dependence of the electromagnetic fields along the y-axis is of the hyperbolic sine type.

A better approximation for the tangent functions can be obtained by using a Taylor series approximation up to the third order:

$$\tan(x) \approx x + \frac{x^3}{3}\,, \tag{2.42}$$

with an error of less than 1% for $x < 0.5$, and less than 0.1% for $x < 0.3$. This leads to the following two-square equation:

$$(\beta_y h)^4\left(1+\epsilon_r\left(\frac{b-h}{h}\right)^3\right)+(\beta_y h)^2\left(3\epsilon_r\left(\frac{b-h}{h}\right)+3+2p^2\right)+p^4+3p^2=0\,, \tag{2.43}$$

where $p \equiv h\beta\sqrt{\epsilon_r-1}$. The solution is:

$$\beta_y h = \sqrt{\frac{-B\pm\sqrt{B^2-4AC}}{2A}}\,, \tag{2.44}$$

where

$$A = 1+\epsilon_r\left(\frac{b-h}{h}\right)^3\,, \tag{2.45a}$$

$$B = 3\epsilon_r\left(\frac{b-h}{h}\right)+3+2p^2\,, \tag{2.45b}$$

$$C = p^4+3p^2\,. \tag{2.45c}$$

Figure 2.4 shows the β_y value, which has been normalized to $\beta = \omega/c$, as a function of ω/ω_c for a partially dielectric-loaded rectangular waveguide with the following parameters: $a = 2\,\text{cm}$, $b = 0.4a$, $h = b/50$, and $\epsilon_r = 8$. The orange line corresponds to the third-order approximation of the tangent functions, and the blue line to that of the first order. The constant value for the first-order approximation indicates the absence of dispersion, which does not correspond to the hybrid character of the mode.

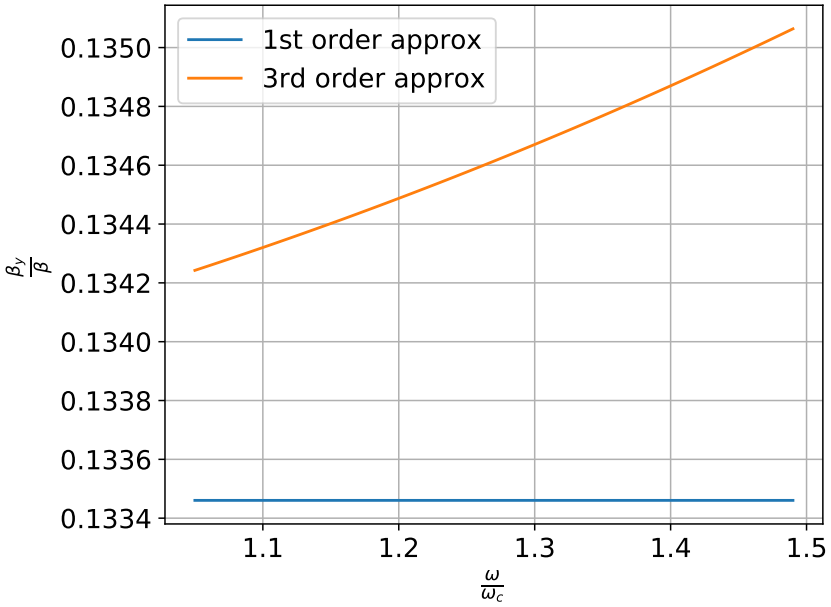

Figure 2.4: Normalized β_y value as a function of ω/ω_c for a partially dielectric-loaded rectangular waveguide with $a = 2\,\text{cm}$, $b = 0.4a$, $h = b/50$, and $\epsilon_r = 8$.

Once β_y is obtained, the value of β_z can be calculated as:

$$\beta_z = \sqrt{\left(\frac{\omega}{c}\right)^2 - \left(\frac{\pi}{a}\right)^2 - \beta_y^2}\,. \tag{2.46}$$

The cut-off frequency ω_c is also provided by the transcendental equation:

$$\epsilon_r\sqrt{u^2-1}\tan\left(\pi\frac{(b-h)}{a}\sqrt{u^2-1}\right) + \sqrt{\epsilon_r u^2-1}\tan\left(\pi\frac{h}{a}\sqrt{\epsilon_r u^2-1}\right) = 0\,, \tag{2.47}$$

where $u = \omega_c a/\pi c$ and $\mu = \mu_0$ has been assumed. If $h \ll b$ then the value of u must be close to one because $u = 1$ will lead to a cut-off frequency equal to that of the TE_{10} mode in the empty rectangular waveguide. Then, in the first-order approximation the tangent functions can be substituted by their arguments, which leads to:

$$\omega_c = \frac{\pi c}{a}\sqrt{1 - \frac{h}{b}\left(1 - \frac{1}{\epsilon_r}\right)}\,, \tag{2.48}$$

On the other side, in the case of the third-order approximation, this becomes:

$$u = \frac{\omega_c a}{\pi c} = \sqrt{\frac{-B \pm \sqrt{B^2 - 4AC}}{2A}}\,, \tag{2.49}$$

where

$$A = \epsilon_r \pi^2 \frac{(b-h)^3 - \epsilon_r h^3}{a^3}\,, \tag{2.50a}$$

$$B = \epsilon_r \frac{b}{a}\left(3 - 2\pi^2 \frac{b^2 - 3bh + 3h^2}{a^2}\right), \tag{2.50b}$$

$$C = \pi^2\left(\frac{\epsilon_r(b-h)^3 + h^3}{a^3}\right) - 3\left(\frac{\epsilon_r(b-h) + h}{a}\right). \tag{2.50c}$$

These approximations for the fundamental mode of a rectangular waveguide with a dielectric layer on the bottom wall will be used in Chapter 3, along with the most general expressions of the fields obtained with the bi-orthogonal vectorial method, in order to assess the validity of the approximations performed.

2.4 Electrostatic field due to an arbitrary charge distribution on the dielectric surface lining the rectangular waveguide

As explained in [43], the calculation of the electrostatic field $\mathbf{E}_{\mathrm{DC}}$ in a dielectric-loaded waveguide due to the generation of an arbitrary charge distribution on the dielectric layer during multipactor evolution is a problem that is currently of great interest to the space industry, because of the lack of rigorous studies into the appearance of the multipactor effect in dielectric-loaded waveguide-based microwave devices in satellite on-board equipment. When electrons impact on the dielectric material in such a waveguide with suitable kinetic energy, the electrons emitted in the dielectric surface charge the dielectric material positively, whereas the electrons absorbed by the dielectric layer in low-energy impacts charge it negatively. These charges give rise to an electrostatic field which has to be taken into account in order to obtain an accurate trajectory for the electrons within the structure (Figure 2.5).

Many researchers have studied the electrostatic field appearing on RF dielectric windows [16, 17, 44, 27, 28, 45, 46, 47] but few have studied the electrostatic field appearing during a multipactor discharge in dielectric-loaded waveguides [19, 20, 21]. Although the problem of determining the electrostatic field originated by an arbitrary charge distribution in free space has been addressed in many electromagnetism texts [48, 49, 50], this is the first time that the problem under consideration in this thesis has been rigorously solved.

In order to determine the electrostatic field:

$$\mathbf{E}_{\mathrm{DC}}(x, y, z) = -\nabla\phi(x, y, z) \tag{2.51}$$

generated by the charges created by the different impacts on the dielectric, the electrostatic potential $G(x, y, z)$ due to a point charge placed on the dielectric surface inside our waveguide must first be calculated.

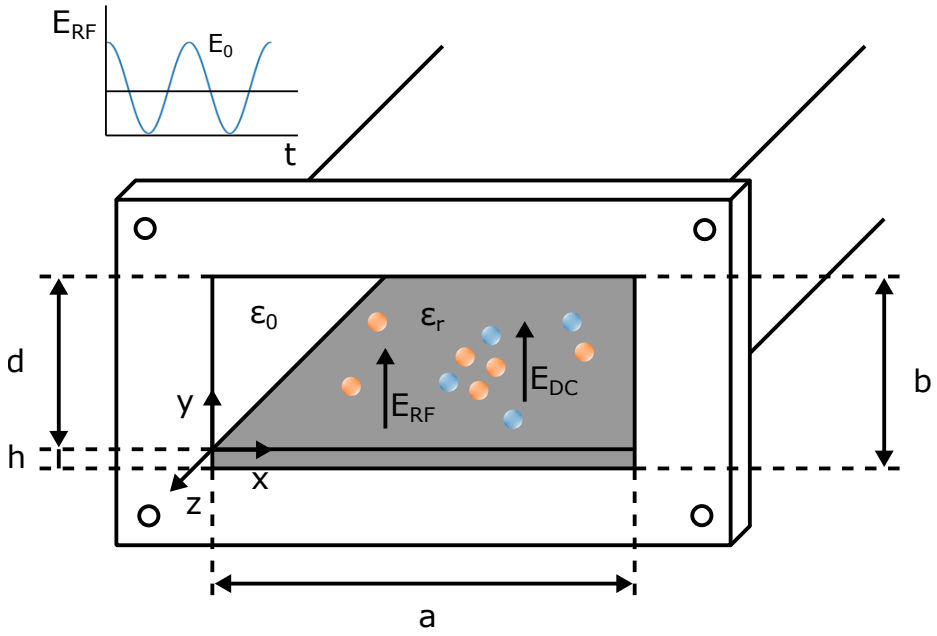

Figure 2.5: Electrostatic field appearing in a partially dielectric-loaded waveguide due to the charge distribution created by emitted and absorbed electrons in the dielectric surface during multipactor evolution. The blue and orange circles represent positive and negative charges, respectively.

For electrostatics, Green's function $G(x, y, z)$ provides a solution to Laplace's equation [3]:

$$\nabla \cdot [\epsilon_r(y) \nabla G(x, y, z)] = -\frac{1}{\epsilon_0} \delta(x - x') \delta(y) \delta(z) \,, \tag{2.52}$$

where ϵ_0 is the free-space dielectric permittivity, and the position of the unit charge is taken as $(x', 0, 0)$ for convenience.

Both the geometric characteristics and the linear nature of the problem under consideration mean that the Dirac delta functions can be expressed as:

$$\delta(x - x') = \frac{2}{a} \sum_{n=1}^{\infty} \sin(k_{xn} x) \sin(k_{xn} x') \,, \tag{2.53}$$

$$\delta(z) = \frac{1}{2\pi} \int_{-\infty}^{\infty} e^{-jk_z z} \, \mathrm{d}k_z \,, \tag{2.54}$$

where $k_{xn} = \frac{n\pi}{a}$ and k_z is the spectral Fourier variable along the longitudinal z-axis.

The expressions above derive from the fact that the eigenfunctions of the differential operator are sinusoidal functions along the x-axis and complex exponential functions along the z-axis, respectively. This is equivalent to applying a discrete sine transform (DST) along the x-axis and an integral transform along the z-axis, namely:

$$G = \frac{1}{\pi a} \int_{-\infty}^{\infty} \mathrm{d}k_z e^{-jk_z z} \sum_{n=1}^{\infty} \sin(k_{xn} x) \sin(k_{xn} x') \tilde{G} \,, \tag{2.55}$$

$$\tilde{G} = \int_{-\infty}^{\infty} \mathrm{d}z e^{jk_z z} \sum_{n=1}^{\infty} \sin(k_{xn}x)\sin(k_{xn}x')G\,, \tag{2.56}$$

where $G = G(x, x', y, z)$ and $\tilde{G} = \tilde{G}(k_{xn}, k_z; y)$.

On the basis of the considerations above, Equation (2.52) can be expressed as the following ordinary differential equation for the spectral Green's function $\widetilde{G}$:

$$\left\{ \frac{\partial}{\partial y}\epsilon_r(y)\frac{\partial}{\partial y} - k_t^2 \right\} \widetilde{G} = -\frac{\delta(y)}{\epsilon_0}\,, \tag{2.57a}$$

$$\widetilde{G}(y = -h) = 0\,, \tag{2.57b}$$

$$\widetilde{G}(y = d) = 0\,, \tag{2.57c}$$

where $k_t^2 = k_{xn}^2 + k_z^2$.

Solving Equation (2.57), the following expression for $\widetilde{G}$ is obtained in the air region $y \geq 0$:

$$\widetilde{G}(k_{xn}, k_z; y) = \frac{\sinh[k_t(d-y)]}{\epsilon_0 k_t[\epsilon_r \coth(k_t h) + \coth(k_t d)]\sinh(k_t d)}\,. \tag{2.58}$$

The Green's function in the spatial domain, G, is achieved by substituting Equation (2.58) into Equation (2.55) to give:

$$G(x, z', y, z) = \frac{2}{\epsilon_0 \pi a} \sum_{n=1}^{\infty} \sin(k_{xn}x)\sin(k_{xn}x') \times \int_0^{\infty} \frac{\sinh[k_t(d-y)]\cos(k_z z)}{k_t[\epsilon_r \coth(k_t h) + \coth(k_t d)]\sinh(k_t d)}\,\mathrm{d}k_z\,. \tag{2.59}$$

In Equation (2.59), if the point charge is placed at $z' \neq 0$, z must be replaced by $(z - z')$. It is worth noting that very efficient numerical summation and integration techniques have to be employed to compute the Green's function with sufficient accuracy and tolerable CPU times. The high computational complexity of Equation (2.59) requires the use of different numerical integration techniques (e.g. Filon, Gauss–Kronrod, Lobatto, etc.). Because of the rapid oscillation of the integrand for large values of z, Filon's integration method is chosen because it is suitable for integrals of the kind:

$$\int_b^a f(x)\cos(kx)\,\mathrm{d}x\,. \tag{2.60}$$

Finally, using superposition, the electrostatic potential in our waveguide due to the set of charges Q_i created by impacts on the dielectric surface can be obtained by adding the individual contribution of each charge:

$$\phi(x, y, z) = \sum_i G(x - x_i', y, |z - z_i'|)Q_i(x_i', 0, z_i')\,. \tag{2.61}$$

In a last step, a numerical differentiation of the potential is carried out by means of the central difference technique to obtain the electrostatic field $\mathbf{E}_{\mathrm{DC}}$ in the air-region of the waveguide.

2.4.1 Convergence analysis and performance optimization

As discussed above, the high computational complexity of the calculation of the electrostatic field $\mathbf{E}_{\mathrm{DC}}$ requires a detailed analysis of the parts forming the solution. In particular, it is useful to understand the spectral Green's function, Equation (2.58), with respect to the integration variable k_z. To perform this convergence analysis, the following waveguide parameters for the geometry and materials are considered: $a = 20\,\mathrm{mm}$, $d = 5\,\mathrm{mm}$, $h = 5\,\mathrm{mm}$ and $\epsilon_r = 2.25$.

In Figure 2.6(a), the function to be integrated, Equation (2.59), is shown in the case of $y = 0.1\,\mathrm{mm}$, $z = 3\,\mathrm{mm}$ and $n = 1$ where the Green's spectral function $\tilde{G}$ is multiplied by ϵ_0 and the oscillatory term $\cos(k_z z)$ (blue line). The envelope function, that is, $\left|\epsilon_0 \tilde{G}\right|$, is represented as a dashed orange line. As can be seen, this envelope is a decreasing monotonic function that will allow us to establish a convergence condition for the integral. Figure 2.6(b) represents the aforementioned envelope function on a logarithmic scale. As shown, $k_z \geq 2 \times 10^4$ has to be considered to achieve convergence.

In terms of the rate of convergence, the worst scenarios are for the cases of low y values and high n values. The same analysis has been performed in the case of $y = 0.1\,\mathrm{mm}$, $z = 3\,\mathrm{mm}$ and $n = 500$. The results are plotted in Figure 2.7. As can be noted, in this case $k_z \geq 8 \times 10^4$ is required for convergence.

The asymptotic behaviour of the integrand, determined by the term $e^{-k_t y}$, allows us to establish a condition by which to stop the computation when convergence is reached, as previously stated. It involves calculating the relative value of the i-th term of the integral with respect to the accumulated value of the integral prior to this iteration. If this relative value is less than a particular convergence tolerance, the computation of the integral is stopped. On the other hand, with regard to the convergence of the series in Equation (2.59), this depends on the product of two sinusoidal functions and no asymptotic behaviour can be observed in this case. For this reason, in order to ensure that convergence is achieved, the series is decomposed into a sum of partial series of ten terms each. The relative value of the i-th partial series with respect to the accumulated value provides the stop condition.

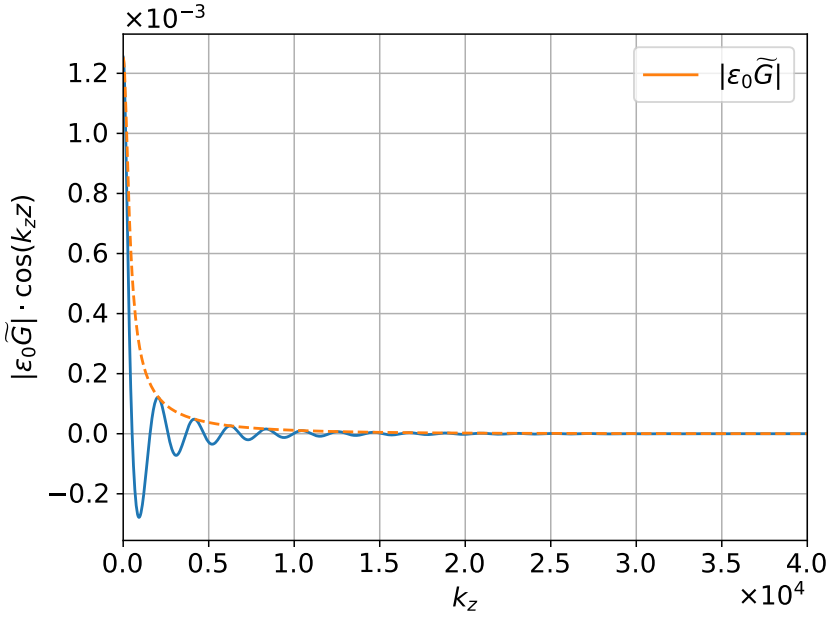

(a)

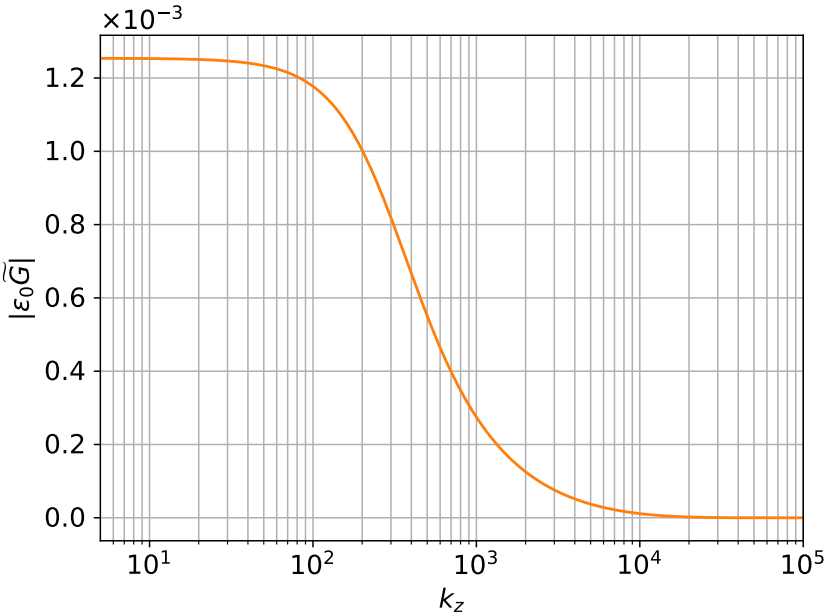

(b)

Figure 2.6: Spectral Green's function for $n = 1$, $y = 0.1\,\text{mm}$ and $z = 3\,\text{mm}$.

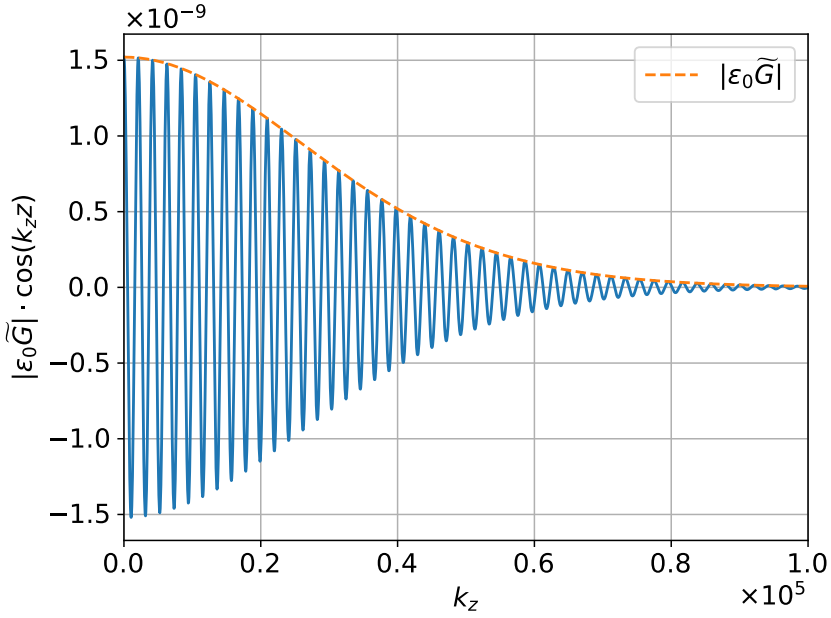

(a)

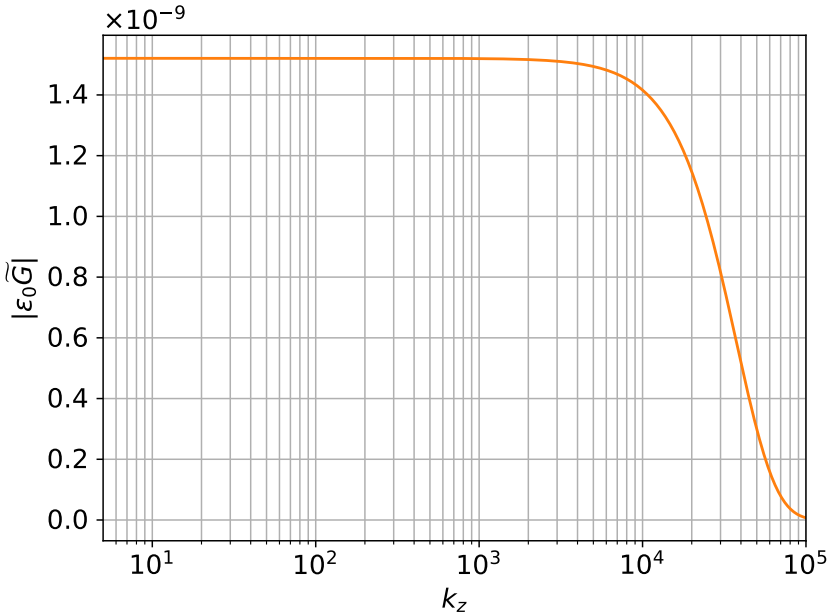

(b)

Figure 2.7: Spectral Green's function for $n = 500$, $y = 0.1\,\text{mm}$ and $z = 3\,\text{mm}$.

2.4.2 Post-processing analysis of the electrostatic potential

As shown in Figure 2.8, false peaks are observed in the Green's function calculated by using Filon's numerical integration. To fix these errors and remove them, an efficient spectral method has been considered: singular spectrum analysis (SSA).

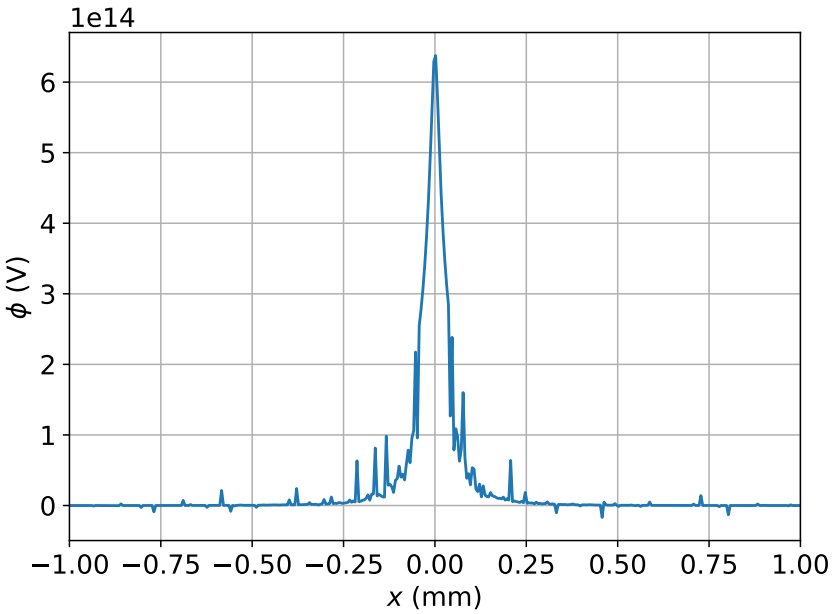

Figure 2.8: Sample of the electrostatic potential obtained from Filon's method.

As detailed in [51], SSA is a technique for data series analysis that incorporates elements of classical data series analysis, multivariate statistics, multivariate geometry, dynamical systems, and signal processing. The method has been widely used for data series analysis across different fields, including meteorology, hydrology, geophysics, climatology, biology, physics and medicine.

In the original formulation of SSA [52, 53, 54], it was assumed that the data series under analysis had a deterministic component (such as a trend and/or a seasonality) with noise superimposed, and that this deterministic component could be successfully extracted from the noise. This formulation is not confined to SSA. What SSA brings to the picture, identifying it as a novel method, is that it accounts for the (auto)covariance structure of the data series without imposing a parametric model upon it. It is thus a data-adaptive, non-parametric method based on embedding a data series in a vector space and, from a practical perspective, a model-free approach. It relies on a decomposition-based approach and its usefulness lies in extracting information from the (auto)covariance structure of a data series. In terms of classical statistics,

SSA is not a statistical method. In particular, we typically do not make any statistical assumptions concerning either signal or noise while performing the analysis and investigating the properties of the algorithms.

Recently, new models to impute and forecast data series by transforming them into a matrix have been under study. As an example, an algorithm based on matrix estimation to recover missing values and perform linear regression to make predictions is proposed [55]. On the other hand, to improve the speed of this technique for large data series and correspondingly large matrices, new approaches have been developed that offer a faster alternative and open the way to noise-reduction applications of the SSA method [56].

The SSA method proceeds by diagonalizing the lag-covariance matrix to obtain spectral information on the data series. It can then be analysed as a sum of simpler, elementary series that correspond to different subgroups of eigentriples (each eigentriple is composed of an eigenvalue and its associated left and right eigenvectors) of the lag-covariance matrix.

Step 1: Embedding

Consider a univariate stochastic process $\{y_t\}_{t\in\mathbb{Z}}$ and suppose that a realization of size N from this process is available. The first step, called embedding, maps the original data series $\{y_1, ..., y_N\}$ to a sequence of multidimensional lagged vectors $\boldsymbol{X} = [\mathbf{y}_1, ..., \mathbf{y}_K]$ where $K = N - L + 1$ and each lagged vector is defined as $\mathbf{y}_i = (y_i, ..., y_{i+L-1})^T$ for $i = 1, ..., K$. Each of these vectors corresponds to a partial view of the original data series, seen through a window of length L, where $2 \leq L \leq N-L+1$. The lag window size L defines the spectral resolution of the algorithm. According to [57], choosing the lag window size L is a matter of balancing the retrieval of information on the structure of the underlying data series and the degree of statistical confidence in the results. The former consideration requires that the window lag should be as wide as possible, that is, a large L, while the latter factor requires as many repetitions of the features of interest as possible, that is, as large a ratio of K/L as possible. Several attempts have been made to estimate a mathematical method for window length selection based on statistical test, such as that proposed by [58]. However, because it is not within the scope of the current work, we use only empirical rules rather than following these mathematical methods to determine the window length.

The trajectory matrix $\boldsymbol{X}$, which is defined as the aforementioned sequence of multidimensional lagged vectors, is a rectangular Hankel matrix of the form:

$$\boldsymbol{X} = \begin{bmatrix} y_1 & y_2 & \cdots & y_K \\ y_2 & y_3 & \cdots & y_{K+1} \\ \vdots & \vdots & \vdots & \vdots \\ y_L & y_{L+1} & \cdots & y_N \end{bmatrix} . \tag{2.62}$$

Step 2: Singular value decomposition (SVD)

The second step consists of the singular value decomposition (SVD) of the trajectory matrix $\boldsymbol{X}$. We denote with $\lambda_1, ..., \lambda_L$ the eigenvalues of the covariance matrix $\boldsymbol{S} = \boldsymbol{X}\boldsymbol{X}^T$ in decreasing order of magnitude ($\lambda_1 \geq \cdots \geq \lambda_L$). We set $d = \max(i \mid \lambda_i > 0) = \text{rank}\boldsymbol{X}$. If we denote $V_i = \boldsymbol{X}^T U_i / \sqrt{\lambda_i}$, then the SVD of the trajectory matrix can be written as:

$$\boldsymbol{X} = \boldsymbol{X}_1 + \cdots + \boldsymbol{X}_d \,, \tag{2.63}$$

where $\boldsymbol{X}_i = \sqrt{\lambda_i} U_i V_i^T$ $(i = 1, ..., d)$. The matrices $\boldsymbol{X}_i$ are rank-one. Therefore, they are elementary matrices; U_i (in SSA literature they are called "factor empirical orthogonal functions" or simply EOFs) and V_i (often called "principal components") stand for the left and right eigenvectors of the trajectory matrix. The set $(\sqrt{\lambda_i}, U_i, V_i)$ is called the i-th eigentriple of the matrix $\boldsymbol{X}$, $\sqrt{\lambda_i}$ $(i = 1, ..., d)$ are the singular values of the matrix $\boldsymbol{X}$, also called the spectrum of the matrix.

Step 3: Grouping

Once the expansion has been obtained, the third step involves the partitioning of these d eigentriples into m disjoint subgroups and summing them within each group, such that it represents a component series described by distinct subsets of eigentriples. The purpose of the grouping step is separation of the additive components of the data series. Let $I = i_1, ..., i_p$ (a group of indices). Then the matrix corresponding to the group I is defined as $\boldsymbol{X}_I = \boldsymbol{X}_{i_1} + \cdots + \boldsymbol{X}_{i_p}$. The split of the set of indices $J = 1, ..., d$ into the disjoint subsets $I_1, ..., I_m$ corresponds to the representation:

$$\boldsymbol{X} = \boldsymbol{X}_{I_1} + \cdots + \boldsymbol{X}_{I_m} \,. \tag{2.64}$$

Step 4: Diagonal averaging or Hankelization

The last step of the SSA algorithm, known as *diagonal averaging*, aims to transform the component matrices $\boldsymbol{X}_I$ into Hankel matrices, which then become the trajectory

matrices of the underlying data series, in such a way that the original data series can be reconstructed as a sum of these components. If z_{ij} represents an element of a matrix $\boldsymbol{Z}$, then the t-th term of the resulting series is obtained by averaging z_{ij} over all i, j such that $t = i + j - 1$. This procedure is a Hankelization of the matrix $\boldsymbol{Z}$: $\mathcal{H}\boldsymbol{Z}$.

For multivariate data series, the multichannel singular spectrum analysis (MSSA) gap-filling algorithm takes advantage of both spatial (cross-multiple data series) and temporal correlation. MSSA is a natural extension of SSA to a set of M data series, also known as channels. An approach to computing the lagged cross covariances is to form the multichannel trajectory matrix:

$$\boldsymbol{D} = [\boldsymbol{X}_1, ..., \boldsymbol{X}_m] \,, \tag{2.65}$$

where $1 \leq m \leq M$.

Listing 2.1 shows a Python implementation of the method. In this case, because the objective of the SSA is to filter the electrostatic potential and therefore to eliminate false spikes due to numerical limitations, it is not necessary to perform the spectral-clustering step (Step 3: Grouping). The actual intention is to eliminate the noise generated by numerical error, and this corresponds to high frequencies. Therefore, only the first EOF has been chosen, $eof = 1$. A lag window of size $m = 4$ is considered for calculation of the trajectory matrix of the electrostatic potential. The reason for choosing this size is that the aim is to minimize or eliminate the false peaks where possible, while affecting the correct values of the potential as little as possible. Choosing a higher value of the window lag m would lead to a reduction of these undesirable effects in the electrostatic potential; however, it would impact the real value of the central peak.

```
def mssa(phi, m, eof):
    def x_to_phi(Xi):
        XRev = Xi[::-1]
        return np.array([XRev.diagonal(i).mean() for i in range(-Xi.shape[0] + 1,
                                                                Xi.shape[1])])
    a, b = phi.shape
    # Step1: Embedding
    k = a - m + 1
    X = np.vstack((np.column_stack(phi[i:i + m, j] for i in range(0, k)) for j in
                   range(0, b)))
    # Step2: SVD
    d = np.linalg.matrix_rank(X)
    U, sigma, V = np.linalg.svd(X)
    V = V.T
    x_elem = np.array([sigma[i] * np.outer(U[:, i], V[:, i]) for i in
                       range(0, d)])
    if not np.allclose(X, x_elem.sum(axis=0), atol=1e-10):
        print("Warning: The sum of X's elementary matrices is not equal to X!")
    # Step3: Grouping
    # Step4: Diagonal averaging
```

```
    phir = []
    for j in range(0, b):
        phir_j = np.zeros((a, 1))
        for i in range(eof):
            phir_i = np.array(x_to_phi(x_elem[i, j * m:(j + 1) * m])).reshape(a, 1)
            phir_j = phir_j + phir_i
        phir.append(phir_j)
    phir = np.hstack(phir)
    return phir
```

Listing 2.1: MSSA Python code.

The result of the data cleaning of the electrostatic potential is shown in Figure 2.9. As can be seen, the SSA/MSSA method achieves the objective accurately.

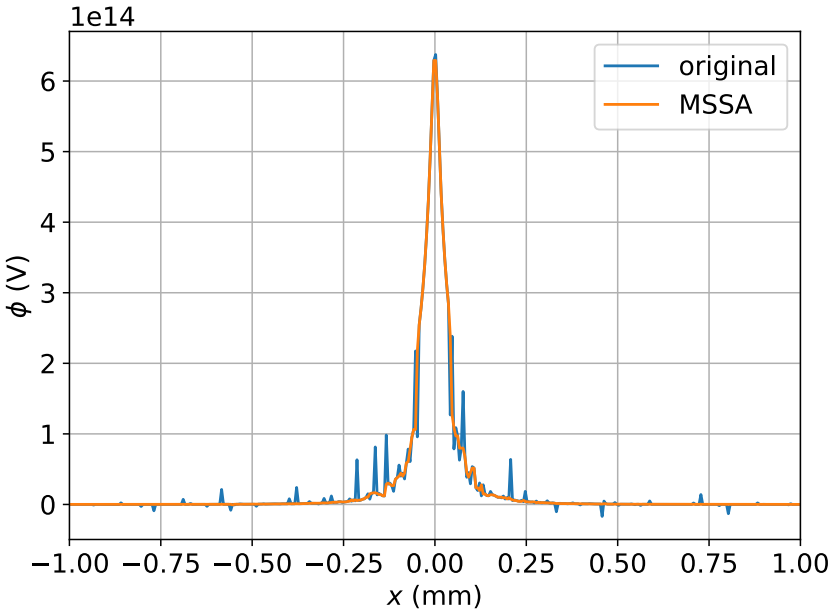

Figure 2.9: Cleaning of the electrostatic potential using the SSA/MSSA method.

2.4.3 Model validation of the electrostatic field

Here, the electrostatic field $\mathbf{E}_{\mathrm{DC}}$ in a dielectric-loaded rectangular waveguide like the one shown in Figure 2.5 is presented. A script based on the expressions given in Section 2.4 has been programmed using Matlab® to provide the results outlined below.

First, in order to validate Equation (2.59), the potential in the air region due to a point charge between two infinite homogeneous mediums ($\epsilon_{r1} = 1$ and ϵ_{r2}) is used as a benchmark:

$$\phi = \frac{1}{4\pi\epsilon_0 \frac{1+\epsilon_{r2}}{2} \sqrt{(x - \frac{a}{2})^2 + y^2 + z^2}} \,. \tag{2.66}$$

The results of Equation (2.59) should approach Equation (2.66) if the dimensions a, d and h are chosen so that the point charge and the observation point are far enough from the walls of the waveguide. In this case, the following parameters are considered: $a = 600\,\text{mm}$, $d = 250\,\text{mm}$, $h = 250\,\text{mm}$, $x = 305\,\text{mm}$, y values from $5\,\text{mm}$ to $245\,\text{mm}$ with $1\,\text{mm}$ width-step, $z = 5\,\text{mm}$, $x' = 300\,\text{mm}$ and $\epsilon_r = 2.25$.

As shown in Figure 2.10, the results of Equations (2.59) and (2.66) agree as long as the observation point is far enough away from the top wall, that is, $y = 25\,\text{mm}$, approximately. However, beyond this y-value, as the observation point approaches the top wall, the approximation is no longer valid and discrepancies appear.

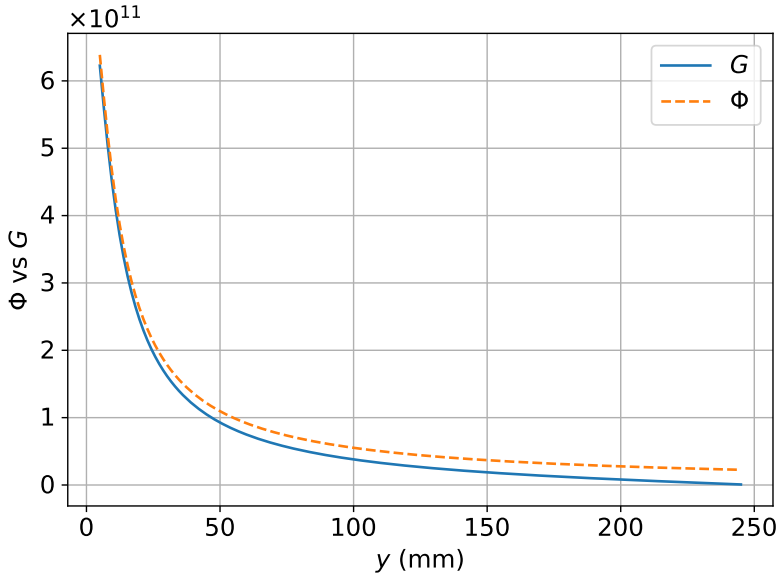

Figure 2.10: Comparison of the potential in the air region due to a point charge between two infinite homogeneous mediums ϕ vs Green's function G for the problem under study.

2.4.4 Electrostatic field due to arbitrary charge distributions

Once the solution of the electrostatic problem, Equation (2.59), has been validated and a convergence study has been carried out, the next step is to consider a real-life situation such as the WR90 rectangular waveguide, whose specifications are highlighted in Table 2.1. Thus, the dimensions of the waveguide under consideration are: $a = 22.86\,\text{mm}$, $d = 10.16\,\text{mm}$, $h = 0.025\,\text{mm}$ and, in this particular case, a dielectric layer of Teflon® is considered, so $\epsilon_r = 2.1$. In this case, the origin has been located at the centre of the waveguide. A total of eleven equidistant point charges has been considered in the calculation.

Table 2.1: Main parameters of the WR90 rectangular waveguide.

WR90 Specifications	
Recommended Frequency Band	8.20 GHz to 12.40 GHz
Cut-off Frequency of Lowest Order Mode	6.557 GHz
Cut-off Frequency of Upper Mode	13.114 GHz
Dimensions	22.86 mm × 10.16 mm

Source: Everything RF website [59].

Figures 2.11-2.13 show the electrostatic fields in a constant z-plane, $z = 0$, containing the point charges due to uniform Q_i^U, triangular Q_i^T, and Gaussian Q_i^G charge distributions, respectively, on the dielectric layer, where e is the electron charge:

$$Q_i^U = (1, 1, 1, 1, 1, 1, 1, 1, 1, 1, 1) \cdot e\,, \tag{2.67a}$$

$$Q_i^T = (0.17, 0.33, 0.5, 0.67, 1, 0.67, 0.5, 0.33, 0.17) \cdot e\,, \tag{2.67b}$$

$$Q_i^G = (0, 0, 0, 0.2, 0.8, 1, 0.8, 0.2, 0, 0, 0) \cdot e\,. \tag{2.67c}$$

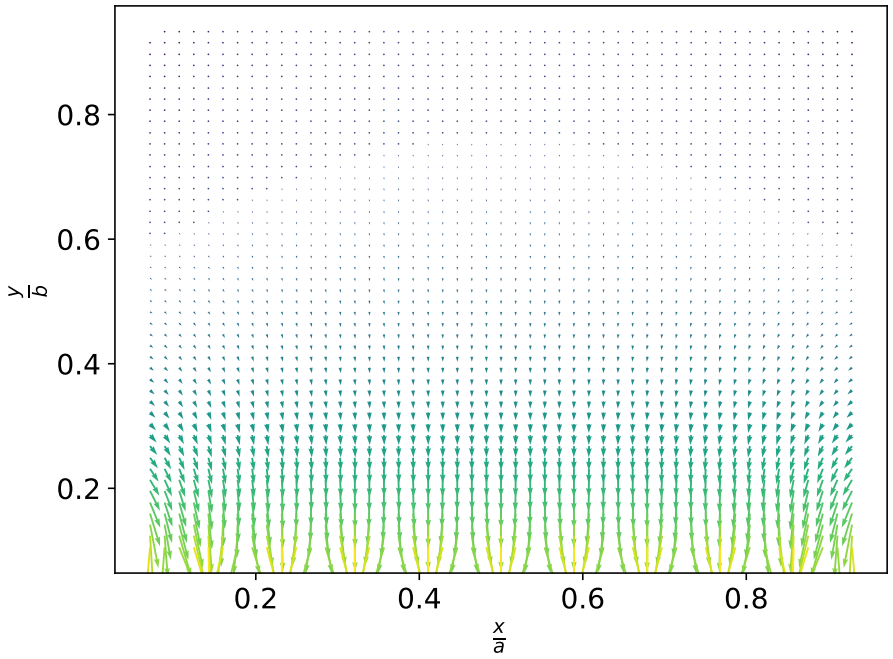

Figure 2.11: Electrostatic field due to a uniform charge distribution in a dielectric-loaded WR90 rectangular waveguide.

As the observation points approach the dielectric layer, where the point charges are located, the electrostatic field intensity becomes higher. Furthermore, as expected, a symmetrical behaviour with respect to the central x-axis, $\frac{x}{a} = 0$, is observed in all cases.

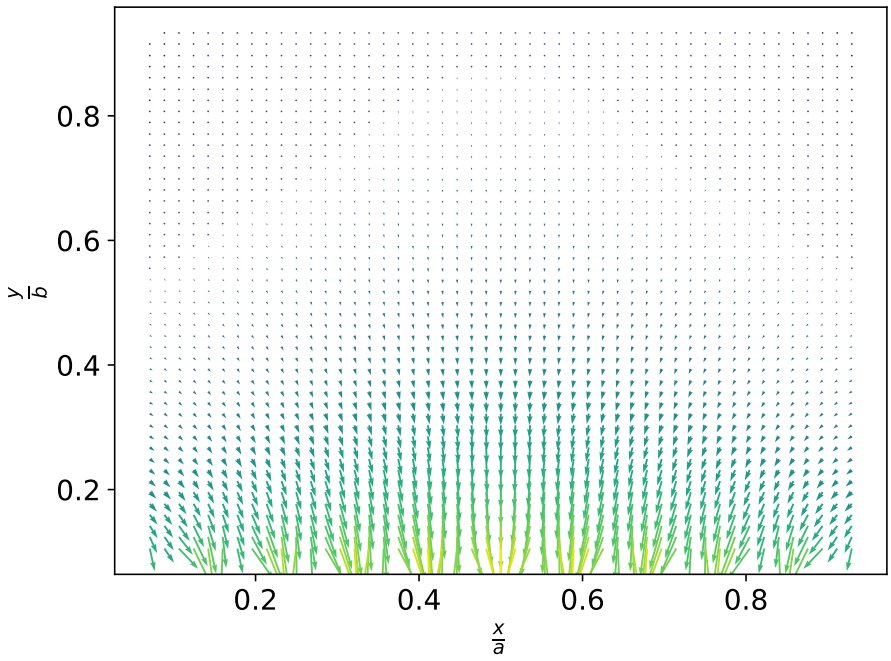

Figure 2.12: Electrostatic field due to a triangular charge distribution in a dielectric-loaded WR90 rectangular waveguide.

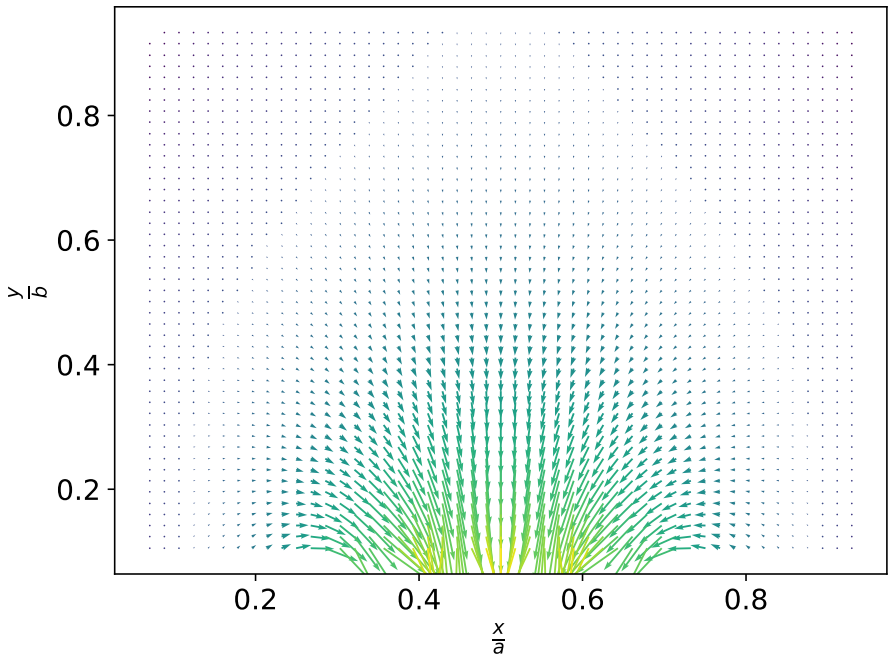

Figure 2.13: Electrostatic field due to a Gaussian charge distribution in a dielectric-loaded WR90 rectangular waveguide.

2.5 Summary

In this chapter, the electromagnetic theory applicable to rectangular waveguides, for both empty and partially dielectric-loaded cases, has been presented. In order to describe the movement of an electron inside the rectangular waveguide accurately, it is necessary to define the electromagnetic field component that interacts with the free charges.

Throughout the chapter, the equations that allow us to obtain these EM field components have been presented. First, the case of the empty rectangular waveguide has been analysed where, in addition to the precise equations for the EM fields, approximations of them have been shown, taking into account (or not) the relativistic term. In order to minimize the complexity of the model, the analytical equations of motion have been derived as a first step before applying numerical techniques.

The same exercise has been performed for the case of the partially dielectric-filled rectangular waveguide. In this case, a rigorous and computationally efficient method to obtain the electromagnetic field in the dielectric-loaded rectangular waveguide has been presented. As has been explained, this is a straightforward and spurious-mode-free method that is able to obtain the complex modal spectrum for inhomogeneously filled waveguides with a lossy dielectric of arbitrary profile. The key element of the approach is to transform the system of differential equations into a linear matrix eigenvalue problem by means of the Galerkin method, using the eigenvectors of an auxiliary problem. From a computational point of view, this method is very efficient because the integrals involved in the matrix elements are, in principle, frequency-independent, so they have to be evaluated only once to obtain the dispersion curves, thus generating a robust and efficient solution.

In addition, a method for calculating the electrostatic field in a dielectric-loaded waveguide due to an arbitrary charge distribution on the dielectric layer has been demonstrated. In order to obtain this electrostatic field value, the potential due to a point charge on the dielectric layer is solved in advance. The high computational complexity of this problem requires the use of efficient numerical integration techniques (e.g. Filon's method) and interpolation methods to minimize computation time. For this reason, it is recommended that a convergence study of the problem under study be conducted. Using the principle of superposition, the potential due to an arbitrary charge distribution on a dielectric layer is obtained by adding the individual contribution of each point charge. There may be critical points in the structure, for example, close to the walls or the dielectric layer, for which the solution

does not converge properly. In these cases, it is proposed to calculate the solution at points close to them and apply extrapolation techniques.

The SSA/MSSA method has been shown for dealing with numerical errors when calculating Green's function. Although Filon's method is suitable for integrating oscillating functions, as is the case for the problem under investigation, for certain points, false peaks in the electrostatic potential are obtained that need to be corrected to avoid their propagation in the calculation of the electrical field generated by the charge distribution on the surface of the dielectric layer. The results obtained with the SSA/MSSA method are accurate enough to address this issue.

Chapter 3

Multipactor effect model for dielectric-loaded rectangular waveguides

3.1 Introduction

Multipactor effect modelling is a complex problem that can be addressed by breaking it down into simpler problems. There are many physical drivers that can influence the appearance of the multipactor effect. The main elements for modelling the multipactor effect in partially dielectric-loaded rectangular waveguides will be described in this chapter.

In order to find the position and the velocity of the electrons inside the rectangular waveguide, the equation of motion that takes into account the entire electric field, that is, the electromagnetic field from the RF generator and the electrostatic one produced by the charges on the dielectric, has to be solved. This will be explained in Section 3.2.

When the surface of a solid is bombarded with particles of sufficient kinetic energy, emission of electrons from the solid may be observed. This phenomenon of secondary electron emission (SEE) was discovered by Austin and Starke in 1902 in a study of the reflection of electrons by metals; they observed that under certain circumstances more electrons were emitted than were incident, indicating that the bombarding primary electrons liberated electrons from the solid [60, 61]. In the present thesis, the bombarding particles are the electrons that move inside the waveguide and that hit its walls. This physical phenomenon is explained in detail in Section 3.3. In this analysis, the effective-electron model (EEM) is applied. As will be explained later, this model is based on the assumption that the electrons in the device move simulta-

neously, and all with the same speed. As a consequence, they compose an infinitely thin sheet that can be represented by a single effective electron. In addition, both the energy distribution and the angular distribution of the emitted electrons are studied. In this respect, the different alternatives to modelling both physical phenomena will be shown, justifying the choice made in this thesis.

Finally, the common graphical representation (known as a multipactor susceptibility chart) that is employed for the visualization of the multipactor regions, and therefore for the design of the devices, is described in Section 3.4.

3.2 Electron dynamics

As explained in [62], the key to understanding the mechanism of a multipactor discharge is to study the behaviour of the electrons within the waveguide, as they are accelerated by the electromagnetic fields $\mathbf{E}_{\mathrm{RF}}$ and $\mathbf{H}_{\mathrm{RF}}$. In this way, sooner or later, these fields will cause an electron to impact with one or other surfaces of the rectangular waveguide, which may result in the emission or absorption of secondary electrons. If the impact occurs on the dielectric surface, unlike the case of impacts on the metallic walls, secondary electron emissions from the dielectric will give rise to a positive charge at the impact position on the dielectric surface, whereas electrons absorbed into the dielectric layer will generate negative charges within it. These charges, which are located on the dielectric surface at positions $\mathbf{r}' = (x', 0, z')$, give rise to an electrostatic field $\mathbf{E}_{\mathrm{DC}}$, which has to be added to the RF fields to accurately obtain the trajectory of the electrons inside the waveguide.

Once the RF and DC fields are known at any instant t, the electron dynamics inside the waveguide can be computed, which is governed by the Lorentz force and related to its linear momentum:

$$\mathbf{F}_L = q(\mathbf{E} + \mathbf{v} \times \mathbf{B}) = \frac{\partial \mathbf{p}}{\partial t}\,, \tag{3.1}$$

where $q = -e$ is the electron charge, $\mathbf{E}$ and $\mathbf{B} = \mu_0 \mathbf{H}$ are the total electric and magnetic fields (incorporating both RF and DC contributions) interacting with the electron, μ_0 is the free-space magnetic permeability, and $\mathbf{v}$ is the velocity vector of the electron. The linear relativistic momentum is defined as:

$$\mathbf{p} = m_0 \gamma \mathbf{v}\,, \tag{3.2}$$

where m_0 is the electron mass at rest, $\gamma = 1/\sqrt{1-(v/c)^2}$ is the relativistic factor, v the magnitude of the velocity vector, and $c = 1/\sqrt{\mu_0 \epsilon_0}$ the free-space speed of light.

Although the relativistic correction in this equation can be discarded for the typical power ranges of most space waveguide devices, it should be considered when extreme velocities are reached ($v/c \geq 0.1$), as in high-power multipactor testing simulations. Expanding Equation (3.1), the following differential equation is obtained:

$$-\mathbf{E} - \mathbf{v} \times \mathbf{B} = M\gamma\mathbf{a} + \frac{M}{c^2}\gamma^3(\mathbf{v}\cdot\mathbf{a})\mathbf{v}\,, \tag{3.3}$$

where $\mathbf{a}$ is the acceleration vector and $M = m_0/e$. The differential equation system to be solved becomes:

$$\ddot{x} = \frac{\dot{z}B_y - \dot{y}B_z - E_x + \dot{x}\dot{\mathbf{r}}\cdot\mathbf{E}/c^2}{M\gamma}\,, \tag{3.4a}$$

$$\ddot{y} = \frac{\dot{x}B_z - \dot{z}B_x - E_y + \dot{y}\dot{\mathbf{r}}\cdot\mathbf{E}/c^2}{M\gamma}\,, \tag{3.4b}$$

$$\ddot{z} = \frac{\dot{y}B_x - \dot{x}B_y - E_z + \dot{z}\dot{\mathbf{r}}\cdot\mathbf{E}/c^2}{M\gamma}\,. \tag{3.4c}$$

The electron trajectory is found by numerically solving the above equations of motion. To this end, the velocity Verlet algorithm (Appendix A) has been used, which assures sufficient accuracy and good efficiency provided that enough time steps are chosen [63]. Regarding this last point, in order to improve the accuracy and efficiency of the simulation, the following adaptive time step has been applied for proximity to the waveguide walls, depending on the electron position:

$$\Delta t = \frac{\Delta t_0}{1 + C_x\left(\dfrac{x - a/2}{a/2}\right)^2 + C_y\left(\dfrac{y - b/2}{b/2}\right)^2}\,, \tag{3.5}$$

where Δt_0 is the initial reference time step, C_x and C_y are constant values, a and b are the width and height, respectively, of the rectangular waveguide (b can be replaced by $d = b - h$ in the case of a rectangular waveguide loaded with a dielectric layer of height h), and x and y are the coordinates of the electron position. Thus, when an electron is located near to the metallic or dielectric surfaces, a shorter time step is used because an accurate collision position is required. On the other hand, when an electron is moving in the vacuum region far away from the walls/surfaces, less accuracy is needed, and a longer time step will suffice.

Figure 3.1 shows the value of the simulation time step as a function of the position of the electron along the x- and y-axes for two different values of C_x and C_y. As shown, for low values of C_x and C_y, the time step decreases less rapidly as the electron gets close to the waveguide walls than for higher values of C_x and C_y. In the multipactor

analysis carried out in this thesis, an empirical value of 4 has been chosen for both parameters, which the results obtained in the simulations have shown to be accurate enough.

3.3 Secondary electron emission

As explained by Hueso in [64], to build up a sufficient electron density, the multipactor discharge effect relies on the electron emissivity of the metallic walls. When an electron impacts the metallic wall, it can trigger different physical mechanisms depending on certain characteristics, such as its kinetic impact energy, its impact angle or the properties of the wall material. After the incident electron has impacted on the metallic surface, the physical mechanisms that it can suffer are, basically, an elastic reflection, absorption into the metallic material, or the emission of new electrons (i.e. secondary electrons) into the waveguide. This physical phenomenon is known as secondary electron emission (SEE).

SEE can play an important role in electronic devices under vacuum conditions. By studying SEE behaviour, we can predict the power range of multipactor occurrences. As stated in Chapter 1, the multipactor effect restricts the attainment of the optimum power limits of devices used in space missions. A large number of bodies in the space industry – research centres and academia – are expending significant resources to suppress, or at least diminish, the secondary emission of electrons and, as a result, the detrimental consequences of multipactor.

The materials used for these particular devices have to be carefully chosen depending on each application, in order to effectively decrease these emissions [65]. It is well known that SEE depends on the material, the energy of the primary electron, its incident angle, and the state of the surface (e.g. its composition, structural morphology, porosity, and roughness) [66, 67].

As mentioned previously, the electrons' trajectories may eventually lead to an impact with any surface. Each collision can result in the emission or absorption of secondary electrons. A significant growth in electron density can occur if the electrons hit the walls with the appropriate energies and at suitable junctures. The number of electrons emitted or absorbed after each impact is determined by the value of the secondary emission yield (SEY) of the material, that is, the δ parameter. Figure 3.2 shows the coordinate system considered in the analysis of the impacts of the effective electron on the walls of the rectangular waveguide.

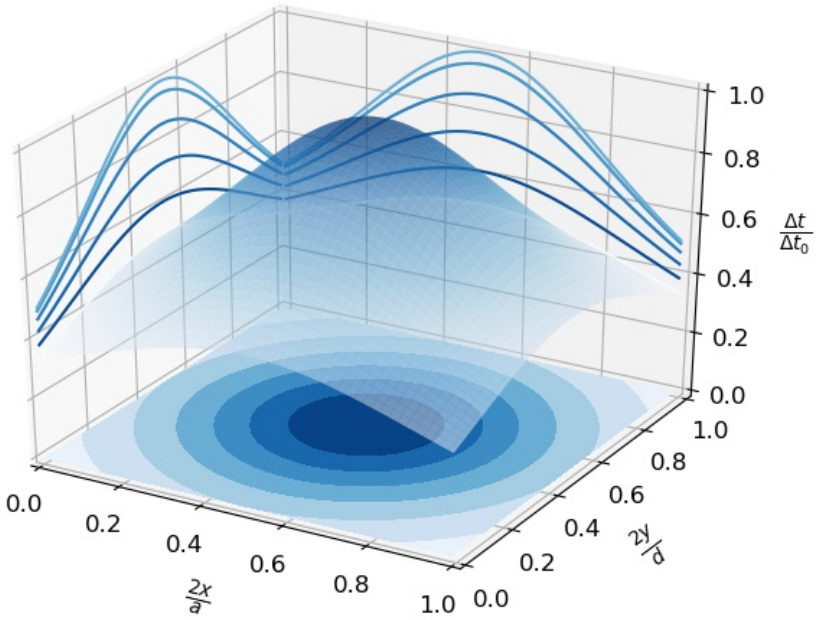

(a) Adaptive time step in the case $C_x = C_y = 1$.

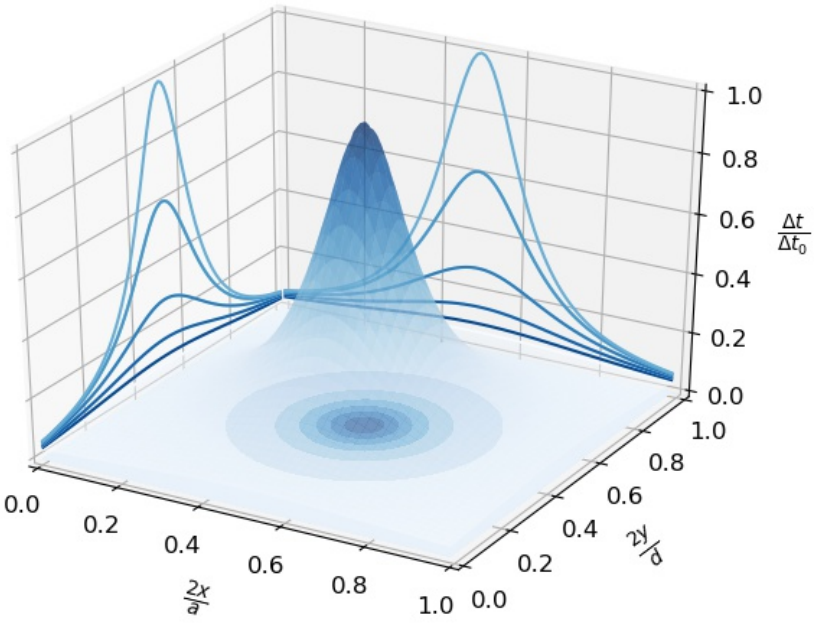

(b) Adaptive time step in the case $C_x = C_y = 4$.

Figure 3.1: Adaptive time steps employed in multipactor simulations.

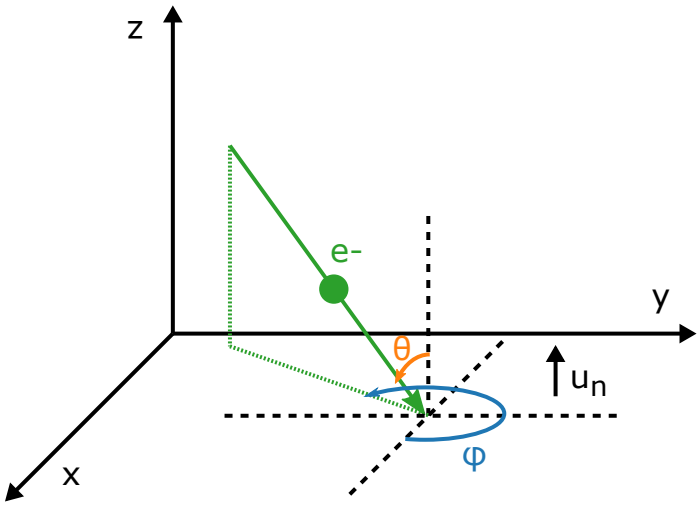

Figure 3.2: Coordinate system employed in the analysis of the impacts of the effective electron on the walls of the rectangular waveguide.

3.3.1 Secondary emission yield

The SEE phenomenon can be quantified with the secondary emission yield (SEY) or δ. This can be defined as the number of secondary emitted electrons per incident electron, and can be either less than or greater than one. When modelling the multipactor effect, there are models such as De Lara's model [68] that consider individual electrons to analyse the evolution of the effect by drawing a random number and using SEY to assign the probability that a certain number of secondary electrons are generated. On the other hand, if we employ the effective-electron model, as in our case, the SEY can be used to directly determine the number of electrons after a collision by multiplying the population of the incident effective electron by the value of SEY after this collision. Materials with a low SEY will be required if discharges in high-RF vacuum equipment are to be avoided.

As already described, the SEY depends on the kinetic energy of the primary electron impact W and its angle of incidence θ. Figure 3.3 shows the main parameters that define the SEY curve of any material. W_1 and W_2 are the primary electron impact kinetic energies that yield $\delta = 1$. $W_{\max}$ is the impact energy necessary for a primary electron to yield $\delta = \delta_{\max}$, which is the maximum value of the SEY function. Finally, W_0 is the value of the primary electron impact energy that serves to limit the occurrence of elastic collisions.

In order to generate a SEY curve, several models have been defined in the litera-

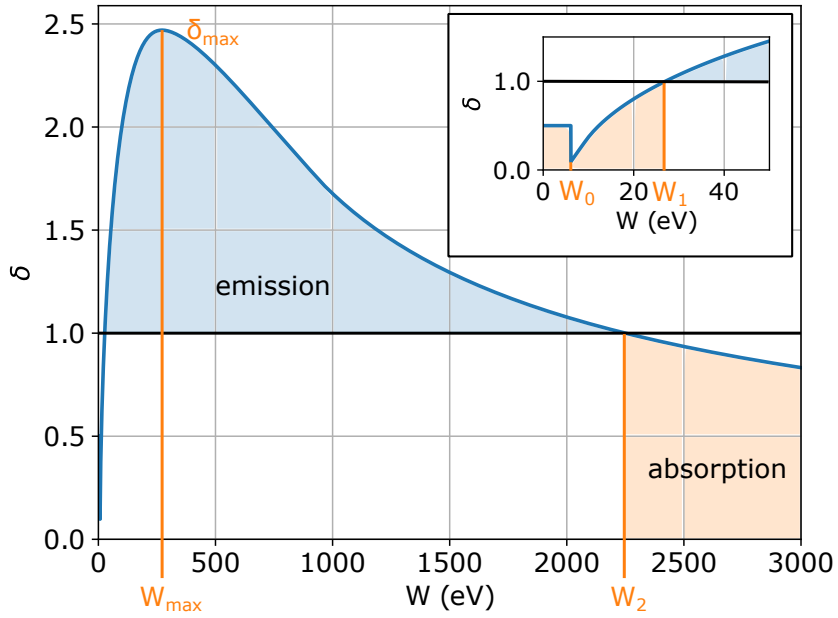

Figure 3.3: Main parameters that define the SEY curve.

ture. For instance, Seiler's model [69] defines:

$$\frac{\delta(W,\theta)}{\delta_{max}} = 1.11\gamma^{1-n}\left(1-e^{-2.3\gamma^n}\right)\left(\frac{1-\cos(\theta)}{2}\right), \tag{3.6}$$

where $n = 1.35$ and γ is defined as the primary energy W normalized to the primary energy W_{max} corresponding to the maximum yield δ_{max} adjusted by an angular factor:

$$\gamma = \frac{W}{W_{max}(\theta)} = \frac{W}{W_{max}(0)}(1+0.7(1-\cos(\theta))), \tag{3.7}$$

where δ_{max} is considered for normal incidence $\theta = 0$. However, this model gives an excessive yield for $\gamma > 5$ when compared to experimental data [70, 71]. This limitation occurs for $W > 1\,\text{keV}$.

According to the model of Lin and Joy [66], the SEY curve is defined as:

$$\frac{\delta(W)}{\delta_{max}} = 1.28\gamma^{1-n}(1-e^{-1.614\gamma^n}), \tag{3.8}$$

where $\gamma = \frac{W}{W_{max}}$ and $n = 1.67$. This model gives a maximum normalized yield δ_{max} slightly greater than 1. Both of these models start from the assumption that the loss of primary electron energy per unit length in the medium is constant. A more sophisticated version of these models can be found in [70].

Ito's model [72] states that:

$$\frac{\delta(W,\theta)}{\delta_{max}} = \frac{4\gamma}{(1+\gamma)^2}, \tag{3.9}$$

where

$$\gamma = \frac{W}{W_{max}(\theta)} = \frac{W}{W_{max}(0)}\sqrt{\cos(\theta)}\,, \tag{3.10}$$

$$\delta_{max}(\theta) = \delta_{max}(0)e^{\alpha(1-\cos(\theta))}\,, \tag{3.11}$$

and α depends on the material with typical values ranging from 0.4 to 0.6.

In De Lara's model [68]:

$$\frac{\delta(W,\theta)}{\delta_{max}} = \frac{s\gamma}{s-1+\gamma^2}\frac{k+1}{k+\cos\theta}\,, \tag{3.12}$$

where $\gamma = \frac{W}{W_{max}}$, s is a parameter that depends on the material, and

$$k = 0.0027Z + r\,. \tag{3.13}$$

In Equation (3.13), Z is the atomic number of the coating material and r is a parameter that characterizes the surface roughness: smooth surface, $r = 0$; very rough surface, $r = 10$; typical value, $r = 5$.

Finally, Vaughan's model [73] defines:

$$\delta(W,\theta) = \begin{cases} \delta_{max}(\theta)(\gamma e^{1-\gamma})^{\kappa(\gamma)}, & \text{if } 0 \le \gamma \le 3.6\,, \\ \delta_{max}(\theta)\frac{r}{\gamma^s}, & \text{if } \gamma > 3.6\,, \end{cases} \tag{3.14}$$

where

$$\gamma(W,\theta) = \frac{W - W_0}{W_{max}(\theta) - W_0}\,, \tag{3.15}$$

$$\delta_{max}(\theta) = \delta_{max}(0)\left(1 + \kappa_W\frac{\theta^2}{2\pi}\right)\,, \tag{3.16}$$

$$W_{max}(\theta) = W_{max}(0)\left(1 + \kappa_\theta\frac{\theta^2}{2\pi}\right)\,, \tag{3.17}$$

$$\kappa(\gamma) = \frac{\kappa_1+\kappa_2}{2} - \frac{\kappa_1+\kappa_2}{\pi}\arctan(\pi\ln(\gamma)) \approx \begin{cases} 0.56, & \text{if } \gamma < 1\,, \\ 0.25, & \text{if } 1 < \gamma \le 3.6\,, \end{cases} \tag{3.18}$$

and the parameters $W_0 = 12.5\,\text{eV}$, $r = 1.125$ and $s = 0.35$ are assigned empirically. Meanwhile, the parameters κ_W and κ_θ depend on the roughness of the material and, according to [74], are set to 1. The application of all of the SEY models described above are represented in Figure 3.4.

Vaughan's model gives rise to two basic problems: 1) at very low energies (i.e. $W < W_0$), the function $\delta(W,\theta)$ is not defined, so that the electron would experience an elastic reflection, without generating secondary electrons; 2) the first crossover energy W_1, at which $\delta = 1$, is not accommodated within the curve. In this thesis, the

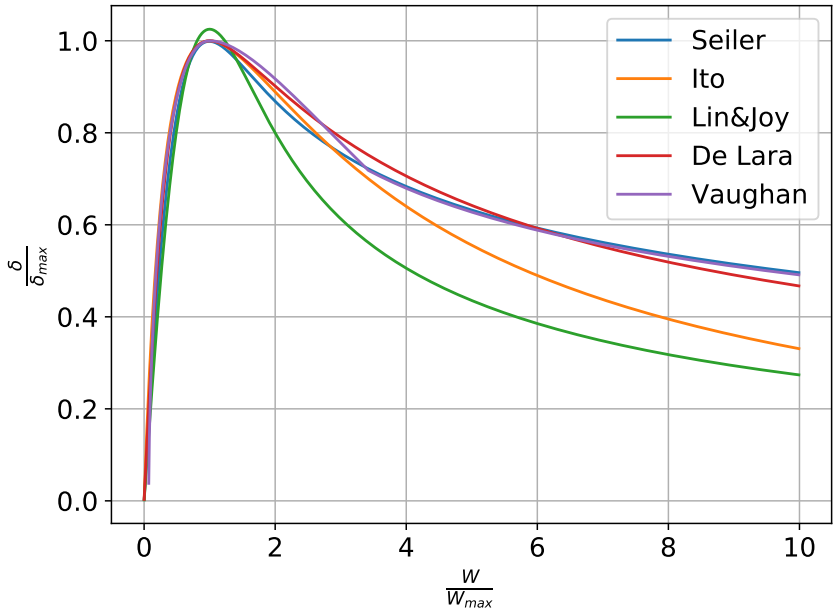

(a) Linear scale.

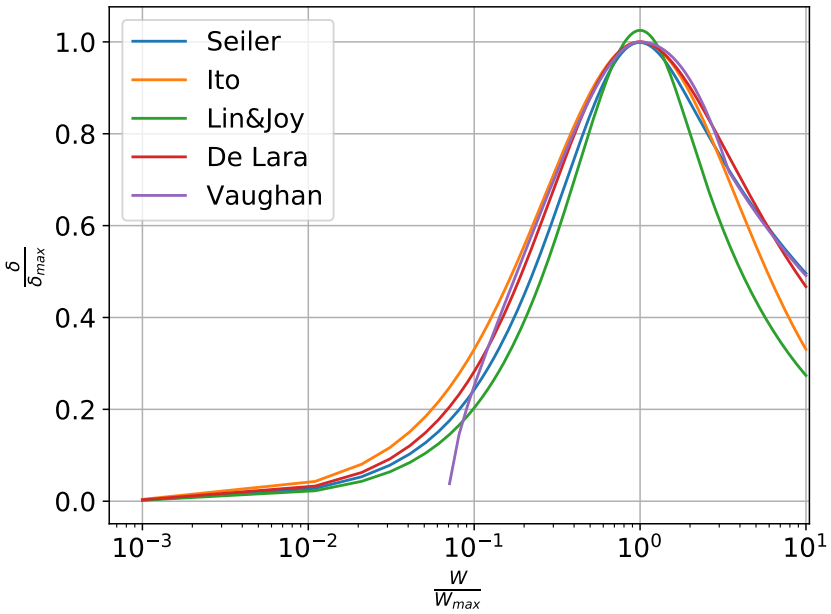

(b) Logarithmic scale.

Figure 3.4: Comparison of various SEY models.

SEY is modelled with a modification of Vaughan's model [73] that includes the effect of reflected electrons for low impact energies of the primary electrons, which have to be considered for accurate results [75, 76] in agreement with the experimental data obtained in [77, 78].

The model adopted is defined as:

$$\delta(W,\theta) = \begin{cases} 0.5, & \text{if } \gamma < 0\,, \\ \delta_{max}(\theta)(\gamma e^{1-\gamma})^{\kappa(\gamma)}, & \text{if } 0 \leq \gamma \leq 3.6\,, \\ \delta_{max}(\theta)\frac{r}{\gamma^s}, & \text{if } \gamma > 3.6\,, \end{cases} \tag{3.19}$$

where

$$\gamma(W,\theta) = \frac{W - W_0}{W_{max}(\theta) - W_0}\,, \tag{3.20}$$

$$\delta_{max}(\theta) = \delta_{max}(0)\left(1 + \kappa_W \frac{\theta^2}{2\pi}\right)\,, \tag{3.21}$$

$$W_{max}(\theta) = W_{max}(0)\left(1 + \kappa_\theta \frac{\theta^2}{2\pi}\right)\,, \tag{3.22}$$

$$\kappa(\gamma) = \frac{\kappa_1 + \kappa_2}{2} - \frac{\kappa_1 + \kappa_2}{\pi}\arctan(\pi \ln(\gamma)) \approx \begin{cases} 0.56, & \text{if } \gamma < 1\,, \\ 0.25, & \text{if } 1 < \gamma \leq 3.6\,. \end{cases} \tag{3.23}$$

Following the procedure described in [75], Vaughan's original model has been modified to overcome the first limitation. Thus, the SEY function assumes $\delta = 0.5$ for low impact energies of the primary electrons (i.e. $\gamma < 0$ or equivalent $W < W_0$). If total absorption were considered instead, an electron that collided with low energy would automatically be lost to the remainder of the multipactor simulation, which can significantly obscure the results obtained when an SEE model is used, as here.

The solution to the second limitation is to adjust the W_0 value by taking the W_1 crossover into account: the W_0 value is set so that $\delta(W_1, 0) = 1$. This is done by evaluating Equation (3.14) for $W = W_1$ and $\theta = 0$. The value of $\gamma(W_1, 0)$ can then be obtained by solving the following transcendental equation:

$$\delta(W_1,0) = \delta_{max}(0)(\gamma(W_1,0)e^{1-\gamma(W_1,0)})^{\kappa(\gamma(W_1,0))} = 1\,, \tag{3.24}$$

and substituting $\gamma(W_1, 0)$ in Equation (3.15) for $W = W_1$ gives us the W_0 value directly.

However, this correction might shift the rest of the model, generating a discontinuity at $\gamma = 3.6$ and shifting the crossover point from W_1. A solution to this issue is to redefine the values of the constants r and s proposed in Vaughan's model, so that the $\delta(W, \theta)$ function becomes continuous.

Considering $\gamma = 3.6$, then Equation (3.19) must satisfy:

$$\delta_{max}(0)(3.6e^{1-3.6})^{\kappa(3.6)} = \delta_{max}(0)\frac{r}{3.6^s}\,, \tag{3.25}$$

and thus:

$$r = k_\gamma 3.6^s\,, \tag{3.26}$$

where $k_\gamma \approx 0.696665$.

The second condition to solve the equation system can be obtained by forcing $\delta(W_2, 0) = 1$ in Equation (3.19), so that:

$$\delta(W_2, 0) = \delta_{max}(0)\frac{r}{\gamma_2^s} = 1\,, \tag{3.27}$$

which leads to:

$$r = \frac{\gamma_2^s}{\delta_{max}(0)}\,. \tag{3.28}$$

Replacing Equations (3.26) and (3.28), the parameter s is obtained:

$$s = \frac{\ln(\delta_{max}(0)k_\gamma)}{\ln\left(\frac{\gamma_2}{3.6}\right)}\,. \tag{3.29}$$

Figure 3.3 shows the SEY curve generated by the modified Vaughan's model that has been applied. At low primary energies, when the penetration depth is much less than the electrons' escape capacity, the secondary electrons easily escape from the material but because the primary energy is so low, only a few secondary electrons are generated. However, as the energy of the primary electrons increases, more secondary electrons are emitted from the material, thereby increasing the SEY as a function of the primary energy. At very high energies, when the penetration of the primary electrons is much greater than the escape capacity of the secondary ones, due to the exponential nature of the escape process of the electrons, the number of secondary electrons that escape from the material decreases and therefore a decrease in the SEY is observed.

The SEY curve describes the average number of electrons emitted from a waveguide wall, which can be either metallic or covered by a dielectric layer, per incident electron impact, in terms of the cited parameters. Each metal and dielectric has a different characteristic SEY curve. Table 3.1 shows the parameters corresponding to the materials used in the simulations and the associated results, which will be discussed later. Meanwhile, Figures 3.5-3.9 show the shapes of the SEY curves for these materials. Because the shapes of the curves are similar to each other, all can be accommodated by the same equations, each material having a set of characteristic

Table 3.1: Secondary electron emission yield properties of the different materials ([1], [2]) employed in the simulations.

Material	$\mathbf{W_{max}}$	$\mathbf{W_1(eV)}$	$\mathbf{W_2(eV)}$	$\mathbf{W_0(eV)}$	$\delta_{\mathbf{max}}$
Alumina	350.00	85.47	1414.00	12.90	1.50
Aluminium	150.00	23.30	5000.00	16.00	2.98
Niobium	200.00	33.00	1500.00	–	1.60
Silver	165.00	30.00	5000.00	16.00	2.22
Teflon®	271.70	27.00	5000.00	6.81	2.47

coefficients. In all cases, as can be seen, for a fixed primary electron impact angle, the SEY increases with the primary electron impact energy until its maximum value W_{max} is reached, and then decreases monotonously. On the other hand, depending on the material, for primary electron impact energies that are sufficiently high, the SEY increases with the electron impact angle.

3.3.2 Effective-electron model

The multipactor effect model in this thesis has been designed according to the effective-electron model (EEM), also referred to as the mono-energetic model or the single-electron model, whereby a high-energy particle is tracked with a numerical electron dynamics model. It is a well-known approach to modelling multipactor in such a way that the number of electrons to be tracked are replaced by a single "effective" electron throughout the simulation.

As described by Sounas in [34], the EEM has been widely used in early studies of multipactor discharge to understand the physical mechanisms of the phenomenon, as well as to establish the basic multipactor theory. The EEM has been used to study the evolution of the discharge in commonly used waveguiding geometries (parallel-plate [19, 20, 21], coaxial [9, 10] or rectangular waveguides [22]), considering both the distribution in secondary emissions energy and the angle of the secondary electrons after each impact on the waveguide walls. The EEM has been successfully used for simulations of multipactor experiments in coaxial transmission lines in the context of the presence of external magnetic static fields [79], demonstrating the validity of this method for complex scenarios.

The model originates from the study of multipactor in the case of two infinite parallel plates. According to the term mono-energetic, the model is based on the assumption that the electrons move simultaneously between the plates, all with the same speed. Thus, they compose an infinitely thin sheet that can be represented by a

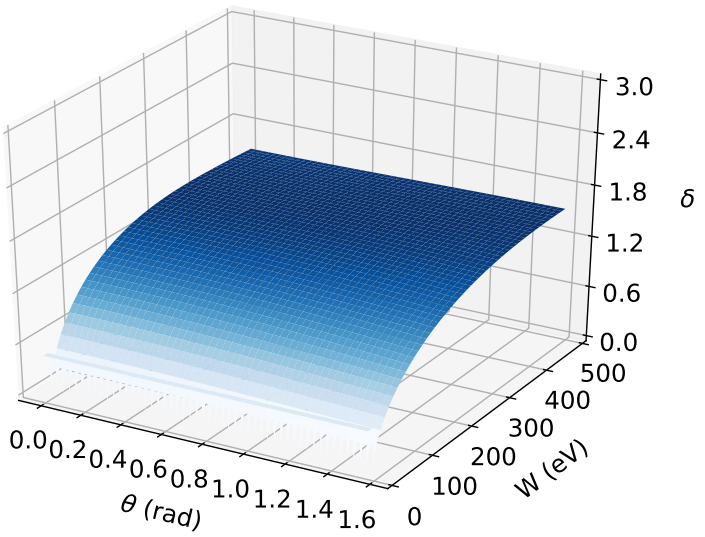

(a) Alumina SEY surface as a function of primary electron impact energy W and impact angle θ.

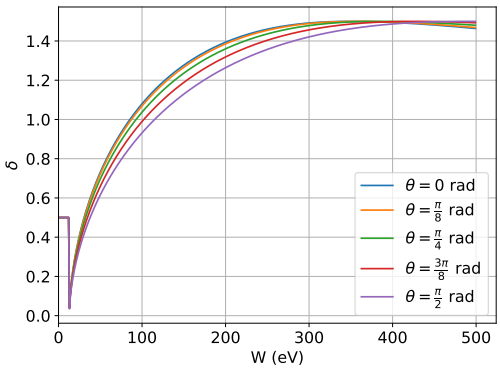

(b) Alumina SEY curves as a function of primary electron impact energy W for several primary electron impact angles θ.

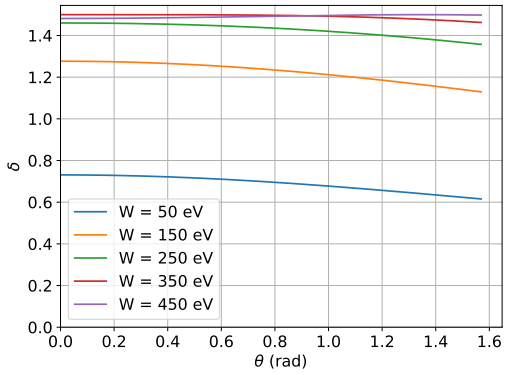

(c) Alumina SEY curves as a function of primary electron impact angle θ for several primary electron energies W.

Figure 3.5: Alumina SEY characteristics.

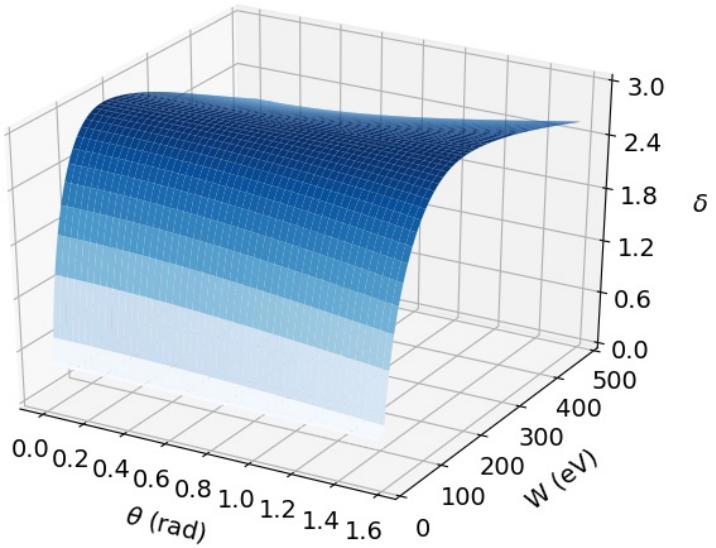

(a) Aluminium SEY surface as a function of primary electron impact energy W and impact angle θ.

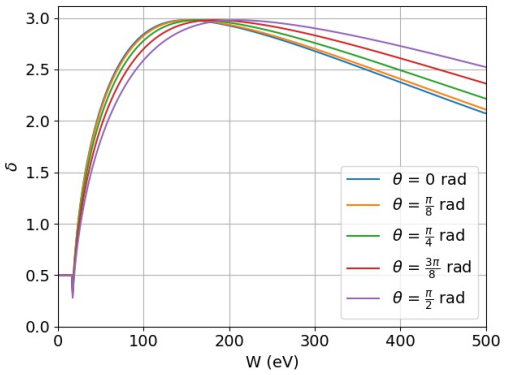

(b) Aluminium SEY curves as a function of primary electron impact energy W for several primary electron impact angles θ.

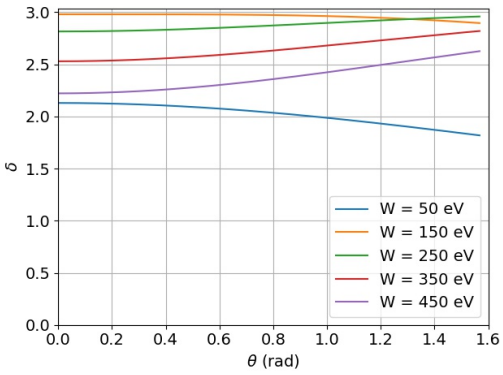

(c) Aluminium SEY curves as a function of primary electron impact angle θ for several primary electron energies W.

Figure 3.6: Aluminium SEY characteristics.

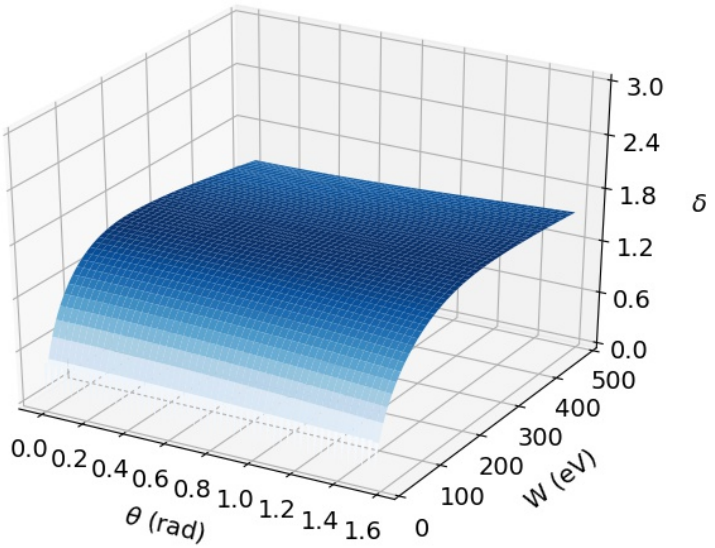

(a) Niobium SEY surface as a function of primary electron impact energy W and impact angle θ.

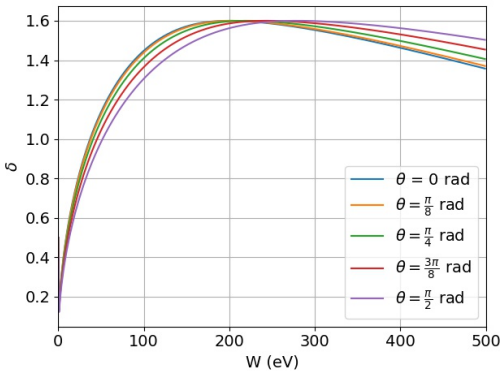

(b) Niobium SEY curves as a function of primary electron impact energy W for several primary electron impact angles θ.

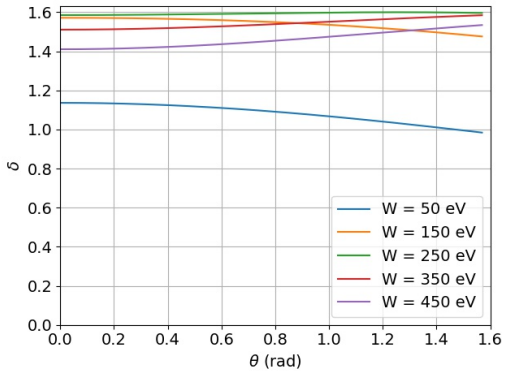

(c) Niobium SEY curves as a function of primary electron impact angle θ for several primary electron energies W.

Figure 3.7: Niobium SEY characteristics.

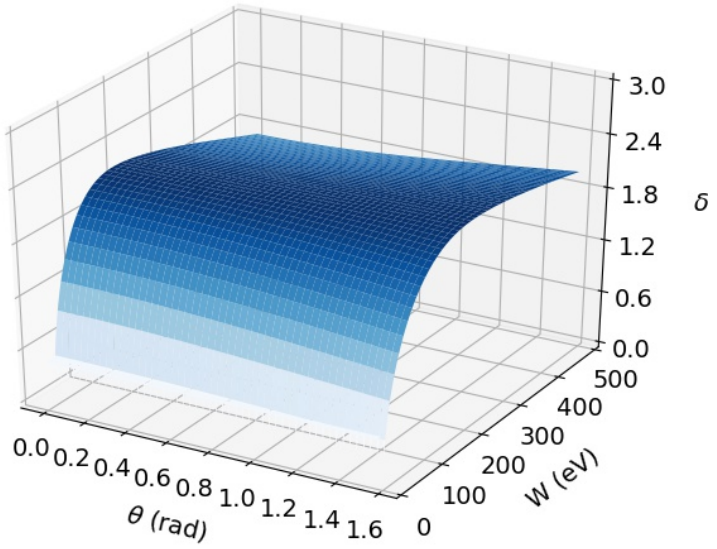

(a) Silver SEY surface as a function of primary electron impact energy W and impact angle θ.

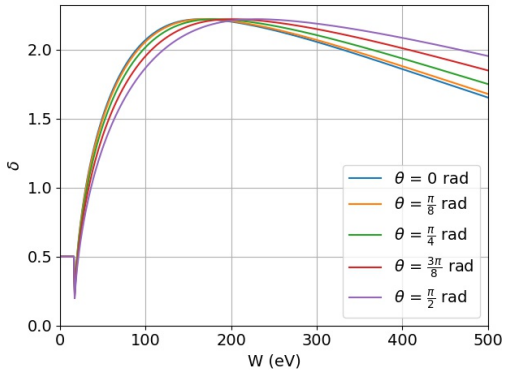

(b) Silver SEY curves as a function of primary electron impact energy W for several primary electron impact angles θ.

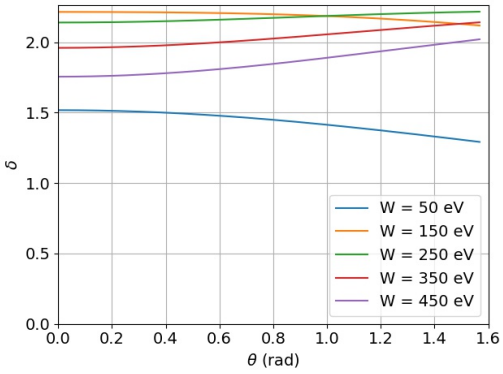

(c) Silver SEY curves as a function of primary electron impact angle θ for several primary electron energies W.

Figure 3.8: Silver SEY characteristics.

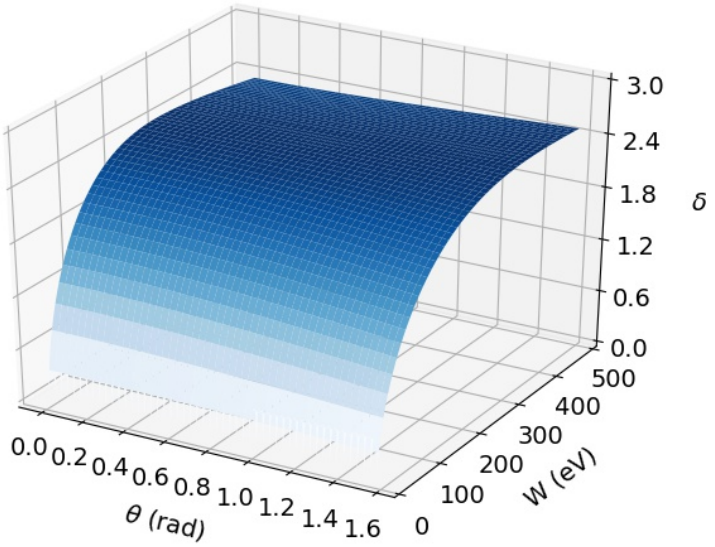

(a) Teflon® SEY surface as a function of primary electron impact energy W and impact angle θ.

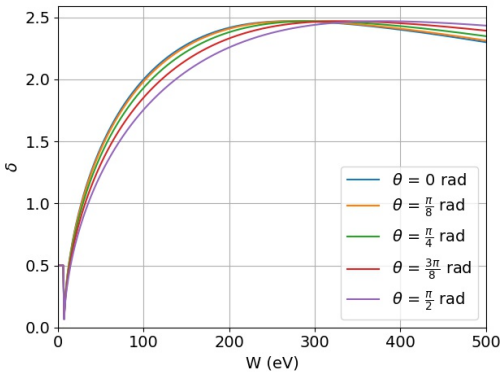

(b) Teflon® SEY curves as a function of primary electron impact energy W for several primary electron impact angles θ.

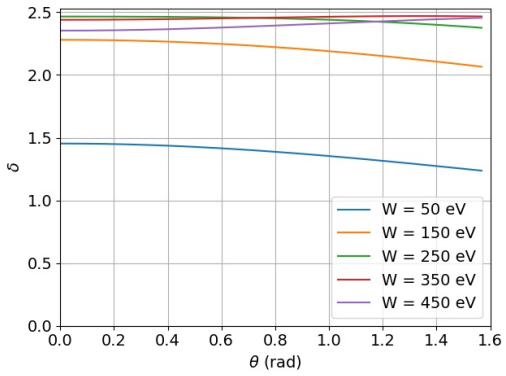

(c) Teflon® SEY curves as a function of primary electron impact angle θ for several primary electron energies W.

Figure 3.9: Teflon® SEY characteristics.

single effective electron. This single-electron approach notably simplifies the analysis of multipactor within infinite parallel plates. Although such a configuration is only encountered even approximately in very few real-world applications, it nevertheless attracts intense interest, particularly for theoretical studies of the discharge. What makes it appealing is the fact that the electron motion can be expressed in analytical form. By applying the single-electron approach, closed analytical formulas can be derived concerning the conditions required for multipactor. Moreover, the single-electron analysis provides physical insights into the multipactor phenomenon through, for instance, the study of the resonant modes or the phase-focusing mechanism.

Aside from theoretical studies, the single-electron model offers significant interest from a practical point of view. Through the well-established multipactor susceptibility chart, one can obtain an overview of the operational zones in which a microwave component will be susceptible to multipactor discharge. The single-electron model can be applied as a first approach to rapidly derive a multipactor susceptibility chart that can be used as an engineering tool for designing components that, locally, resemble the parallel plates configuration; for example, a rectangular waveguide with a small height-to-width ratio. Several studies have been conducted into the analytical derivation of the susceptibility zones for the case of parallel plates. Indeed, some of them have been used as a basis for deriving standards for multipactor avoidance [80]. In addition to the parallel plates problem, the applicability of the single-electron approach can be extended to any other configuration that, within reason, resembles a 1D geometry, such as a rectangular waveguide.

The EEM relies on two basic assumptions. First, the electrons are all moving in one direction, meaning that they are subjected to a unidirectional RF electric field. Second, the secondary electrons are all emitted with the same energy, and in the normal direction to the surface. Both assumptions can reasonably be considered valid in the case of a multipactor discharge within infinite parallel plates. In particular, in the context of the fundamental TEM mode, the electric field is unidirectional and normal to the surfaces, thus forcing the electrons to follow a 1D motion. Even if the secondary electrons are emitted in a direction that is slightly different to the normal one, their motion, driven by the field, can be well approximated by a 1D trajectory. Similarly, despite a spread of initial velocities, the secondary electrons tend to converge towards resonant motions of a fixed (mono-energetic) emission velocity.

Because of its 1D mono-energetic nature, the single-electron model neglects the magnetic field force as well as the mutual repulsion between the electrons, two mechanisms that could potentially affect the electrons' motion. As a first approach, the

effect of the magnetic field can be neglected by assuming that the velocity of the electrons is much lower than the speed of light. In this event, which is the most likely scenario in multipactor regimes, the motion of the electrons is essentially dominated by the electric field and, therefore, the effect of the magnetic field is almost negligible. On the other hand, the electron cloud generated during the discharge has traditionally been modelled by an infinitely thin, flat and continuous charge distribution (an electron sheet) [81, 82, 33, 20] using the theory of Sombrin [83], in which the initial speed of all the secondary electrons is the same. Previous studies based on multiple-electron models, including space charge effects in dielectric-loaded microwave components, have shown that space charge basically constitutes an inhibitory factor in the evolution of the discharge [20]. However, the consideration of the space charge effect in a rectangular waveguide (either empty or partially dielectric-loaded) is not an easy task. Following Kishek and Lau [82], the self-field of the electron sheet when calculating its equations of motion has not been considered in our model in relation to the space charge effects in the motion of the electron cloud, because tracking the evolution of all the electrons involved in the multipactor discharge would be needed and this would impose an unaffordable computational cost. In addition, the space charge starts to affect multipactor evolution only when the population approaches the saturation stage. Hence, when focusing on the beginning or onset of the multipactor process (electron avalanche/no electron avalanche), the space charge can safely be omitted from the analysis.

Apart from the infinite parallel-plate scenario, the conditions assumed in the single-electron model are also met in other, more realistic structures with a unidirectional-like electric field. Such cases include rectangular structures, like waveguides and filters, with a small height-to-width ratio. In terms of the fundamental mode, the electric field in the central area of the rectangular cavity resembles that of the parallel plates. Because the electric field is strongest in the central area, the discharge is most likely to occur there and, hence, a local 1D multipactor analysis can be performed as a first approximation.

When a multipactor discharge evolves in a partially dielectric-loaded waveguide, as is the case in the study conducted in this thesis, the DC field distribution originated by the charges appearing on the dielectric surface has to be updated after each electron impacts on the dielectric. The most realistic approach would be to follow the trajectory of each emitted electron. However, because this is not computationally efficient, the EEM has been selected for this thesis. The effective electron represents a larger (or smaller) number of electrons, depending on the accumulated SEY values

at each impact. Even though this approach is extremely useful in many cases and provides reliable results in many geometries, it cannot be universally applied. In this thesis, the use of the EEM has been proved to account properly for the charging of the dielectric material loaded in the rectangular waveguide, given that the discharge time for dielectrics is much longer than the typical time for a multipactor discharge. Furthermore, we have checked with numerical simulations that, under resonance conditions, the EEM produces realistic charge distributions on the dielectric, similar to those obtained by tracking a population of several thousands of electrons. In Chapter 4, the results obtained with the proposed model will be presented, such that this use of the EEM will be validated.

In terms of the theory described above, the effective electron moves inside the air gap in the rectangular waveguide and could impact any wall. At the moment of collision, the electron impacts with an energy W_c related to its kinetic velocity in the non-relativistic approximation $\mathbf{v}_c$ and at an angle θ_c with respect to the normal surface vector $\mathbf{u}_n$:

$$W_c = \frac{1}{2} m_0 \|\mathbf{v}_c\|^2 \,, \tag{3.30a}$$

$$\theta_c = \arccos\left(-\frac{\mathbf{v}_c \mathbf{u}_n}{\|\mathbf{v}_c\|}\right) = \arccos\left(-\frac{v_{c,x}u_{n,x} + v_{c,y}u_{n,y} + v_{c,z}u_{n,z}}{\sqrt{v_{c,x}^2 + v_{c,y}^2 + v_{c,z}^2}}\right) , \tag{3.30b}$$

where m_0 is the mass at rest of the electron. In Table 3.2, a summary of these parameters according to the collision side is shown.

Table 3.2: Normal vector $\mathbf{u}_n$ and angle θ_c to the sidewall according to the collision side.

	Collision side			
	Top	**Bottom**	**Left**	**Right**
$\mathbf{u}_n$	(0, -1, 0)	(0, 1, 0)	(1, 0, 0)	(-1, 0, 0)
θ_c	$\arccos\left(\frac{v_{c,y}}{\|\mathbf{v}_c\|}\right)$	$\arccos\left(\frac{-v_{c,y}}{\|\mathbf{v}_c\|}\right)$	$\arccos\left(\frac{-v_{c,x}}{\|\mathbf{v}_c\|}\right)$	$\arccos\left(\frac{v_{c,x}}{\|\mathbf{v}_c\|}\right)$

Thus, in the EEM assumed in this study, after the effective electron impacts at time t with any surface, $N_i(t)$ is modified according to the δ value provided by the SEY function as follows:

$$N_i(t + \Delta t) = \delta N_i(t) \,, \tag{3.31}$$

where $N_i(t)$ represents the population of electrons inside the waveguide at the instant t, and Δt is the time step used in the simulations.

3.3.3 Energy distribution of the emitted electrons

As explained by Ding et al. in [84], many experimental measurements on secondary electron emission have been conducted in the past and these observations have revealed common features of secondary electron emission from metal and dielectric surfaces. First, the energy spectra of secondary electrons peak at about 1 eV to 5 eV, whilst the full breadth of this peak is around 3 eV to 15 eV. The energy distribution curve is thus quite universal for metals when normalized at their most probable energies. Second, a convenient definition of true secondary electrons is that their energies are less than 50 eV, while backscattering electrons are defined as having energies greater than 50 eV.

The mechanism of secondary electron generation depends upon a cascade process, because only in this way the amount of secondary electrons generated inside the sample can be multiplied such that the emitted current will be higher than the incident current. The primary feature of the energy distribution of secondary electrons relates to this cascade process. The energy distribution increases monotonously but with decreasing energy. Therefore, by also taking into account the angular distribution of secondary electron emissions from the surface when overcoming the surface barrier, the energy distribution exhibits a peak at an energy above that of the surface barrier [84].

Several models can be found in the literature for modelling the energy distribution of the emitted electrons. In Chung and Everhart's model [85]:

$$\frac{\mathrm{d}N_s}{\mathrm{d}W_d} = \frac{6\phi^2 W_d}{(W_d+\phi)^4}\,, \tag{3.32}$$

where N_s is the number of secondary electrons of energy W_d and ϕ is the work function of the medium. The maximum of the spectrum corresponds to $W_m = W_d/3$. Using the normalized energy $u \equiv W_d/W_m$, where W_m is the energy of the maximum of the spectrum (i.e. the most probable energy value for the departing electron), and normalizing the spectrum to unit height, the previous expression reads:

$$F(u) = u\left(\frac{4}{u+3}\right)^4\,, \tag{3.33}$$

where $F(u) \equiv (\mathrm{d}N_s/\mathrm{d}u)/(\mathrm{d}N_s/\mathrm{d}u)_m$ and the subindex m refers to the maximum.

In Ang's model [16]:

$$F(u) = ue^{-u}\,, \tag{3.34}$$

where $W_m \cong 2\,\mathrm{eV}$.

In Vicente's model [75], the emission spectrum is described as following a Maxwellian distribution (presumably, the author is referring to the Maxwell–Boltzmann energy spectrum for gas equilibrium):

$$\frac{\mathrm{d}N_s}{\mathrm{d}W_d} = \frac{2}{\sqrt{\pi}kT}\sqrt{\frac{W_d}{kT}}e^{-\frac{W_d}{kT}} \,. \tag{3.35}$$

The maximum of this distribution is reached at $W_m = kT/2$ and therefore it can be expressed as:

$$F(u) = \frac{1}{\sqrt{2\pi}}\sqrt{u}e^{-\frac{u}{2}} \,. \tag{3.36}$$

Because it does not make much sense to talk about the temperature of electrons in a situation so far from thermodynamic equilibrium, it must be assumed that the author, instead of using $W_m = kT/2$, uses a similar distribution with a W_m energy corresponding to the maximum emission spectrum.

In Coves's model [20], the secondary electron emission is assumed to follow a Rayleigh probability density function of the following form:

$$\frac{\mathrm{d}N_s}{\mathrm{d}W_d} = \frac{W_d}{W_m^2}e^{-\frac{W_d^2}{2W_m^2}} \,, \tag{3.37}$$

or its equivalent:

$$F(u) = ue^{-\frac{u^2}{2}} \,, \tag{3.38}$$

where the maximum of the distribution is assumed to be $W_m = 3\,\mathrm{eV}$ for the material used.

None of these distribution models consider the limitation imposed by the law of conservation of energy. If the energy of the primary electron is large enough relative to W_m, this is not a serious limitation. Because W_m is typically 2–3 eV, for primary electrons with energies of less than about 10 eV ($W_d/W_m \approx 3.5$) the effect could be relevant, depending on the spectrum model used.

In De Lara's model [68], an estimate of the number of secondary emitted electrons is made and their output energy is obtained sequentially, taking into account in each case the remaining available energy. The spectrum used is:

$$\frac{\mathrm{d}N_s}{\mathrm{d}x} = \frac{2\frac{\tan\left(\frac{\pi}{2}x\right)}{\tan\left(\frac{\pi}{2}x_{cs}\right)}\left(1+\tan\left(\frac{\pi}{2}x\right)\right)}{1+\left(\frac{\tan^2\left(\frac{\pi}{2}x\right)}{\tan\left(\frac{\pi}{2}x_{cs}\right)}\right)^2} \,, \tag{3.39}$$

where

$$x \equiv \left(\frac{E}{E_p}\right)^{n_s} \,, \tag{3.40}$$

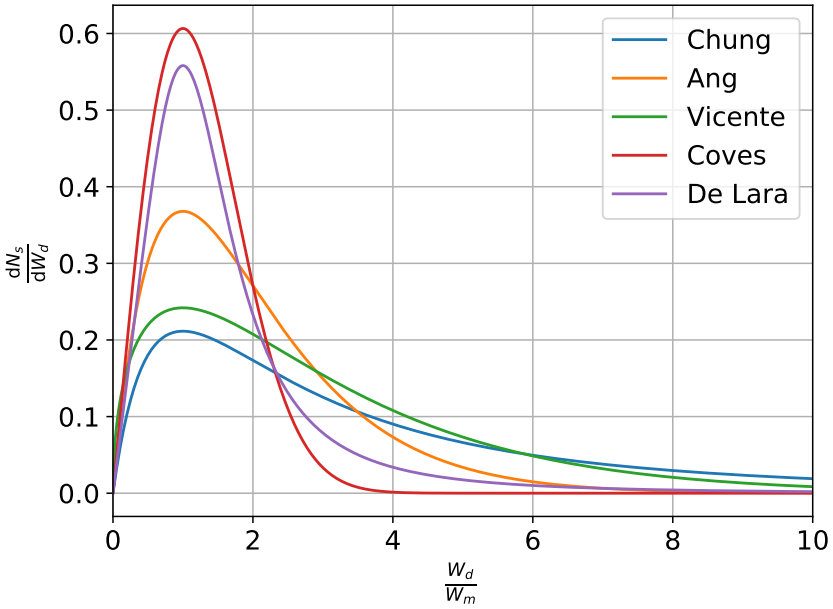

Figure 3.10: Probability density function of the secondary electrons' departing kinetic energy after each electron impact, according to various models.

and n_s depends on the material; x_{cs} is a function of the material and the primary energy E_p.

In this thesis, the secondary electrons' departing kinetic energy W_d after each electron impact is assumed to fit the following probability density function [71]:

$$\frac{\mathrm{d}N_s}{\mathrm{d}W_d} = e^{-\frac{\ln^2\left(\frac{W_d}{W_m}\right)}{2\tau^2}}, \tag{3.41}$$

or its equivalent:

$$F(u) = e^{-\frac{\ln^2(u)}{2\tau^2}}, \tag{3.42}$$

where the parameter τ (typical value 0.7–0.8) determines the width of the distribution and W_m (typical value 3–4 eV) is the energy of the maximum of the spectrum (i.e. the most probable energy value of the secondary electrons on departure following electron impact). Figure 3.11 depicts the shape of this function.

In order to determine W_d, the acceptance-rejection sampling method has been used [86, 87]. As explained by Glen in [88], this sampling is a Monte Carlo method to simulate random samples from an unknown (or difficult to sample) distribution $f(x)$ (called the target distribution) by using random samples from a similar, more convenient distribution $g(x)$. A random subset of the generated samples are rejected, the rest are accepted. The goal is for the accepted samples to be distributed as if they

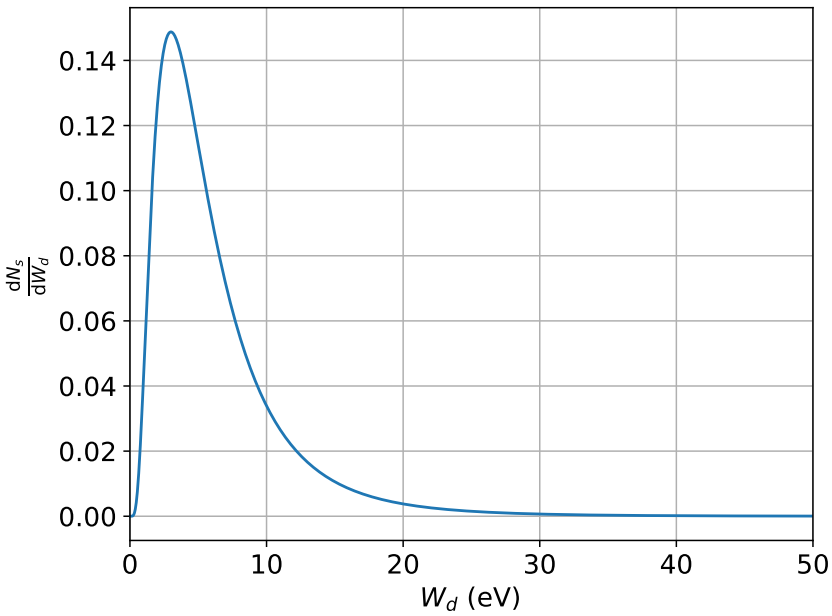

Figure 3.11: Probability density function of the secondary electrons' departing kinetic energy after each electron impact.

were from the target distribution. Let us assume that we need to sample from the inverse of a particular function, but an explicit inverse does not exist. We could use a similar distribution, making sure that the two distributions look as similar as possible and both functions have the same support (i.e. both cumulative distribution functions vanish or do not vanish over the same set of real numbers). The general steps for sampling from a probability distribution with cumulative distribution function $f(x)$ using a second function $g(x)$ are: 1) generate a sample x from a distribution that has a density proportional to $g(x)$, where $g(x) \geq f(x)$ for all x; 2) generate a uniform random number $u \in [0, 1)$. If $u > f(x)/g(x)$, reject the sample and return to step 1, otherwise accept x as a sample [89]. For further details of this acceptance-rejection sampling method see Appendix C.

Following the acceptance-rejection sampling method described above, a random number from the uniform distribution U over the range $0 \leq u < 1$ is first generated. Then, W_d is calculated by multiplying the impact energy W_c by the random value u. Finally, using Equation (3.42), W_d is recomputed such that the condition $p(W_d) < u$ is satisfied.

3.3.4 Angular distribution of the emitted electrons

Once the departure energy of the effective electron after the impact with any of the waveguide walls is known, the next step is to determine the departure velocity $\mathbf{v}_d$. The electron's energy can be converted into a velocity according to:

$$\|\mathbf{v}_d\| = \sqrt{2W_d \frac{e}{m_0}}\,, \tag{3.43}$$

where e and m_0 are the charge and the mass at rest of the electron, respectively.

In the case of inelastic impacts, the secondary electrons are emitted following the cosine law distribution of the polar angle, almost independent of the angle of incidence of the primary electrons [5, 69, 90]. As detailed by Greenwood in [91], in terms of the electrons leaving a surface, the electron flux $\mathrm{d}n$ across a plane surface element A, due to all electrons having velocity vectors with directions within a small solid angle $\mathrm{d}\Omega$, whose axis makes an angle θ with the normal to A, is given by the cosine law formula. So that:

$$\mathrm{d}n = \left(\frac{N v_a}{4}\right) \frac{1}{\pi} A \cos\theta \mathrm{d}\Omega\,, \tag{3.44}$$

where N is the number density of molecules and $v_a = \langle v \rangle$ is the average molecular velocity.

In the system of spherical polar co-ordinates (Figure 3.2), the solid angle, $\mathrm{d}\Omega$, is given by:

$$\mathrm{d}\Omega = \sin\theta \mathrm{d}\theta \mathrm{d}\phi\,. \tag{3.45}$$

Hence, Equation (3.44) can be written in terms of the polar and azimuthal angles (θ, ϕ):

$$\mathrm{d}n = \frac{N A v_a}{4\pi} \cos\theta \sin\theta \mathrm{d}\theta \mathrm{d}\phi\,. \tag{3.46}$$

From kinetic theory [92], we have the result that the total molecular flux N_0 from A is:

$$N_0 = \frac{N A v_a}{4}\,. \tag{3.47}$$

Hence, the cosine law can conveniently be written as:

$$\mathrm{d}n = \frac{N_0}{\pi} \cos\theta \sin\theta \mathrm{d}\theta \mathrm{d}\phi\,. \tag{3.48}$$

The angular probability distributions for electrons scattered with a cosine distribution can be determined from Equation (3.48). Electrons emitted with a particular azimuth ϕ occur with a range of polar angles θ. Therefore, to obtain the azimuthal

angular-probability distribution function $f(\phi)$, which is the probability that an electron will have a velocity vector of any allowed θ value in the azimuthal angular range $\phi = \phi + \mathrm{d}\phi$, Equation (3.48) should be integrated over all θ to determine the electron flux $\mathrm{d}n_\phi$ in the range:

$$\mathrm{d}n_\phi = \frac{N_0}{\pi}\mathrm{d}\phi \int_0^{\pi/2} \cos\theta \sin\theta \mathrm{d}\theta \,. \tag{3.49}$$

The integral evaluates to $\frac{1}{2}$. Hence, after rearrangement, we can specify:

$$f(\phi) = \frac{1}{N_0}\frac{\mathrm{d}n_\phi}{\mathrm{d}\phi} = \frac{1}{2\pi} \,. \tag{3.50}$$

Electrons with a particular polar direction θ occur with a range of azimuthal angles ϕ. Therefore, to discover the polar angular-probability distribution function $g(\theta)$, Equation (3.48) should be integrated over all ϕ:

$$\mathrm{d}n_\theta = \frac{N_0}{\pi} \cos\theta \sin\theta \mathrm{d}\theta \int_0^{2\pi} \mathrm{d}\phi \,, \tag{3.51}$$

that is:

$$\mathrm{d}n_\theta = 2N_0 \cos\theta \sin\theta \mathrm{d}\theta \,, \tag{3.52}$$

and therefore:

$$g(\theta) = \frac{1}{N_0}\frac{\mathrm{d}n_\theta}{\mathrm{d}\theta} = 2\cos\theta\sin\theta = \sin 2\theta \,. \tag{3.53}$$

Thus, $g(\theta)\mathrm{d}\theta$ gives the fraction of electrons that have velocity vectors between θ and $\theta + \mathrm{d}\theta$.

Random number generation of the angular distributions of Equations (3.50) and (3.53) to produce a cosine distribution of electron flux can be achieved in a number of ways. In the first case, generating the azimuthal angle is mathematically trivial. The simplest approach is to generate a uniformly distributed random number u_1 in the range $0 < u_1 \leq 2\pi$, and then to assign $\phi_d = u_1$. Alternatively, if the random number can only be generated in a limited range, for example $0 < u_1 \leq 1$, then $f(\phi_d)$ can be generated by scaling u_1:

$$\phi_d = 2\pi u_1 \,. \tag{3.54}$$

The polar angle can be generated from a single uniformly distributed random number u_2 in the range $0 < u_2 \leq 1$. Following [93], integrating the polar angular-probability distribution gives:

$$u_2 = \frac{\int_0^{\theta_d} g(\theta)\mathrm{d}\theta}{\int_0^{\pi/2} g(\theta)\mathrm{d}\theta} = \frac{\int_0^{\theta_d} \sin 2\theta \mathrm{d}\theta}{1} = 1 - \cos^2\theta_d = \sin^2\theta_d \,, \tag{3.55}$$

that is:

$$\theta_d = \arcsin\sqrt{u_2}\,. \tag{3.56}$$

Table 3.3 shows the value of the departure velocity components, depending on the collision side, as a function of the polar angles. However, in the case of an elastic effective-electron impact, the departure energy will be exactly the same as the collision energy, according to the principle of energy conservation, and the departure velocity vector will be modified in the opposite direction from the normal direction to the metal surface.

Table 3.3: Departure velocity of the effective electron after each inelastic collision.

	Collision side			
	Top	**Bottom**	**Left**	**Right**
$v_{d,x}$	$\|\mathbf{v}_d\| \cdot A$	$\|\mathbf{v}_d\| \cdot A$	$-\|\mathbf{v}_d\|\cos(\theta_d)$	$\|\mathbf{v}_d\|\cos(\theta_d)$
$v_{d,y}$	$-\|\mathbf{v}_d\|\cos(\theta_d)$	$\|\mathbf{v}_d\|\cos(\theta_d)$	$\|\mathbf{v}_d\| \cdot B$	$\|\mathbf{v}_d\| \cdot B$
$v_{d,z}$	$\|\mathbf{v}_d\| \cdot B$	$\|\mathbf{v}_d\| \cdot B$	$\|\mathbf{v}_d\| \cdot A$	$\|\mathbf{v}_d\| \cdot A$

* $A \equiv \sin(\theta_d)\sin(\phi_d)$ and $B \equiv \sin(\theta_d)\cos(\phi_d)$.

3.4 Multipactor susceptibility regions

As explained in [64], the SEY models establish an impact energy region (between W_1, γ_1 and W_2, γ_2) where secondary electrons can be generated and, therefore, the multipactor effect can occur. This means that, under impact energies below or above this region, the free electron density in the structure will naturally decrease. This concept helps in the understanding of the multipactor susceptibility charts (Figure 3.12). Such a chart warns of the risk of multipactor discharge in terms of the input power/voltage and the frequency-gap. The dashed lines mark the boundaries of the multipactor-susceptible regions, also known as multipactor orders. The multipactor susceptibility diagram indicates the range of RF power over which a device may be subject to multipactor. If the design parameters lie within the multipactor boundaries (positive growth rate) then multipactor is possible and the design needs to be modified [27].

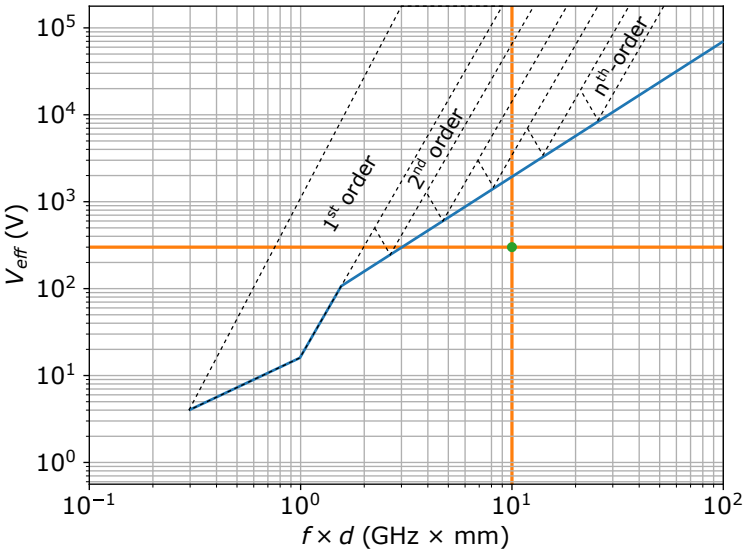

Figure 3.12: Multipactor susceptibility chart example in which $f \times d = 12\,\mathrm{GHz\,mm}$ has been considered as the operating frequency-gap. This structure would have a multipactor voltage threshold of around 730 V. The design coordinate is marked with a green circle, at around 310 V.

In the horizontal axis of the susceptibility chart, the product $f \times d$, corresponding to the operating frequency-gap, is plotted. Meanwhile, in the vertical axis, the effective voltage V_{eff} is represented, which in the rectangular waveguide has been numerically calculated as the line integral of the E_y component of the electric field (evaluated at the centre of the waveguide $x = a/2$) from $y_1 = 0$ to $y_2 = d$. In the equivalent parallel-plate waveguide, this voltage is obtained as $E_0 \times (d - h)$, E_0 being the RF field amplitude, which in this case can be calculated as [19]:

$$E_0 = \frac{\epsilon_r V_{eff}}{h + \epsilon_r (d - h)} \,. \tag{3.57}$$

As illustrated in Figure 3.12, for a particular $f \times d$ product, we start from zero and travel towards positive peak voltages. Once the blue line is crossed, a voltage value V_{th} has been reached that is capable of inducing a multipactor discharge. Increasing the voltage further will cause a second crossing at a certain V_{eff} value, which indicates the exit from the multipactor-sensitive region. The same principle applies for the remaining multipactor-order regions, although higher orders are more unstable due to the longer travel time of the electron between impacts. Nevertheless, a common practice is to set an envelope threshold V_{th} (the blue line in Figure 3.12) below the lower boundaries of all the multipactor-order regions, which establishes a conservative maximum threshold for design purposes [64].

3.5 Summary

A detailed description of the main drivers that define the multipactor effect have been presented in this chapter.

First of all, it should be pointed out that to successfully predict multipactor, the trajectory of the electrons in the waveguide must be calculated. To achieve this goal, the position of the electrons needs to be determined over time. In this chapter, the relevant electron dynamics have been entirely described.

Second, the different alternatives available in the literature for modelling the SEY curves have been presented, from which a modified Vaughan model has been chosen. Defined as the number of secondary electrons emitted per incident electron and being specific to the material, the SEY is one of the main elements that describes the multipactor effect, because it is an important part of the emission process. As previously described, the SEY is highly dependent on the incident angle of impact. Therefore, for every collision event, the angle between the trajectory of the electron and the normal vector to the surface must be calculated.

Third, the EEM has been chosen to simulate the behaviour of the electrons inside the waveguide. This model consists of tracking the individual trajectories of an effective electron, as well as its accumulated electron population. The effective electron gains or loses charge and mass after every impact with the device walls depending on the SEY value at impact time. The main advantages and limitations of this model have been presented.

Fourth, once the emission energy of the electron has been defined, the angular distribution must be assigned for all secondary electrons. In this case, a cosine law distribution for the polar angle has been assumed, being almost independent of the angle of incidence of the primary electrons.

Finally, the so-called multipactor susceptibility chart has been presented. This is a design figure that allows us to visualize the areas where the multipactor effect could occur, given a specific voltage (or power) input and working frequency.

Chapter 4

Simulation and analysis of the multipactor effect

4.1 Introduction

Having presented the theoretical framework of the new multipactor model developed in this research work, different configurations of waveguide will be studied in this chapter that will allow a better understanding of the effects that cause the appearance of multipactor.

To carry out this work, the simulation tool that has been developed on the basis of the theory described in the previous chapters will be presented in Section 4.2. Simulations of several waveguide configurations will be performed, taking into consideration different assumptions and approximations. For instance, in Section 4.3, the results obtained by applying a simplified analytical solution will be compared with those of an accurate numerical solution for the electromagnetic fields inside the device. In addition, in Section 4.4, the differences between the parallel-plate (widely used in this field to date) and rectangular waveguide models will also be explored. Finally, in Section 4.5, we will address the validation of the effective-electron model (EEM) used in our multipactor study. Moreover, the effect of introducing several dielectric sheets into a rectangular waveguide will be analysed, together with the implications for their associated susceptibility charts.

4.2 Multipactor simulation tool

An in-house computer-aided design (CAD) simulation tool based on the Monte Carlo method described in Chapter 3 has been developed to analyse the multipactor effect in partially dielectric-loaded rectangular waveguides. The software has been designed to

analyse the multipactor effect for both the most generic case of a partially dielectric-loaded rectangular waveguide, and that of an empty rectangular waveguide. It has been developed in the Fortran programming language for two main reasons: 1) computational efficiency –the simulations that must be performed make heavy computational demands, and Fortran is still considered one of the most efficient programming languages for calculations with complex variables; 2) the software for calculating electromagnetic fields in a partially filled dielectric rectangular waveguide, which is needed for the multipactor analysis in these waveguides, was implemented in Fortran too [37].

The implementation is based on the vector modal method described in Chapter 2, which provides the first modes of the waveguide under study (the electromagnetic fields and propagation constants), although the multipactor effect is usually studied in the single-mode case. In this version of the software, all the electromagnetic field components are considered without approximations. Likewise, the relativistic term has been included, which allows us to precisely resolve the trajectory of the electrons even at high power levels. That said, an additional version has also been developed to analyse the multipactor effect in an empty rectangular waveguide, using the equations of motion for the electron in the waveguide described in Subsection 2.2.2 under certain approximations: 1) the magnetic field components are ignored because they are much less intense than those of the electric field; 2) the relativistic term is not considered, on the assumption that high levels of power will not be reached. Both versions of the software have in common the function for calculating the SEY value following the collisions of the electrons with the metal walls of the waveguide, and the function that calculates the departure energy of the secondary electrons emitted.

The pseudocode of the multipactor simulation tool is shown in Algorithms 1-5. Algorithm 1 describes the procedure to obtain the position of the electron $\mathbf{r_i}$ at each instant of time t_i. To calculate the susceptibility chart of the waveguide under analysis, a frequency ω_0, ..., ω_{M-1} and a voltage V_{eff_0}, ..., $V_{eff_{N-1}}$ sweep are performed. At each point in this double sweep, a Monte Carlo simulation of the multipactor effect is performed for a specified number of initial phase points ψ_0, ..., ψ_{L-1} of the electromagnetic field. In this way, if the number of electrons generated inside the waveguide increases exponentially in any of the simulations, it will be considered that the multipactor effect has occurred at that frequency and voltage working point.

At each instant, the electron may be moving inside the waveguide or it may impact one of the walls of the device. In the event of the latter, the procedure for Algorithm 2 is triggered, which determines both the SEY value generated after the impact of

the electron as a function of the energy W_c and angle θ_c of the collision, and the type of impact: elastic or non-elastic. The software is designed to work with both experimental values and theoretical models of the SEY curve of the materials used in the design, as can be seen in Algorithm 3.

Finally, in the case of a non-elastic impact, both the energy W_d and the departure angles ϕ_d and θ_d of the secondary electrons emitted are calculated using the functions shown in Algorithms 4 and 5.

4.2.1 Model validation

As explained previously, our model solves the electron dynamics for the field components numerically, without considering any approximation, and including the relativistic term. Before starting on the multipactor analysis of different waveguide designs, it is proposed to validate the model developed in this thesis. For this purpose, the problem discussed in this subsection consists of an empty rectangular waveguide, previously studied by Chojnacki [4].

The rectangular waveguide has dimensions $a = 43.2\,\text{cm}$ and $b = 10.2\,\text{cm}$, and it is excited by a time-harmonic signal at $f = 500\,\text{MHz}$. The material of the waveguide walls is niobium, whose SEY properties are given in Table 3.1 and can be expressed with the simple model proposed by Geng and Padamsee [94]. A schematic of this waveguide is provided in Figure 4.1.

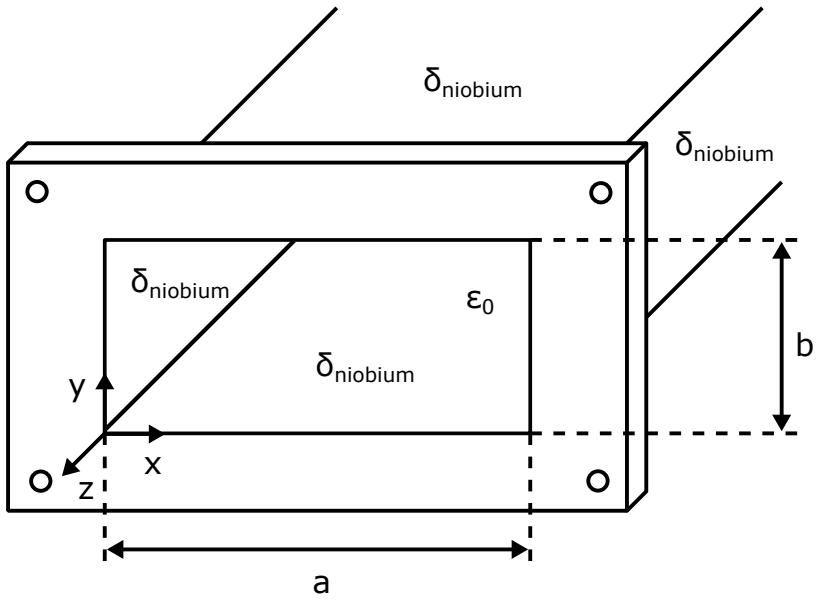

Figure 4.1: Transverse section of the empty rectangular waveguide, air-filled (ϵ_0), of width $a = 43.2\,\text{cm}$ and height $b = 10.2$ cm, used for validation.

Algorithm 1 Electron dynamics

procedure ELECTRONDYNAMICS
  for all $\omega_m \mid m = 0, ..., M-1$ **do** ▷ Frequency loop
    for all $V_{eff_n} \mid n = 0, ..., N-1$ **do** ▷ Voltage loop
      $E_{0_n} \leftarrow V_{eff_n}$
      for all $\psi_l \mid l = 0, ..., L-1$ **do** ▷ Phase loop
        $t_0 \leftarrow 0$
        $\mathbf{r_0} \leftarrow (x_0 = 0, y_0, z_0 = 0)$
          where $-0.5b + h_d \leq y_0 = \text{random}() \leq 0.5b - h_u$
        $\mathbf{E_{RF}}(\mathbf{r_0}, t_0) \leftarrow \mathbf{e}(x_0, y_0), \mathbf{H_{RF}}(\mathbf{r_0}, t_0) \leftarrow \mathbf{h}(x_0, y_0)$
        $Q_i(\mathbf{r'_i}) \leftarrow 0, \mathbf{E_{DC}}(\mathbf{r_i}) \leftarrow 0$
        $\mathbf{E}(\mathbf{r_0}, t_0) \leftarrow \mathbf{E_{RF}}(\mathbf{r_0}, t_0) + \mathbf{E_{DC}}(\mathbf{r_0}), \mathbf{H}(\mathbf{r_0}, t_0) \leftarrow \mathbf{H_{RF}}(\mathbf{r_0}, t_0)$
        $\mathbf{v_0} \leftarrow (v_{x0}, v_{y0}, v_{z0})$
          where $\|\mathbf{v_0}\| = \text{random}(), \theta_0 = \text{random}(), \phi_0 = \text{random}()$
        $\mathbf{a_0} \leftarrow (a_{x0}, a_{y0}, a_{z0})$
        while $(t_i \leq T) \wedge (N \leq N_{min})$ **do** ▷ Time loop, $N_{min} = 10^{-5}$
          $\Delta t_i(x_i, y_i), t_i \leftarrow t_{i-1} + \Delta t_i$
          $\mathbf{r_i} \leftarrow (x_i, y_i, z_i)$
          if $(y_{i-1} < 0.5b - h_u) \wedge (y_i \geq 0.5b - h_u)$ **then**
            COLLISION$(side = top)$
          else if $(y_{i-1} > -0.5b + h_d) \wedge (y_i \leq -0.5b + h_d)$ **then**
            COLLISION$(side = bottom)$
          else if $(x_{i-1} > -0.5a) \wedge (x_i \leq -0.5a)$ **then**
            COLLISION$(side = left)$
          else if $(x_{i-1} < 0.5a) \wedge (x_i \geq 0.5a)$ **then**
            COLLISION$(side = right)$
          else
            $\mathbf{E_{RF}}(\mathbf{r_i}, t_i) \leftarrow \mathbf{e}(x_i, y_i), \mathbf{H_{RF}}(\mathbf{r_i}, t_i) \leftarrow \mathbf{h}(x_i, y_i)$
            $\mathbf{E_{DC}}(\mathbf{r_i}) \ \forall Q_i(\mathbf{r'_i})$
            $\mathbf{E}(\mathbf{r_i}, t_i) \leftarrow \mathbf{E_{RF}}(\mathbf{r_i}, t_i) + \mathbf{E_{DC}}(\mathbf{r_i}), \mathbf{H}(\mathbf{r_i}, t_i) \leftarrow \mathbf{H_{RF}}(\mathbf{r_i}, t_i)$
            $\mathbf{v_i} \leftarrow (v_{xi}, v_{yi}, v_{zi})$
            $\mathbf{a_i} \leftarrow (a_{xi}, a_{yi}, a_{zi})$
          end if
        end while
      end for
    end for
  end for
end procedure

Algorithm 2 Collision

procedure COLLISION
    compute $W_c(\mathbf{v}_{i-1}), \theta_c(\mathbf{v}_{i-1}, \mathbf{u_n})$
    if $(side = top) \vee (side = bottom)$ **then**
        if $is\_dielectric = True$ **then**
            if $is\_experimental =$ **True then**
                $\delta, is\_elastic \leftarrow$ YIELD$(W_c, measures = diel, type = exp)$
            else
                $\delta, is\_elastic \leftarrow$ YIELD$(W_c, \theta_c, params = diel, type = model)$
            end if
        else
            if $is\_experimental =$ **True then**
                $\delta, is\_elastic \leftarrow$ YIELD$(W_c, measures = metal, type = exp)$
            else
                $\delta, is\_elastic \leftarrow$ YIELD$(W_c, \theta_c, params = metal, type = model)$
            end if
        end if
    else
        if $is\_experimental =$ **True then**
            $\delta, is\_elastic \leftarrow$ YIELD$(W_c, measures = metal, type = exp)$
        else
            $\delta, is\_elastic \leftarrow$ YIELD$(W_c, \theta_c, params = metal, type = model)$
        end if
    end if
    if $is\_elastic =$ **True then**
        $\mathbf{r_i} \leftarrow (x_i, y_i, z_i)$
        $\mathbf{E_{RF}}(\mathbf{r_i}, t_i) \leftarrow \mathbf{e}(x_i, y_i), \mathbf{H_{RF}}(\mathbf{r_i}, t_i) \leftarrow \mathbf{h}(x_i, y_i)$
        $\mathbf{E_{DC}}(\mathbf{r_i}) \; \forall Q_i(\mathbf{r'_i})$
        $\mathbf{E}(\mathbf{r_i}, t_i) \leftarrow \mathbf{E_{RF}}(\mathbf{r_i}, t_i) + \mathbf{E_{DC}}(\mathbf{r_i}), \mathbf{H}(\mathbf{r_i}, t_i) \leftarrow \mathbf{H_{RF}}(\mathbf{r_i}, t_i)$
        $\mathbf{v_i} \leftarrow (v_{xi}, v_{yi}, v_{zi})$
        $\mathbf{a_i} \leftarrow (a_{xi}, a_{yi}, a_{zi})$
    else
        if $W_c < W_m$ **then**
            $W_d \leftarrow W_c$
        else
            $W_d \leftarrow$ DEPARTUREENERGY(τ, W_m, W_c)
            while $\delta W_d > W_c$ **do**
                $W_d \leftarrow$ DEPARTUREENERGY(τ, W_m, W_c)
            end while
        end if
        $\phi_d, \theta_d \leftarrow$ COSINELAW()
    end if
end procedure

Algorithm 3 Secondary emission yield

function YIELD($W_c, \theta_c, measures, params, type$)
    if $type = exp$ **then**
        $\delta, is\_elastic \leftarrow$ linear_interpolation($W_c, measures$)
    else
        $\delta, is\_elastic \leftarrow$ sey_model($W_c, \theta_c, params$)
    end if
    return $\delta, is\_elastic$
end function

Algorithm 4 Departure Energy

function DEPARTURE_ENERGY(τ, W_m, W_c)
    $x = 0, u = 0$
    if $W_c \geq 50$ **then**
        $W_c = 50$
    end if
    while $x \leq y$ **do**
        $z \leftarrow Z \sim U[0, 1)$
        $W_d \leftarrow zW_c$
        $x \leftarrow \mathrm{F}(\tau, W_m, W_c)$ ▷ F refers to Equation (3.42)
        $y \leftarrow Y \sim U[0, 1)$
    end while
    return W_d
end function

Algorithm 5 Cosine Law

function COSINE_LAW()
    $x \leftarrow X \sim U[0, 1), y \leftarrow Y \sim U[0, 1)$
    $\phi_d \leftarrow 2\pi x$
    $\theta_d \leftarrow \arcsin\sqrt{y}$
    return ϕ_d, θ_d
end function

In the algorithm of the simulator used by Chojnacki [4], for each power level considered in the waveguide, the initial electron is launched at $x = a/2$, and the simulation is run 42 times, corresponding to the same number of equidistant phases of the RF field. The arithmetic mean of the final population of electrons after 20 collisions of the effective electron with the walls is calculated using all 42 simulations. In addition, both the initial and secondary electrons generated after each collision are launched perpendicular to the surface impacted by the electron with an energy of 2 eV. The maximum simulation lifetime of each electron is $t_{\max} = 1000$ RF cycles, and the simulation is stopped if the impact energy is lower than 0.1 eV or if the accumulated population of electrons is below 10^{-3}. To reproduce the same simulation conditions, our CAD tool has been adapted accordingly. Because the power range is relatively high in all cases, the relativistic effect is taken into account when calculating the electron motion.

In Figure 4.2, the results of the mean population of electrons $\overline{N}$ computed with our code (blue lines) are compared with the curves presented by Chojnacki [4] (orange lines). In this figure we can see some power regions at high risk of multipactor. Both curves show good agreement in terms of the shape and location of these multipactor windows.

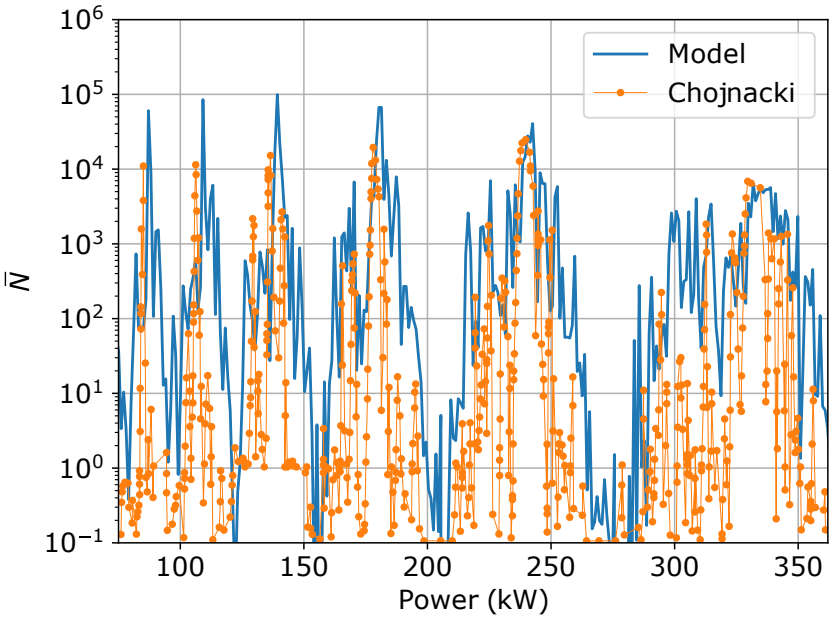

Figure 4.2: Comparison with Chojnacki [4] of the mean value of $\overline{N}$ over all launch phases in an empty rectangular waveguide ($a = 43.1$ cm and $b = 10.1$ cm) driven at $f = 500$ MHz with a maximum of 20 impacts from a single initial launch location on the midline of the waveguide.

4.3 Analytical and numerical approaches

As discussed in Section 2.2, under certain conditions the electromagnetic field components can be approximated allowing us to obtain analytical solutions for the trajectory of the electron inside the waveguide. The soundness of this approximation will be discussed below, comparing the results with the numerical model without approximations.

The path followed by the electron inside the waveguide will be calculated under the same initial conditions. The waveguide chosen for comparison corresponds to the standard WR34 rectangular waveguide, whose parameters are detailed in Table 4.1. However, for the multipactor study a much lower waveguide height than the standard

Table 4.1: Main parameters of the WR34 rectangular waveguide.

WR34 Specifications	
Recommended Frequency Band	22.0 GHz to 33.00 GHz
Cut-off Frequency of Lowest-order Mode	17.357 GHz
Cut-off Frequency of Upper Mode	34.715 GHz
Dimensions	8.636 mm × 4.318 mm

Source: Everything RF website [59].

one has been chosen, so that a multipactor effect of order one can occur. In particular, $b = 0.05\,\text{mm}$ has been set. The material assumed for the empty rectangular waveguide is aluminium. Figure 4.3 shows a schematic of it.

The movement of the effective electron along the x- and y-axes after 25 RF cycles given an input power of 250 W and a frequency of 22 GHz is plotted in Figure 4.4. This trajectory followed by the electron has been obtained by launching the effective electron from the same initial position and with the same velocity in both models. In addition, after each impact, the kinetic energy and departure angle have been fixed in order to be able to compare the results. As can be seen, the analytical and numerical models implemented in this thesis show very close alignment with one another. In both cases, the effective electron moves synchronously on the y-axis according to the applied RF electromagnetic field, following a first-order multipactor movement. A slight misalignment can be observed in the x-direction, which may be due to numerical precision issues, although it may also be a consequence of the approximations applied for the field components in the analytical model.

In terms of the population of electrons inside the waveguide, N determines whether or not the multipactor effect has occurred. The results of the simulation are presented

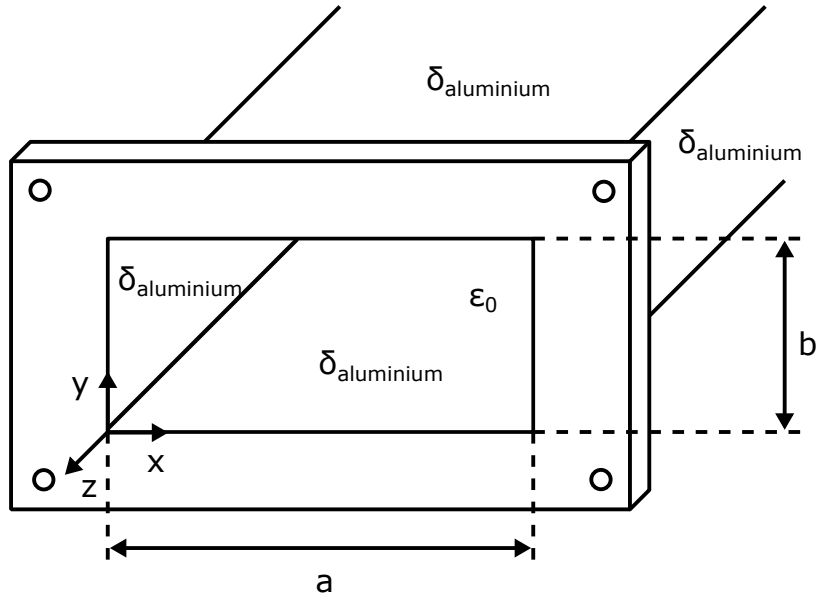

Figure 4.3: Transverse section of the empty WR34 rectangular waveguide, air-filled (ϵ_0), used for the comparison of the analytical and numerical approaches.

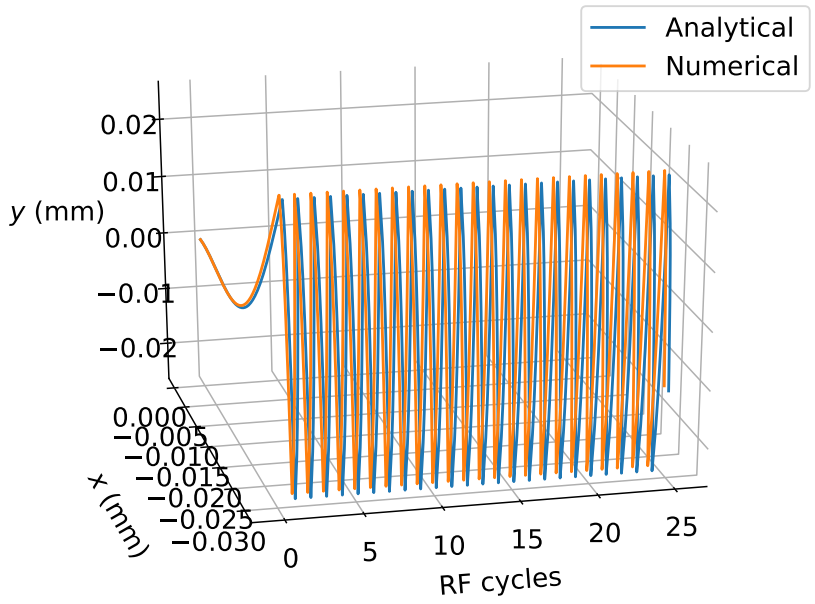

Figure 4.4: Electron trajectory in the x- and y-axes after 25 RF cycles; $b = 50\,\mu\text{m}$.

in Figure 4.5. It can be observed that, after approximately 42 RF cycles, the population of electrons begins to grow exponentially in both models, reaching a high value very quickly and thus resulting in a multipactor point.

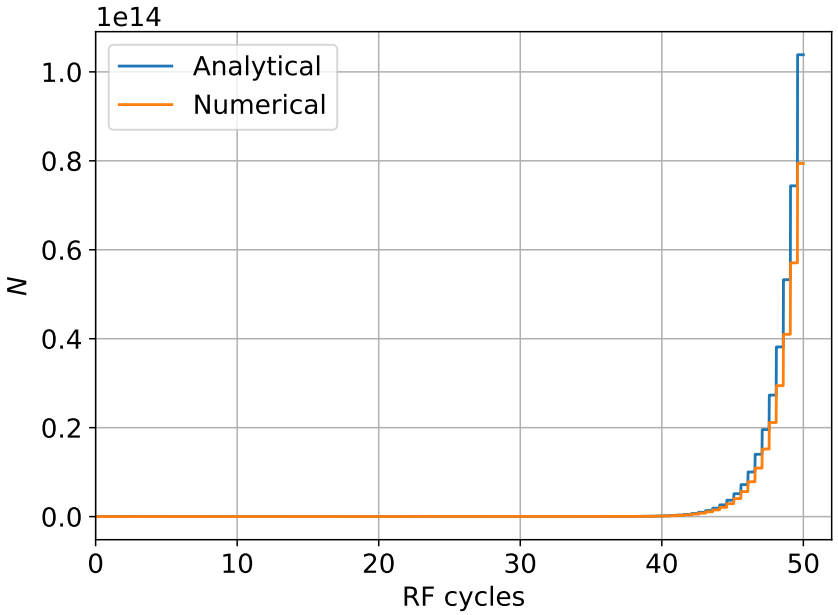

Figure 4.5: Total number of electrons N after 50 RF cycles; $b = 50\,\mu\text{m}$.

Finally, Figures 4.6 and 4.7 show the multipactor threshold power P_{th} as a function of frequency for two different values of waveguide height, $b = 50\,\mu\text{m}$ and $b = 200\,\mu\text{m}$, respectively. In these figures, the results obtained for the multipactor threshold power in the analysed empty waveguide with the models developed in this thesis (with and without approximations) have been compared with those provided by commercial software (FEST3D®)[1]. This software, based on integral equation technique theory and the method of moments (MoM), enables the analysis of homogeneous rectangular waveguides, including any type of discontinuities, which will be of great interest for validation purposes in more complex geometries such as impedance transformers, as will be shown later. As can be seen, the threshold power levels obtained with the numerical model developed in this thesis and with FEST3D® software present very similar results for the entire analysed frequency range (i.e. from 18 GHz to 25 GHz). In contrast, in the analytical case, which includes some approximations for field components, a slight increase in the multipactor threshold power is observed. This difference becomes more significant as the working frequency f and the waveguide height b increase.

[1] https://www.3ds.com/products-services/simulia/products/fest3d/

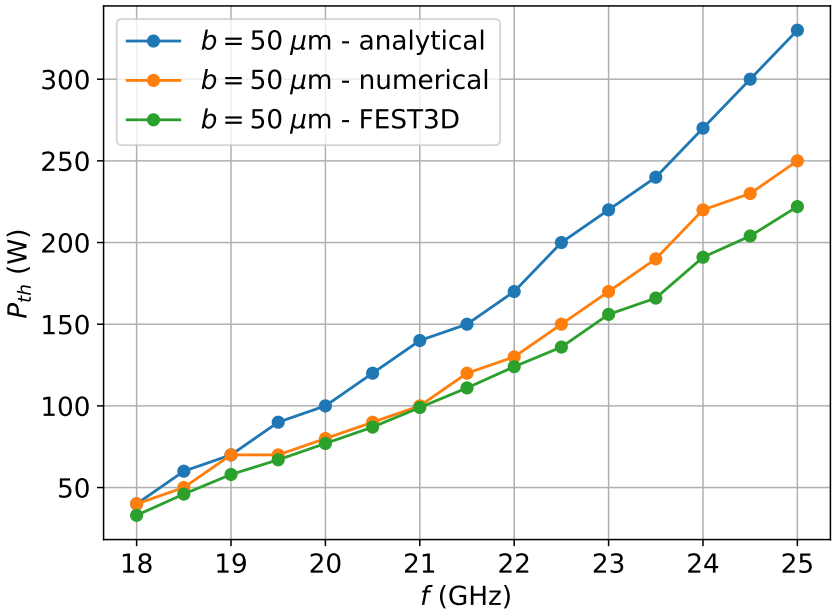

Figure 4.6: Multipactor power threshold P_{th} of the WR34 rectangular waveguide; $b = 50\,\mu\text{m}$.

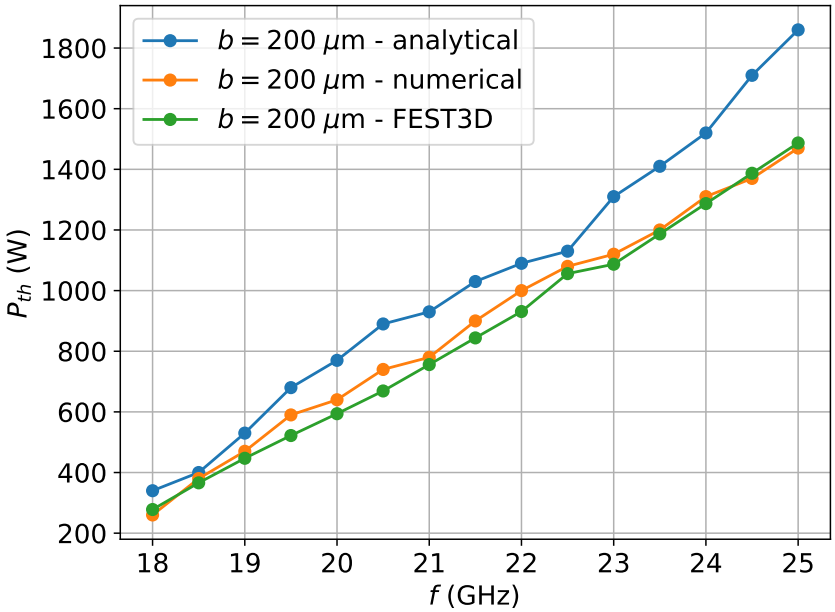

Figure 4.7: Multipactor power threshold P_{th} of the WR34 rectangular waveguide; $b = 200\,\mu\text{m}$.

4.4 Parallel-plate and rectangular waveguide models

The parallel-plate waveguide is a simple and commonly used transmission line, which is illustrated in Figure 4.8. It can support TE, TM and TEM modes because it is formed from two flat conducting plates. In this example, the parallel plates have spacing d and width w, and the wave propagation is in the z-direction. The plate width w is assumed to be much greater than the separation d, so that fringing fields and any variation in x can be ignored. A material with permittivity ϵ_0 is assumed to fill the region between the two plates. For a wave propagating in the z-direction with amplitude E_0, angular frequency ω and wave number k, the electric field $\mathbf{E}$ is given by:

$$\mathbf{E} = E_0 \sin(\omega t - k_z z)\hat{\mathbf{y}}\,, \tag{4.1}$$

where the amplitude E_0 is calculated by means of an electrostatic approach:

$$E_0 = \frac{V_{eff}}{d}\,. \tag{4.2}$$

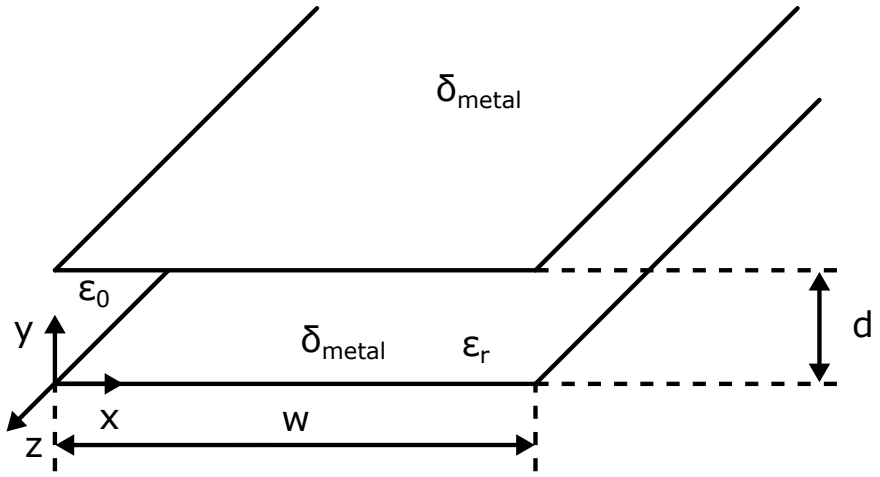

Figure 4.8: Transverse section of a parallel-plate waveguide, air-filled (ϵ_0), of width w and height d.

As explained by Sorolla and Mattes in [95], the parallel-plate waveguide is a good model in which to study many constructs, such as small gaps, where the electric field is reasonably homogeneous [96]. The physical mechanism behind classical multipactor breakdown has been studied by several authors. Initially, analytical expressions for the equations of motion of the electrons within a parallel-plate waveguide were derived without considering space charge effects [14, 81]. These were used to explain the

conditions that lead to multipactor onset and to calculate the voltage threshold that would trigger the electron avalanche. Nevertheless, they could not predict a limit to the number of electrons released by secondary emission, although a tentative description of the saturation taking into account the thermal spread in the initial velocity of the secondary electrons was made, and the consequent bunch breakup produced by the mutual repulsion between electrons was considered [81].

In this section, a comparative study of the results provided by our model for a very wide rectangular waveguide (i.e. $a \gg b$) with those generated by the model developed by Torregrosa et al. [19, 20, 21] for a parallel-plate waveguide has been conducted, both based on the EEM that incorporates the spread in secondary emission energy and the angle of the secondary electrons after each impact on the waveguide walls. For the very wide rectangular waveguide, we have checked that when the initial effective electron is launched in the centre of the waveguide, where the field is most intense, it moves slightly in the x-direction during the simulation, and thus the field intensity that accelerates the effective electron in the y-direction will be nearly constant.

First, the empty rectangular and parallel-plate waveguides will be compared, followed by their dielectric-loaded equivalents, in order to highlight their differences. It is important to note that a key difference between the multipactor models for the parallel-plate waveguide and the rectangular waveguide is the saturation mechanism predicted in the parallel-plate waveguide after a sufficient number of RF cycles, given that it includes the space charge effect. To compare the multipactor effect in both waveguides, the 1D model developed by Torregrosa et al. [19, 20, 21], which analyses the multipactor effect in a parallel-plate waveguide partially filled with dielectric, has been extended to a 3D model. It has been shown that the extension of the electron movement model from 1D to 2D or 3D appreciably reduces the multipactor threshold in the waveguide under study [97]. This is because in the 1D case, all of the output energy after each inelastic impact is used directly to shift the effective electron away from the waveguide wall, while in the 2D or 3D models part of the energy is employed to push the electron towards the opposite wall, losing some synchronization with the RF field.

4.4.1 Empty case

The schemes of the geometries and dimensions of the empty waveguides studied are shown in Figure 4.9. For the parallel-plate waveguide, the distance between the top and bottom plates is $d = 3\,\text{mm}$. Similarly, in the case of the equivalent rectangular waveguide, the waveguide height has been set to $b = 3\,\text{mm}$. With regard to the

waveguide width a, it has been chosen to be much wider than the waveguide height ($a \gg b$), and checked to ensure that there is at least one propagative mode in the frequency range analysed. Figure 3.8 documents the SEY characteristics of the silver material employed in the waveguides considered. The parameters are $W_1 = 30\,\text{eV}$, $W_2 = 5000\,\text{eV}$, $W_{max} = 165\,\text{eV}$, $W_0 = 16\,\text{eV}$, and $\delta_{max} = 2.22$.

First, a comparative study of the susceptibility charts for the parallel-plate waveguide and its rectangular equivalent with the same height is performed. For each V_0 and $f \times d$ pair, the simulation is run 72 times, corresponding to a set of equidistant phases of the RF field ranging from 0° to 360° in 5° increments. Further, for each simulation the effective electron is launched at $x = a/2$, $z = 0$, and a random position y_0 on the y-axis between $y = 0$ and $y = d$. The departing kinetic energy of the electrons emitted follows a probability density function given in Scholtz et al. [71] with a cosine distribution of the polar angle. Each simulation lasts 100 RF cycles, with 5000 time intervals per cycle. The arithmetic mean of the final population of electrons after 100 RF cycles is calculated using all 72 simulations. If this mean value is greater than one, then a multipactor discharge is assumed to have occurred.

In Figures 4.10-4.13, the comparable susceptibility charts of both the empty silver parallel-plate waveguide and its rectangular equivalent are shown, for both 1D and 3D models[2].

The differences between the susceptibility charts are evident. The multipactor region experiences a significant decrease when 3D movement inside the empty parallel-plate waveguide is considered. This decrease is observed not only as a multipactor threshold reduction, that is, a decrease of the voltage threshold at each $f \times d$ point, but also in the high-voltage regions. The decrease observed for the multipactor region in the 3D movement case is due to a slight desynchronization of the electron's resonant movement after each impact, given that the secondary electron's departing kinetic energy is distributed among three velocity components in the 3D model, whilst in a 1D model all of the secondary electron's departing kinetic energy is used to push the effective electron towards the opposite wall. In the case of the 3D rectangular waveguide model, the susceptibility chart appears very similar to its 3D parallel-plate equivalent, that is, a significant decrease in the multipactor region can be seen when compared to the 1D parallel-plate waveguide model.

Secondly, in order to perform a detailed analysis of the physical behaviour and the dynamics of the effective electron inside the waveguides under study, different

[2]Results were also obtained for a 2D model but are not shown here because the results were quite similar to those of the 3D model.

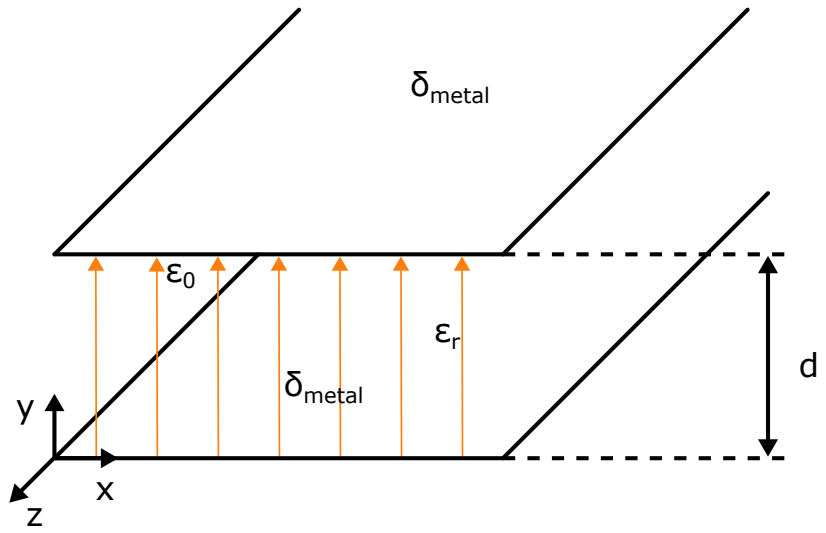

(a) Empty parallel-plate waveguide.

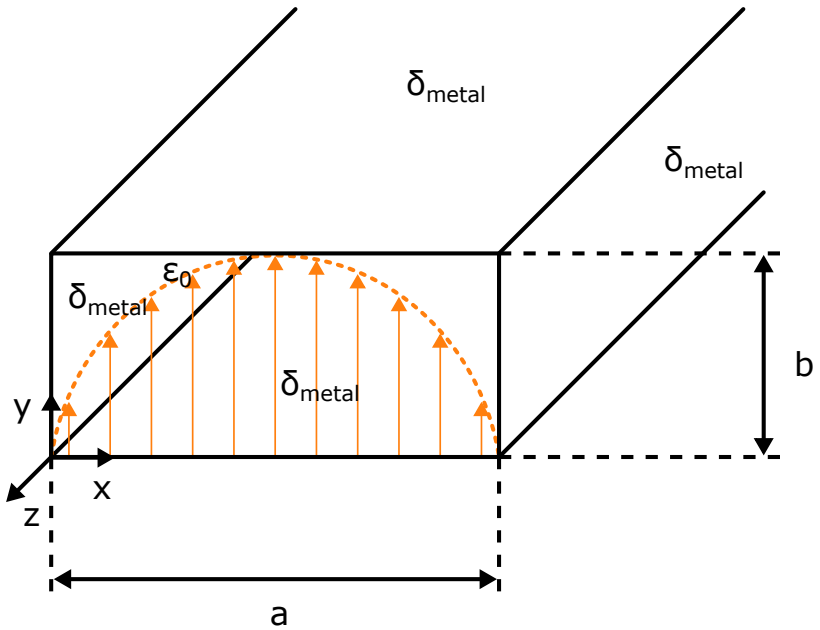

(b) Empty rectangular waveguide.

Figure 4.9: Schemes of the geometries and dimensions of the empty parallel-plate and equivalent rectangular waveguides.

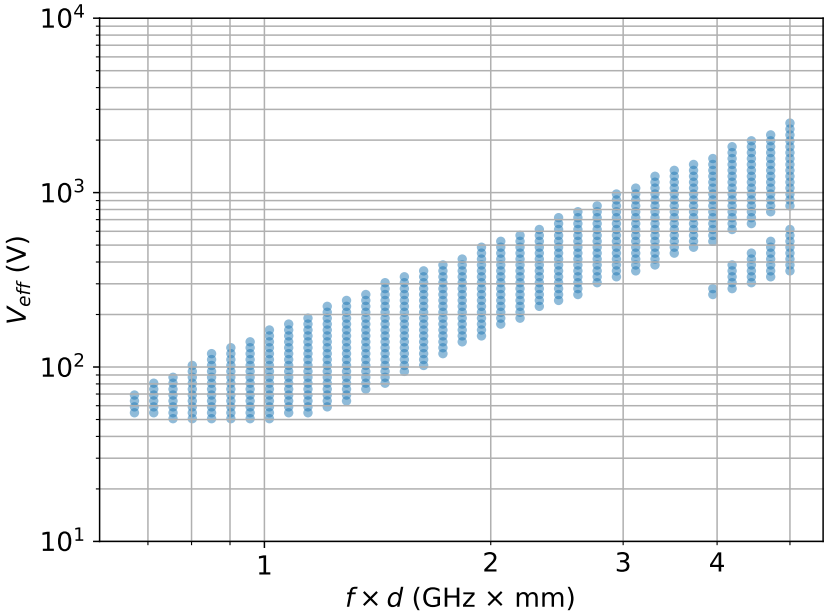

Figure 4.10: Susceptibility chart for the empty silver parallel-plate waveguide using a 1D model.

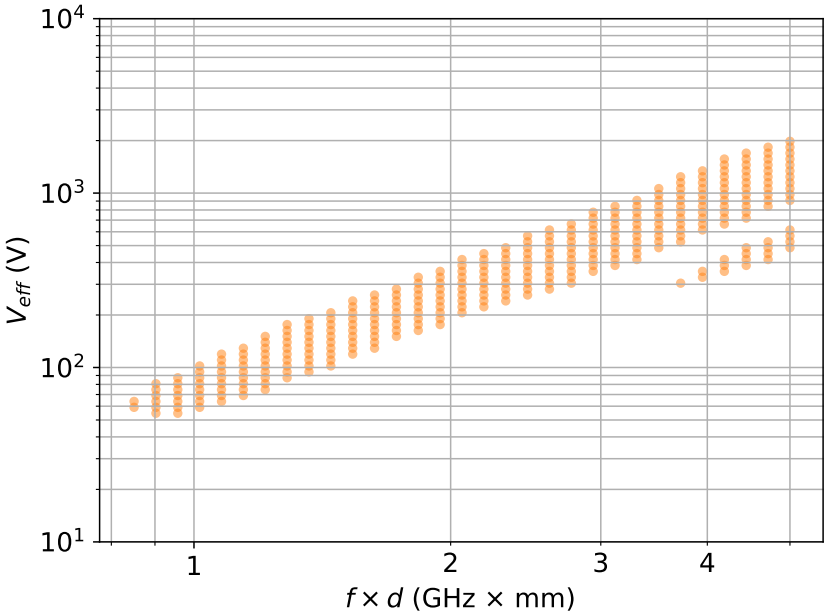

Figure 4.11: Susceptibility chart for the empty silver parallel-plate waveguide using a 3D model.

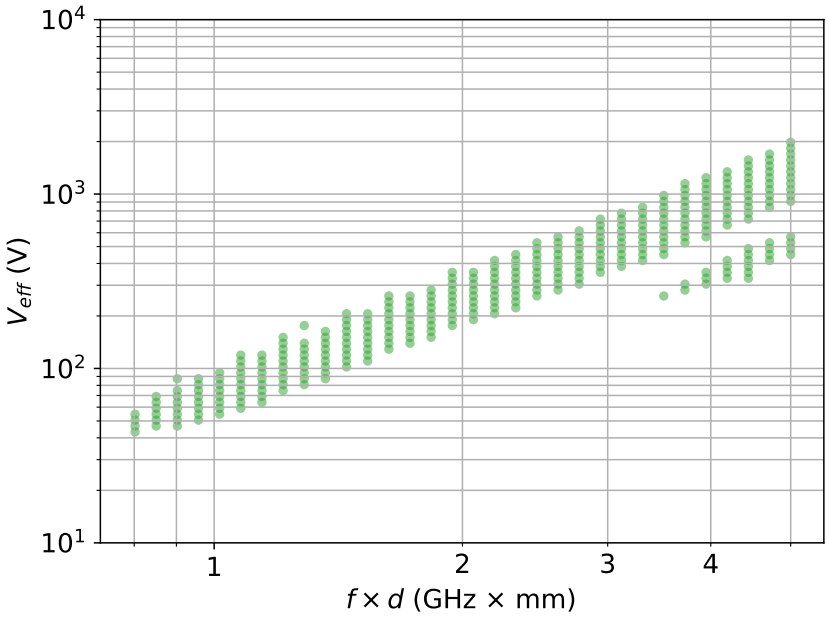

Figure 4.12: Susceptibility chart for the empty silver rectangular waveguide using a 3D model.

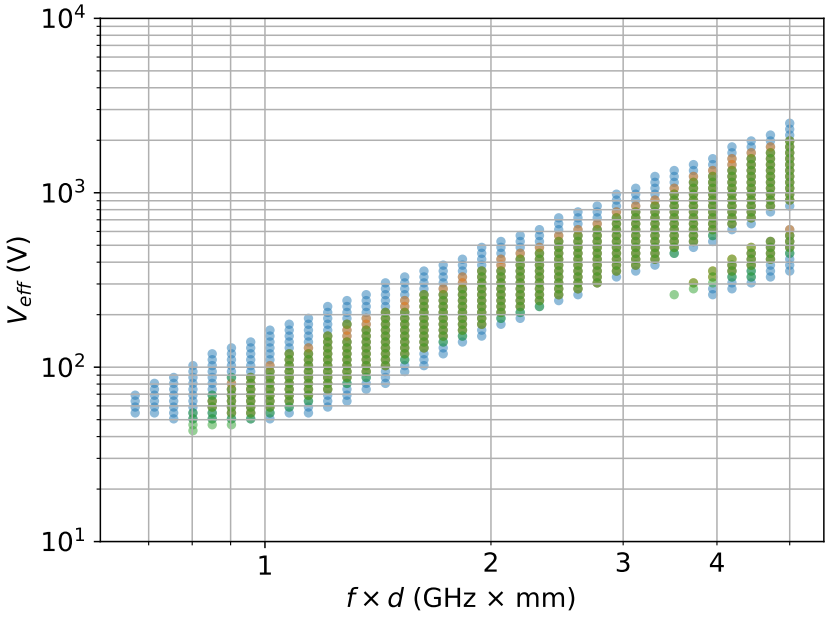

Figure 4.13: Comparison of the susceptibility charts for the empty silver parallel-plate waveguide using 1D and 3D models (blue and orange points, respectively) and the equivalent rectangular waveguide using a 3D model (green points).

parameters have been compared by considering a point within the multipactor region. In all cases, $V_0 = 70\,\mathrm{V}$, $f \times d = 1\,\mathrm{GHz\,mm}$ is the point considered.

In Figures 4.14-4.16, the populations of electrons after 100 RF cycles are shown. For the 1D parallel-plate waveguide model, the population of electrons rises steadily until a saturation level of around 10^{10} electrons is reached because of the space charge effect, after approximately 25 RF cycles. Similar results are obtained for the 3D parallel-plate waveguide model, except that the saturation level is reached after 50 RF cycles. In terms of the 3D rectangular waveguide model, no saturation level can be seen after 100 RF cycles because no space charge effect has been considered for this waveguide. However, the same electron population level as in the 3D parallel-plate waveguide model is achieved after 45 RF cycles, which corroborates the notion that in this 3D model there is a desynchronization of the electrons' resonant movement after each impact.

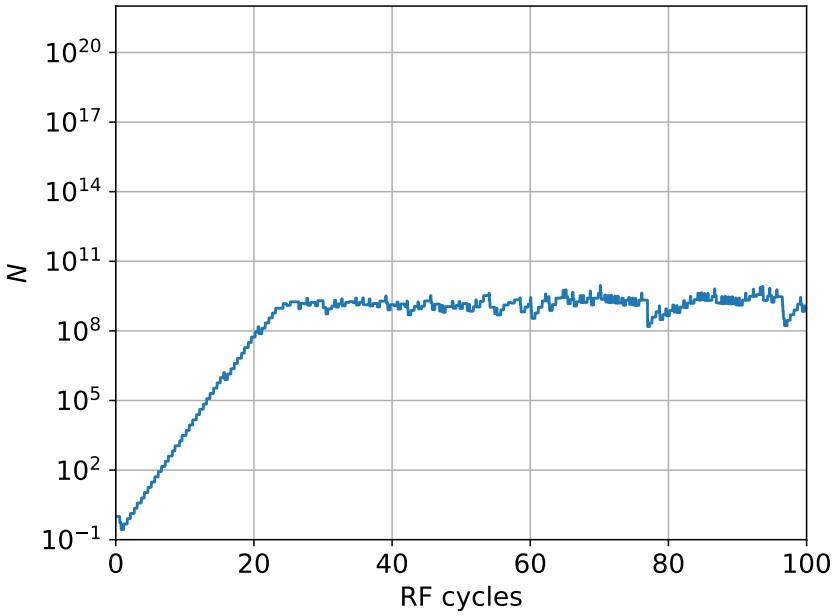

Figure 4.14: Total number of electrons N in the empty silver parallel-plate waveguide after 100 RF cycles using a 1D model.

Finally, the y-coordinate position of the effective electron over 30 RF cycles is shown in Figures 4.17-4.19. As can be seen, for the 3D models of both the parallel-plate and the rectangular waveguides, there is a slight desynchronization in the path followed by the electron, mainly in the initial RF cycles.

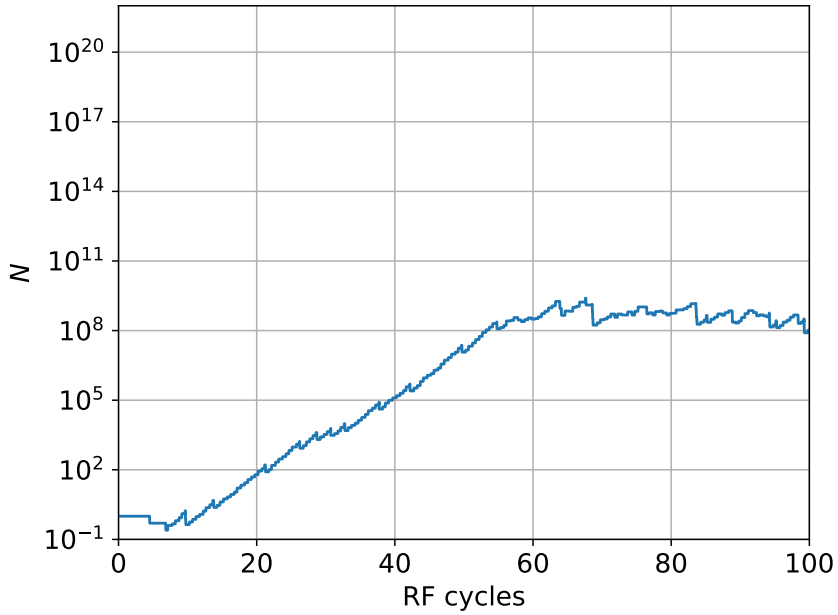

Figure 4.15: Total number of electrons N in the empty silver parallel-plate waveguide after 100 RF cycles using a 3D model.

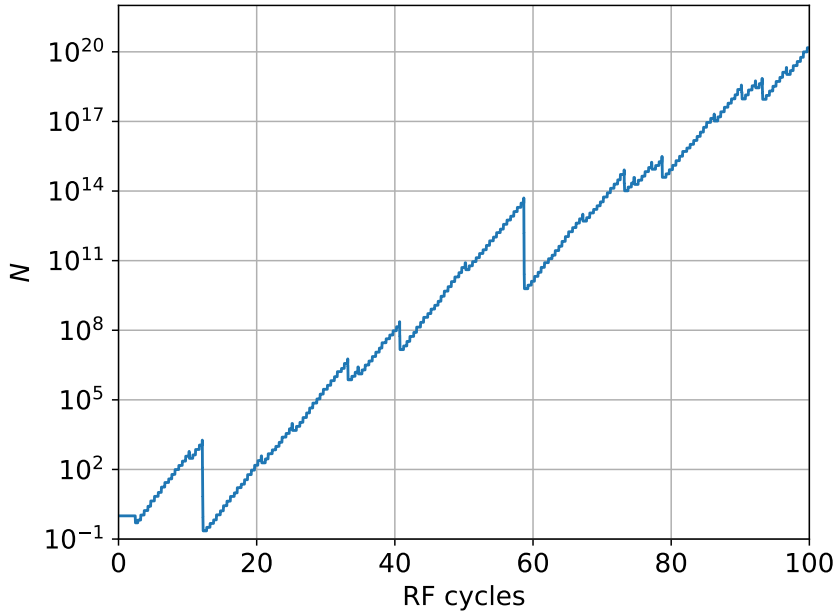

Figure 4.16: Total number of electrons N in the empty silver rectangular waveguide after 100 RF cycles using a 1D model.

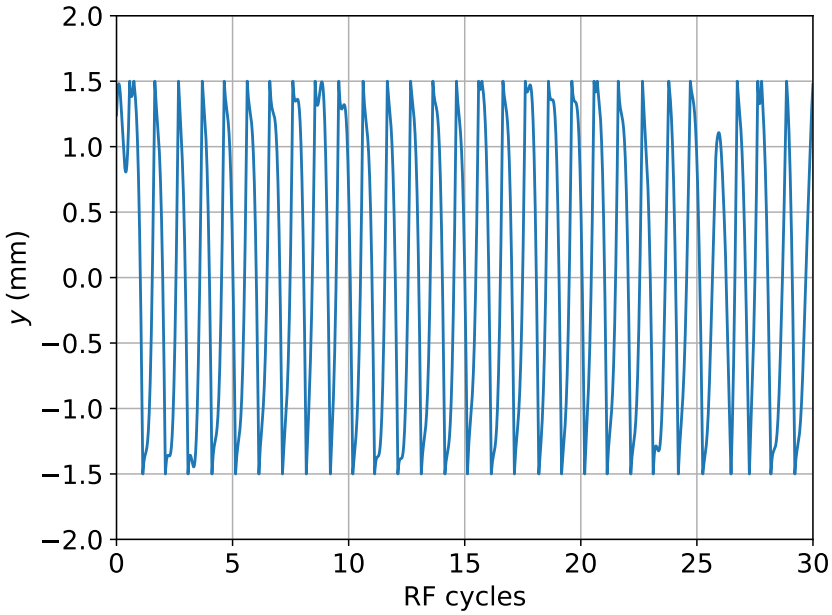

Figure 4.17: Electron path in the y-axis over 30 RF cycles in the empty silver parallel-plate waveguide using a 1D model.

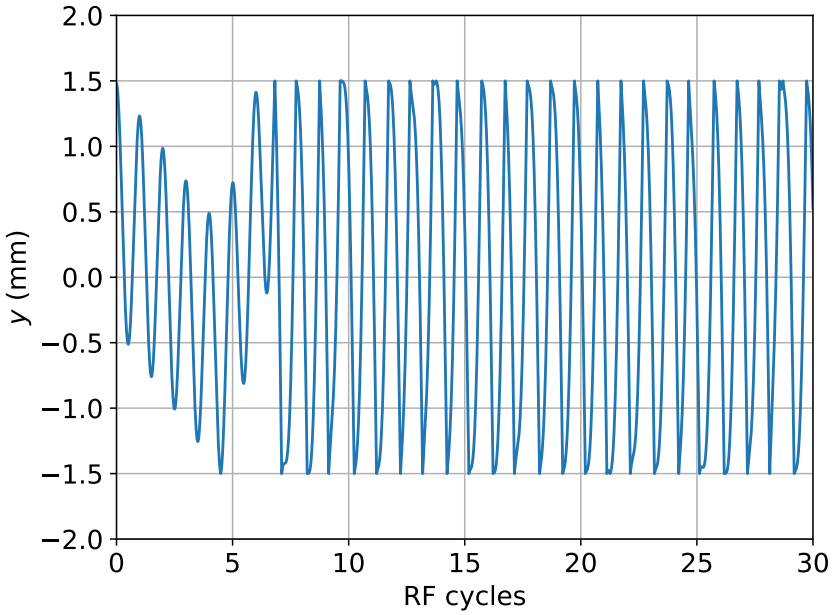

Figure 4.18: Electron path in the y-axis over 30 RF cycles in the empty silver parallel-plate waveguide using a 3D model.

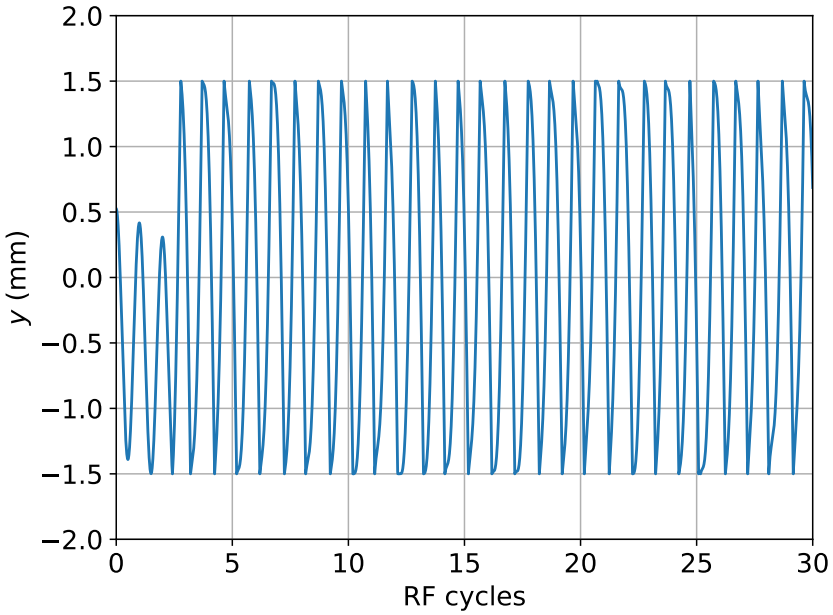

Figure 4.19: Electron path in the y-axis over 30 RF cycles in the empty silver rectangular waveguide using a 3D model.

4.4.2 Dielectric-loaded case

The analysis is now extended to a partially dielectric-loaded rectangular waveguide, which is a problem of great interest in the space industry that has not yet been rigorously investigated in the literature. It is important to note that in order to be able to experimentally measure the multipactor effect, as will be shown in Chapter 5, it is necessary to reduce the height of the rectangular waveguide under analysis; otherwise, the input power required would not be achievable with the available test equipment. For this reason, many of the analyses presented here involve waveguides whose height has been significantly reduced in comparison to standard ones; however, the results remain valid.

Figure 4.20(a) shows the cross section of a partially dielectric-loaded rectangular waveguide of width a and height b, which has been initially loaded with a dielectric slab of relative permittivity ϵ_r and dimensions $a \times h$ placed over the bottom waveguide wall, d being the remaining empty waveguide height within which the effective electron travels. We have analysed the multipactor effect in a non-standard silver-plated rectangular waveguide of width $a = 19.05\,\text{mm}$ and height $b = 0.4\,\text{mm}$, in which a thin Teflon® dielectric[3] layer of thickness $h = 0.025\,\text{mm}$ and $\epsilon_r = 2.1$ has been placed over the bottom surface of the waveguide, $d = b - h$ being the vertical air gap in

[3]DuPont Teflon® FEP Fluoroplastic Film is a dielectric film commonly used in space applications.

the waveguide. The standard values for the SEY parameters of silver [1] are given in Table 3.1, and the SEY parameters of Teflon® have been measured at the ESA-VSC High Power Space Materials Laboratory [2].

The analysis of the partially dielectric-loaded rectangular waveguide has been restricted to the single-mode regime, in which only the fundamental mode TM_{10}^{y} propagates [39]. Although the solution for this mode can be calculated by solving a transcendental equation, we can also obtain it with the modal method implemented in our model.

As with the empty case, a study of the susceptibility chart for this waveguide has been performed and compared with the results of an equivalent parallel-plate waveguide partially loaded with the same dielectric layer (Figure 4.20(b)), in which the charge appearing on the dielectric surface is considered to be uniformly distributed over an area A. The effect of the inhomogeneity of both the RF fields and charge distribution appearing on the dielectric surface in the rectangular waveguide in relation to the parallel-plate waveguide should be stressed. For the comparison, the multipactor simulation model developed by Torregrosa et al. [20, 21] for a parallel-plate waveguide, which includes the 3D motion of the electrons, has again been employed. Although this model is able to consider both multiple effective electrons and space charge effects, they have been discounted for the purposes of this comparison.

To obtain the susceptibility chart, the simulation is run for 100 RF cycles at each V_{eff} and $f \times d$ point, and repeated a sufficient number of times. Commonly, a higher number of repeats is needed at the edges of the multipactor zone than inside or outside it. In each simulation, the effective electron is launched at $x = a/2$, $z = 0$, and a random position y_0 on the y-axis between $y = 0$ and $y = d$, following a cosine distribution of the polar angle, and with a departing kinetic energy that follows the probability density function specified by Scholtz [71]. In the parallel-plate case, the charge appearing on the dielectric surface has been considered to be uniformly distributed over an area $A = 10$ cm^2. In all simulations, the multipactor discharge is assumed to have occurred when the arithmetic mean of the final population of electrons is greater than one. In addition, given that the emission or absorption of electrons by the dielectric surface gives rise to an increasing DC field in the waveguide that may eventually turn off the discharge [98], a minimum mean value of the remaining E_{DC} field in the waveguide in all simulations is also used as an additional criterion to indicate that a multipactor discharge has occurred at a given V_{eff} and $f \times d$ point.

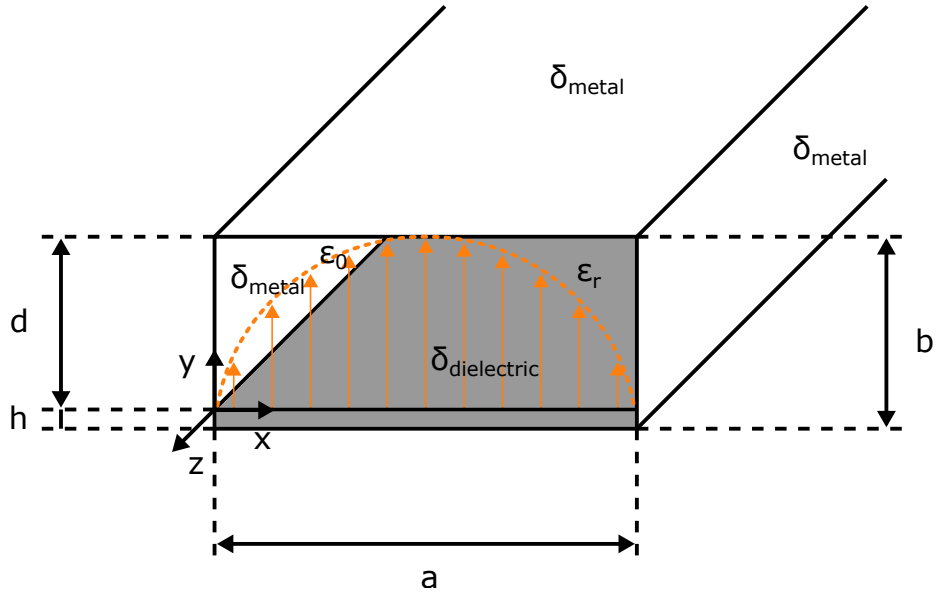

(a) Partially dielectric-loaded rectangular waveguide.

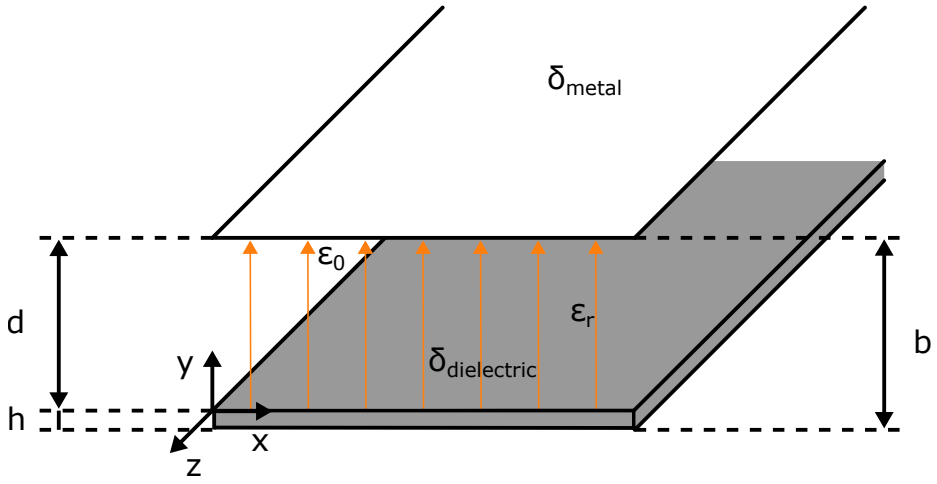

(b) Partially dielectric-loaded parallel-plate waveguide.

Figure 4.20: Schemes of the geometries and dimensions of the partially dielectric-loaded rectangular and equivalent parallel-plate waveguides.

Figure 4.21 shows the aforementioned susceptibility chart. On the vertical axis, the effective voltage V_{eff} is plotted, which in the rectangular waveguide has been numerically calculated as the line integral of the E_y component of the electric field, evaluated at the centre of the waveguide $x = a/2$, from $y_1 = 0$ to $y_2 = d$:

$$V_{eff} = \int_0^d E_y \mathrm{d}y \,. \tag{4.3}$$

In the equivalent parallel-plate waveguide, this voltage is obtained as [19]:

$$E_0 = \frac{\epsilon_r V_{eff}}{h + \epsilon_r (d - h)} \,, \tag{4.4}$$

where E_0 is the RF electric field amplitude. On the horizontal axis, the product $f \times d$ has been plotted. The multipactor discharge zones in the partially dielectric-loaded rectangular waveguide have been represented with blue points, while the orange points correspond to the multipactor discharge region in the partially dielectric-loaded parallel-plate waveguide. Looking at this chart, it can be seen that in the multipactor regions observed in the analysed V_{eff} and $f \times d$ ranges, a higher multipactor threshold is predicted for the partially dielectric-loaded rectangular waveguide than its parallel-plate equivalent. Moreover, this difference is constant for all values of $f \times d$. And, in contrast, the upper limit of the multipactor region is lower for the partially dielectric-loaded rectangular waveguide than for its parallel-plate equivalent.

This susceptibility chart is only applicable to these particular waveguides, and not to every waveguide with an air gap d, given that the electromagnetic field distribution depends on the characteristics of the dielectric layer (i.e. on its dimensions and relative permittivity).

With the purpose of getting a better understanding of the differences in multipactor evolution in the equivalent partially dielectric-loaded rectangular and parallel-plate waveguides, several simulations of the multipactor evolution in different regions of the susceptibility charts obtained for both models are performed and analysed. Simulations based on different initial phases of the RF field have been conducted, and similar results were obtained.

An initial point inside the first-order multipactor region in both waveguides has been chosen, corresponding to $f \times d = 4.01\,\mathrm{GHz\,mm}$ and $V_{eff} = 908\,\mathrm{V}$ (highlighted in green in Figure 4.21). In Figures 4.22 and 4.23, the evolution of the following measures have been represented in each case: total number of electrons N (green line), $E_{y,\mathrm{DC}}$ at the electron position (blue line), $E_{y,\mathrm{RF}}$ (orange line), and electron

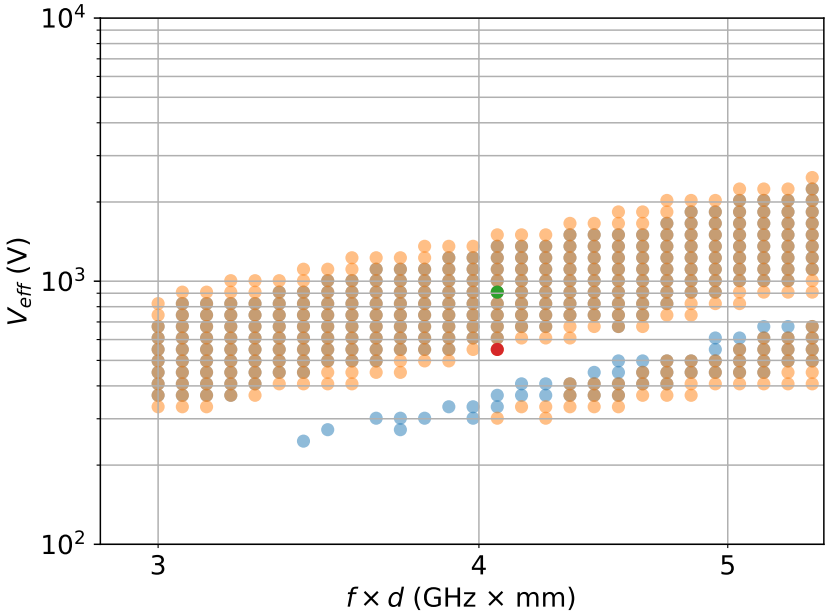

Figure 4.21: Comparison of the susceptibility chart of a rectangular waveguide partially filled with Teflon® (blue points) with that of its parallel-plate equivalent (orange points). The operating points $f \times d = 4.06\,\text{GHz}\,\text{mm}$, $V_{eff} = 908.64\,\text{V}$ and $f \times d = 4.06\,\text{GHz}\,\text{mm}$, $V_{eff} = 550.27\,\text{V}$ are highlighted in green and red points, respectively.

position y (grey line). The other DC and RF field components have turned out to be several orders of magnitude lower than those represented in the cases under study and have not been displayed.

In Figure 4.22, the multipactor evolution in the partially dielectric-loaded rectangular waveguide case is plotted. Given that resonance conditions are met at this point (the centre of the first multipactor region), once the effective electron is synchronized with the RF field after a few RF cycles, the y-coordinate of its trajectory (represented with a grey line) shows collisions with the top metallic and bottom dielectric surfaces in a first-order multipactor process until the 13th RF cycle; it remains in the proximity of $x = a/2$ and $z = 0$, given that the electron has nearly no acceleration in these directions. In this first stage of the multipactor evolution, the total number of electrons N (green line) follows an exponential growth. This progressive growth of N entails the appearance of charges on the surface of the dielectric, whose value is proportional to the emitted or absorbed electrons from each impact on this surface. Such charges give rise to the appearance of an electrostatic field in the empty air gap. Once the population of electrons reaches a significant number ($N \approx 10^8$ in the conditions under study), the y-component of the DC field, $E_{y,\text{DC}}$ (which has been plotted

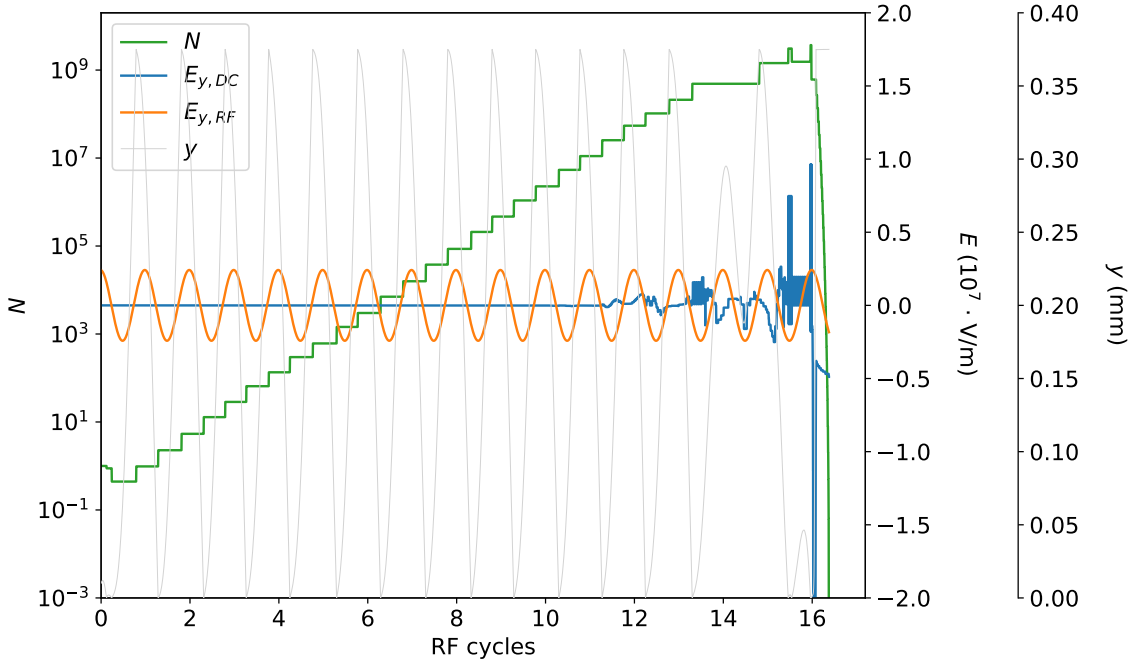

Figure 4.22: Multipactor evolution in the partially dielectric-loaded rectangular waveguide at $f \times d = 4.01\,\mathrm{GHz\,mm}$ and $V_{eff} = 908\,\mathrm{V}$: total number of electrons N (green line), $E_{y,DC}$ at the electron position (blue line), $E_{y,\mathrm{RF}}$ (orange line) and electron position y (grey line).

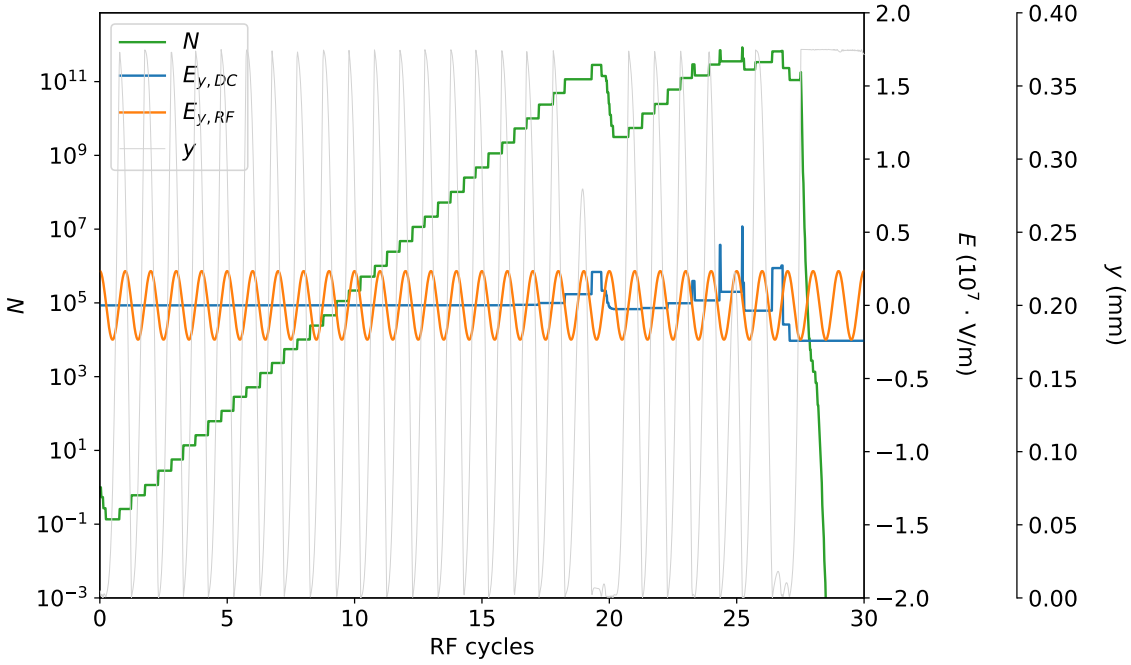

Figure 4.23: Multipactor evolution in the partially dielectric-loaded parallel-plate waveguide at $f \times d = 4.01\,\mathrm{GHz\,mm}$ and $V_{eff} = 908\,\mathrm{V}$: total number of electrons N (green line), $E_{y,DC}$ at the electron position (blue line), $E_{y,\mathrm{RF}}$ (orange line) and electron position y (grey line).

in Figure 4.22 at the electron position with a blue line), becomes comparable to $E_{y,\mathrm{RF}}$ (orange line), and the effective electron loses its earlier multipactor synchronization. From this moment on, the electrons collide with the top metallic or bottom dielectric surfaces much sooner or later than the instants when the RF electric field changes its sign, which implies low impact energy collisions and, consequently, the absorption of electrons, giving rise to the appearance of greater charges on the dielectric surface, and contributing to a larger DC field acting on the waveguide. A high negative value of this field near the dielectric surface finally results in a single-surface multipactor regime on the metallic surface (see the y-position of the electron from RF cycle 16), with successive low impact energy collisions, until the discharge turns off. The remaining DC field in the waveguide at the end of the simulation is the proof that a discharge has occurred.

Equivalent results are plotted in Figure 4.23 for the partially dielectric-loaded parallel-plate waveguide under the same circumstances, which also correspond to the resonance conditions of the effective electron with the RF field. This can be checked through the exponential growth in the total number of electrons N (green line) until RF cycle 17. In the same way, the dielectric surface of the waveguide charges proportionately to the electrons emitted or absorbed by it in each impact, giving rise to an increasing electrostatic field, which in this case is assumed to be constant in the empty gap. Once the $E_{y,\mathrm{DC}}$ (blue line) becomes comparable to the $E_{y,\mathrm{RF}}$ (red line), the synchronization of the effective electron with the RF field is lost, and after a few RF cycles, the appearance of a negative DC field pushes the electrons to the upper metallic surface, and successive low impact energy collisions take place in a single-surface multipactor regime, turning off the discharge. Again, the DC field remaining in the waveguide proves that there has been a multipactor discharge. Therefore, a qualitatively similar behaviour is observed with both simulation models at this point, and only quantitative differences in the maximum population of electrons N reached and the final DC field are found, which are basically due to the inhomogeneity of the charge distribution appearing on the dielectric surface in the rectangular waveguide, rather than being uniformly distributed over a given area.

Next, a different point of the susceptibility chart in the lower limit of the first-order multipactor region is analysed, corresponding to $f \times d = 4.01\,\mathrm{GHz\,mm}$ and $V_{eff} = 550\,\mathrm{V}$. Indeed, no multipactor discharge has been observed in the rectangular waveguide at this point; although a total number of 360 simulations have been performed, none of them has shown a growth of the population of electrons. This fact

is illustrated by looking at one such simulation of multipactor evolution in the rectangular waveguide, as represented in Figure 4.24, where although the y-coordinate of the effective electron (grey line) in the first RF cycles shows some collisions with the top metallic or bottom dielectric surfaces that cause N to increase, there is no exponential growth in this total number of electrons and, consequently, no DC field is observed in the waveguide. In the following RF cycles, as the effective electron moves away from the centre of the guide to positions of lower $E_{y,\mathrm{RF}}$ (red line) due to the Miller force[4], there are only low impact energy collisions, and N progressively decreases until the discharge finally turns off.

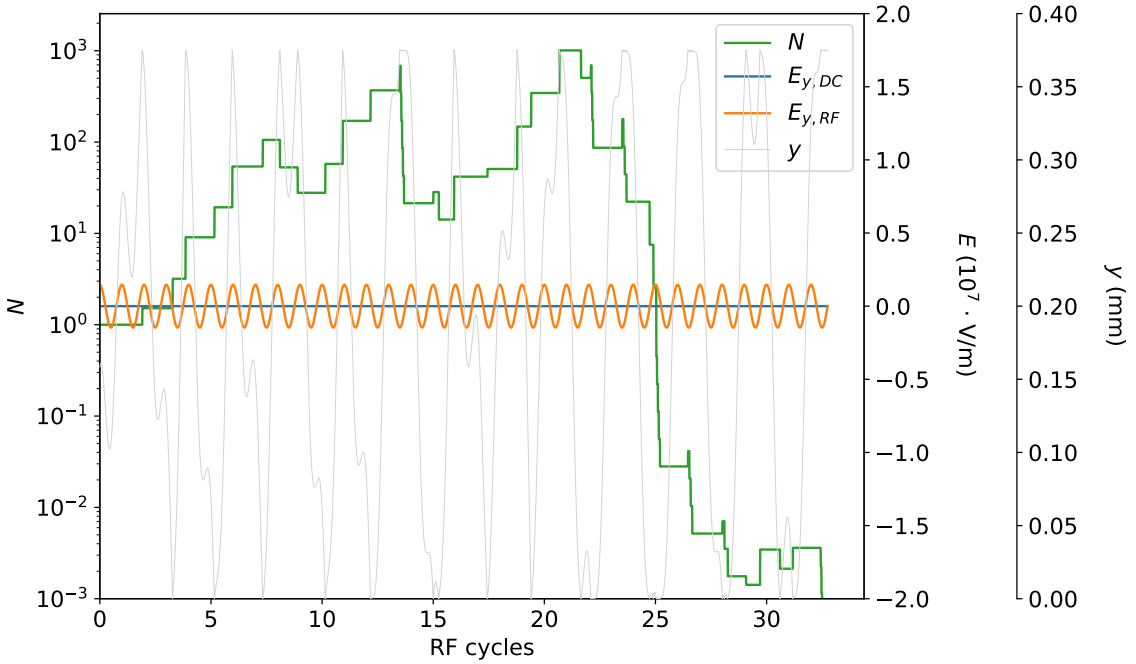

Figure 4.24: Multipactor evolution in the partially dielectric-loaded rectangular waveguide at $f \times d = 4.01\,\mathrm{GHz\,mm}$ and $V_{eff} = 550\,\mathrm{V}$: total number of electrons N (green line), $E_{y,DC}$ at the electron position (blue line), $E_{y,\mathrm{RF}}$ (orange line) and electron position y (grey line).

A different result is observed for this V_{eff} and $f \times d$ point in the partially dielectric-loaded parallel-plate waveguide, in which 3 out of 360 simulations show a net growth

[4]The Miller force is a non-linear force that a charged particle experiences in an inhomogeneous oscillating electromagnetic field. It causes the particle to move towards the area of weakest field strength, rather than oscillating around an initial point as happens in a homogeneous field. This occurs because the particle experiences a greater magnitude of force during the half of the oscillation period while it is in the area with the stronger field. The net force during its period in the weaker area in the second half of the oscillation does not offset the net force of the first half, and so over a complete cycle this causes the particle to move towards the area of lesser force [99].

in the population of electrons after 100 RF cycles, yielding an arithmetic mean for the final population of electrons across all simulations that is greater than one (note that this point is depicted in red in Figure 4.21 for the parallel-plate waveguide, corresponding to a multipactor point). Figure 4.25 represents the multipactor evolution in one such simulation, in which there is no longer a first-order multipactor resonance regime at the site of the y-coordinate of the effective electron and, consequently, there is slower growth in the value of N (in any case, it is not exponential), attaining a final upper value of 10^8 electrons at the end of the simulation. In the same way, there is no significant DC field appearing in the waveguide in this simulation (it is several orders of magnitude lower than the RF field), and added to the fact that the RF field in this waveguide does not depend on the x-coordinate, this regime of progressive increase of N is not broken throughout the simulation. Thus, it can be concluded that a different evolution of the multipactor effect is observed at this point in the lower limit of the first-order multipactor: an initial growth of the population of electrons in the rectangular waveguide in the first RF cycles, ending in the turning off of the discharge due to the effect of the Miller force, while in the parallel-plate waveguide a slow but progressive increase of the population of electrons throughout the simulation associated with the uniformity of the RF and DC fields in this waveguide.

4.5 Dielectric-loaded rectangular waveguide

In addition to the results already described for the multipactor effect in the case of a partially dielectric-loaded rectangular waveguide, in this section both the validation of the EEM approach and the consequences of including more than one dielectric sheet inside the waveguide will be presented.

For the first of these aims, a waveguide with the same dimensions and configuration as that analysed in Section 4.4.2 will be considered (Figure 4.26), but a different working point will be selected. Figure 4.27 shows the susceptibility chart for the rectangular waveguide partially filled with Teflon® (blue points). The lowest $f \times d$ value is above the cut-off frequency of the fundamental mode of this waveguide. For purposes of comparison, this figure also shows the susceptibility chart for an equivalent empty waveguide with the same vertical air gap (represented with orange points). It can be seen that both the empty and the partially dielectric-loaded waveguides with the same vertical air gap produce similar multipactor susceptibility charts, because the SEY properties of silver and Teflon® are quite similar.

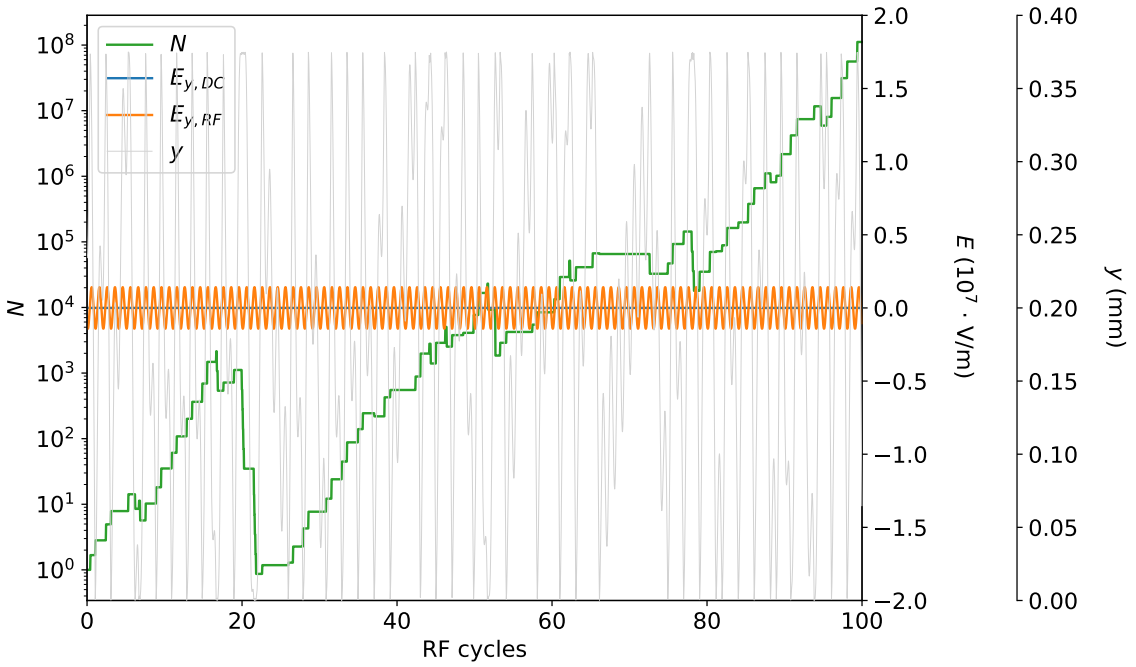

Figure 4.25: Multipactor evolution in the partially dielectric-loaded parallel-plate waveguide at $f \times d = 4.01\,\mathrm{GHz\,mm}$ and $V_{eff} = 550\,\mathrm{V}$: total number of electrons N (green line), $E_{y,DC}$ at the electron position (blue line), $E_{y,\mathrm{RF}}$ (orange line) and electron position y (grey line).

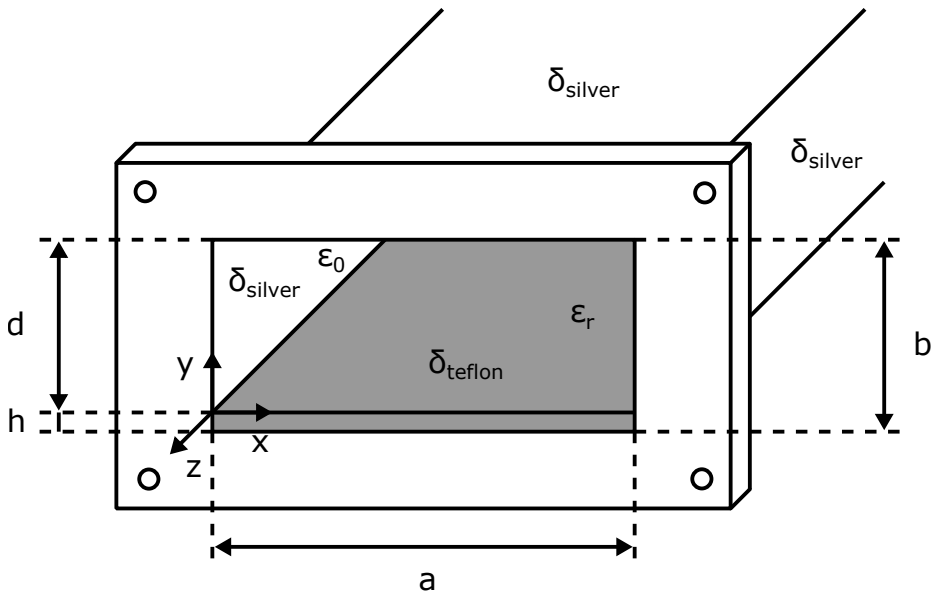

Figure 4.26: Partially dielectric-loaded rectangular waveguide with Teflon® layer on bottom surface.

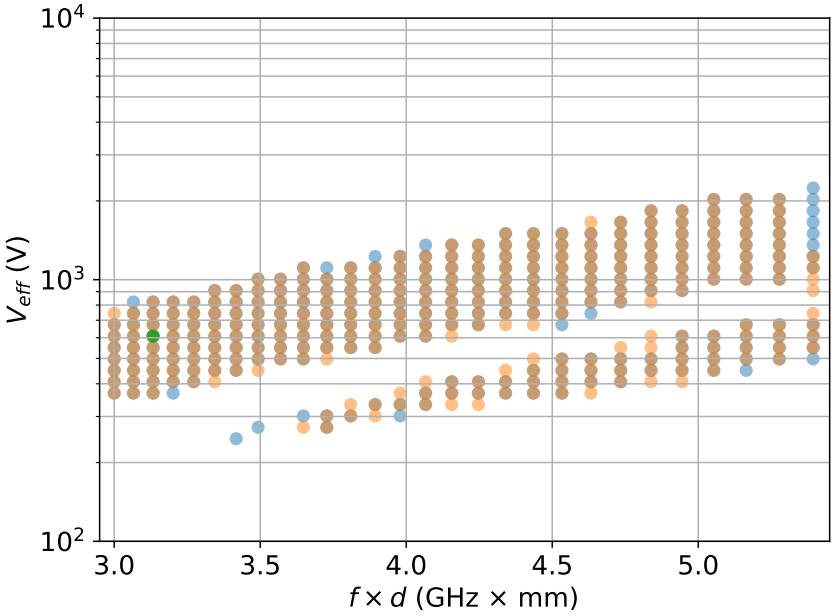

Figure 4.27: Comparison of the susceptibility chart for a rectangular waveguide partially filled with Teflon® (blue points) with that of its equivalent empty waveguide (orange points). An operating point corresponding to $f \times d = 3.13\,\text{GHz}\,\text{mm}$ and $V_{eff} = 608\,\text{V}$ is highlighted in green.

A point within the multipactor region has been chosen, corresponding to $V_{eff} = 608\,\text{V}$ and $f \times d = 3.13\,\text{GHz}\,\text{mm}$ (highlighted in green). For this simulation, the electron is launched with an initial phase of the RF field $\phi_0 = 0^o$. It should be pointed out that other simulations assuming different initial phases were performed, and similar results were obtained.

The evolution over time of the total number of electrons N, as well as the y-components of both the RF and DC electric fields, are shown in Figure 4.28. The distribution of the normalized charges appearing on the dielectric surface as a consequence of the multiple electron impacts can be seen in Figure 4.29. The positive and negative charges are represented, respectively, by blue and orange circles; their size being proportional to the charge magnitude on a log scale.

It is worth mentioning that the switching off of the discharge observed in the latter stages of multipactor evolution in this waveguide has been speeded up by the application of the EEM, although this does not change the dynamics of the discharge under these conditions in qualitative terms. To validate the EEM for the partially dielectric-loaded waveguide configuration and the evolution of multipactor over time within it, it has to be demonstrated that there is no great dispersion of electrons in

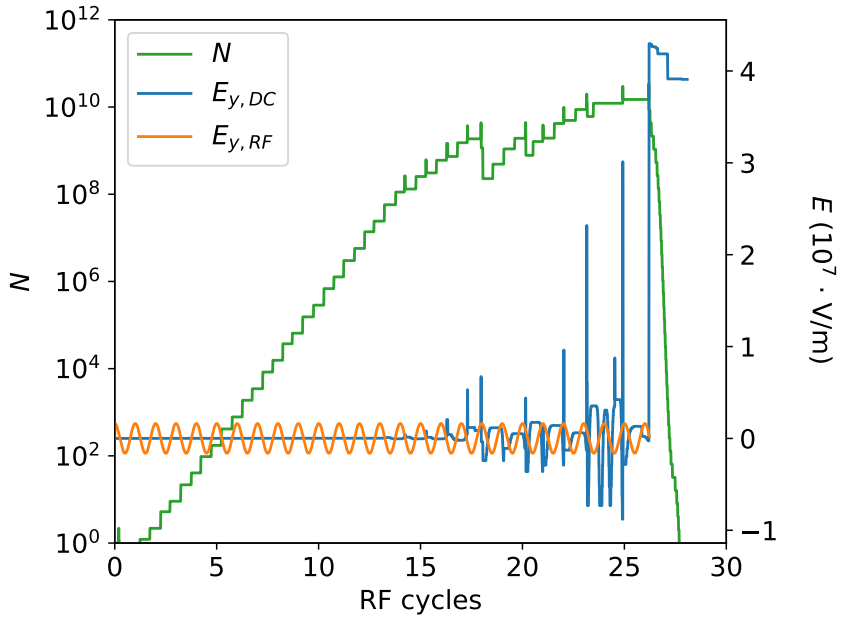

Figure 4.28: Evolution over time of the total number of electrons N (green line) and of $E_{y,\mathrm{RF}}$ (orange line) and $E_{y,\mathrm{DC}}$ (blue line).

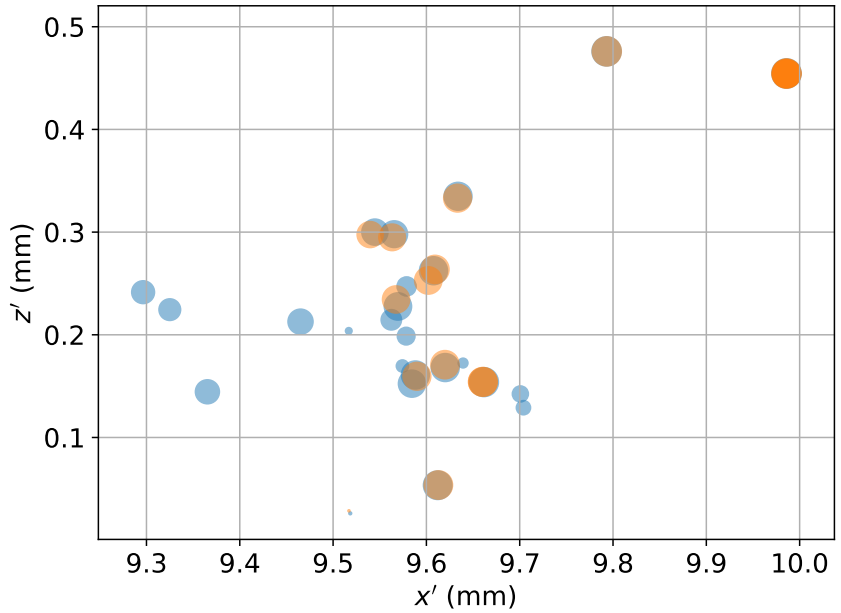

Figure 4.29: Distribution of the normalized charges $\overline{Q}_i = Q_i/e$ appearing on the dielectric surface.

the transverse direction of the waveguide during a typical simulation of an electron discharge.

To this end, several simulations were performed by using the multipactor simulation tool developed herein. In particular, a total of 1000 effective electrons have been launched from the centre of the bottom waveguide wall, that is, the dielectric surface, taking into consideration random energies and initial angles. The incident locations of the electrons at the top wall can be fitted rather well to a 2D Gaussian distribution with $\sigma_x \simeq \sigma_z \simeq 44\,\mu\text{m}$.

Figure 4.30 shows the simulation results. Following the process of successive impacts at both walls, and assuming resonance conditions, the distribution of arrival locations in the n-th impact can be easily obtained by performing a convolution of the Gaussian of the previous step with a 2D Gaussian of standard deviation 44 μm. The result is a new 2D Gaussian with $\sigma_x = \sigma_z \simeq \sqrt{n} \cdot 44\,\mu\text{m}$, n being the impact number.

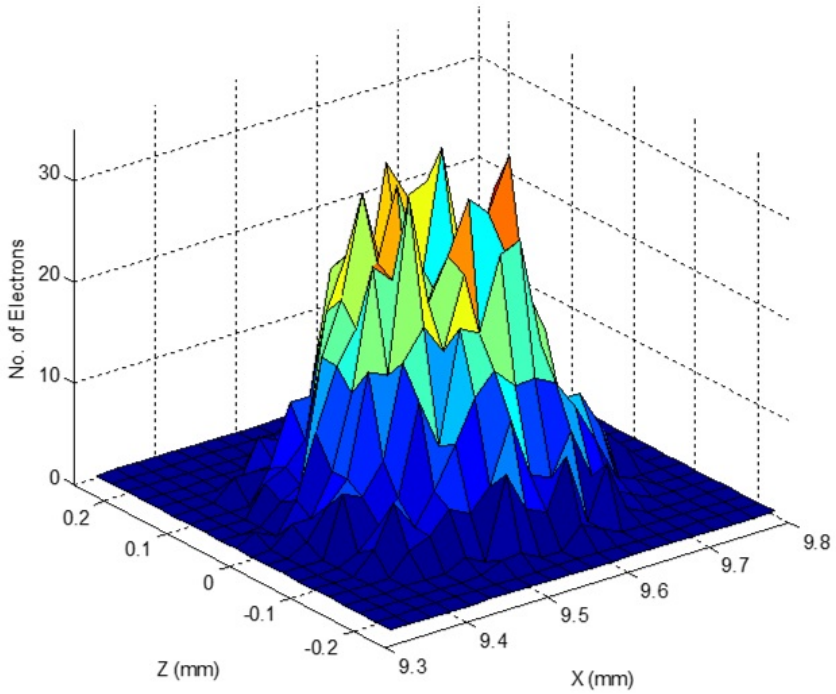

Figure 4.30: Arrival locations of the effective electron at the top wall after 1,000 simulated effective electron launches from the centre of the bottom dielectric surface, taking into consideration random energies and initial angles.

Given that, for each RF cycle, there are two impacts at the selected first-order multipactor regime point, one on each wall, then $\sigma_x = \sigma_z \simeq \sqrt{2N_{cycles}} \cdot 44\,\mu\text{m}$. After

17.5 RF cycles, we have a 2D Gaussian distribution of the impact positions with standard deviation $\sigma_x = \sigma_z \simeq \sqrt{2 \cdot 17.5} \cdot 44\,\mu\text{m} = 260.31\,\mu\text{m}$. That is, after 17.5 RF cycles, when the exponential growth regime finishes due to the appearance of the DC field because of the charging of the dielectric, the diameter of the spot is about 0.5 mm. Such simulations show that the EEM can be used for high kinetic energies of the impacting electrons, as is the case in the multipactor resonance condition when launching the effective electron near the waveguide centre, where the electric field is highest.

Finally, the consequences of using dielectric materials with different SEY characteristics to cover the walls of the rectangular waveguide are also studied. To this end, we have compared the susceptibility charts for two different configurations, represented in Figure 4.31. In the first case, both the bottom and top walls of the waveguide have been coated with the same Teflon® dielectric layer of thickness $h = 0.025\,\text{mm}$. In the second configuration, the Teflon® coating of the top wall of the waveguide has been replaced with alumina. The selected dielectric materials have different SEY parameters (Table 3.1), the first energy crossover W_1, which is the most relevant parameter affecting the multipactor region, being greater in the case of the alumina.

As illustrated in Figure 4.32, we can see that the use of materials with different SEY characteristics leads to significant changes in the shape of the multipactor susceptibility chart, allowing us to adjust the regions of multipactor according to the needs of the design.

4.6 Summary

Many published works in multipactor analysis begin with a parallel-plate waveguide set-up because the EM field distribution and physics are well known. Thus, an infinite parallel-plate approach was taken as the initial basis for this thesis. However, the 1D parallel-plate waveguide model, which is commonly used in multipactor effect analysis in a wide variety of passive microwave components, is not sufficiently accurate at either the lower or upper edges of the multipactor region. There is an x-coordinate dependence in the electron trajectory that is not considered in the 1D parallel-plate waveguide model. For this reason, in this thesis, a 3D model that takes into account this dependence has been demonstrated, for both parallel-plate and rectangular waveguides. In addition, in the rectangular waveguide there is also a dependency of the fields on the x-coordinate that must be taken into account too, which

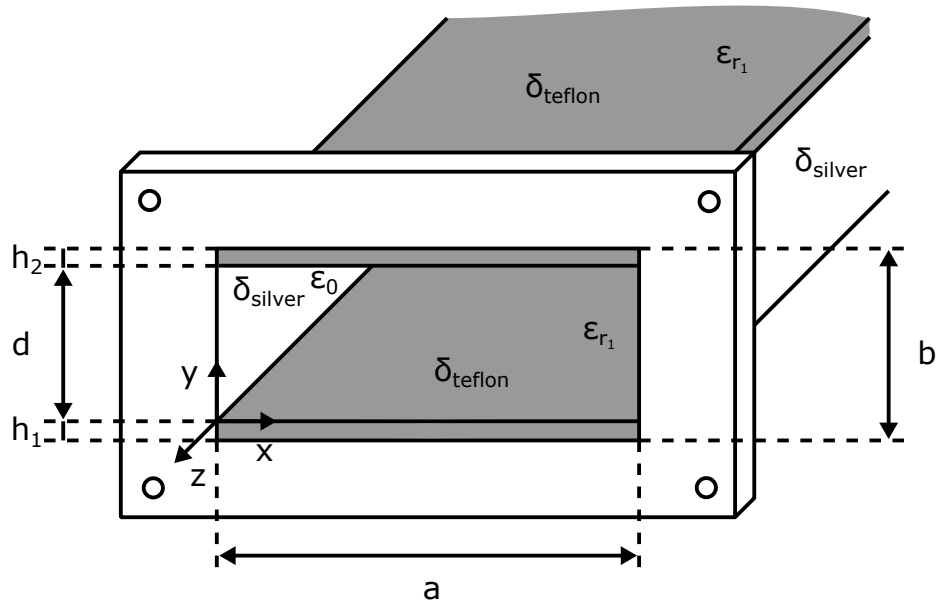

(a) Teflon® dielectric layer on both the bottom and top waveguide surfaces.

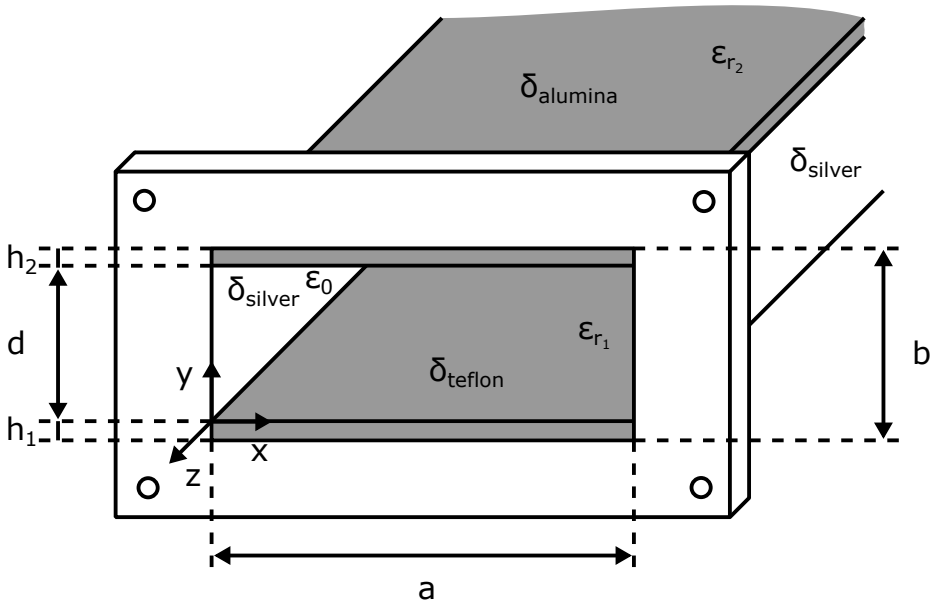

(b) Teflon® and alumina dielectric layers, respectively, on the bottom and top waveguide surfaces.

Figure 4.31: Two different configurations of a partially dielectric-loaded rectangular waveguide.

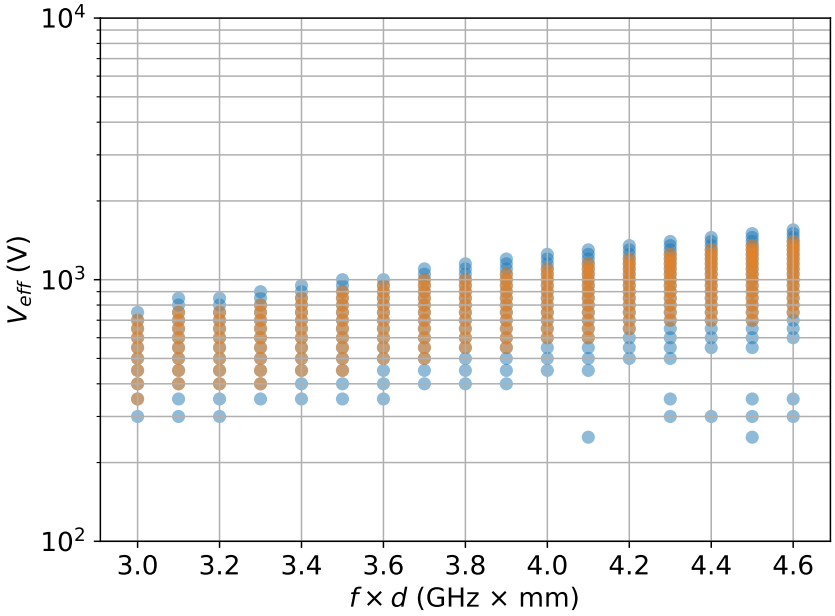

Figure 4.32: Comparison of the susceptibility charts for a rectangular waveguide partially filled with Teflon® on both the bottom and top waveguide surfaces (blue points), and the same waveguide with Teflon® and alumina on, respectively, the bottom and top surfaces (orange points).

means that the multipactor model of a parallel-plate waveguide does not provide correct results for the multipactor region of a rectangular one. The results presented in this chapter show the differences between the 1D and 3D models in a parallel-plate waveguide and, more particularly, for a 3D model of a rectangular waveguide.

In order to highlight the similarities and differences between the multipactor results obtained for a partially dielectric-loaded rectangular waveguide and for its parallel-plate equivalent of the same height, a comparative study of the susceptibility charts for both cases has been performed. The conclusion of this study is that the inhomogeneity of the electric field inside the rectangular waveguide basically modifies the edges of the multipactor region in its susceptibility chart with respect to those predicted by the parallel-plate waveguide simulation code. In order to get a proper insight into this result, the evolution of the population and trajectory of the effective electron and the DC field appearing in the waveguide at a point well inside the multipactor region, as obtained with the two models, has been investigated, revealing some quantitative differences in multipactor evolution, but similar qualitative behaviours. However, when a different point of the susceptibility chart, at the lower limit of the first-order multipactor region, is selected, a different evolution of the multipactor effect is observed in the two cases; that is, an initial growth of the population of

electrons in the rectangular waveguide in the first RF cycles, ending in the turning off of the discharge due to the Miller force effect, whereas in the parallel-plate waveguide we see a slow but progressive increase of the population of electrons throughout the simulation, associated with the fact that the RF field in this waveguide does not depend on the x-coordinate.

Finally, a study of the multipactor effect in a partially dielectric-loaded rectangular waveguide has been carried out that takes into account the RF electromagnetic fields (obtained with a very efficient vectorial modal method) as well as the DC field caused by the appearance of a charge distribution on the dielectric layer. The susceptibility chart for a partially dielectric-loaded rectangular waveguide has been computed, and the evolution over time of a discharge in this waveguide has been studied and discussed. The simulations performed reveal that multipactor discharges in this type of dielectric-loaded waveguide turn off by themselves due to the electrostatic field associated with the dielectric surface charges that evolve with the multipactor process. In addition, the effects of using dielectric materials with different SEY characteristics to cover the walls of the rectangular waveguide have also been investigated.

Chapter 5

Experimental study of the multipactor effect

5.1 Introduction

In Chapter 4, we showed the results of the theoretical study of the multipactor effect in different rectangular waveguide configurations, both empty and partially filled with dielectric. Next, the experimental results associated with a partially dielectric-loaded standard aluminium rectangular waveguide (WR75) will be presented. Because the preceding theoretical study was based on a silver rectangular waveguide, the susceptibility chart analysis will be repeated.

The multipactor discharge tests were performed at the VSC/ESA Laboratory in Valencia (Spain). This has the capacity to generate microwave signals at different frequency bands, up to mm-waves, and can be configured for testing waveguide or coaxial devices. State-of-the-art high-power amplifiers and vector network analysers allow the handling of the increasing frequency and power requirements of new microwave components for space applications. The test environment provides certified clean-room conditions, avoiding contamination of the test samples by impurities such as dust, humidity, and so on. The essential equipment to reproduce space scenario conditions are a vacuum chamber and different high-energy particle generators, such as radioactive sources or regulated electron guns. The vacuum chambers available can reduce pressure levels below 10^{-7} mbar and actively control temperatures between -120°C and 150°C [64, 2].

To study the multipactor effect in the WR75 waveguide, the multipactor simulation code based on the Monte Carlo method presented in Section 4.2 has been used. In the simulations, both the RF and DC fields inside the waveguide have been

considered, the latter being associated with the charge distribution appearing on the dielectric surface during the multipactor discharge.

To avoid the use of high input power levels to generate a multipactor effect in the standard aluminium rectangular waveguide (WR75), it is necessary to minimize the height b of the waveguide. To achieve this, an impedance transformer has been designed with capacitive E-plane discontinuities such that the final height of the WR75 waveguide is reduced to the small dimension of $b = 0.4\,\text{mm}$. The impedance transformer has been symmetrically designed, so that both the input and output waveguide ports correspond to standard WR75 waveguides. The requirements and estimation of the design parameters will be explained in detail, and the transformer has been manufactured according to this design.

In Section 5.2, a description of the SEY characteristics of the materials employed in the experimental analysis is provided. In Section 5.3, the impedance transformer design that reduces the height b of the original standard WR75 waveguide will be presented. Finally, in Section 5.4, the theoretical and experimental results for the multipactor threshold voltage under three different configurations that vary the position of the dielectric layer inside the structure are shown, comprising the following cases: 1) an empty waveguide; 2) a partially dielectric-loaded waveguide in which the bottom wall is covered by the dielectric film; 3) a partially dielectric-loaded waveguide in which both top and bottom walls are covered by the dielectric film.

5.2 Secondary emission yield measurement

The dielectric film that has been chosen to partially fill the standard aluminium waveguide (WR75) is DuPont Teflon® Fluorinated Ethylene Propylene (FEP) Fluoroplastic Film Type C [100], which is commonly used in space applications, having $\epsilon_r = 2.1$ and a very small thickness $h = 0.025\,\text{mm}$. Therefore, the electrical performance of the waveguide transformer will barely be modified when adding the dielectric film, which will avoid us having to build different transformers for the three measurement configurations: empty waveguide, waveguide with its bottom wall covered by the dielectric film, and waveguide with both its top and bottom walls covered by dielectric film.

The SEY properties of the metallic and dielectric materials employed in this experiment have been measured at the VSC/ESA Laboratory, Valencia (Spain) [2], and they have been used in the multipactor simulations described in the following subsections. The facilities are available to measure the SEY in both metallic and dielectric

materials, at sample level or component level. In addition, experimental capabilities are available to measure SEY as a function of temperature, from −100°C to 500°C, and with different incident angles [2].

As was explained in Section 3.3, the SEY depends on the properties of the material, the kinetic energy of the primary electron, its incident angle, and the state of the surface (i.e. composition, morphology of the structure, porosity and roughness) [101, 78]. For the materials under consideration, the SEY at normal incidence was determined as a function of primary electron kinetic energy in the range 5 eV to 1000 eV. In the case of aluminium, this was done by measuring the current when bombarded by a calibrated continuous primary electron beam of about 5 nA. In the case of Teflon®, the measurement of the SEY was done by using an electron gun configured in pulsed mode to send a single electron dose of less than $10^6\, e\,\mathrm{cm}^{-2}$. After each dose, and before varying the primary electron kinetic energy, the sample was electrically neutralized. Figure 5.1 shows an optical microscope image, obtained with a charge-coupled device (CCD) camera, of the surface of the as-received aluminium material employed in the fabrication of the waveguide transformer, in which we can observe the roughness of this particular sample.

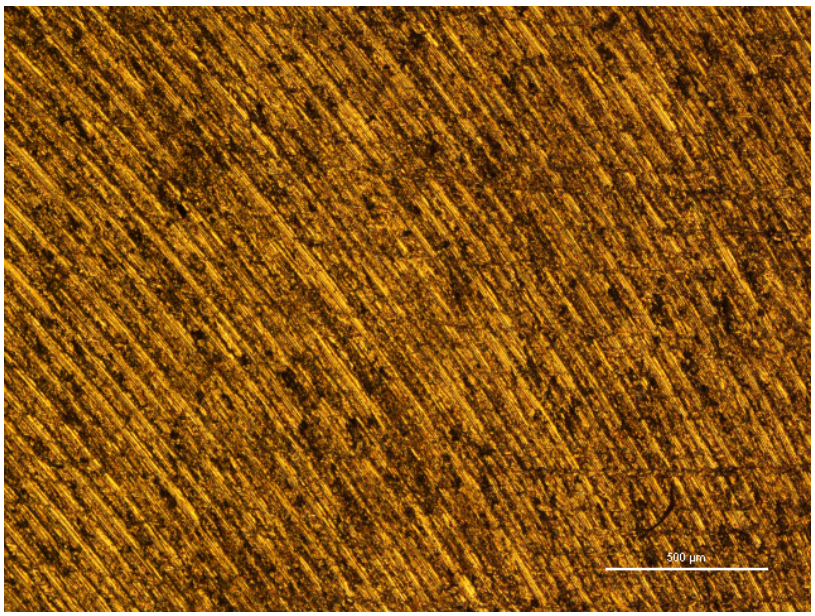

Figure 5.1: Image of the surface of the aluminium employed in the fabrication of the waveguide transformer.

Figure 5.2 shows the SEY curves for aluminium and Teflon®. It is worth noting that the maximum SEY, that is, 2.8, measured for Teflon® is quite similar to that measured for aluminium, that is, 2.6. By contrast, aluminium shows a lower first

crossover energy in its SEY curve ($W_1 = 15\,\text{eV}$) than that measured for Teflon® ($W_1 = 36\,\text{eV}$). These features determine the multipactor results, which follow.

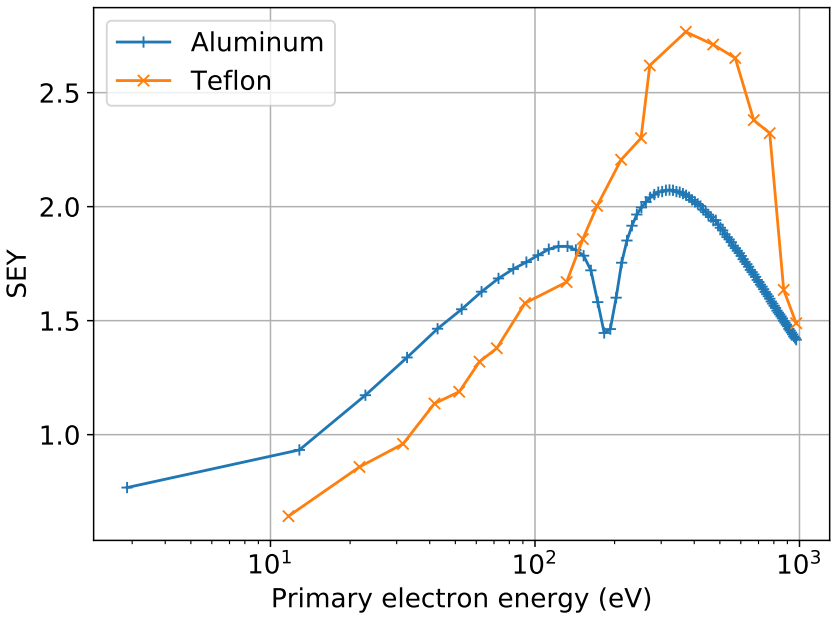

Figure 5.2: Experimental SEY curves for aluminium and Teflon®.

5.3 Impedance transformer

A waveguide discontinuity is defined as any interruption in the translational symmetry of a waveguide [102]. A transmission line discontinuity can be represented as an equivalent circuit at some point on the transmission line. Depending on the type of discontinuity, the equivalent circuit may be a simple shunt or series element across the line. The component values of the equivalent circuit will depend on the parameters of the line and the discontinuity, as well as on the frequency of operation. In some cases the equivalent circuit involves a shift in the phase reference planes on the transmission lines [35].

In the context of such waveguide discontinuities, transformers are structures designed to transfer a signal that travels in a given mode from one transmission system to another. The input and output systems between which the signal must be adapted can be of different types, such as a rectangular waveguide and a circular one, or can have the same geometry but with different dimensions (e.g. two rectangular waveguides of different heights). When two waveguides of different sizes are connected in this way, reflection losses may occur in the system. Impedance transformers allow

the connection of waveguides with different shapes and dimensions so that specific design requirements are met for the transmitted and reflected power, as well as for the bandwidth.

5.3.1 Quarter-wave transformer

Quarter-wave transformers are structures mainly used as intermediate matching devices, when it is necessary to connect two waveguide systems with different characteristic impedances. If we directly connect a load to a line with a different characteristic impedance, a reflected wave would be created that may decrease the power supplied to the load and could also have adverse effects on the generator. If only a narrow-band impedance match is required, a single-section transformer may suffice. However, multi-section quarter-wave transformer designs can be synthesized in a methodical manner to yield optimum matching characteristics across a broader frequency band as required.

Figure 5.3 shows a single-section quarter-wave matching transformer circuit.

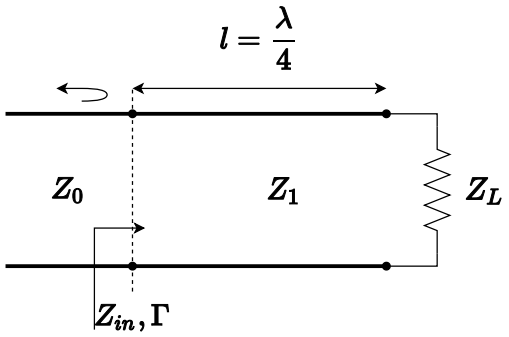

Figure 5.3: A single-section quarter-wave matching transformer.

As explained by Pozar in [35], the characteristic impedance of the matching section Z_1 is defined as:

$$Z_1 = \sqrt{Z_0 Z_L}\,, \tag{5.1}$$

where Z_L is a resistive impedance load. If the load has a reactive component, then either a series or shunt reactive element, or a line section of suitable length, must be added between the quarter-wave matching transformer and the load, so that we achieve a resistive impedance in the load plane of the quarter-wave transformer.

It is important to note that at the design frequency f_0, the electrical length of the matching section is $\lambda_0/4$, but at other frequencies the length is different, so a perfect match is no longer obtained.

The input impedance can be derived from:

$$Z_{in} = Z_1 \frac{Z_L + jZ_1 t}{Z_1 + jZ_L t}\,, \tag{5.2}$$

where $t = \tan \beta l = \tan \theta$ and $\beta l = \theta = \pi/2$ at the design frequency f_0.

The reflection coefficient is obtained from:

$$\Gamma = \frac{Z_{in} - Z_0}{Z_{in} + Z_0} = \frac{Z_1(Z_L - Z_0) + jt(Z_1^2 - Z_0 Z_L)}{Z_1(Z_L + Z_0) + jt(Z_1^2 + Z_0 Z_L)}\,. \tag{5.3}$$

Because $Z_1^2 = Z_0 Z_L$, Equation (5.3) can be expressed as:

$$\Gamma = \frac{Z_L - Z_0}{Z_L + Z_0 + j2t\sqrt{Z_0 Z_L}}\,. \tag{5.4}$$

The reflection coefficient magnitude $|\Gamma|$ can be derived from Equation (5.4):

$$|\Gamma| = \frac{1}{\sqrt{1 + \frac{4Z_0 Z_L}{(Z_L - Z_0)^2}\sec^2\theta}}\,, \tag{5.5}$$

where $1 + t^2 = 1 + \tan^2\theta = \sec^2\theta$. In the case of operation near the design frequency f_0 then $l \approxeq \lambda_0/4$ and $\theta \approxeq \pi/2$. Thus, the reflection coefficient magnitude $|\Gamma|$ can be approximated as:

$$|\Gamma| \approxeq \frac{|Z_L - Z_0|}{2\sqrt{Z_0 Z_L}} |\cos\theta|\,. \tag{5.6}$$

This result represents the approximate mismatch of the quarter-wave transformer near the design frequency, as illustrated in Figure 5.4.

If a maximum value Γ_m is set as an acceptable reflection coefficient magnitude, then the bandwidth of the matching transformer yields:

$$\Delta\theta = 2\left(\frac{\pi}{2} - \theta_m\right)\,, \tag{5.7}$$

because the response of Equation (5.3) is symmetric about $\theta = \pi/2$, and $\Gamma = \Gamma_m$ at $\theta = \theta_m$ and at $\theta = \pi - \theta_m$. Equating Γ_m to the exact expression for the reflection coefficient magnitude in Equation (5.3) allows us to obtain θ_m:

$$\frac{1}{\Gamma_m^2} = 1 + \left(\frac{2\sqrt{Z_0 Z_L}}{ZL - Z_0}\sec\theta_m\right)^2\,, \tag{5.8}$$

or

$$\cos\theta_m = \frac{\Gamma_m}{\sqrt{1 - \Gamma_m^2}} \frac{2\sqrt{Z_0 Z_L}}{|Z_L - Z_0|}\,. \tag{5.9}$$

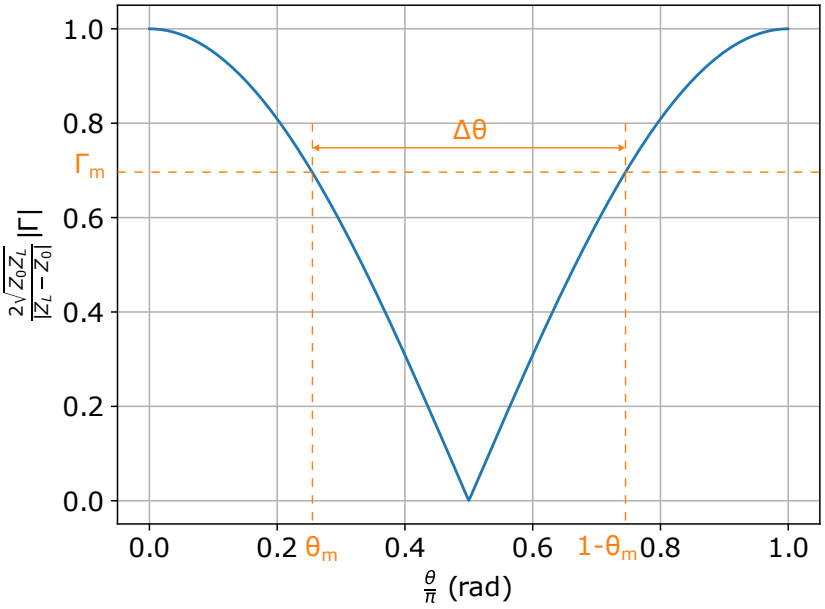

Figure 5.4: Approximate behaviour of the reflection coefficient magnitude for a single-section quarter-wave transformer operating near its design frequency.

5.3.2 Chebyshev transformer

The quarter-wave transformer provides a simple means of matching any real load impedance to any transmission line impedance. For applications requiring more bandwidth than a single quarter-wave section can provide, multi-section transformers can be used. The total reflection coefficient caused by the partial reflections from the several small discontinuities that are implicit in the transformer design is studied in the *theory of small reflections*. However, in our case, this theory does not provide accurate results because there is a significant difference between the two impedances (Z_0 and Z_L) that are to be adapted, as explained by both Pozar and Collin [35, 3].

In the case under study, the procedure described by Collin [3] must be followed, in which the precise formulation and theory of multi-section quarter-wave impedance transformers is considered, using equivalent circuit models of a rectangular waveguide [103]. The ratio between the available power (incident power) and the actual power delivered to the load is defined as the power loss ratio P_{LR}. If the incident power is P_i, the reflected power is $\rho^2 P_i$, and the power delivered to the load is $(1-\rho^2)P_i$, then:

$$P_{LR} = \frac{P_i}{(1-\rho^2)P_i} = \frac{1}{1-\rho^2}\,, \tag{5.10a}$$

$$\rho = \sqrt{\frac{P_{LR}-1}{P_{LR}}}\,. \tag{5.10b}$$

The power loss ratio is given by:

$$P_{LR} = 1 + \frac{(Z_L - Z_0)^2}{4Z_L Z_0} \frac{(\sec^2\theta_z \cos^2\theta - 1)^2 \cos^2\theta}{\tan^4\theta_z}\,, \tag{5.11}$$

where θ_z is the value of θ at the lower zero where ρ vanishes.

The passband tolerance k^2 is given by:

$$k^2 = \frac{(Z_L - Z_0)^2}{4Z_L Z_0} \left(\frac{2\cos\theta_z}{3\sqrt{3}\tan^2\theta_z}\right)^2 . \tag{5.12}$$

It can be demonstrated that the maximum value of the reflection coefficient ρ_m is:

$$\rho_m = \sqrt{\left(\frac{k^2}{1+k^2}\right)}\,. \tag{5.13}$$

It is important to highlight that specifying k^2 determines the bandwidth, and vice versa. The value of θ_m that yields ρ_m is given by:

$$\theta_m = \arccos\frac{2}{\sqrt{3}}\cos\theta_z\,. \tag{5.14}$$

In Table 5.1, the required impedance values for a three-section Chebyshev quarter-wave transformer are shown for several values of the passband tolerance k^2. We have used this table to design the three-section transformer, as will be described below.

Table 5.1: Chebyshev quarter-wave-transformer design data [3].

	$\Delta f/f_0 = 0.2$		$\Delta f/f_0 = 0.4$		$\Delta f/f_0 = 0.6$	
Z_L/Z_0	Z_1/Z_0	k^2	Z_1/Z_0	k^2	Z_1/Z_0	k^2
2	1.09247	$1.19 \cdot 10^{-7}$	1.09908	$7.89 \cdot 10^{-6}$	1.10830	$9.57 \cdot 10^{-5}$
4	1.19474	$5.35 \cdot 10^{-7}$	1.20746	$3.55 \cdot 10^{-5}$	1.23087	$4.31 \cdot 10^{-4}$
10	1.34900	$1.92 \cdot 10^{-7}$	1.37482	$1.28 \cdot 10^{-4}$	1.42320	$1.55 \cdot 10^{-3}$
20	1.48359	$4.29 \cdot 10^{-7}$	1.52371	$2.85 \cdot 10^{-4}$	1.60023	$3.45 \cdot 10^{-3}$
100	1.87411	$2.33 \cdot 10^{-6}$	1.97500	$1.55 \cdot 10^{-3}$	2.17928	$1.87 \cdot 10^{-2}$

* $Z_2 = \sqrt{Z_L Z_0}$, $Z_3 = Z_L Z_0 / Z_1$.

5.3.3 Design of a three-section impedance transformer

As previously described, to achieve the multipactor regime in the standard aluminium waveguide (WR75) without using high input power levels it is necessary to minimize the height b of the waveguide. To accomplish this, an impedance transformer has been designed that takes capacitive E-plane discontinuities into account such that the final height of the WR75 waveguide is reduced to $b = 0.4\,\text{mm}$. The requirements

Table 5.2: Main parameters of the WR75 rectangular waveguide.

WR75 Specifications	
Recommended Frequency Band	10.00 GHz to 15.00 GHz
Cut-off Frequency of Lowest-order Mode	7.869 GHz
Cut-off Frequency of Upper Mode	15.737 GHz
Dimensions	19.05 mm × 9.525 mm

Source: Everything RF website [59].

and estimation of the parameters of this impedance transformer are considered below.

Figure 5.5 shows the scheme of the third-order impedance transformer. The symmetry of the problem allows us to analyse it such that the aim is its reverse, that is, to adapt a rectangular waveguide with a height b that is smaller than the standard WR75 waveguide. The circuit to address the problem in reverse is shown in Figure 5.6, and comprises a three-section Chebyshev transformer.

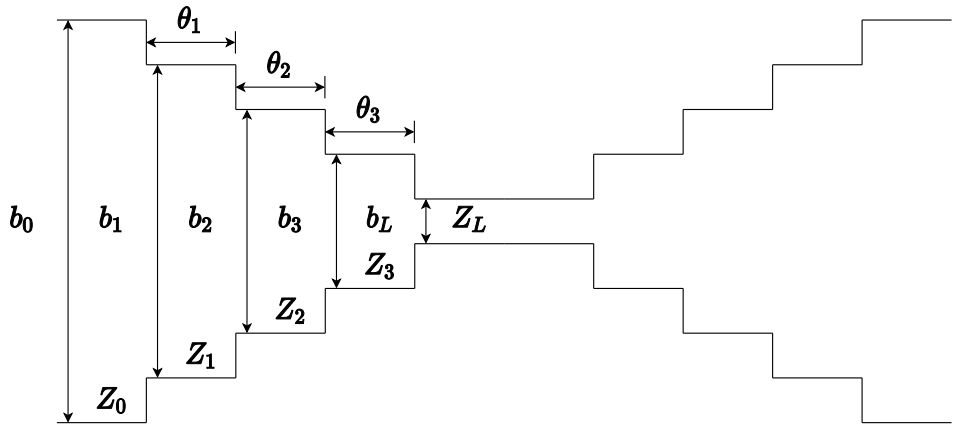

Figure 5.5: Electrical sketch of the third-order impedance transformer.

The established initial dimensions of the transformer are: $a = 19.05\,\text{mm}$, $b_0 = 0.4\,\text{mm}$ and $b_L = 9.525\,\text{mm}$. A central working frequency $f = 12.5\,\text{GHz}$ and a bandwidth of $\Delta f = 5\,\text{GHz}$ have been chosen, that is, $\Delta f/f = 0.4$.

In a rectangular waveguide, the voltage and current cannot be uniquely defined because there is no TEM mode, unlike in the case of two-conductor transmission lines. Ishihara and Shinichi have established a simple relationship between the mode impedance and the characteristic impedance [104]: the characteristic impedance is considered as the mode impedance multiplied by the term b/a, where a and b are the dimensions of the waveguide in the usual notation. However, they also add

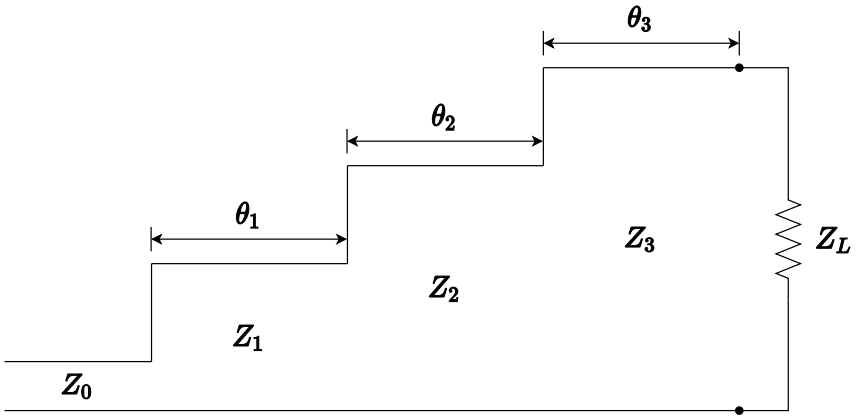

Figure 5.6: Circuit diagram of a three-section Chebyshev transformer.

a constant k that depends on the definition of the characteristic impedance. For instance, it could be defined as the voltage between the upper and lower surfaces in the centre of the waveguide divided by the current in the axial direction, or it could be determined such that the power carried by the waveguide matches the definition valid for line transmission, and so on. Therefore, although there is some ambiguity in the definition, we have assumed that the characteristic impedance Z_c for the rectangular waveguide of dimension $a \times b$ can be defined as:

$$Z_c = \frac{2b}{a\sqrt{1 - \frac{\left(\frac{\pi}{a}\right)^2}{\left(\frac{\omega}{c}\right)^2 - \left(\frac{\pi}{a}\right)^2}}}\,, \tag{5.15}$$

where $c = c_0 = 3 \cdot 10^8\,\mathrm{m\,s^{-1}}$ and $\omega = 2\pi f$.

The input Z_0 and load Z_L characteristic impedances can be obtained from Equation (5.15) by substituting the known values of b_0 and b_L, which gives $Z_0 = 0.072\ \Omega$ and $Z_L = 1.710\ \Omega$. The ratio $Z_L/Z_0 = 23.81$ can be approximated to $Z_L/Z_0 \approx 20$, allowing us to apply the Chebyshev quarter-wave-transformer design data shown in Table 5.1. On this basis, we obtain the following values: $Z_1/Z_0 = 1.52371$ and thus $Z_1 = 0.109\,\Omega$, $Z_2 = \sqrt{Z_L Z_0} = 0.350\,\Omega$, $Z_3 = Z_L Z_0/Z_1 = 1.122\,\Omega$ and $k^2 = 2.85 \cdot 10^{-4}$.

Once the characteristic impedances of each of the transformer sections have been obtained, the lengths of each of them are calculated. These can be derived from:

$$\lambda = \frac{2\pi}{\beta} = \frac{2\pi}{k\sqrt{1 - \left(\frac{k_c}{k}\right)^2}} = \frac{\lambda_0}{\sqrt{\epsilon_r\left(1 - \left(\frac{k_c}{k}\right)^2\right)}}\,, \tag{5.16}$$

and thus:

$$\lambda = \frac{\lambda_0}{\sqrt{\epsilon_r \left(1 - \left(\frac{f_c}{f}\right)^2\right)}}\,. \tag{5.17}$$

Taking into account that $\lambda_0 = c/f = 0.024\,\mathrm{m}$, where $c = c_0 = 3 \cdot 10^8\,\mathrm{m\,s^{-1}}$ and $f = 12.5\,\mathrm{GHz}$, the cut-off frequency for the fundamental mode TE_{10} is $f_c = c/2a = 7.87\,\mathrm{GHz}$, and $\epsilon_r = 1$ in air, we get the values $\lambda_i = 0.031\,\mathrm{m}$ for $i = 1, 2$ and 3. Finally, because we have $\theta = \lambda/4$, the lengths of the transformer sections are $\theta_i = 7.72\,\mathrm{mm}$ for $i = 1, 2$ and 3.

The simulation of the electrical response of the transformer in the selected frequency range was carried out using Ansys-HFSS® software, with the aim of ensuring that the design specifications were met. Figure 5.7 shows the representation of the reflection coefficient (S_{11}). The matched condition ($\mathrm{S}_{11} = 0$) in the selected frequency range should be approximately exhibited. Using Equation (5.13) and being $k^2 = 2.85 \cdot 10^{-4}$, the return loss RL in the range 10.00 GHz to 15.00 GHz should be approximately:

$$RL = -20\log(\rho_m) = -20\log\left(\sqrt{\left(\frac{k^2}{1+k^2}\right)}\right) \approx 35\,\mathrm{dB}\,. \tag{5.18}$$

However, as can be seen in Figure 5.7, this is not the case. The transformer does not behave as desired and, therefore, it is necessary to carry out an optimization process, the heights and lengths of the intermediate sections being the variables to be optimized.

5.3.4 Optimization and experimental validation

As an alternative to the approach described above, we have used the design tool available in FEST3D® software for designing waveguide transformers. This program is formulated on the basis of the integral equation technique, and it allows analysis of waveguide junctions of any profile. As a special feature, it supports the automated design of an impedance transformer between two different waveguide sections, given a specific operational bandwidth. With the aid of this tool, an initial impedance transformer was designed to the specifications provided previously, that is, $a = 19.05\,\mathrm{mm}$, $b_0 = 0.4\,\mathrm{mm}$ and $b_L = 9.525\,\mathrm{mm}$, with a desired working central frequency $f = 12.5\,\mathrm{GHz}$ and bandwidth $\Delta f = 5\,\mathrm{GHz}$.

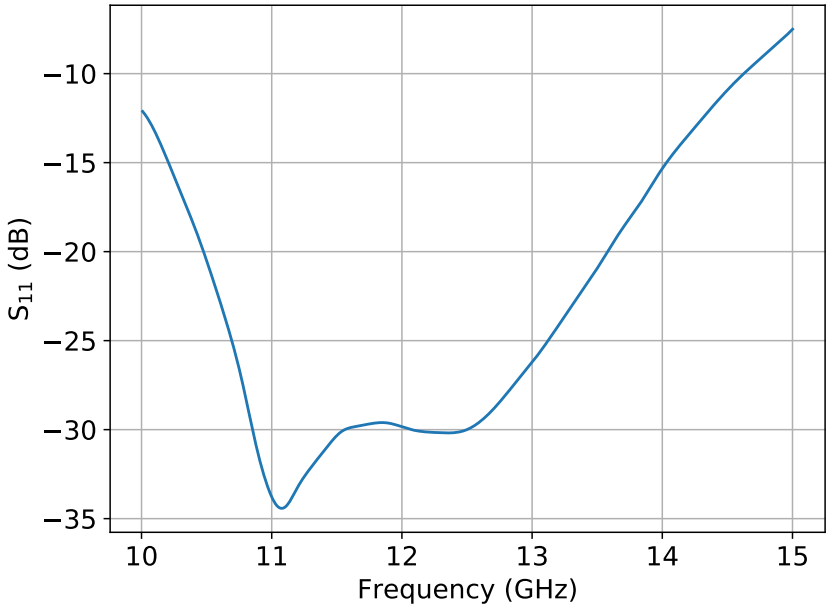

Figure 5.7: Reflection coefficient (S_{11}) of the unoptimized impedance transformer.

Once the input design parameters had been introduced into FEST3D®, it was found that in order to achieve a good response, four waveguide steps were necessary, yielding an electrical response that satisfied the design conditions, and obtaining a reflection below −20 dB across the entire bandwidth. Next, the initial impedance transformer was modified to the final desired structure, that is, a symmetrical impedance transformer, such that the impedance transformer obtained begins and ends with a standard WR75 waveguide. The resulting design is shown in Figure 5.8, whilst the electrical response of the transformer is plotted in Figure 5.9. To validate the results obtained with FEST3D®, the same transformer has been simulated with Ansys-HFSS®. A scheme of the transformer is shown in Figure 5.10. It is important to highlight that in the subsequent analysis to be carried out on the multipactor effect in the transformer, it will be partially covered with Teflon® layers. However, the FEST3D® simulation software does not allow the analysis of this type of structure with dielectric materials. Therefore, the same transformer has been simulated with Ansys-HFSS®, which does offer the functionality to analyse this problem. As can be seen in the figure, both electromagnetic simulation tools return practically identical responses throughout the entire frequency band. In addition, the response obtained with Ansys-HFSS® for the same transformer taking into consideration the losses of the waveguide material (aluminium) is also represented. The responses are almost the same, except at the edges of the band. This is because the aluminium losses are

very low.

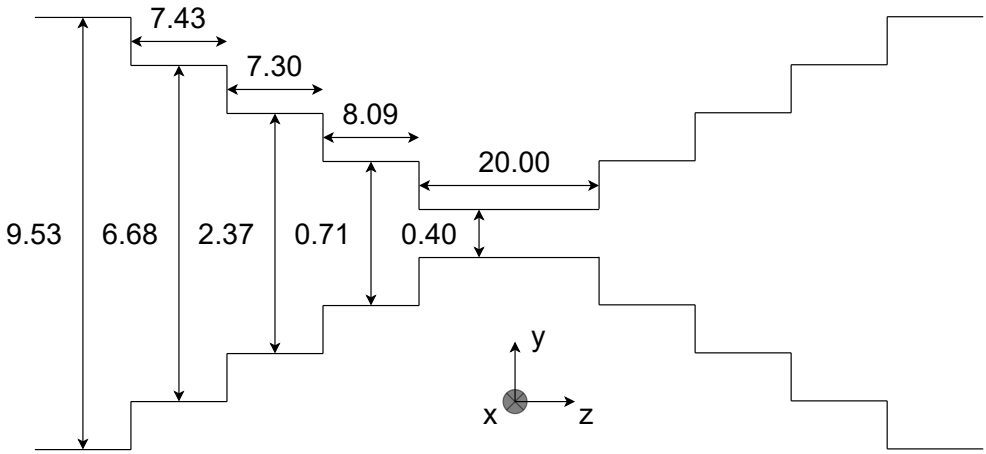

Figure 5.8: Scheme of a symmetric E-plane rectangular waveguide transformer. Dimensions in mm.

To ensure that the electrical response of the transformer is correct when it is partially filled with Teflon®, it has been simulated in Ansys-HFSS® in three different configurations: 1) without dielectric material; 2) covering only the bottom surface of the waveguide with a thin film of Teflon®, of thickness $h = 0.025\,\text{mm}$ and $r = 2.1$; 3) covering both top and bottom surfaces of the waveguide with the same Teflon® film. The electrical responses obtained in each case are shown in Figure 5.11. As can be seen, the response of the transformer when the bottom wall alone is covered with dielectric is worse than that of the empty transformer. The S_{11} value is above $-25\,\text{dB}$ in the upper frequency band. In the case of partially filling the transformer by covering both top and bottom walls with Teflon®, it can be seen that the electrical response gets even worse. In this case, the S_{11} value is above $-20\,\text{dB}$ in the upper frequency band. Therefore, despite the fact that it is only a thin dielectric sheet (it has a thickness of just $25\,\mu\text{m}$) with an ϵ_r not significantly different from that of vacuum, because the height of the central section of the transformer is only $400\,\mu\text{m}$, coating this section with dielectric significantly affects the performance of the designed transformer, and therefore could not be used in the three desired multipactor measurement campaigns. The solution has been to optimize the dimensions of the transformer for the second case. In this way, it is expected that the three configurations will show an acceptable response in the desired operating band, that is, S_{11} should be below $-20\,\text{dB}$ for the entire band.

The final scheme and dimensions of the transformer are shown in Figure 5.12 (note that the width of the rectangular waveguides involved is $a = 19.05\,\text{mm}$). Photographs

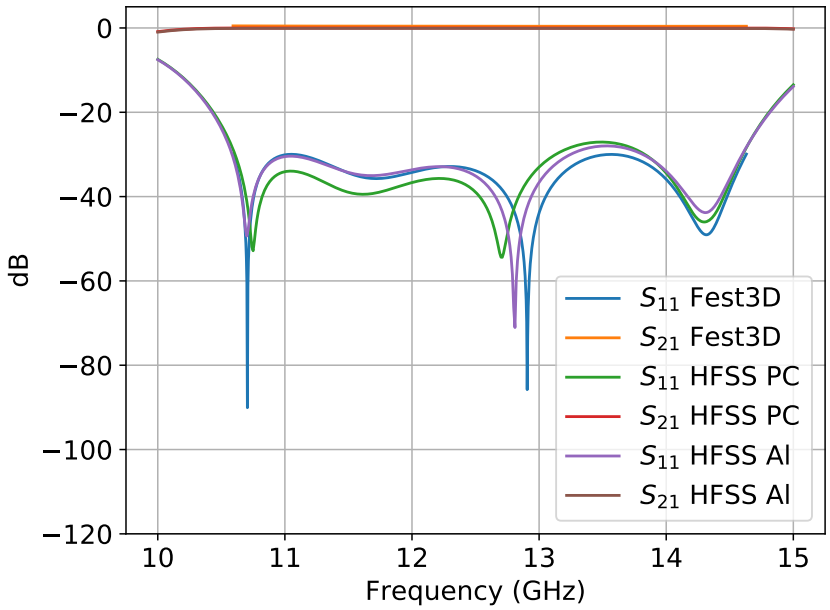

Figure 5.9: Comparison of the electrical response simulations of the empty impedance transformer.

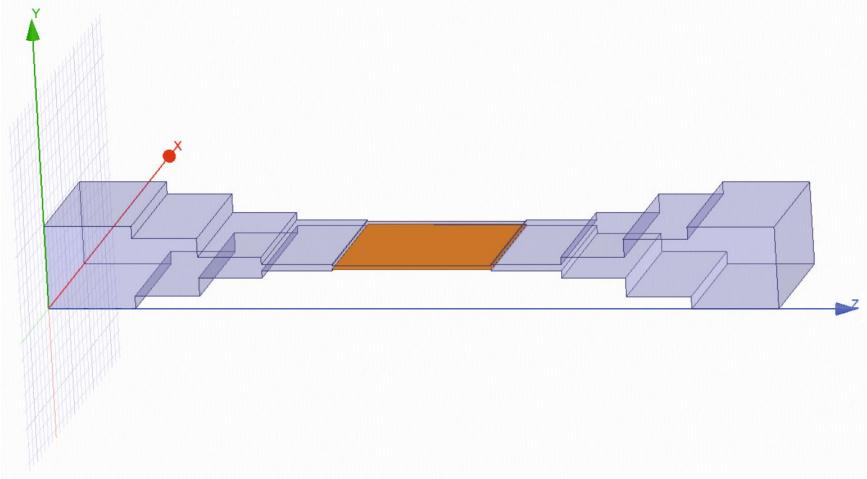

Figure 5.10: Scheme of the impedance transformer in Ansys-HFSS®.

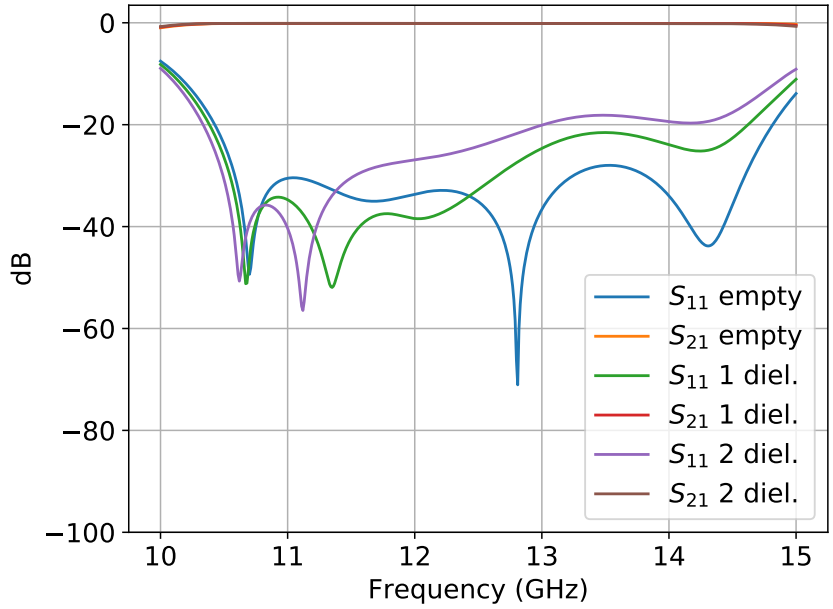

Figure 5.11: Comparison of the electrical response of the impedance transformer when empty and when partially filled with dielectric.

of the fabricated transformer are shown in Figure 5.13. The S-parameters measured for the three configurations are shown in Figure 5.14, where some discrepancies with their simulations can be observed. First, a frequency shift towards lower frequencies for the minimum S_{11} value measured, and second, lower levels for the return losses measured in the three configurations. Nevertheless, the S-parameters for all cases still show very good matches (better than 20 dB) and low insertion losses (lower than 0.3 dB) for the range from 10.4 GHz to 10.77 GHz. This demonstrates that the comparison of the experimental results with the simulations is valid at $f = 10.7$ GHz, the frequency of the experimental multipactor test.

5.4 Multipactor breakdown threshold

An experimental multipactor test campaign was carried out at the VSC/ESA Laboratory. The operational test frequency was $f = 10.707$ GHz. We have used the experimental SEY curves shown in Figure 5.2 to compute the multipactor breakdown threshold in the aluminium rectangular waveguide of width $a = 19.05$ mm and height $b = 0.4$ mm under study, considering the three aforementioned configurations. Thus, the empty gap waveguide in the vertical dimension $d = b - h$ where the electrons can travel in each case will take values of 0.4 mm, 0.375 mm and 0.35 mm, respectively.

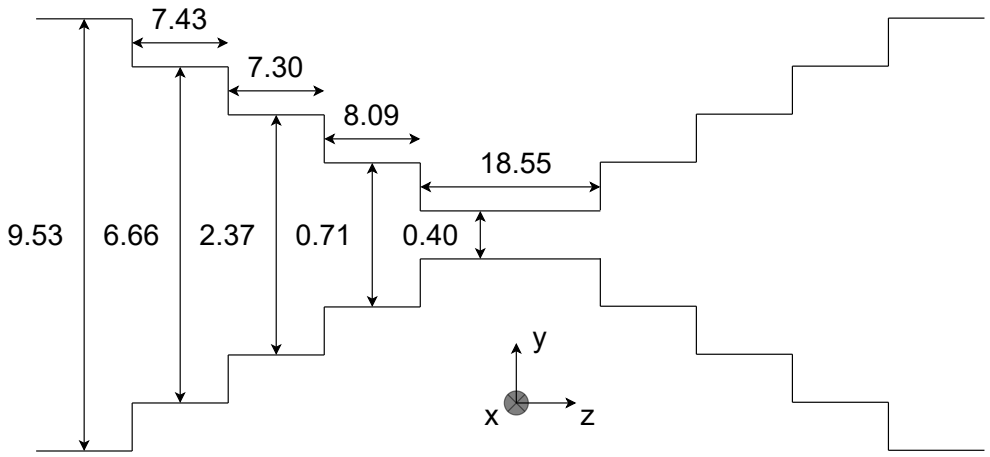

Figure 5.12: Scheme of the optimized symmetric E-plane rectangular waveguide transformer. Dimensions in mm.

In order to compute the RF multipactor V_{th} at a given $f \times d$ point, a procedure similar to the one already described in the previous chapter has been followed. For each $f \times d$ point, a sweep of the effective voltage V_{eff} has been performed, calculated numerically as the line integral of the vertical electric field component and evaluated at the centre of the waveguide and along the entire empty gap. For each V_{eff}, a statistical study of the final population of electrons after 100 RF cycles is performed using a sufficiently high number of simulations, corresponding to different initial phases of the RF field. Both the spread in secondary emission kinetic energy and angle of the secondary electrons after each impact on the waveguide walls has been considered. We have calculated the maximum effective voltage (V_{eff}^{1W}) in the central section of the transformer (calculated from the maximum y-component of the electric field, as explained at the beginning of this section) in the three configurations considered, assuming an input power of 1 W. Thus, a given RF input power P_{inp} can be related to the applied voltage in the critical gap region as:

$$V_{eff} = V_{eff}^{1W} \sqrt{P_{inp}}\,. \tag{5.19}$$

Such a method has been used to estimate the RF multipactor V_{th} in the three aforementioned configurations as a function of $f \times d$, which is shown by lines in Figure 5.15. The measured power levels at which the multipactor discharge was detected were 580 W (empty waveguide) and 600 W (both one and two dielectric sheet(s)), and the corresponding RF V_{th} values have been highlighted with squares in Figure 5.15, showing excellent agreement between the theoretical and experimental data. It can be seen that, for a given empty gap value $d = b - h$, the empty waveguide shows a slightly

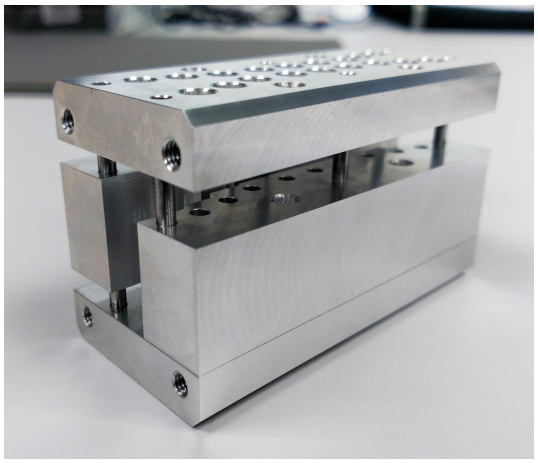

(a)

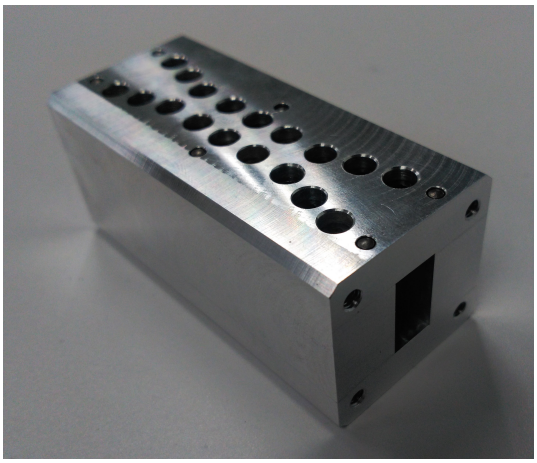

(b)

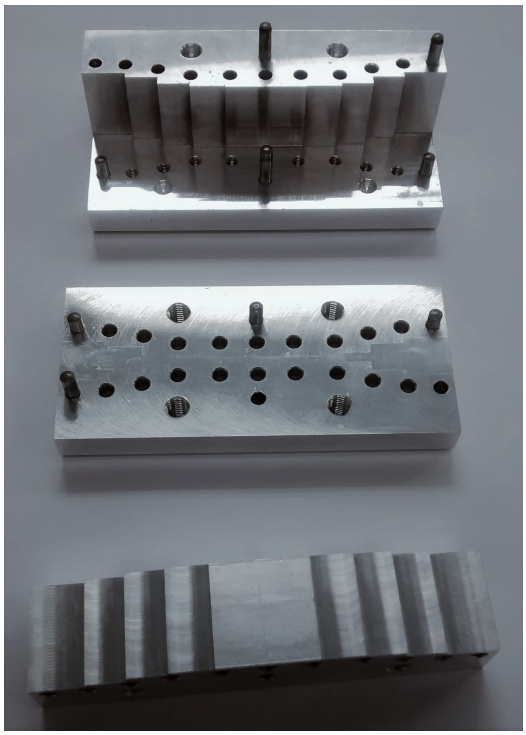

(c)

Figure 5.13: Photographs of the fabricated E-plane rectangular waveguide transformer.

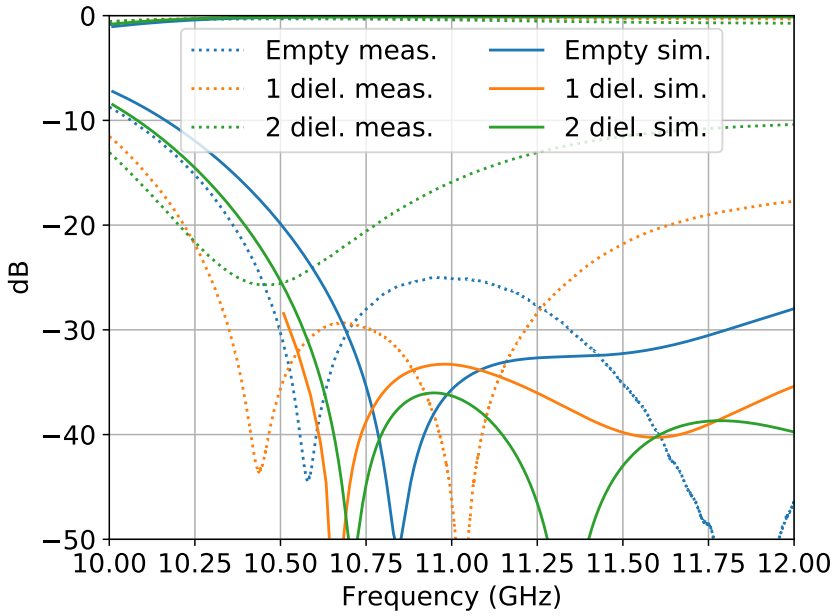

Figure 5.14: Electrical response of the symmetric E-plane waveguide transformer.

lower V_{th} than the one- and two-sided partially dielectric-loaded waveguides. Given that the field distribution is quite similar in all three cases, the observed difference in Figure 5.15 is basically conditioned by the lower W_1 of aluminium (15 eV) compared to that of Teflon® (36 eV), as could be expected.

5.5 Summary

In this chapter, the multipactor threshold results have been presented for an aluminium WR75 symmetric E-plane rectangular waveguide transformer, considering three configurations of the top and bottom walls of the waveguide: 1) metal-metal, 2) metal-dielectric, and 3) dielectric-dielectric.

The SEY properties of the different materials employed in the experiment have been measured and used in the numerical simulations. For this structure, the variation of the RF multipactor V_{th} has been analysed theoretically (with and without dielectric material), and compared with actual multipactor measurements, demonstrating excellent agreement between the theoretical and the experimental data. Both theoretical and experimental results show an increase in the RF multipactor V_{th} at a given empty gap waveguide value when the dielectric material is incorporated.

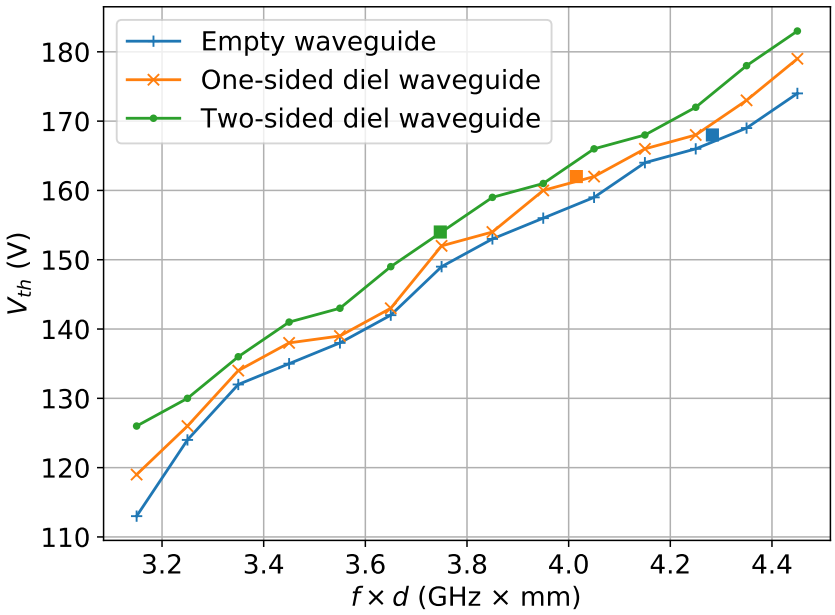

Figure 5.15: RF multipactor V_{th} of the rectangular waveguide for the three configurations studied. The squares correspond to the experimental data.

Chapter 6

Conclusions and future work

6.1 Conclusions

The multipactor effect is an important mechanism of failure in many modern RF systems operating at or close to vacuum conditions. The phenomenon manifests itself as an avalanche-like increase of free electrons, which is caused by secondary electron emission from the device walls when hit by energetic electrons being accelerated by the RF field. Multipactor breakdown is becoming an increasingly severe problem in different RF applications, such as space-borne communication, RF accelerators, and high-power microwave generators. This development is the result of increasing microwave power, along with a tendency to fabricate microwave devices as compactly as possible. Because multipactor discharges can significantly limit or even damage RF systems, understanding these discharges is critical to RF operation. The contribution of this work to a fast-growing body of multipactor studies will enable researchers to better design RF systems.

The multipactor effect has been investigated both theoretically and experimentally over almost 70 years. However, there still exist fundamental questions, for instance, in relation to the multipactor discharges from dielectric materials, which are poorly understood. In addition, the present rate of technical development tends to give rise to new situations in which established theory is not wholly applicable. Consequently, multipactor theory is in urgent need of further development, by both analytical and numerical means.

To date, most works on the multipactor effect have considered only relatively simple geometries (e.g. parallel-plane models) and monochromatic RF fields. This situation is rapidly becoming acutely unsatisfactory, as the telecommunications industry increasingly tends to make use of multi-carrier operation and devices with

more complicated geometrical and material configurations, particularly in terms of dielectrics.

The work within this thesis has involved theoretical studies based on both analytical and numerical methods, and the resulting predictions have also been compared with experimental results. One of the main objectives of the research has been a detailed investigation of multipactor discharges on the surface of dielectric materials. The aim has been an ability to calculate the power threshold at which multipactor discharges will occur in dielectric-loaded rectangular waveguides irradiated by powerful microwaves. The theoretical predictions have been compared with experimental data also obtained in the course of the thesis. Particular attention has been given to calculation of the charge deposited on dielectric surfaces by multipacting electrons and to estimation of the electrostatic field caused by this.

In addition to the deep study of the multipactor effect, the second part of the thesis has involved detailed numerical simulations of multipactor discharges inside several rectangular waveguides containing dielectric materials. These simulations have been carried out using code specifically developed for this purpose in the course of the research work presented.

In summary, the work carried out in this thesis provides a new and improved model for multipactor discharges in rectangular waveguides partially-loaded with dielectric. The model developed in this research takes into consideration many aspects of the physical process of the multipactor effect, such as secondary electron emission and the electrostatic field caused by emitted electrons. This investigation contributes to the current understanding of these discharges by developing a generalized procedure for a multipactor model that can efficiently predict the breakdown levels of some of the complex structures that are used in the space industry.

6.2 Future work

Experimentally, there are still many different aspects of multipactor discharges that it is necessary to investigate. Much of this future work may be possible with the sophisticated simulation tools available today, but as this research has demonstrated, direct experimental investigation can also bring new information to light.

Because secondary electron emission models are completely probabilistic, numerous distribution functions may be used to assign secondary electron yield, energy and direction. Some of the major distribution functions used in many such models include uniform, Poisson and Maxwell distributions. An advanced analysis feature

would allow the user to define the probability distribution function(s) to be used in a simulation, in order to observe the effect each distribution has on particle trajectories and, ultimately, predicted breakdown levels. This has large implications for academic research in secondary emission modelling. The same could be done for the numerical methods, wherein the numerical integrator, in addition to the proposed velocity Verlet algorithm, could be user-defined within a set of advanced methods (Runge-Kutta, Leap Frog, or even more exotic ones). The differences in, and trade-offs between, the accuracy and computation time of these methods in the context of studying multipactor breakdown have not yet been studied in any detail.

Finally, although different structures have been simulated using our developed code, more irregularly shaped structures that can be found in the industry should be tested, although a few modifications will have to be made beforehand. The secondary emission models studied in this thesis have been extensive, but space charge and electron cloud effects are not considered in our model. This means that the electron dynamics between electrons, such as the mutual repulsion that causes the saturation phenomenon in breakdowns, cannot be modelled. Including these effects would give invaluable insight into the behaviour of the plasma that is created during breakdown, and how it affects the scattering parameters and generates noise and harmonics in the microwave device. However, including these in the model would mean a considerable increase in computational load and simulation durations. Therefore, as highlighted before, there is an important future line of work regarding the search for numerical methods that enable improvements in the model without reducing its efficiency.

Conclusiones y trabajo futuro

Conclusiones

El efecto multipactor es un importante mecanismo de fallo en muchos sistemas modernos que operan en condiciones de vacío o próximas a ésta. El fenómeno se manifiesta como un incremento en avalancha de electrones libres, la cual es provocada por la emisión de electrones secundarios desde las paredes del dispositivo cuando son golpeadas por electrones energéticos acelerados por el campo de RF. La ruptura por multipactor se está convirtiendo en un problema cada vez mayor en diferentes aplicaciones de RF como la comunicación espacial, los aceleradores de RF, y los generadores de microondas de alta potencia. Esta situación es consecuencia del incremento de la potencia de microondas junto con la tendencia a fabricar dispositivos de microondas cada vez más compactos. Puesto que las descargas de multipactor pueden limitar significativamente e incluso dañar los sistemas de RF, comprender estas descargas es fundamental para la operación en RF. La contribución de este trabajo a un conjunto cada vez más grande y de rápido crecimiento de estudios multipactores permitirá a los investigadores diseñar mejor sistemas de RF.

El efecto multipactor ha sido investigado tanto teórica como experimentalmente durante casi 70 de años. Sin embargo, todavía existen cuestiones fundamentales, por ejemplo, la descarga de multipactor en materiales dieléctricos, que son poco entendidas. Además, el desarrollo técnico actual tiende a crear nuevas situaciones en las que la teoría establecida no es aplicable. Por lo tanto, la teoría de multipactor necesita de forma urgente ser desarrollada en mayor detalle, tanto de forma analítica como numérica.

En la actualidad, la mayoría de los trabajos sobre el efecto multipactor solo consideran geometrías relativamente simples (por ejemplo, los modelos de placas planoparalelas) y campos monocromáticos de RF. Esta situación se está volviendo rápidamente insuficiente ya que la industria de las telecomunicaciones tiende cada vez más a

emplear, por ejemplo, la operación con multiportadora y dispositivos con configuraciones geométricas y materiales más complicados, en particular materiales dieléctricos.

El trabajo realizado dentro de esta tesis ha involucrado estudios teóricos basados tanto en métodos analíticos como numéricos, y las predicciones también se han comparado con resultados experimentales. Uno de los principales objetivos del trabajo de investigación propuesto ha sido una investigación detallada de las descargas de multipactor en la superficie de materiales dieléctricos. El objetivo es poder calcular la potencia umbral para que se produzcan descargas de multipactor en guías de ondas rectangulares cargadas con dieléctrico irradiadas por potentes microondas. Las predicciones teóricas también se han comparado con datos experimentales obtenidos dentro de la tesis. Se ha prestado especial atención al cálculo de la carga depositada en superficies dieléctricas como consecuencia de los electrones multipactantes y a la estimación del campo electrostático causado por ellos.

Además del estudio detallado del multipactor, la segunda parte de la tesis ha involucrado simulaciones numéricas detalladas de descargas de multipactor dentro de diferentes guías de ondas rectangulares con materiales dieléctricos. Estas simulaciones se han llevado a cabo utilizando un código particularmente desarrollado dentro del trabajo de investigación presentado.

En resumen, el trabajo realizado en esta tesis proporciona un modelo nuevo y mejorado para las descargas de multipactor en guías de ondas rectangulares parcialmente cargadas con dieléctrico. El modelo desarrollado en esta investigación toma en consideración muchos aspectos del proceso físico del efecto multipactor, como la emisión de electrones secundarios o el campo electrostático causado por los electrones emitidos. Esta investigación contribuye a la comprensión de estas descargas desarrollando un procedimiento generalizado para un modelo multipactor que pueda predecir de forma eficiente los niveles de ruptura de estructuras complejas que se pueden encontrar en la industria espacial.

Trabajo futuro

Experimentalmente, todavía es necesario investigar muchos aspectos diferentes de las descargas de multipactor. Gran parte del trabajo futuro podría ser posible con las sofisticadas herramientas de simulación disponibles en la actualidad, pero como en esta investigación se ha demostrado, la investigación experimental directa podría sacar nueva información a la luz.

Dado que los modelos de emisión secundaria de electrones son completamente probabilísticos, numerosas funciones de distribución se pueden utilizar para asignar el número, energía y dirección de los electrones secundarios generados. Algunas de las principales funciones de distribución utilizadas en muchos modelos incluyen la distribución uniforme, la distribución de Poisson y la distribución de Maxwell, por nombrar algunas. Una característica avanzada para el análisis podría permitir al usuario definir las funciones de distribución de probabilidad que se utilizarán en la simulación, para observar el efecto que tiene cada distribución en la trayectoria de las partículas y, eventualmente, en los niveles de degradación predichos. Esto tiene grandes implicaciones para la investigación académica en el modelado de emisiones secundarias. Lo mismo podría hacerse con los métodos numéricos en los que el integrador numérico, además del algoritmo Velocity-Verlet propuesto, podría ser definido por el usuario entre un conjunto de métodos avanzados (Runge-Kutta, Leap Frog o incluso más exóticos). Las diferencias entre la precisión y el tiempo de cálculo en el contexto del estudio de la descomposición de multipactor aún no se han estudiado en detalle.

Finalmente, aunque se han simulado diferentes estructuras usando nuestro código, se deberían probar estructuras con formas más irregulares que se podrían encontrar en la industria, aunque primero se deberán realizar algunas modificaciones. Los modelos de emisión secundaria estudiados en esta tesis han sido extensos, pero la carga espacial o los efectos de la nube de electrones no se consideran en nuestro modelo. Esto significa que la dinámica de electrones entre ellos mismos, como la repulsión mutua que causa el fenómeno de saturación en ruptura, no se puede modelar. Incluir estos efectos proporcionaría información muy valiosa sobre el comportamiento del plasma que se crea durante la descomposición y cómo afectaría a los parámetros de dispersión y el ruido y armónicos generados en el dispositivo de microondas. Sin embargo, incluirlos en el modelo supondría un aumento considerable de la carga computacional y los tiempos de simulación. Por tanto, como se ha destacado anteriormente, existe una importante línea de trabajo de futuro en cuanto a la búsqueda de métodos numéricos que permitan incluir mejoras en el modelo sin reducir la eficiencia.

Conclusions i treball futur

Conclusions

L'efecte multipactor és un important mecanisme de fallada en molts sistemes moderns que operen en condicions de buit o pròximes a aquesta. El fenomen es manifesta com un increment en devessall d'electrons lliures, la qual és provocada per l'emissió d'electrons secundaris des de les parets del dispositiu quan són colpejades per electrons energètics accelerats pel camp de RF. La ruptura per multipactor s'està convertint en un problema cada vegada major en diferents aplicacions de RF com la comunicació espacial, els acceleradors de RF, i els generadors de microones d'alta potència. Aquesta situació és conseqüència de l'increment de la potència de microones juntament amb la tendència a fabricar dispositius de microones cada vegada més compactes. Com que les descàrregues de multipactor poden limitar significativament i fins i tot danyar els sistemes de RF, comprendre aquestes descàrregues és fonamental per a l'operació en RF. La contribució d'aquest treball a un conjunt cada vegada més gran i de ràpid creixement d'estudis multipactores permetrà als investigadors dissenyar millor sistemes de RF.

L'efecte multipactor ha sigut investigat tant teòrica com experimentalment durant quasi 70 d'anys. No obstant això, encara existeixen qüestions fonamentals, per exemple, la descàrrega de multipactor en materials dielèctrics, que són poc enteses. A més, el desenvolupament tècnic actual tendeix a crear noves situacions en les quals la teoria establida no és aplicable. Per tant, la teoria de multipactor necessita de manera urgent ser desenvolupada en major detall, tant de manera analítica com numèrica.

En l'actualitat, la majoria dels treballs sobre l'efecte multipactor només consideren geometries relativament simples (per exemple, els models de plaques pla-paral · leles) i camps monocromàtics de RF. Aquesta situació s'està tornant ràpidament insuficient ja que la indústria de les telecomunicacions tendeix cada vegada més a emprar, per exemple, l'operació amb multiportadora i dispositius amb configuracions geomètriques i materials més complicats, en particular materials dielèctrics.

El treball realitzat dins d'aquesta tesi ha involucrat estudis teòrics basats tant en mètodes analítics com numèrics, i les prediccions també s'han comparat amb resultats experimentals. Un dels principals objectius del treball de recerca proposat ha sigut una investigació detallada de les descàrregues de multipactor en la superfície de materials dielèctrics. L'objectiu és poder calcular la potencia llindar perquè es produïsquen descàrregues de multipactor en guies d'ones rectangulars carregades amb dielèctric irradiades per potents microones. Les prediccions teòriques també s'han comparat amb dades experimentals obtingudes dins de la tesi. S'ha prestat especial atenció al càlcul de la càrrega depositada en superfícies dielèctriques com a conseqüència dels electrons multipactantes i a l'estimació del camp electroestàtic causat per ells.

A més de l'estudi detallat del multipactor, la segona part de la tesi ha involucrat simulacions numèriques detallades de descàrregues de multipactor dins de diferents guies d'ones rectangulars amb materials dielèctrics. Aquestes simulacions s'han dut a terme utilitzant un codi particularment desenvolupat dins del treball de recerca presentat.

En resum, el treball realitzat en aquesta tesi proporciona un model nou i millorat per a les descàrregues de multipactor en guies d'ones rectangulars parcialment carregades amb dielèctric. El model desenvolupat en aquesta investigació pren en consideració molts aspectes del procés físic de l'efecte multipactor, com l'emissió d'electrons secundaris o el camp electroestàtic causat pels electrons emesos. Aquesta investigació contribueix a la comprensió d'aquestes descàrregues desenvolupant un procediment generalitzat per a un model multipactor que puga predir de manera eficient els nivells de ruptura d'estructures complexes que es poden trobar en la indústria espacial.

Treball futur

Experimentalment, encara és necessari investigar molts aspectes diferents de les descàrregues de multipactor. Gran part del treball futur podria ser possible amb les sofisticades eines de simulació disponibles en l'actualitat, però com en aquesta investigació s'ha demostrat, la investigació experimental directa podria traure nova informació a la llum.

Atés que els models d'emissió secundària d'electrons són completament probabilístics, nombroses funcions de distribució es poden utilitzar per a assignar el número,

energia i direcció dels electrons secundaris generats. Algunes de les principals funcions de distribució utilitzades en molts models inclouen la distribució uniforme, la distribució de Poisson i la distribució de Maxwell, per nomenar algunes. Una característica avançada per a l'anàlisi podria permetre a l'usuari definir les funcions de distribució de probabilitat que s'utilitzaran en la simulació, per a observar l'efecte que té cada distribució en la trajectòria de les partícules i, eventualment, en els nivells de degradació predits. Això té grans implicacions per a la investigació acadèmica en el modelatge d'emissions secundàries. El mateix podria fer-se amb els mètodes numèrics en els quals l'integrador numèric, a més de l'algorisme Velocity-Verlet proposat, podria ser definit per l'usuari entre un conjunt de mètodes avançats (Runge-Kutta, Leap Frog o fins i tot més exòtics). Les diferències entre la precisió i el temps de càlcul en el context de l'estudi de la descomposició de multipactor encara no s'han estudiat detalladament.

Finalment, encara que s'han simulat diferents estructures usant el nostre codi, s'haurien de provar estructures amb formes més irregulars que es podrien trobar en la indústria, encara que primer s'hauran de realitzar algunes modificacions. Els models d'emissió secundària estudiats en aquesta tesi han sigut extensos, però la càrrega espacial o els efectes del núvol d'electrons no es consideren en el nostre model. Això significa que la dinàmica d'electrons entre ells mateixos, com la repulsió mútua que causa el fenomen de saturació en ruptura, no es pot modelar. Incloure aquests efectes proporcionaria informació molt valuosa sobre el comportament del plasma que es crea durant la descomposició i com afectaria els paràmetres de dispersió i el soroll i harmònics generats en el dispositiu de microones. No obstant això, incloure'ls en el model suposaria un augment considerable de la càrrega computacional i els temps de simulació. Per tant, com s'ha destacat anteriorment, existeix una important línia de treball de futur quant a la cerca de mètodes numèrics que permeten incloure millores en el model sense reduir l'eficiència.

Appendix A

Integration of equations of motion

As explained by Holm in [105], the molecular dynamics method (MDM) is a very general method for modelling the physical movements of atoms and molecules. The atoms and molecules are allowed to interact for a fixed period of time, giving a view of the dynamic evolution of the system. In the simplest case, Newton's second law of motion, that is:

$$\mathbf{F} = m_0 \mathbf{a}\,, \tag{A.1}$$

can be used to integrate the classical equations of motion that each particle in the system obeys.

The basic idea in numerical integration of the equations of motion is the discretization of time. Therefore we use finite differences, particularly, we approximate:

$$\frac{\partial \mathbf{r}(t)}{\partial t} = \lim_{\Delta t \to 0} \frac{\mathbf{r}(t+\Delta t) - \mathbf{r}(t)}{\Delta t}\,. \tag{A.2}$$

This is almost equivalent to a Taylor expansion with an appropriate order of accuracy:

$$\mathbf{r}(t+\Delta t) = \mathbf{r}(t) + \mathbf{v}(t)\Delta t + \frac{\mathbf{a}(t)}{2}\Delta t^2\,. \tag{A.3}$$

Such an integration scheme, in which terms of higher order than Δt^2 are truncated, is called the *Euler scheme*. It is one of the simplest methods of numerical integration.

A.1 Verlet algorithm

The Verlet integrator offers greater stability than the much simpler Euler method and, more importantly, preserves the physical properties of a system. It was first introduced by Loup Verlet in 1967. The original approach of Verlet was to consider a Taylor expansion of the positional coordinate in two different directions of time:

$$\mathbf{r}(t+\Delta t) = \mathbf{r}(t) + \mathbf{v}(t)\Delta t + \frac{\mathbf{a}(t)}{2}\Delta t^2\,, \tag{A.4a}$$

$$\mathbf{r}(t-\Delta t) = \mathbf{r}(t) - \mathbf{v}(t)\Delta t + \frac{\mathbf{a}(t)}{2}\Delta t^2 \,. \tag{A.4b}$$

By summing Equations (A.4a) and (A.4b), we get the Verlet integration step for the position:

$$\mathbf{r}(t+\Delta t) = 2\mathbf{r}(t) - \mathbf{r}(t-\Delta t) + \mathbf{a}(t)\Delta t^2 \,. \tag{A.5}$$

It should be noted that no velocities are needed for the computation of the new positions. However, if a velocity is needed (for example, velocity-dependent forces or the determination of system temperature), it can be derived by subtracting Equations (A.4a) and (A.4b):

$$\mathbf{r}(t+\Delta t) - \mathbf{r}(t-\Delta t) = 2\mathbf{v}(t)\Delta t \,, \tag{A.6}$$

and then

$$\mathbf{v}(t) = \frac{\mathbf{r}(t+\Delta t) - \mathbf{r}(t-\Delta t)}{2\Delta t} \,. \tag{A.7}$$

The velocities calculated via the Verlet scheme are less accurate than the positions, but for capturing the kinetic energy in relation to temperature, generally suffice.

A.2 Velocity Verlet algorithm

An algorithm that yields the positions, velocities and forces at the same time is the velocity Verlet algorithm, which was first introduced in 1982 [106]. Being mathematically equivalent to the Verlet scheme, the derivation approach is quite similar but explicitly incorporates velocity, solving the first time-step problem in the basic Verlet algorithm as discussed above. The positions and velocities are updated according to:

$$\mathbf{r}(t+\Delta t) = \mathbf{r}(t) + \mathbf{v}(t)\Delta t + \frac{\mathbf{a(t)}}{2}\Delta t^2 \,, \tag{A.8a}$$

$$\mathbf{v}(t+\Delta t) = \mathbf{v}(t) + \frac{\mathbf{a}(t) + \mathbf{a}(t+\Delta t)}{2}\Delta t \,. \tag{A.8b}$$

Despite its simplicity, the velocity Verlet algorithm is very stable and has become perhaps the most widely used molecular dynamics algorithm. The velocity Verlet scheme is a symplectic integrator, that is, it preserves the volume in phase-space. Note that the computational application of the velocity algorithm does not necessarily consume more memory, because it is not necessary to keep track of the velocity of every time step during the simulation.

A.3 Electron dynamics via the velocity Verlet algorithm

As was explained in Section 3.2, the differential equation system to be solved in order to obtain the trajectory of the electron becomes:

$$\ddot{x} = \frac{\dot{z}B_y - \dot{y}B_z - E_x + \dot{x}\dot{\mathbf{r}} \cdot \mathbf{E}/c^2}{M\gamma}\,, \tag{A.9a}$$

$$\ddot{y} = \frac{\dot{x}B_z - \dot{z}B_x - E_y + \dot{y}\dot{\mathbf{r}} \cdot \mathbf{E}/c^2}{M\gamma}\,, \tag{A.9b}$$

$$\ddot{z} = \frac{\dot{y}B_x - \dot{x}B_y - E_z + \dot{z}\dot{\mathbf{r}} \cdot \mathbf{E}/c^2}{M\gamma}\,. \tag{A.9c}$$

On the basis of the velocity Verlet algorithm described previously, the position, velocity and acceleration of the electron in the waveguide are solved for each of the i-th iterations as follows [64]:

- Calculate new position of the electron $\mathbf{r}(t + \Delta t) \equiv \mathbf{r}_i$ by applying Equation (A.8a) based on the previous position $\mathbf{r}(t) \equiv \mathbf{r}_{i-1}$, velocity $\mathbf{v}(t) \equiv \mathbf{v}_{i-1}$, and acceleration $\mathbf{a}(t) \equiv \mathbf{a}_{i-1}$.

- Compute the electromagnetic fields $\mathbf{E}(t + \Delta t) \equiv \mathbf{E}_i$ and $\mathbf{B}(t + \Delta t) \equiv \mathbf{B}_i$ at this new position $\mathbf{r}_i$.

- The acceleration at the current time step $\mathbf{a}(t + \Delta t) \equiv \mathbf{a}_i$ is calculated using the (A.9) equations and the new values of $\mathbf{E}_i$ and $\mathbf{B}_i$. Therefore, the acceleration at this point will depend on the value of $\mathbf{v}(t + \Delta t) \equiv \mathbf{v}_i$.

- The previous $\mathbf{v}_{i-1}$ and $\mathbf{a}_{i-1}$ and the current $\mathbf{a}_i$ are substituted in Equation (A.8b). The final result is an equation in which the only unknown is $\mathbf{v}_i$.

The implementation scheme for this algorithm is shown in Figure A.1.

An expanded formulation of this last step is shown in the (A.10) equations, where the term $\dot{\mathbf{r}} \cdot \mathbf{E}/c^2$ has been substituted by the constant C_r:

$$v_{x,i} = v_x + \frac{\Delta t}{2M\gamma}(v_z B_y - v_y B_z - E_x + v_x C_r + v_{z,i} B_{y,i} - v_{y,i} B_{z,i} - E_{x,i} + v_{x,i} C_r)\,, \tag{A.10a}$$

$$v_{y,i} = v_y + \frac{\Delta t}{2M\gamma}(v_x B_z - v_z B_x - E_y + v_y C_r + v_{x,i} B_{z,i} - v_{z,i} B_{x,i} - E_{y,i} + v_{y,i} C_r)\,, \tag{A.10b}$$

$$v_{z,i} = v_z + \frac{\Delta t}{2M\gamma}(v_y B_x - v_x B_y - E_z + v_z C_r + v_{y,i} B_{x,i} - v_{x,i} B_{y,i} - E_{z,i} + v_{z,i} C_r)\,. \tag{A.10c}$$

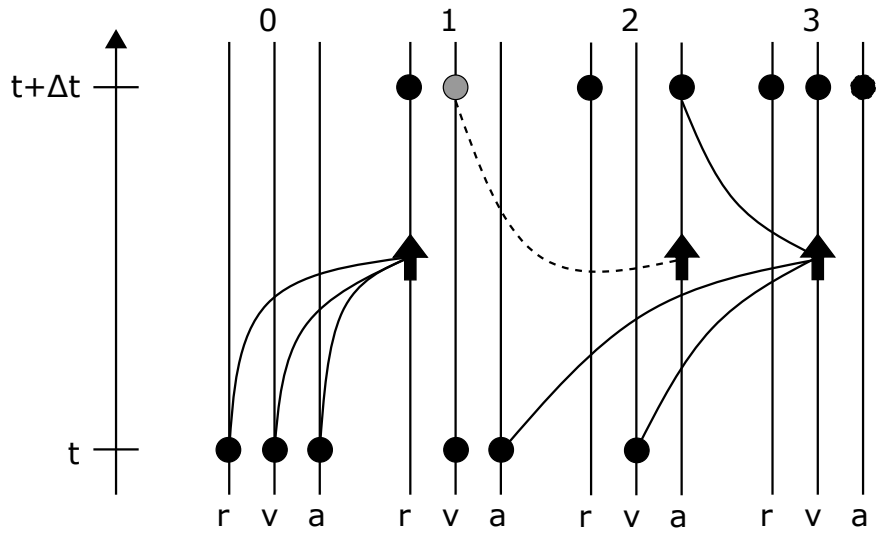

Figure A.1: Scheme of the velocity Verlet algorithm.

Note that $C_{r,i}$ has been approximated as C_r. The discrepancy is negligible, because c^2 is still much higher than $\dot{\mathbf{r}} \cdot \mathbf{E}$ or $\dot{\mathbf{r}}_\mathbf{i} \cdot \mathbf{E}_\mathbf{i}$. The system to be solved is Equation (A.11):

$$\begin{bmatrix} v_x + A(v_z B_y - v_y B_z + v_x C_r - E_x - E_{x,i}) \\ v_y + A(v_x B_z - v_z B_x + v_y C_r - E_y - E_{y,i}) \\ v_z + A(v_y B_x - v_x B_y + v_z C_r - E_z - E_{z,i}) \end{bmatrix} = \begin{bmatrix} 1 - AC_r & AB_{z,i} & -AB_{y,i} \\ -AB_{z,i} & 1 - AC_r & AB_{x,i} \\ AB_{y,i} & -AB_{x,i} & 1 - AC_r \end{bmatrix} \begin{bmatrix} v_{x,i} \\ v_{y,i} \\ v_{z,i} \end{bmatrix}, \tag{A.11}$$

where $A = \frac{\Delta t}{2M\gamma}$.

The analytical expression of the future velocities is:

$$\mathbf{v}_i = \frac{\mathbf{a}}{(2M\gamma - C_r\Delta t)\left[(2M\gamma)^2 - 4M\gamma C_r \Delta t + \Delta t^2 (B_{x,i}^2 + B_{y,i}^2 + B_{z,i}^2 + C_r^2)\right]}, \tag{A.12}$$

where the acceleration components are:

$$\begin{aligned} a_x = & (2M\gamma)^3 v_x \\ & + 2M\gamma\Delta t \begin{Bmatrix} 2M\gamma[v_z(B_y + B_{y,i}) - v_y(B_z + B_{z,i}) - E_x - E_{x,i} - C_r v_x] \\ +\Delta t B_{y,i}[v_y(B_x + B_x, i) - v_x B_y - E_z - E_{z,i}] \\ +\Delta t B_{z,i}[v_z(B_x + B_x, i) - v_x B_z - E_y - E_{y,i}] \\ +\Delta t[v_x(B_{x,i}^2 - C_r^2) + 2C_r(v_y B_z - v_z B_y + E_x + E_{x,i})] \end{Bmatrix}, \\ & + \Delta t^3 \begin{Bmatrix} (B_{x,i}^2 + C_r^2)(v_z B_y - v_y B_z + C_r v_x - E_x - E_{x,i}) \\ +(B_{x,i}B_{y,i} + C_r B_{z,i})(v_x B_z - v_z B_x + C_r v_y - E_y - E_{y,i}) \\ +(B_{x,i}B_{z,i} - C_r B_{y,i})(v_y B_x - v_x B_y + C_r v_z - E_z - E_{z,i}) \end{Bmatrix} \end{aligned} \tag{A.13}$$

$$
\begin{aligned}
a_y = &(2M\gamma)^3 v_y \\
&+ 2M\gamma\Delta t \begin{Bmatrix} 2M\gamma[v_x(B_z + B_{z,i}) - v_z(B_x + B_{x,i}) - E_y - E_{y,i} - C_r v_y] \\ +\Delta t B_{x,i}[v_x(B_y + B_y, i) - v_y B_x + E_z + E_{z,i}] \\ +\Delta t B_{z,i}[v_z(B_y + B_y, i) - v_y B_z - E_x - E_{x,i}] \\ +\Delta t[v_y(B_{y,i}^2 - C_r^2) + 2C_r(v_z B_x - v_x B_z + E_y + E_{y,i})] \end{Bmatrix}. \\
&+ \Delta t^3 \begin{Bmatrix} (B_{y,i}^2 + C_r^2)(v_x B_z - v_z B_x + C_r v_y - E_y - E_{y,i}) \\ +(B_{y,i}B_{z,i} + C_r B_{x,i})(v_y B_x - v_x B_y + C_r v_z - E_z - E_{z,i}) \\ +(B_{x,i}B_{y,i} - C_r B_{z,i})(v_z B_y - v_y B_z + C_r v_x - E_x - E_{x,i}) \end{Bmatrix}
\end{aligned}
\tag{A.14}
$$

$$
\begin{aligned}
a_z = &(2M\gamma)^3 v_z \\
&+ 2M\gamma\Delta t \begin{Bmatrix} 2M\gamma[v_y(B_x + B_{x,i}) - v_x(B_y + B_{y,i}) - E_z - E_{z,i} - C_r v_z] \\ +\Delta t B_{x,i}[v_x(B_z + B_z, i) - v_z B_x - E_y - E_{y,i}] \\ +\Delta t B_{y,i}[v_y(B_z + B_z, i) - v_z B_y + E_x + E_{x,i}] \\ +\Delta t[v_z(B_{z,i}^2 - C_r^2) + 2C_r(v_x B_y - v_y B_x + E_z + E_{z,i})] \end{Bmatrix}, \\
&+ \Delta t^3 \begin{Bmatrix} (B_{z,i}^2 + C_r^2)(v_y B_x - v_x B_y + C_r v_z - E_z - E_{z,i}) \\ +(B_{y,i}B_{z,i} - C_r B_{x,i})(v_x B_z - v_z B_x + C_r v_y - E_y - E_{y,i}) \\ +(B_{x,i}B_{z,i} + C_r B_{y,i})(v_z B_y - v_y B_z + C_r v_x - E_x - E_{x,i}) \end{Bmatrix}
\end{aligned}
\tag{A.15}
$$

Appendix B

Filon's integration method

As explained by Milovanović and Stanić in [107], when we refer to a highly oscillating function, we mean one with large numbers of local maxima and minima over some given interval. The computation of integrals of highly oscillating functions is one of the most important issues in numerical analysis. The standard methods of numerical integration often require too much computational work in relation to highly oscillating functions and cannot be successfully applied. As a result, there are a large number of special approaches for integrals of highly oscillating functions, which are effective.

B.1 Theory

The first known numerical quadrature scheme for oscillatory integrals was developed by Filon [108]. Filon presented a method for efficiently computing the Fourier integrals:

$$\int_a^b f(x)\cos(kx)\,\mathrm{d}x\,, \tag{B.1a}$$

$$\int_a^b f(x)\sin(kx)\,\mathrm{d}x\,. \tag{B.1b}$$

where k is large because of the rapid oscillation of the integrands. If the interval $[a, b]$ is divided into n equal parts of length h so that:

$$h = \frac{b-a}{n}\,, \tag{B.2}$$

where n is even, and if over each double subinterval of length $2h$ the function is approximated by the second-degree polynomial agreeing with $f(x)$ at the three relevant division points, a development analogous to that which leads to Simpson's rule produces formulas associated with the name of Filon.

With the previously used variables:

$$x_r = x_0 + rh \qquad f(x_r) = f_r \qquad (r = 0, 1, ..., n)\,, \tag{B.3}$$

where $x_0 = a$ and $x_n = b$, we first define the even and odd cosine sums:

$$C_e = \frac{1}{2}f_0\cos(kx_0) + f_2\cos(kx_2) + f_4\cos(kx_4) + ... + f_{n-2}\cos(kx_{n-2}) + \frac{1}{2}f_n\cos(kx_n)\,, \tag{B.4a}$$

$$C_o = f_1\cos(kx_1) + f_3\cos(kx_3) + ... + f_{n-1}\cos(kx_{n-1})\,, \tag{B.4b}$$

where C_e involves only ordinates with even subscripts, and C_o involves only those with odd subscripts. It may be noted that $2hC_e$ and $2hC_o$ would afford the trapezoidal and repeated midpoint approximations, respectively, to the cosine integral relative to the spacing $2h$.

With the additional variables:

$$\alpha(\theta) = \frac{\theta^2 + \frac{1}{2}\theta\sin(2\theta) - 2\sin^2(\theta)}{\theta^3}\,, \tag{B.5a}$$

$$\beta(\theta) = 2\frac{\theta(1 + \cos^2(\theta)) - \sin(2\theta)}{\theta^3}\,, \tag{B.5b}$$

$$\gamma(\theta) = 4\frac{\sin(\theta) - \theta\cos(\theta)}{\theta^3}\,, \tag{B.5c}$$

where $\theta = kh = \frac{k(b-a)}{n}$, Filon's cosine formula can be written in the form:

$$\int_a^b f(x)\cos(kx)\,\mathrm{d}x = h[\alpha(f_n\sin(kx_n) - f_0\sin(kx_0)) + \beta C_e + \gamma C_o] + E\,, \tag{B.6}$$

where the error term E vanishes accordingly when $f(x)$ is a polynomial of degree 2 or less.

In fact, the error associated with a typical subinterval $[x_{2r}, x_{2r+2}]$ is expressible in the form:

$$-\frac{h^5}{90}[f^{iv}(\psi_1)\cos(k\psi_2) - 4kf'''(\psi_3)\sin(k\psi_4)]\,, \tag{B.7}$$

where all values of ϕ lie in the subinterval. Because the total error E is the superposition of $n/2$ such contributions, it follows that if:

$$|f'''(x)| \le M_3 \qquad |f^{iv}(x)| \le M_4 \qquad (a \le x \le b)\,, \tag{B.8}$$

then:

$$|E| \le \frac{b-a}{180}h^4(M_4 + 4kM_3)\,. \tag{B.9}$$

In addition, Filon's sine formula can be written in the form:

$$\int_a^b f(x)\sin(kx)\,\mathrm{d}x = h[-\alpha(f_n\cos(kx_n) - f_0\cos(kx_0)) + \beta S_e + \gamma S_o] + E\,, \quad \text{(B.10)}$$

where S_e and S_o are the even and odd sine sums obtained by replacing cos by sin in Equations (B.4a) and (B.4b), respectively, and where the error E differs somewhat from the corresponding term in Equation (B.6) but again satisfies Equation (B.9).

Because the attainable bound can be written in the form:

$$|E| \leq \frac{b-a}{45}h^3\left(\theta M_3 + \frac{h}{4}M_4\right)\,, \quad \text{(B.11)}$$

it follows that $|E|$ may be expected to increase linearly with θ when θ is reasonably large, so that $\theta = kh$ will not exceed about 1.0 or 1.5.

Appendix C

Acceptance-rejection method

The acceptance-rejection method is a classical sampling method which allows sampling from a target distribution that is difficult or impossible to simulate by an inverse transformation. Instead, samples are taken from an instrumental density and accepted according to a carefully chosen probability. The resulting sample is effectively equivalent to a sample drawn from the target density.

In this appendix we will explain the details of this method and its application in the present study for the estimation of the departing kinetic energy after each impact of the effective electron on the walls of a rectangular waveguide.

C.1 General principle

As explained by Robert and Casella in [109], there are many distributions that it is difficult, or even impossible, to directly simulate. Moreover, in some cases, we are not even able to represent the distribution in a usable form, such as a transformation or a mixture. In such settings, it is impossible to exploit direct probabilistic properties to derive a simulation method. We thus turn to another class of methods that only requires us to know the functional form of the density $f(x)$ of interest up to a multiplicative constant; no deep analytical study of $f(x)$ is necessary. The key to this method is to use a simpler density $g(x)$ from which the simulation is actually taken. Thus, for a given density $g(x)$, called the instrumental density, there are many densities $f(x)$, called the target densities, that can be simulated in this way. We refer to the subsequent algorithm as the acceptance-rejection method, and its basic form is shown in Algorithm 6. Thus, given a (target) density of interest $f(x)$, the first requirement is the determination of an instrumental density $g(x)$ and a constant K such that:

$$f(x) \leq K \cdot g(x)\,, \tag{C.1}$$

where $x \in \mathbb{R}^n$, $f(x)$ is the denormalized target density, and K is the potentially unknown normalizing constant.

Algorithm 6 The acceptance-rejection method

1: **procedure**
2: Generate $z \sim g(x)$, $u \sim U_{[0,1]}$
3: Return z if $u \leq f(z)/K \cdot g(z)$
4: Otherwise, return to 2
5: **end procedure**

To get a better understanding of the acceptance-rejection method, it will be explained with a simple example. As detailed in [110], consider a target distribution consisting of a Gaussian mixture:

$$f(x) = \mathcal{N}(30, 10) + \mathcal{N}(80, 20). \tag{C.2}$$

A plot of this target distribution is shown in Figure C.1. Notice that this distribution

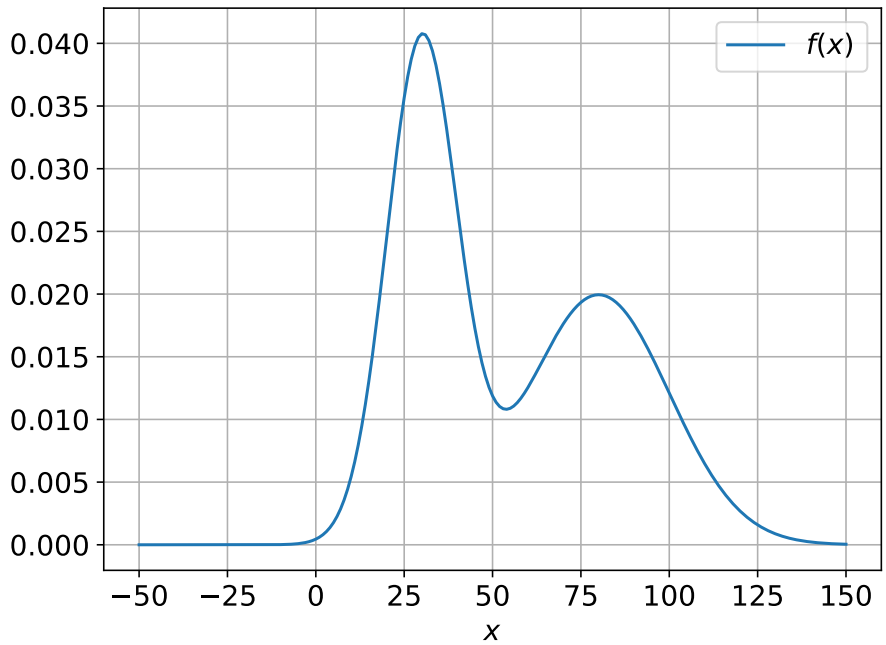

Figure C.1: Target distribution $f(x)$ consisting of a Gaussian mixture.

is not normalized. Suppose that we want to get samples from this distribution. To do this, the following density function $g(x)$ is chosen:

$$g(x) = \mathcal{N}(50, 30). \tag{C.3}$$

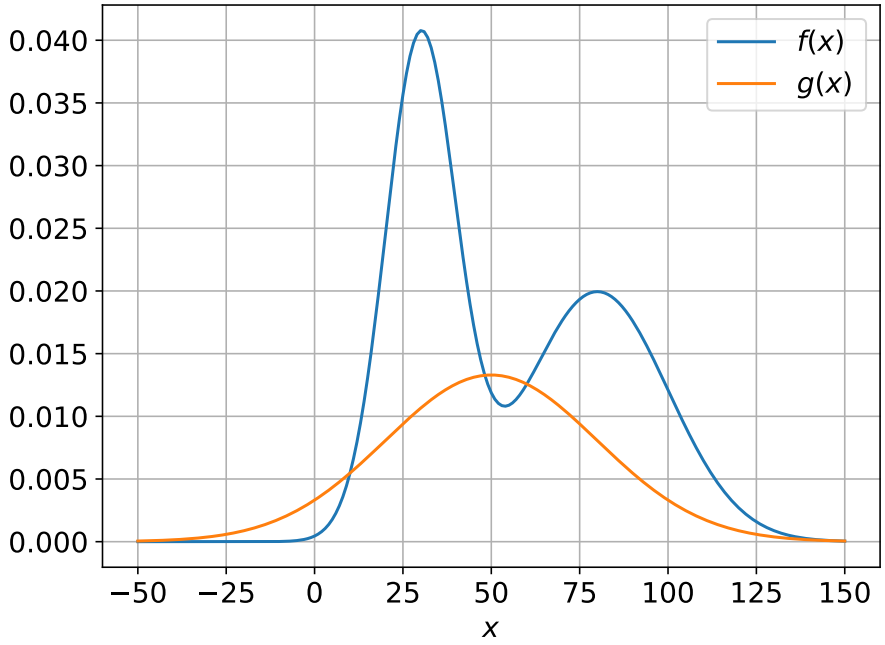

Figure C.2: Instrumental density $g(x)$ derived from a Gaussian function.

Figure C.2 shows this proposed function.

Sampling directly on $g(x)$ and using the acceptance-rejection method will fail, because the high-probability areas of $f(x)$ are not represented by $g(x)$. Intuitively, the acceptance rate will be lower if $g(x)$ is not correctly enveloping $f(x)$, which results in far fewer samples from these high-probability areas than there should be.

To remedy this, a scaling factor K must be applied, such that $K \cdot g(x)$ will envelop $f(x)$ entirely (Figure C.3). To find it, the maximum ratio of $f(x)$ to $g(x)$ has to be calculated, which will just be:

$$K = max\left(\frac{f(x)}{g(x)}\right), \tag{C.4}$$

for all x.

The main sampling algorithm involves the production of a lot of samples from the proposed distribution $g(x)$, $z \sim g(x)$, then choosing a uniform height for the distribution, such that it will be $u \sim U(0, K \cdot g(z))$. Now the sample of (z, u) will be uniform under the $K \cdot g(x)$ function. Then, we should just need to evaluate the height of our target distribution $f(x)$ at point z. Then, intuitively, we accept (z, u) samples that are under the $f(x)$ curve.

Given a sufficiently long time to run and generate samples, this will converge to $f(x)$. The result of this simulation is illustrated in Figure C.4. It is important to

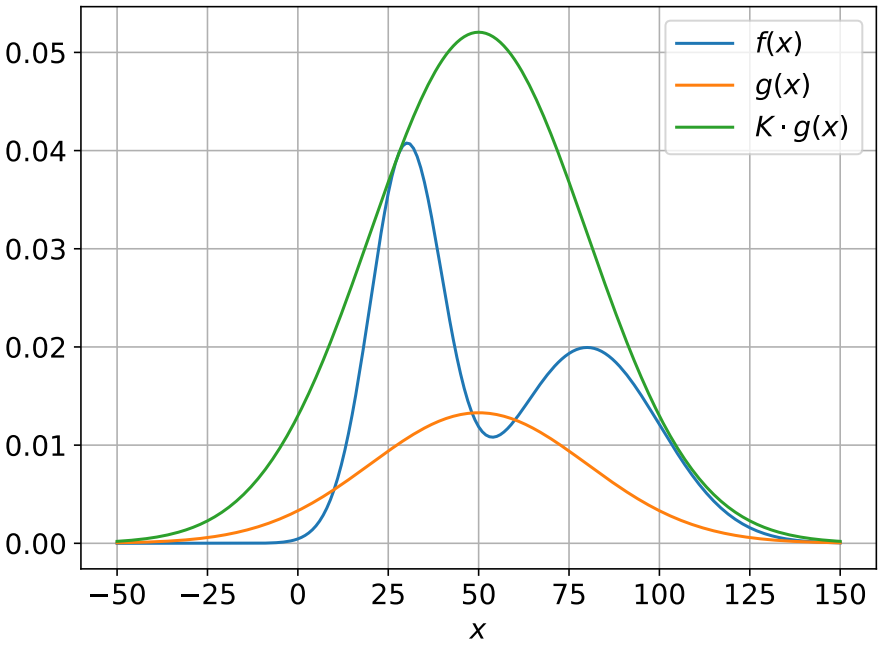

Figure C.3: $K \cdot g(x)$ envelops $f(x)$ entirely.

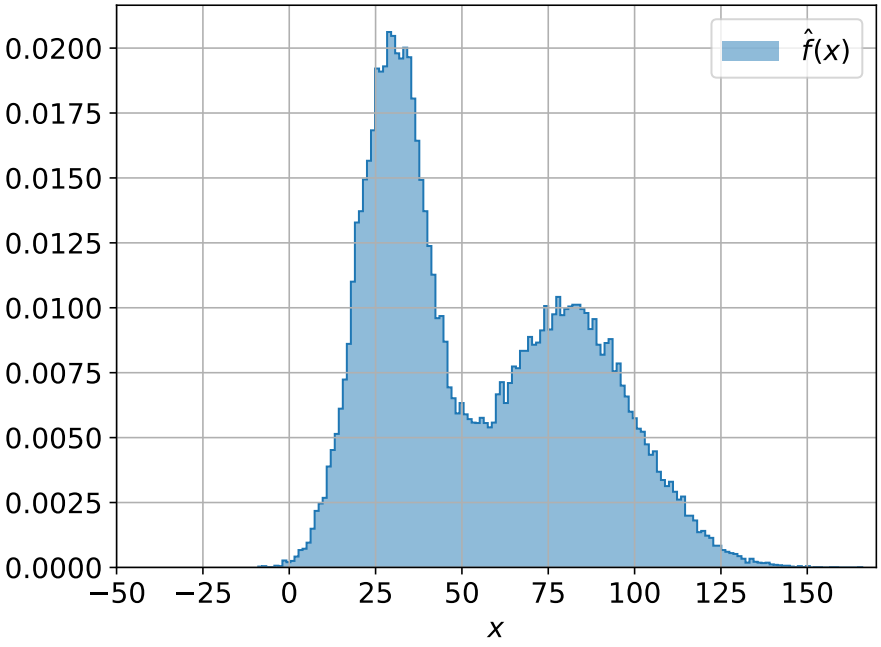

Figure C.4: Histogram of 100,000 samples obtained by application of the acceptance-rejection method.

note that the target distribution used in the acceptance-rejection method has not been normalized. However, given the samples, it is possible to reconstruct the proper distribution, so that a function proportional to the true target distribution is all that is needed.

As has been demonstrated, the acceptance-rejection method is quite simple. However, having a good heuristic for choosing the proposed distribution $g(x)$ is important. It has to envelop the target distribution. Given a complicated target distribution $f(x)$, it could be hard to estimate its shape, and it would, therefore, be difficult to choose the proposed distribution $g(x)$.

In addition, when computing the scaling factor we have to be careful to make it just large enough to envelop the target distribution, because the rejection rate will be proportional to the ratio of $f(x)$ to $g(x)$. Using a really large $g(x)$ ensures that the $f(x)$ function is enveloped, but it also means that there is a lot of wasted space that the algorithm will reject, which means wasted computational time.

C.2 Application in the case under study

The acceptance-rejection method has been employed to estimate the kinetic energy on departure following each collision of the effective electron. As mentioned in Section 3.3.3, it is assumed that this departure energy follows the probability density function $f(x)$ described in Equation (3.42). We will now consider an instrumental function $g(x)$ that corresponds to the uniform distribution function U. To ensure that the target function is enveloped by the proposed function, the scaling factor K is calculated. A plot of these functions is shown in Figure C.5.

In Listing C.1, a Python implementation of the acceptance-rejection method for obtaining the departing kinetic energy of the secondary electron after each electron impact is presented. Using this algorithm and launching 100,000 simulations, a histogram of the electron output energy is obtained, as shown in Figure C.6. As can be seen, the output energy profile reflects the target distribution very well.

```
1  import numpy as np
2  import random
3
4
5  def departure_energy(tau, w_m, w_c):
6      '''
7      Python implementation of acceptance-rejection method for
8      obtaining the secondary electron departure kinetic energy W_d
9      after each electron impact.
10     '''
11
12     x = 0.0
13     u = 0.0
```

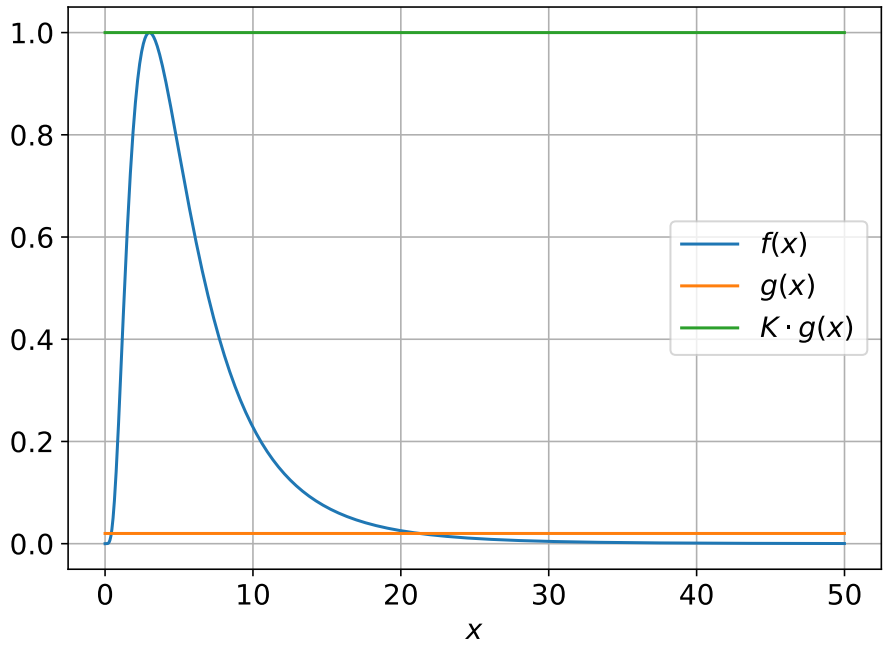

Figure C.5: Target distribution $f(x)$, instrumental density $g(x)$ and $K \cdot g(x)$ function used to obtain samples from the proposed probability density function for the secondary electron departing kinetic energy.

```
14      if w_c >= 50.0:
15          w_c = 50.0
16      else:
17          pass
18      while x <= u:
19          z = random.random()
20          w_d = z * w_c
21          x = np.exp(-np.log(w_d / w_m) / (2 * tau ** 2))
22          u = random.random()
23      return w_d
```

Listing C.1: Python code for the acceptance-rejection method.

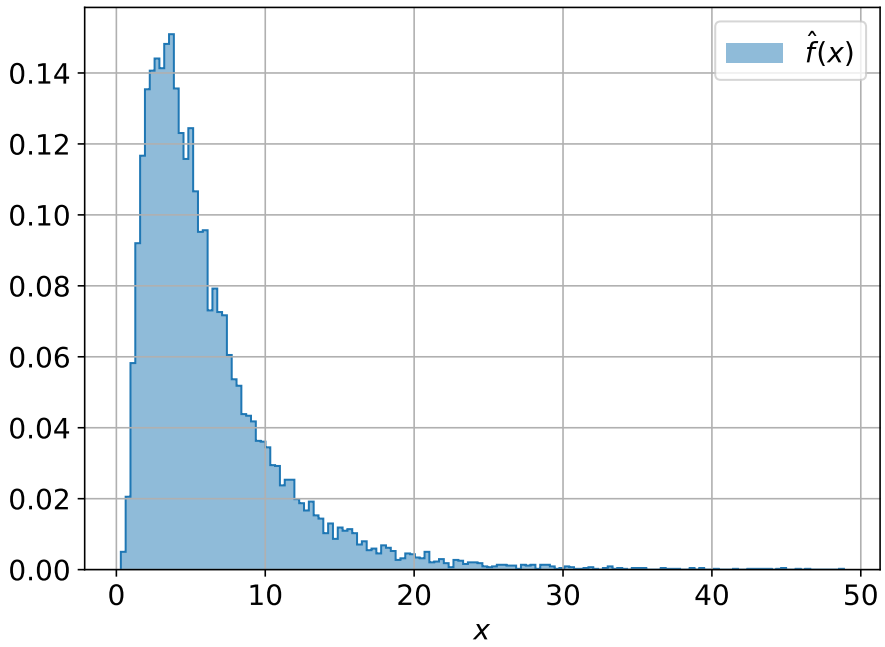

Figure C.6: Histogram of 100,000 samples of the secondary electron departing kinetic energy, obtained by application of the acceptance-rejection method.

Appendix D

Publications

In this appendix the publications in journals resulting from the work carried out during the development of this thesis are presented. These publications are listed below in chronological order:

- A. Berenguer, A. Coves, B. Gimeno, E. Bronchalo and V. E. Boria, "Experimental Study of the Multipactor Effect in a Partially Dielectric-Loaded Rectangular Waveguide", *IEEE Microwave and Wireless Components Letters*, vol. 29, no. 9, pp. 595–597, Sep. 2019, DOI: 10.1109/LMWC.2019.2929488.
- A. Berenguer, A. Coves, F. Mesa, E. Bronchalo and B. Gimeno, "Analysis of Multipactor Effect in a Partially Dielectric-Loaded Rectangular Waveguide", *IEEE Transactions on Plasma Science*, vol. 47, no. 1, pp. 259–265, Jan. 2019, DOI: 10.1109/TPS.2018.2880652.

Experimental Study of the Multipactor Effect in a Partially Dielectric-Loaded Rectangular Waveguide

Andrés Berenguer, Ángela Coves, *Senior Member, IEEE* Benito Gimeno, *Member, IEEE*, Enrique Bronchalo, and Vicente E. Boria, *Fellow*

***Abstract*—This letter presents the experimental study of the multipactor threshold in a partially dielectric-loaded rectangular waveguide, whose results validate a multipactor model recently developed by the authors, which includes the charge distribution appearing on the dielectric surface during the multipactor discharge. First, the variation of the multipactor RF voltage threshold has been theoretically analyzed in different waveguide configurations: in an empty waveguide, and also in the cases of a one-sided and two-sided dielectric-loaded waveguides. To reach this aim, an in-house Monte-Carlo simulation tool has been developed. The Secondary Electron Yield (SEY) of the metallic and dielectric materials used in the numerical simulations have been measured experimentally. Finally, an aluminum WR-75 symmetric E-plane rectangular waveguide transformer has been designed and fabricated, in which several multipaction tests have been carried out to validate the in-house software tool, demonstrating an excellent agreement between the simulation results and the experimental data.**

***Index Terms*—Multipactor effect, RF breakdown, dielectric, rectangular waveguide, waveguide transformer, Secondary Electron Yield (SEY).**

I. Introduction

MULTIPACTOR is a well-known and undesired high-power effect affecting microwave components operating under high-vacuum conditions [1]. Such multipactor-affected components are present in a wide range of different scenarios, such as passive components of satellite communication payloads, klystrons, and particle accelerators. Multipactor consists of a generation of an electron avalanche that might result in a resonant discharge with harmful consequences for the involved device. Among these negative effects, it is worth mentioning the degradation of the component, detuning of resonant cavities, power dissipation, and a significant increase of noise in communications. Multipactor has been deeply investigated in several types of microwave waveguides with simple geometries, such as parallel-plate [1], rectangular [2]–[4], circular [5], elliptical [6], and coaxial waveguides [7], [8]. However, there are few contributions to the study of the multipactor effect in partially dielectric-loaded waveguides in the scenario of RF systems for space applications [9]–[12], and most of them use the parallel-plate waveguide approach. In a recent work of the authors [13], the multipactor effect in a partially dielectric-loaded rectangular waveguide has been analyzed from a theoretical point of view for the first time, considering both the RF fields inside the waveguide and the charge distribution appearing on the dielectric surface during the multipactor discharge. In order to validate the numerical method presented in [13] with experimental data, in this letter we present the multipactor threshold results on an aluminum WR-75 symmetric E-plane rectangular waveguide transformer, partially filled with a thin dielectric layer, specially designed for this experiment. The Secondary Emission Yield (SEY) properties of the different materials employed in this experiment have been measured and used in the numerical simulations. The variation of the multipactor RF voltage threshold has been theoretically analyzed for this waveguide with and without dielectric material, and its high power behaviour has been measured, demonstrating an excellent agreement between the simulated results and the experimental data.

Manuscript received December 27, 2018; revised May 8, 2019; accepted July 15, 2019.

A. Berenguer, Á. Coves and E. Bronchalo are with the Department of Communications Engineering, Universidad Miguel Hernández de Elche, Elche, Spain (e-mail: angela.coves@umh.es).

B. Gimeno is with the Department of Applied Physics and Electromagnetism-IFIC, Universidad de Valencia, Burjasot, Spain.

V. E. Boria is with the Departamento de Comunicaciones-ITEAM, Universitat Politècnica de València, Valencia, Spain.

II. Simulation model and SEY measurements

In this work, the multipactor effect in a non-standard aluminum rectangular waveguide of width $a = 19.05\,\text{mm}$ and heigth $b = 0.4\,\text{mm}$, which is partially filled with a thin dielectric layer and corresponds to the central waveguide section of a symmetric E-plane waveguide transformer, has been analyzed and measured. To study the multipactor effect in this waveguide, a multipactor simulation code based on the Monte-Carlo method has been developed [13], which is an extension of previous studies of multipactor on a partially dielectric-loaded parallel-plate waveguide [9], [10]. In the employed multipactor code, both the RF and DC fields inside the waveguide have been rigorously considered, the last one being associated to the charge distribution appearing on the dielectric surface during the multipactor discharge. In order to determine this DC field, the electrostatic potential due to a unit point charge inside the waveguide has been first calculated by means of very efficient numerical summation and integration techniques [13]. Then, using the superposition principle, the electrostatic potential in the waveguide due to the set of charges on the dielectric surface can be obtained rigorously by adding the individual contribution of each charge, and finally the Edc field is obtained by numerical differentiation. The chosen dielectric film is DuPont Teflon® Fluorinated Ethylene Propylene (FEP) Fluoroplastic Film Type C [14], which is commonly used in space applications, with $\epsilon_r = 2.1$ and a

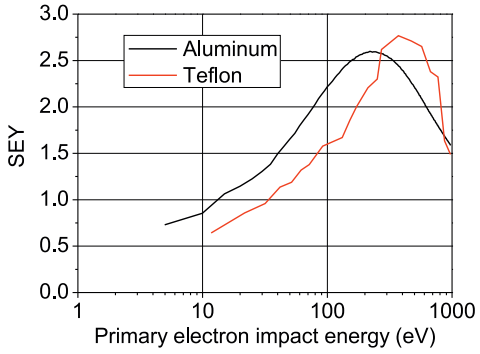

Fig. 1. SEY measured curves for the materials employed in this work.

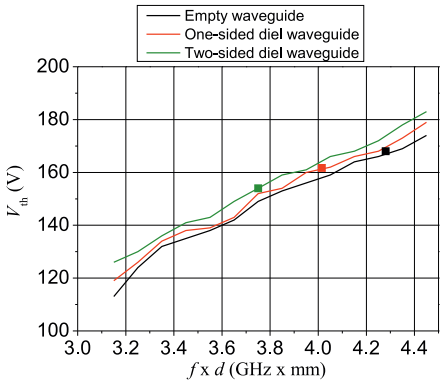

Fig. 2. RF Multipactor V_{th} of the rectangular waveguide for the three studied configurations. The squares correspond to the experimental data.

very small thickness $h = 0.025$ mm. Therefore, the electrical performance of the waveguide transformer will scarcely be modified when adding the dielectric film. It is well known that the SEY depends on material, primary electron kinetic energy, incident angle and surface state (surface composition, morphology of the structure, porosity and roughness) [15], [16]. The SEY properties of the metallic and dielectric materials employed in this experiment have been measured at the VSC/ESA laboratory, Valencia (Spain) [17], and they have been used in the multipactor simulations shown in the next section. For these materials, SEY at normal incidence was determined as a function of primary electron kinetic energy in the range 5-1000 eV, by measuring the sample current to ground when bombarded by a calibrated continuous primary electron beam of about 5 nA in the case of aluminum. In the case of teflon, the measurement of the secondary electron emission was done by using an electron gun configured in pulsed mode for sending a single electron dose of less than 10^6 e/cm^2. After each dose, and before varying the primary electron energy, the sample was electrically neutralized.

Fig. 1 shows the measured SEY curves for aluminum and Teflon®. It is worth mentioning that the maximum SEY of 2.8 measured for teflon is quite similar to the maximum SEY measured for aluminum (2.6). On the other hand, aluminum shows a lower first cross-over energy for the SEY curve ($W_1 =$ 15 eV) than the measured first cross-over value in teflon ($W_1 =$ 36 eV). These features are going to condition the multipactor results shown next.

III. Numerical and Experimental Results

We have used the experimental SEY curves shown in Fig. 1 to compute the RF multipactor threshold voltage V_{th} in the aluminum rectangular waveguide of width $a = 19.05$ mm and heigth $b = 0.4$ mm under study, considering three different configurations: 1: without dielectric material; 2: covering the bottom surface of the waveguide with a thin film of teflon (which has thickness $h = 0.025$ mm and $\epsilon_r = 2.1$); 3: covering the top and bottom surfaces of the waveguide with teflon. Thus, the empty gap waveguide in the vertical dimension $d = b - h$ where the electrons can travel in each case will take values of 0.4, 0.375 and 0.35 mm, respectively. In order to compute the multipactor RF V_{th} at a given $f \times d$ point, the same procedure used in [13] has been followed: for each $f \times d$ point, a sweep of the effective voltage V_{eff} has been performed (calculated numerically as the line integral of the vertical component of the electric field, evaluated at the center of the waveguide and along the whole empty gap). For each V_{eff}, an statistical study of the final population of electrons after 100 RF cycles is performed using a sufficiently high number of simulations, corresponding to different initial phases of the RF field. We have considered both the spread in secondary emission kinetic energy and angle of the secondary electrons after each impact on the waveguide walls. Such method has been used to estimate the RF multipactor V_{th} in the aforementioned three configurations as a function of $f \times d$, which is shown in Fig. 2 with lines. It can be checked that, for a given empty gap value $d = b - h$, the empty waveguide shows a slightly lower V_{th} than the one-sided and two-sided partially dielectric-loaded waveguides. Given that the field distribution is quite similar in all three cases, the observed difference in Fig. 2 is basically conditioned by the lower W_1 of aluminum (15 eV) than that of Teflon (36 eV), as already advanced in the previous section.

In order to validate the proposed model, a symmetric E-plane waveguide transformer has been designed and optimized (with Ansys HFSS) for a maximum return loss in the three aforementioned configurations at a frequency of $f = 10.7$ GHz, corresponding to the experimental test campaign to be performed in this waveguide. The scheme and final dimensions of the transformer are shown in Fig. 3 (note that the width of the involved rectangular waveguides is $a = 19.05$ mm). A photograph of the fabricated transformer is shown in Fig. 4. The measured S-parameters of this device in the three studied configurations are also shown in Fig. 5, where some discrepancies with simulations can be observed (a frequency shift towards lower frequencies of the minimum measured S_{11} value, and also lower levels in the measured return losses in the three analyzed configurations). Nevertheless, the measured S-parameters of the three studied configurations still show very good matching levels (better than 20 dB) and low insertion losses (lower than 0.3 dB) from 10.4 to 10.77 GHz. This guarantees that the comparison of the experimental results with

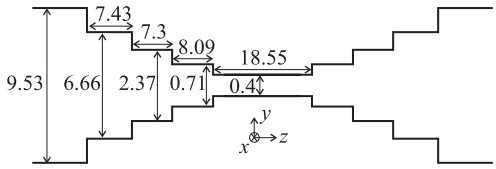

Fig. 3. Scheme of a symmetric E-plane rectangular waveguide transformer (dimensions in mm).

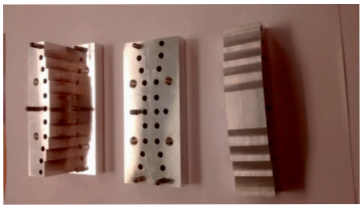

Fig. 4. Photograph of the fabricated E-plane rectangular waveguide transformer.

the simulations is valid at $f = 10.7$ GHz (the frequency of the experimental multipactor test).

We have calculated the maximum effective voltage (V_{eff1W}) in the central section of the transformer (calculated from the maximum y component of the electric field, as explained at the beginning of this section) in the three considered configurations, assuming an input power of 1 W. Thus, a given RF input power P_{inp} can be related to the applied voltage in the critical gap region as $V_{eff} = V_{eff1W}\sqrt{P_{inp}}$. An experimental multipactor test campaign has been carried out at the VSC/ESA laboratory at the operational test frequency $f = 10.707$ GHz. The measured power levels at which the multipactor discharge was detected were 580 W (empty waveguide), 600 W (1 dielectric sheet) and 600 W (2 dielectric sheets), and the corresponding RF V_{th} values have been highlighted with squares in Fig. 2, showing an excellent agreement between the theoretical and the experimental data.

IV. Conclusion

In this letter, the authors present the multipactor threshold results obtained for an aluminum WR-75 symmetric E-plane rectangular waveguide transformer, considering three configurations of the waveguide top and bottom walls: only metal, metal-dielectric, and only dielectric. The SEY properties of the different materials employed in this experiment have been measured and used in the numerical simulations. For this structure, the variation of the multipactor RF V_{th} has been theoretically analyzed (with and without dielectric material), and compared with multipaction measurements, demonstrating an excellent agreement between the theoretical and the experimental data. Both numerical and experimental results show the rise of the multipactor RF V_{th} at a given empty gap waveguide value when adding the dielectric material.

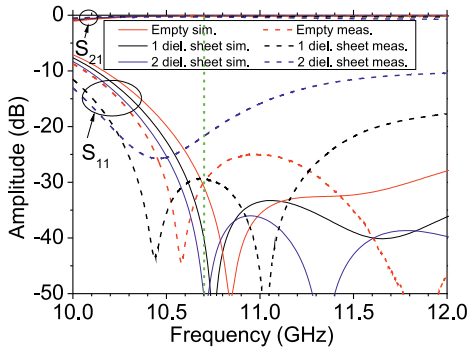

Fig. 5. Electrical response of the symmetric E-plane waveguide transformer.

Acknowledgment

This work was supported by the Agencia Estatal de Investigación (AEI) and by the Unión Europea through the Fondo Europeo de Desarrollo Regional – FEDER -– "Una manera de hacer Europa" (AEI/FEDER, UE), under the Research Projects TEC2016-75934-C4-2-R and TEC2016-75934-C4-1-R.

References

[1] J. Vaughan, "Multipactor," *IEEE Trans. Electron Devices*, Vol. 35, No. 7, pp. 1172–1180, Jul. 1988.

[2] V. E. Semenov, E. I. Rakova, D. Anderson, M. Lisak, and J. Puech, "Multipactor in rectangular waveguides," *Phys. Plasmas*, Vol. 14, No. 3, pp. 033501-1–033501-8, 2007.

[3] C. Vicente, M. Mattes, D. Wolk, B. Mottet, H. L. Hartnagel, J. R. Mosig, and D. Raboso, "Multipactor breakdown prediction in rectangular waveguide based components," *2005 IEEE MTT-S International Microwave Symposium Digest,* Long Beach, CA, USA, Jun. 2005, pp. 1055–1058.

[4] E. Chojnacki, "Simulation of a multipactor-inhibited waveguide geometry," *Physical Review Special Topics - Accelerators and Beams*, Vol. 3, p. 032001, Mar. 2000.

[5] A. M. Pérez, V. E. Boria, B. Gimeno, S. Anza, C. Vicente, and J. Gil, "Multipactor analysis in circular waveguides," *J. Electromagn. Waves Appl.*, Vol. 23, No. 11/12, pp. 1575–1583, 2009.

[6] A. Frotanpour, B. Gimeno, and S. Esfandiarpour, "Multipactor in dualmode elliptical waveguide," *31st International Review of Progress in Applied Computational Electromagnetics (ACES),* Williamsburg, VA, USA, May 2015.

[7] A. M. Pérez, C. Tienda, C. Vicente, S. Anza, J. Gil, B. Gimeno, V. E. Boria, and D. Raboso, "Prediction of multipactor breakdown thresholds in coaxial transmission lines for traveling, standing, and mixed waves," *IEEE Trans. Plasma Sci.*, Vol. 37, No. 10, pp. 2031–2040, Oct. 2009.

[8] D. González-Iglesias, O. Monerris, B. Gimeno, E. Díaz, V. E. Boria, and P. Martín-Iglesias, "Multipactor RF breakdown in coaxial transmission lines with digitally modulated signals," *IEEE Trans. Electron Devices*, Vol. 63, No. 10, pp. 4096–4103, Oct. 2016.

[9] G. Torregrosa, A. Coves, C. P. Vicente, A. M. Pérez, B. Gimeno, and V. E. Boria, "Time evolution of an electron discharge in a parallel-plate dielectric-loaded waveguide," *IEEE Electron Device Lett.*, Vol. 27, No. 7, pp. 629–631, Jul. 2006.

[10] A. Coves, G. Torregrosa-Penalva, C. P. Vicente, A. M. Pérez, B. Gimeno, and V. E. Boria, "Time evolution of an electron discharge in a parallel-plate dielectric-loaded waveguide," *IEEE Trans. Electron Devices*, Vol. 55, No. 9, pp. 2505–2511, Sep. 2008.

[11] E. Sorolla, M. Belhaj, J. Sombrin, and J. Puech, "New multipactor dynamics in presence of dielectrics," *IEEE Trans. Plasma Sci.*, Vol. 24, No. 10, p. 103508, 2017.

[12] G. Torregrosa-Penalva, A. Coves, B. Gimeno, I. Montero, C. Vicente, and V. E. Boria, "Multipactor susceptibility charts of a parallel-plate dielectric-loaded waveguide," *IEEE Trans. Electron Devices*, Vol. 57, No. 5, pp. 1160–1166, May. 2010.

[13] A. Berenguer, A. Coves, F. Mesa, E. Bronchalo, and B. Gimeno, "Analysis of multipactor effect in a partially dielectric-loaded rectangular waveguide," *IEEE Trans. Plasma Science*, Vol. 47, No. 1, pp. 259–265, Jan. 2019.

[14] *https://www.chemours.com/.*

[15] K. Nishimura, T. Itotani, and K. Ohya, “Influence of surface roughness on secondary electron emission and electron backscattering from metal surface,” *Jpn. J. Appl. Phys*, Vol. 33, No. 8, pp. 4727–4734, Aug. 1994.
[16] E. Bronchalo, A. Coves, B. Gimeno, I. Montero, L. Galán, V. E. Boria. L. Mercadé, and Esteban Sanchís, “Secondary electron emission of Pt: experimental study and comparison with models in the multipactor energy range,” *IEEE Trans. Electron Devices*, Vol. 63, No. 8, pp. 3270–3277, Aug. 2016.
[17] *https://www.val-space.com/.*

Analysis of Multipactor Effect in a Partially Dielectric-Loaded Rectangular Waveguide

Andrés Berenguer, Ángela Coves, *Member, IEEE,* Francisco Mesa, *Fellow,* Enrique Bronchalo, and Benito Gimeno, *Member, IEEE*

***Abstract*—This work presents a study of the multipactor effect in a partially dielectric-loaded rectangular waveguide. To obtain the simulations presented in this paper, a detailed analysis of the dynamics of the electron inside this waveguide has been performed, taking into account the RF electromagnetic fields propagating in the waveguide and the DC electric field that appears because of the charging of the dielectric layer. This electrostatic field is obtained by computing the electric potential produced by an arbitrary charge distribution on the dielectric layer in a dielectric-loaded waveguide. The electron trajectory is then found by numerically solving the equations of motion. The results obtained show that multipactor discharges do turn off by themselves under certain circumstances when they occur in such dielectric-loaded waveguide.**

***Index Terms*—multipactor, waveguide, secondary emission.**

I. Introduction

MULTIPACTOR is a high-power resonant electron discharge frequently observed in microwave and millimeterwave subsystems operating under vacuum conditions [1] present in a wide range of different scenarios, such as passive components of satellite communication payloads, traveling-wave tubes or particle accelerators. In an ultra-high vacuum environment, free electrons inside a microwave device are accelerated by the radio frequency (RF) electromagnetic fields, impacting against its metallic walls. If the electron impact energy is high enough, one or more secondary electrons might be released from the surface. When some resonance conditions are satisfied, secondary electrons get synchronized with the RF fields, and the electron population inside the device grows exponentially leading to a multipactor discharge. This multipactor discharge has some negative effects that degrade the device performance: increase of signal noise and reflected power, heating of the device walls, outgassing, detuning of resonant cavities, and even the partial or total destruction of the component.

Multipactor research lines are aimed to study and characterize the phenomenon to predict the conditions for its appearance [2], [3]. Some RF devices, such as filters, multiplexers, and RF satellite payloads, include dielectric materials commonly employed as resonators and supporting elements. In [4] it is presented a review of multipactor discharge on metals and dielectric windows that takes into account the surface materials, and the effects of space charge and cavity loading. The multipactor effect including the presence of dielectric materials in single-surface multipactor regime has been widely investigated in the context of particle accelerators; for instance, in ceramic RF windows [5], [6] and in alumina-based dielectric-loaded accelerating structures [7]. In contrast, very few contributions can be found about multipactor breakdown on dielectrics in the scenario of RF systems for space applications [8]–[10], and mostly under the parallel-plate waveguide approximation. In [11], [12] the effective electron model (EEM) has been sucesfully used for simulations of multipaction experiments in coaxial transmission lines considering the presence of external magnetic static fields, demonstrating the validity of this method in complex scenarios. Multipactor inside an empty rectangular waveguide has also been studied in [13], [14], where conventional resonance theory gives correct predictions for the multipactor threshold if the height of the waveguide is very small and first-order resonance multipactor dominates. When the waveguide height exceeds a certain critical value, which depends on the waveguide width, an accurate prediction of the multipactor threshold requires considering the RF fields inside the waveguide without approximations. Therefore, there is a need to accurately predict the electron discharge on devices involving partially dielectric-loaded rectangular waveguides, which are of more practical interest for satellite technology. The main aim of this investigation is to extend the results of previous works [8]–[10], where an EEM was succesfully applied to study the multipactor in a parallel-plate dielectric-loaded waveguide, to the analysis of multipactor effect in a partially dielectric-loaded rectangular waveguide.

In Section II, the theoretical model employed for the simulations is discussed. In Sec. III the multipactor prediction results of an empty rectangular waveguide are analyzed and compared with results from the technical literature for validation purposes. Then, the susceptibility chart of a partially dielectric-loaded rectangular waveguide is obtained with the developed model, and the time evolution of a discharge in this waveguide is studied and discussed. Finally Sec. IV outlines the main conclusions of the present work.

II. Theory

A. Computation of RF and DC fields in a partially dielectric-loaded waveguide

Figure 1 shows the scheme of a partially dielectric-loaded rectangular waveguide of width a and height b, and whose

Andrés Berenguer, Á. Coves and E. Bronchalo are with the Department of Communications Engineering, Universidad Miguel Hernández de Elche, Elche, Spain (e-mail: angela.coves@umh.es).

Francisco Mesa is with the Microwaves Group, Department of Applied Physics 1, ETS de Ingeniería Informática, Universidad de Sevilla, Seville, Spain.

B. Gimeno is with the Department of Applied Physics and Electromagnetism-ICMUV, Universidad de Valencia, Burjasot, Spain.

dielectric material has relative permittivity ϵ_r. In the problem under study, the dielectric slab of thickness h and width a is placed over the bottom waveguide wall, being d the empty waveguide heigth where the effective electron travels (see Fig. 1). The RF electromagnetic field is assumed to propagate along the positive direction of the z-axis. For the sake of simplicity, the waveguide is supposed to be infinite along the z direction, and a time-harmonic dependence of the type $\mathrm{e}^{\mathrm{j}\omega t}$ is implicitly assumed, with $f = \omega/2\pi$ being the frequency and t the time measured in the laboratory reference system. To analyze the multipactor evolution in this waveguide, a multipactor simulation code based on the Monte-Carlo method has been developed. The software code, similar to the one described in [8], [9], employs the single EEM [15]. This assumption avoids the consideration of space-charge effects, what is a strong simplification. Space-charge effects are often neglected in the analysis of the first stages of the multipactor discharge [13], [14], but they are doubtless important at high electron populations, when the discharge is fully developed. Simulation results of some published works [16], [17] indicate an important role of space-charge in the evolution of the multipactor process to a saturation stage. In this work, however, we are mainly interested in studying the influence of dielectric charging in the multipactor process. The inclusion of space-charge effects, although providing a more realistic description of the global process, would increase the computational burden very much, as the DC field due to dielectric charging has to be evaluated in every effective electron position. Besides, the interpretation of simulation results would become difficult, as dielectric charging and space-charge can both lead to a repulsion of the freshly emitted secondary electrons back to the surface.

The effective electron at $\mathbf{r} = (x, y, z)$ can move in the air region of height d of the rectangular waveguide. The electromagnetic fields $\mathbf{E}_{\mathrm{RF}}$ and $\mathbf{H}_{\mathrm{RF}}$ acting on the effective electron correspond to the modes of the partially dielectric-loaded rectangular waveguide (Fig. 1), which are hybrid modes of TM^y and TE^y kinds [18]. We have restricted our study to the monomode regime, where only the fundamental mode, TM^y_{10}, propagates in the waveguide. The instantaneous field vectors interacting with the effective electron are given by

$$\mathbf{E}_{\mathrm{RF}}(x, y, z, t) = E_0 \Re\Big(\mathbf{e}(x, y)\, \mathrm{e}^{\mathrm{j}(\omega t - \beta z + \varphi_0)}\Big) \tag{1a}$$

$$\mathbf{H}_{\mathrm{RF}}(x, y, z, t) = H_0 \Re\Big(\mathbf{h}(x, y)\, \mathrm{e}^{\mathrm{j}(\omega t - \beta z + \varphi_0)}\Big) \tag{1b}$$

where φ_0 is the initial phase and E_0, H_0 constants related to the transmitted power in the waveguide. The modal fields $\mathbf{e}(x, y)$ and $\mathbf{h}(x, y)$ and the propagation constant β of the TM^y_{10} mode can be found in [18], [19]. These expressions can be directly extended if higher order modes must be taken into account (i.e., in waveguide discontinuities) by using the mode-matching technique.

The key for understanding the mechanism of a multipactor discharge is to study the behavior of the electrons within the waveguide, which are accelerated by the aforementioned electromagnetic fields $\mathbf{E}_{\mathrm{RF}}$ and $\mathbf{H}_{\mathrm{RF}}$. In this way, sooner or later, these fields will make an electron impact with any surface

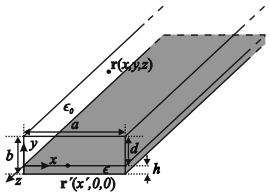

Fig. 1. Geometry and dimensions of the problem under investigation.

of the rectangular waveguide, which can result in the emission or absorption of secondary electrons. If the impacts occur on the dielectric surface, unlike the case of impacts on the metallic walls, the secondary electrons emitted by the dielectric give rise to positive charges at the impact positions on the dielectric surface, while the electrons absorbed in the dielectric layer will generate negative charges in it. These charges, which are located on the dielectric surface at positions $\mathbf{r}' = (x', 0, z')$, give rise to an electrostatic field $\mathbf{E}_{\mathrm{DC}}$, which has to be added to the RF fields to obtain accurately the trajectory of the electrons inside the waveguide. In order to determine the electrostatic field, $\mathbf{E}_{\mathrm{DC}}(x, y, z) = -\nabla\phi(x, y, z)$, generated by the charges on the dielectric, the potential $\phi(x, y, z)$ inside the waveguide has to be first calculated. Using superposition, the potential in the waveguide due to the set of charges Q_i on the dielectric surface can be obtained by adding the individual contribution of each charge:

$$\phi(x, y, z) = \sum_i G(x - x'_i, y, |z - z'_i|) Q_i(x'_i, 0, z'_i) \tag{2}$$

where $G(x, y, z)$ is the electrostatic potential due to a unit point charge, that is, the Green's function for this problem.

The above Green's function, $G(x, y, z)$, is the solution to the following Laplace's equation [20], [21]:

$$\nabla \cdot [\epsilon_r(y) \nabla G(x, y, z)] = -\frac{1}{\epsilon_0} \delta(x - x') \delta(y) \delta(z) \tag{3}$$

where ϵ_0 is the free-space dielectric permittivity and the position of the unit charge is taken at $(x', 0, 0)$ for convenience. Both the geometric characteristics and the linear nature of the problem under consideration makes that the Dirac delta functions can be expressed as [21]

$$\delta(x - x') = \frac{2}{a} \sum_{n=1}^{\infty} \sin(k_{xn} x) \sin(k_{xn} x') \tag{4}$$

$$\delta(z) = \frac{1}{2\pi} \int_{-\infty}^{\infty} \mathrm{e}^{-\mathrm{j}k_z z} \mathrm{d}k_z \tag{5}$$

where $k_{xn} = n\pi/a$ and k_z is the spectral Fourier variable along the longitudinal direction z. The above expressions come from the fact that the eigenfunctions of the differential operator are sinusoidal functions along x-axis and complex exponential functions along the z-axis, respectively. This is equivalent to

apply the discrete sine transform (DST) along the x-axis and the integral transform along the z-axis; namely,

$$G = \frac{1}{\pi a}\int_{-\infty}^{\infty} \mathrm{d}k_z\, \mathrm{e}^{-\mathrm{j}k_z z} \sum_{n=1}^{\infty} \sin(k_{xn}x)\sin(k_{xn}x')\,\widetilde{G} \quad (6)$$

$$\widetilde{G} = \int_{-\infty}^{\infty} \mathrm{d}z\, \mathrm{e}^{\mathrm{j}k_z z} \sum_{n=1}^{\infty} \sin(k_{xn}x)\sin(k_{xn}x')\,G \quad (7)$$

where $G = G(x, x', y, z)$ and $\widetilde{G} = \widetilde{G}(k_{xn}, k_z; y)$.

According to the above considerations, Eq. (3) can be expressed as the following ordinary differential equation for the spectral Green's function $\widetilde{G}$:

$$\left\{\frac{\mathrm{d}}{\mathrm{d}y}\epsilon_r(y)\frac{\mathrm{d}}{\mathrm{d}y} - k_t^2\right\}\widetilde{G} = -\frac{\delta(y)}{\epsilon_0} \quad (8a)$$

$$\widetilde{G}(y = -h) = 0 \quad (8b)$$

$$\widetilde{G}(y = d) = 0 \quad (8c)$$

where $k_t^2 = k_{xn}^2 + k_z^2$. Solving (8), the following expression for $\widetilde{G}$ is obtained in the air region $y \geq 0$:

$$\widetilde{G}(k_{xn}, k_z; y) = \frac{\sinh[k_t(d-y)]}{\epsilon_0 k_t[\epsilon_r \coth(k_t h) + \coth(k_t d)]\sinh(k_t d)}\,. \quad (9)$$

The Green's function in the spatial domain, G, is achieved by replacing (9) into (6) to give

$$G(x, x', y, z) = \frac{2}{\epsilon_0 \pi a}\sum_{n=1}^{\infty}\sin(k_{xn}x)\sin(k_{xn}x') \times \int_0^{\infty} \frac{\sinh[k_t(d-y)]\cos(k_z z)}{k_t[\epsilon_r \coth(k_t h) + \coth(k_t d)]\sinh(k_t d)}\,\mathrm{d}k_z\,. \quad (10)$$

In (10), if the point charge is placed at $z' \neq 0$, z must be replaced by $(z - z')$. Here it is worth noting that very efficient numerical summation and integration techniques have to be employed to compute the Green's function with sufficient accuracy and tolerable CPU times [22].

Once the Green's function has been calculated, the $\mathbf{E}_{\mathrm{DC}}$ field is obtained by numerical differentiation of (2) by means of the central difference technique.

B. Multipactor evolution in the partially dielectric-loaded waveguide

Once the RF and DC fields are known at any instant t, the electron dynamics inside the waveguide can be computed, which is governed by the Lorentz force and related to its linear momentum,

$$\mathbf{F}_L = q(\mathbf{E} + \mathbf{v}\times\mathbf{B}) = \frac{\mathrm{d}\mathbf{p}}{\mathrm{d}t} \quad (11)$$

where $q = -e$ is the electron charge, $\mathbf{E}$ and $\mathbf{B} = \mu_0\mathbf{H}$ are the total electric and magnetic fields (both RF and DC contributions) interacting with the electron, μ_0 is the free-space magnetic permeability, and $\mathbf{v}$ is the velocity vector of the electron. The linear relativistic momentum is defined as

$$\mathbf{p} = m_0\gamma\mathbf{v} \quad (12)$$

where m_0 is the electron rest mass, $\gamma = 1/\sqrt{1-(v/c)^2}$ the Lorentz factor, v the magnitude of the velocity vector, and $c = 1/\sqrt{\mu_0\epsilon_0}$ the speed of light in vacuum. Although the relativistic correction in this equation can be discarded for the typical power ranges of most space waveguide devices, it must be considered when high velocities are reached ($v/c \geq 0.1$), as in high-power multipactor simulations. Expanding (11), the following differential equation is obtained:

$$-\mathbf{E} - \mathbf{v}\times\mathbf{B} = M\gamma\mathbf{a} + \frac{M}{c^2}\gamma^3(\mathbf{v}\cdot\mathbf{a})\mathbf{v} \quad (13)$$

where $\mathbf{a}$ is the acceleration vector and $M = m_0/e$. The differential equation to be solved becomes

$$\ddot{\mathbf{r}} = \frac{-\dot{\mathbf{r}}\times\mathbf{B} - \mathbf{E} + \dot{\mathbf{r}}\cdot(\dot{\mathbf{r}}\cdot\mathbf{E})/c^2}{M\gamma} \quad (14)$$

The electron trajectory is found by numerically solving the above equations of motion. For that purpose, a velocity-Verlet algorithm [23] has been used, which assures sufficient accuracy and good efficiency provided the time step is small enough. Regarding this last point, in order to improve the accuracy and efficiency of the simulation, the following adaptive time step has been applied in the proximity of the waveguide walls, depending on the electron position:

$$\Delta t = \frac{\Delta t_0}{1 + \xi\left(\dfrac{x - a/2}{a/2}\right)^2 + \xi\left(\dfrac{y - d/2}{d/2}\right)^2} \quad (15)$$

where Δt_0 is the initial reference time step, ξ is a constant value (in this case a value of 4.0 has been chosen), and x and y are the coordinates of the electron position.

As mentioned above, the computed electrons trajectories may lead to an eventual impact with a surface. Each collision can result in the emission or absorption of secondary electrons. A relevant growth in the electron density can develope if the electrons hit the walls with the appropriate energy and at suitable instants. The number of electrons emitted or absorbed after each impact is determined by the value of the Secondary Electron Yield (SEY) parameter δ ($\delta > 1$ if secondary electrons are emitted, and $\delta < 1$ if they are absorbed). The SEY is modeled by a modification of the Vaughan's model [24] that includes the effect of reflected electrons for low impact energies of primary electrons, which has to be accounted for to obtain accurate results [25], [26] in agreement with experimental data obtained in [27], [28]. The SEY properties for surface materials can be defined by the following parameters: the primary electron impact kinetic energies which yield $\delta = 1$, W_1, and W_2; the impact energy $W_{\max}$ necessary for a primary electron to yield $\delta = \delta_{\max}$, which is the maximum value of the SEY function; and the value of the primary electron impact energy $W_0(\delta = 0)$ that limits the region of elastic collisions.

When a multipactor discharge evolves in the partially dielectric-loaded waveguide under study, the DC field distribution has to be updated after each electron impacts on the dielectric surface. However, tracking the evolution of all the electrons involved in the multipactor discharge would suppose a big computational cost. Thus, we have made use of an EEM, but considering both the spread in secondary emission energy and the angle of the secondary electrons after each impact on

TABLE I
SECONDARY ELECTRON EMISSION YIELD PROPERTIES OF DIFFERENT MATERIALS [31], [32]

Material	$\mathbf{W_{max}}$(eV)	$\mathbf{W_1}$(eV)	$\mathbf{W_2}$(eV)	$\mathbf{W_0}$(eV)	$\delta_{\mathbf{max}}$
Niobium	200.0	33	1500	–	1.6
Silver	165.0	30	5000	15.99	2.22
Teflon	271.7	27	5000	6.81	2.47

the waveguide walls. This assumption has proved to account properly for the charging of the dielectric material, given that the discharging time for dielectrics is much higher than the typical time for a multipactor discharge. Thus, in the EEM assumed in this study, after the effective electron impacts at time t with any surface, $N_i(t)$ is modified according to the δ value provided by the SEY function as follows:

$$N_i(t + \Delta t) = \delta N_i(t) \tag{16}$$

where $N_i(t)$ represents the population of the ee inside the waveguide at the instant t, and Δt is the time step used in the simulations.

The secondary electron departure kinetic energy E_s after each electron impact is assumed to fit the following probability density function [29]:

$$\frac{\mathrm{d}p(E_s)}{\mathrm{d}E_s} = C\,\exp\left[-\frac{\ln^2(E_s/E_m)}{2\tau^2}\right] \tag{17}$$

where C is a normalization constant, the parameter τ (typical values 0.7-0.8) determines the width of the distribution and E_m (typical values 3-4 eV) is the energy of the maximum of the spectrum . Finally, the secondary electrons after inelastic impacts are emitted following a cosine distribution of the polar angle.

III. NUMERICAL RESULTS AND DISCUSSION

A in-house simulation computer-aided design (CAD) tool based on the Monte-Carlo method described in the last section has been developed to analyze the multipactor effect in partially dielectric-loaded rectangular waveguides. The first problem analyzed consists of an empty rectangular waveguide previously studied in [14], whose multipactor prediction results have been used for validation purposes. The rectangular waveguide has dimensions $a = 43.2\,\mathrm{cm}$ and $b = 10.2\,\mathrm{cm}$, and is excited by a time-harmonic signal at $f = 500\,\mathrm{MHz}$. The material of the waveguide walls is niobium, whose SEY properties are given in Table I and can be expressed with the simple model proposed in [30]. In the algorithm of the simulator used in [14], for each RF power considered in the waveguide, the initial electron is launched at $x = a/2$, and the simulation is run 42 times, corresponding to 42 equidistant phases of the RF field. The mean value of the final population of electrons after 20 impacts of the ee against the walls is calculated using all the 42 simulations. Also, the secondary electrons generated after every collision are launched with an energy of 2 eV normal to the impacting surface. The maximum simulation lifetime of each ee is $t_{\max} = 1000$ RF cycles, and the simulation is stopped if the impact energy is lower than

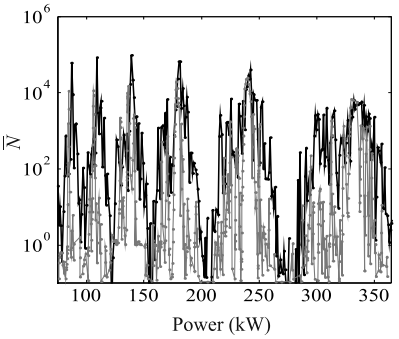

Fig. 2. Comparison with [14] of the mean value of N over all launch phases in a rectangular waveguide ($a = 43.1\,\mathrm{cm}$ and $b = 10.2\,\mathrm{cm}$) driven at $f = 500\,\mathrm{MHz}$ with a maximum of 20 impacts from a single initial launch location on the midline of the empty rectangular waveguide.

0.1 eV or if the accumulated population of electrons is under 10^{-3}. To model the same simulation conditions, our CAD tool has been adapted accordingly. In Fig. 2, the results of the mean population of electrons, $\overline{N}$, computed with our code (black lines) are compared with the curves presented in [14] (gray lines). In this figure we can see some high-risk multipactor power regions. Both curves show a good agreement in the shape and location of these multipactor windows.

Once the model has been validated for an empty waveguide, next we analyze the multipactor effect in a partially dielectric-loaded rectangular waveguide. The selected waveguide configuration for the multipactor analysis is a non-standard silver-plated rectangular waveguide of width $a = 19.05\,\mathrm{mm}$ and heigth $b = 0.4\,\mathrm{mm}$, in which a thin dielectric layer has been placed over the bottom surface of the waveguide. A realistic dielectric material has been chosen as teflon (DuPont Teflon FEP Fluoroplastic Film Type), which is a dielectric film commonly used in space applications, of thickness $h = 0.025\,\mathrm{mm}$ and $\epsilon_r = 2.1$; thus $d = b - h = 0.375$ mm. Standard values for the SEY parameters of silver [31] are given in Table I, and SEY parameters of teflon have been measured at the ESA-VSC High Power Space Materials Laboratory (Valencia, Spain) [32]. Firstly, a study of the susceptibility chart of this waveguide has been performed. Since it is a partially dielectric-loaded rectangular waveguide, the factor $f \times d$ is plotted in the horizontal axis of the susceptibility chart. In the vertical axis it is plotted an effective voltage, V_{eff}, which has been calculated numerically as the line integral of the E_y component of the electric field (evaluated at the center of the waveguide $x = a/2$) from $y_1 = 0$ to $y_2 = d$. To obtain this susceptibility chart for each V_{eff} and $f \times d$ pair, the simulation is run 72 times, corresponding to 72 equidistant initial phases of the RF field separated 5 degrees. In each run, an initial single ee is launched at $x = a/2$ and $z = 0$ and at a random position y_0 in the y axis between $y = 0$ and $y = d$. The initial electron is launched with a departure kinetic energy given by the probability density function shown in (17) and following a cosine distribution of the polar angle. Each simulation was stopped after 100 RF cycles. In the empty waveguide, the arithmetic mean of the final population of electrons after 100 RF cycles is calculated using all the

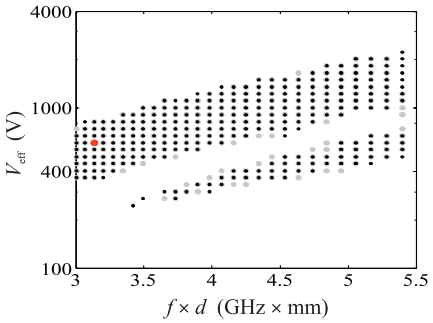

Fig. 3. Comparison of the susceptibility chart of a rectangular waveguide partially filled with teflon (black points) with that of its equivalent empty waveguide (gray points). An operating point corresponding to $f \times d = 3.13\,\text{GHz·mm}$ and $V_{\rm eff} = 608\,\text{V}$ is highlighted in red.

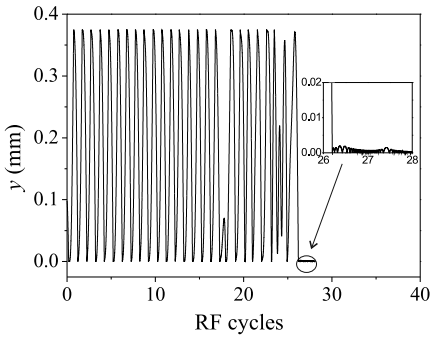

Fig. 4. Trajectory (y coordinate) of the ee in the air gap of the rectangular waveguide partially filled with teflon as a function of the RF cycle.

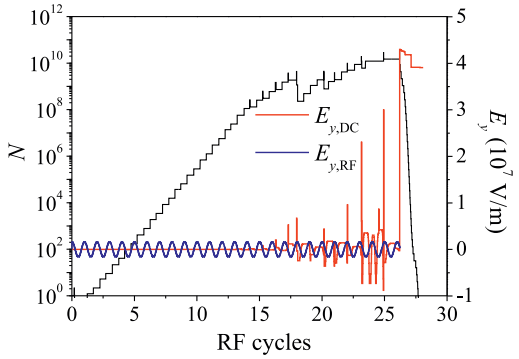

Fig. 5. Time evolution of the total number of electrons N (black line), $E_{y,\rm RF}$ (blue line) and $E_{y,\rm DC}$ at the electron position (red line).

72 simulations. If this mean value is greater than 1, then the multipactor discharge is assumed to have occurred. However, in a partially dielectric-loaded waveguide, it has been shown in previous works [8]–[10] that the emission or absorption of electrons by the dielectric surface gives rise to an increasing DC field in the waveguide, which eventually turns off the discharge. Thus, in this case, a minimum mean value of the magnitude of $E_{\rm DC}$ field in the waveguide after 100 RF cycles is used as the criterion to assume that a multipactor discharge has occurred at a given operating point.

Figure 3 shows the computed susceptibility chart of the rectangular waveguide partially filled with teflon (black points). The lowest $f \times d$ value is above the cutoff frequency of the fundamental mode in this waveguide. In this figure, the susceptibility chart of the equivalent empty waveguide with the same vertical air gap is also represented with gray points for comparison. It can be checked that both the empty and the partially dielectric-loaded waveguide with the same vertical air gap show similar multipactor susceptibility charts, given that the SEY properties of silver and teflon are similar. This susceptibility chart is not generally applicable to any rectangular waveguide with an air gap d, given that the electromagnetic field distribution depends on the geometry and dimensions of the dielectric layer with respect to the waveguide dimensions, and also on its relative permittivity.

From the results previously shown, and with the purpose of having a better understanding of the dynamics of the electron inside the partially dielectric-loaded waveguide, a point within the multipactor region has been chosen (highlighted in red in Fig. 3), corresponding to $V_{\rm eff} = 608\,\text{V}$ and $f \times d = 3.13\,\text{GHz·mm}$. In this case, the evolution of the multipactor discharge in the partially dielectric-loaded waveguide under study has been analyzed as a function of the time normalized to the RF period. For this simulation, the electron is launched with an initial phase of the RF field $\varphi_0 = 0^{\rm o}$. Simulations assuming different initial phases have been performed, and similar results were obtained. The obtained simulation is shown in Fig. 4, where it is plotted the y-coordinate followed by the ee within the waveguide as a function of the normalized time. In the selected multipactor regime, which is inside the multipactor region, the electron initially collides with the top metallic and bottom dielectric surface consecutively in what seems to be a first-order multipactor process during the first 17 RF cycles, remaining in the vicinity of $x = a/2$ and $z = 0$ —given that the electron has nearly no acceleration in such directions. As shown in Fig. 5, in the first cycles the total number of electrons N (black solid line) follows an exponential growth. This progressive growing of N makes that the number of charges appearing on the dielectric surface increases, number which is proportional to the emitted or absorbed electrons in each impact, as seen in Fig. 6 (positive charges are represented with red circles, while negative charges are represented with blue circles; the circles' size is proportional to the charge magnitude in log scale). Such charges on the dielectric interface give rise to the appearance of an electrostatic field in the empty gap during the time between impacts. Once the population of electrons reaches a significant number ($N \approx 10^9$ in the conditions under study), the y-component of the DC field, $E_{y,\rm DC}$ (which has been plotted in Fig. 5 with red line at the positions (x, y, z) where the effective electron is located in the displayed instants in this figure) becomes comparable to $E_{y,\rm RF}$, and the effective electron is unable to keep up with its previous multipactor synchronization. From this moment on, the DC field makes that, in some impacts, the electrons collide with the top metallic or bottom dielectric surface much sooner or later than the instants when the RF electric field changes its sign, which

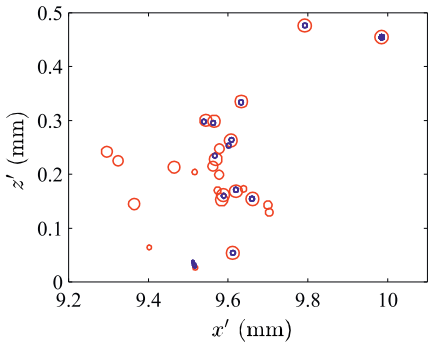

Fig. 6. Distribution of normalized charges $\overline{Q}_i = Q_i/e$ appearing on the dielectric surface.

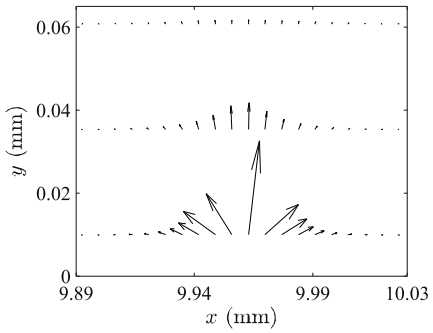

Fig. 7. Transverse distribution of the DC electric field in the proximity of the main charge point in the waveguide air region at RF cycle 26.2, at $z = 0.45$ mm.

implies low impact energy collisions so that electrons are absorbed in such impacts. In collisions at the dielectric surface, the absorption or emission of electrons yield the appearance of growing charges on the dielectric layer, contributing to a higher DC field acting on the waveguide. The distribution of this high DC field in the proximity of the main charge point in the waveguide air region is shown in Fig. 7 at RF cycle 26.2 in the plane $z = 0.45$ mm (corresponding to the z position of the electron at this instant). The action of this field may result in the appearance of a single-surface multipactor regime in the dielectric surface (see the y position of the electron in the figure inset in Fig. 4 from RF cycle 26.2), with successive low impact energy collisions, which eventually leads to the turning off of the discharge itself (as can be appreciated in Fig. 5 from RF cycle 26.2 on). From this instant, the DC field distribution in the waveguide remains nearly constant, given that N drops very quickly. The final value of the y-component of the DC field accounts for the balance between the emitted and absorbed electrons by the dielectric surface in the whole process. Then, although the final population of electrons after RF cycle 100 is 0, the remaining high DC field in the waveguide indicates that a multipactor discharge has taken place in the waveguide in this simulation. It is worth mentioning that the observed turning off of the discharge observed in the last stages of the multipactor evolution in this waveguide has been speeded up due to the use of the EEM, although this does not change qualitatively the dynamics of the discharge under these conditions.

IV. Conclusion

A study of the multipactor effect in a partially dielectric-loaded rectangular waveguide has been carried out. In this study we have considered the RF electromagnetic fields (obtained with a very efficient vectorial modal method) as well as the DC field caused by the appearance of a charge distribution in the dielectric layer. The solution of the electrostatic problem has required the use of different numerical integration techniques and interpolation methods. The electron trajectory has been numerically solved by using a velocity-Verlet algorithm, providing sufficient accuracy and good efficiency. As a first example, the multipactor prediction results of an empty rectangular waveguide have been obtained for validation purposes. Secondly, the susceptibility chart of a partially dielectric-loaded rectangular waveguide has been computed, and the time evolution of a discharge in this waveguide has been studied and discussed. The performed simulations reveal that multipactor discharges in this type of dielectric-loaded waveguides turn off by themselves due to the electrostatic field associated to the dielectric surface charges that evolves with the multipactor process.

Acknowledgment

This work was supported by the Agencia Estatal de Investigación (AEI) and by the Unión Europea through the Fondo Europeo de Desarrollo Regional – FEDER -– "Una manera de hacer Europa" (AEI/FEDER, UE), under the Research Projects TEC2016-75934-C4-2-R and TEC2017-84724-P.

References

[1] J. Vaughan, "Multipactor," *IEEE Trans. Electron Devices*, Vol. 35, No. 7, pp. 1172–1180, Jul. 1988, DOI: 10.1109/16.3387.

[2] V. E. Semenov, E. I. Rakova, A. G. Sazontov, I. M. Nefedov, V. I. Pozdnyakova, I. A. Shereshevskii, D. Anderson, M. Lisak, and J. Puech, "Simulations of multipactor thresholds in shielded microstrip lines," *J. Phys. D, Appl. Phys.*, Vol. 42, No. 20, pp. 205204-1–205204-7, Sep. 2009, DOI: 10.1109/TMAG.2017.2658671.

[3] A. M. Pérez, C. Tienda, C. Vicente, S. Anza, J. Gil, B. Gimeno, V. E. Boria, and D. Raboso, "Prediction of multipactor breakdown thresholds in coaxial transmission lines for traveling, standing, and mixed waves," *IEEE Trans. Plasma Sci.*, Vol. 37, Vol. 10, pp. 2031–2040, Oct. 2009, DOI: 10.1109/TPS.2009.2028428.

[4] R. A. Kishek, "Multipactor discharge on metals and dielectrics: Historical review and recent theories," *Phys. Plasmas*, Vol. 5, No. 5, pp. 2120–2126, May 1998, DOI: 10.1063/1.872883.

[5] L. K. Ang, Y. Y. Lau, R. A. Kishek, and M. Gilgenbach, "Power deposited on a dielectric by multipactor," *IEEE Trans. Plasma Sci.*, Vol. 26, No. 3, pp. 290–295, Jun. 1998, DOI: 10.1109/27.700756.

[6] A. Valfells, L. K. Ang, Y. Y. Lau, and R. M. Gilgenbach, "Effects of an external magnetic field, and of oblique radio-frequency electric fields on multipactor discharge on a dielectric," *Phys. Plasmas*, Vol. 7, No. 2, pp. 750–757, Feb. 2000, DOI: 10.1063/1.873861.

[7] J. Power, W. Gai, S. H. Gold, A. K. Kinkead, R. Konecny, C. Jing, W. Liu, and Z. Yusof, "Observation of multipactor in an alumina-based dielectric-loaded accelerating structure," *Phys. Rev. Lett.*, Vol. 92, No. 16, pp. 164801-1–164801-4, Apr. 2004, DOI: 10.1103/PhysRevLett.92.164801.

[8] G. Torregrosa, A. Coves, C. P. Vicente, A. M. Pérez, B. Gimeno, and V. E. Boria, "Time evolution of an electron discharge in a parallel-plate dielectric-loaded waveguide," *IEEE Electron Device Lett.*, Vol. 27, No. 7, pp. 629–631, Jul. 2006, DOI: 10.1109/LED.2006.877284.

[9] A. Coves, G. Torregrosa-Penalva, C. P. Vicente, A. M. Pérez, B. Gimeno, and V. E. Boria, "Multipactor discharges in parallel-plate dielectric-loaded waveguides including space-charge effects," *IEEE Trans. Electron Devices*, Vol. 55, No. 9, pp. 2505–2511, Sep. 2008, DOI: 10.1109/TED.2008.927945.

[10] G. Torregrosa-Penalva, A. Coves, B. Gimeno, I. Montero, C. Vicente, and V. E. Boria, "Multipactor susceptibility charts of a parallel-plate dielectric-loaded waveguide," *IEEE Trans. Electron Devices*, Vol. 57, No. 5, pp. 1160–1166, May. 2010, DOI: 10.1109/TED.2010.2043182.

[11] D. González-Iglesias, A. M. Pérez, S. Anza, J. Vague, B. Gimeno, V. E. Boria, D. Raboso, C. Vicente, J. Gil, F. Caspers, and L. Conde, "Multipactor in a coaxial line under the presence of an axial DC magnetic field," *IEEE Electron Device Lett.*, Vol. 33, No. 5, pp. 727–729, May 2012, DOI: 10.1109/LED.2012.2186952.

[12] D. González-Iglesias, A. M. Pérez, S. Anza, J. Vague, B. Gimeno, V. E. Boria, D. Raboso, C. Vicente, J. Gil, F. Caspers, and L. Conde, "Multipactor mitigation in coaxial lines by means of permanent magnets," *IEEE Trans. Electron Devices*, Vol. 61, No. 12, pp. 4224–4231, Dec. 2014, DOI:10.1109/TED.2014.2361172.

[13] V. E. Semenov, E. I. Rakova, D. Anderson, M. Lisak, and J. Puech, "Multipactor in rectangular waveguides," *Phys. Plasmas*, Vol. 14, No. 3, pp. 033501-1–033501-8, Mar. 2007, DOI: 10.1063/1.2480678.

[14] E. Chojnacki, "Simulation of a Multipactor-Inhibited Waveguide Geometry," *Physical Review Special Topics - Accelerators and Beams*, Vol. 3, p. 032001, Mar. 2000, DOI 10.1103/PhysRevSTAB.3.032001.

[15] E. Somersalo, P. Yl-Oijala, D. Proch, and J. Sarvas, "Computational methods for analyzing electron multipacting in RF structures," *Particle Accelerators*, Vol. 95, pp. 107–141, 1998.

[16] M. Buyanova, V. E. Semenov, D. Anderson, M. Lisak, and J. Puech, "Influence of secondary emission yield on the saturation properties of multipactor discharges between two parallel metal plates," *Phys. Plasmas*, Vol. 17, p. 043504, 2010, DOI 10.1063/1.3374430.

[17] C. J. Lingwood, G. Burt, A. C. Dexter, J. D. A. Smith, P. Goudket, and P. H. Stoltz, "Phase space analysis of multipactor saturation in rectangular waveguide," *Phys. Plasmas*, Vol. 19, p. 032106, 2012, DOI 10.1063/1.3692060.

[18] R. F. Harrington, "Time-Harmonic Electromagnetic Fields," *Wiley-IEEE Press*, 2001.

[19] C. A. Balanis, "Advanced Engineering Electromagnetics," *2nd Ed., Wiley*, 2012.

[20] D. J. Griffiths, "Introduction to Electrodynamics," *3rd Ed., Pearson*, 2008.

[21] R. E. Collin, "Field Theory of Guided Waves," *2nd Ed., IEEE Press*, 1990.

[22] A. Berenguer, A. Coves, F. Mesa, E. Bronchalo, B. Gimeno, and V. E. Boria, "Calculation of the Electrostatic Field in a Dielectric-loaded Waveguide Due to an Arbitrary Charge Distribution on the Dielectric Layer," in *Proc. PIERS*, Shanghai, China, pp. 3251–3255, Aug. 2016, DOI: 10.1109/PIERS.2016.7735274.

[23] A. Berenguer, A. Coves, E. Bronchalo, B. Gimeno, and V. E. Boria, "Analysis of multipactor effect in parallel-plate and rectangular waveguides," in *Proc. PIERS*, Prague, Czech Republic, pp. 1564–1568, Jul. 2015, DOI:10.1063/1.2480678.

[24] R. Vaughan, "A New Formula for Secondary Emission Yield," *IEEE Trans. Elec. Devices*, vol. 36, pp. 1963—1967, 1989, DOI: 10.1109/16.34278.

[25] C. Vicente, M. Mattes, D. Wolk, B. Mottet, H. L. Hartnagel, J. R. Mosig, and D. Raboso, "Multipactor breakdown prediction in rectangular waveguide based components," *2005 IEEE MTT-S International Microwave Symposium Digest,*, Long Beach, CA, USA, Jun. 2005, pp. 1055–1058, DOI: 10.1109/MWSYM.2005.1516852.

[26] R. Seviour, "The role of elastic and inelastic electron reflection in multipactor discharges," *IEEE Trans. Electron Devices*, Vol. 52, No. 8, pp. 1927–1930, Aug. 2005, DOI: 10.1109/TED.2005.851854.

[27] R. Cimino, I. R. Collins, M. A. Furman, M. Pivi, F. Ruggiero, G. Rumolo, and F. Zimmermann, "Can Low-Energy Electrons Affect High-Energy Physics Accelerators?," *Phys. Rev. Lett.*, Vol. 93, p. 014801, 2004, DOI: 10.1103/PhysRevLett.93.014801.

[28] E. Bronchalo, A. Coves, B. Gimeno, I. Montero, L. Galań, V. E. Boria. L. Mercadé, and Esteban Sanchís, "Secondary electron emission of Pt: experimental study and comparison with models in the multipactor energy range," *IEEE Trans. Electron Devices*, Vol. 63, No. 8, pp. 3270–3277, Aug. 2016, DOI: 10.1109/TED.2016.2580199.

[29] J. J. Scholtz, D. Dijkkamp, and R.W.A. Schmitz, "Secondary electron emission properties," *Philips J. Res.*, Vol. 50, pp. 375–389, 1996, DOI: 10.1016/S0165-5817(97)84681-5.

[30] R. L. Geng, and H. S. Padamsee, "Exploring multipacting characteristics of a rectangular waveguide," *1999 Particle Accelerator Conference*, New York, 1999, pp. 429–431, DOI: 10.1109/PAC.1999.795724.

[31] "Multipacting design and test," ESTEC Document ECSS-20-01, Apr. 2000.

[32] www.val-space.com.

Andrés Berenguer was born in Elche (Alicante), Spain. He received the Ingeniero de Telecomunicación degree from Universidad Miguel Hernandez de Elche, where he is actually a PhD student. His current research interests are focused on multipactor processes in waveguides.

Ángela Coves (S'04–M'05) received the Licenciado and Doctor degrees in Physics from the Universidad de Valencia, Valencia, Spain. She is an Associate Professor at Universidad Miguel Hernández de Elche. Her research interests are focused on microwave passive components and RF breakdown high-power effects.

Francisco Mesa (M'93–SM'11–F'14) received the Licenciado and Doctor degrees in physics from the Universidad de Sevilla, Seville, Spain. He is a Professor in the Departamento de Física Aplicada 1, Universidad de Sevilla. His research interests include electromagnetic propagation/radiation in planar structures.

Enrique Bronchalo received the Physics degree from the Universidad Complutense de Madrid, and the Ph.D. on Physics from the Universidad de Alcalá. He is an Associate Professor at Universidad Miguel Hernández de Elche. His research is focused on passive microwave devices and multipactor processes in waveguides.

Benito Gimeno (M'01) received the Licenciado and Doctor degrees in physics from the University of Valencia, Valencia, Spain. He is a Professor at the University of Valencia. His research interests include microwave passive components and RF breakdown high-power effects.

References

[1] ESTEC, *Multipacting design and test*, ecss-20-01 ed., Apr. 2000.

[2] Val Space Consortium. `https://www.val-space.com`.

[3] R. E. Collin, *Field Theory of Guided Waves*. IEEE Press, 2nd ed., 2008.

[4] E. Chojnacki, "Simulation of a multipactor-inhibited waveguide geometry," *Physical Review Special Topics - Accelerators and Beams*, vol. 3, p. 032001, Mar. 2000. DOI: 10.1103/PhysRevSTAB.3.032001.

[5] A. Telang, *Efficient method for geometry independent multipactor modelling*. Ph.D. thesis, University of Waterloo, 2009.

[6] G. Francis, A. V. Engel, and F. A. Lindemann, "The growth of the high-frequency electrodeless discharge," *Philosophical Transactions of the Royal Society of London. Series A, Mathematical and Physical Sciences*, vol. 246, no. 909, pp. 143–180, 1953. DOI:10.1098/rsta.1953.0012.

[7] S. Riyopoulos, D. Chernin, and D. Dialetis, "Theory of electron multipactor in crossed fields," *Physics of Plasmas*, vol. 2, no. 8, pp. 3194–3213, 1995. DOI:10.1063/1.871151.

[8] V. E. Semenov, "Simulations of multipactor thresholds in shielded microstrip lines," *Journal of Physics D Applied Physics*, vol. 42, pp. 205204–1–205204–7, Sep. 2009. DOI: 10.1088/0022-3727/42/20/205204.

[9] A. M. Pérez, "Prediction of multipactor breakdown thresholds in coaxial transmission lines for travelling, standing, and mixed waves," *IEEE Transactions on Plasma Science*, vol. 37, pp. 2031–2040, Sep. 2009. DOI: 10.1109/TPS.2009.2028428.

[10] A. M. Pérez, V. E. Boria, B. Gimeno, S. Anza, C. Vicente, and J. Gil, "Multipactor analysis in circular wave-guides," *Journal of Electromagnetic Waves and Applications*, vol. 23, pp. 1575–1583, Jan. 2009. DOI: 10.1163/156939309789476356.

[11] D. González-Iglesias, P. Soto, S. Anza, B. Gimeno, V. E. Boria, C. Vicente, and J. Gil, "Multipactor susceptibility charts for ridge and multiridge waveguides," *IEEE Transactions on Electron Devices*, vol. 59, pp. 3601–3607, Dec. 2012. DOI: 10.1109/TED.2012.2215611.

[12] H. Esteban, J. V. Morro, V. E. B. C. Bachiller, A. S. Blas, and J. Gil, "Multipaction modelling of low-cost h-plane filters using an electromagnetic field analysis tool," *IEEE Antennas and Propagation Society Symposium*, pp. 2155–2158, Jun. 2004. DOI: 10.1109/APS.2004.1330637.

[13] F. Quesada, V. Boria, B. Gimeno, D. Caete, J. Pascual, A. Álvarez, J. Hueso, D. Schmitt, D. R. C. Ernst, and I. Hidalgo, "Investigation of multipactor phenomena in inductively coupled passive waveguide components for space applications," in *IEEE MTT-S International Microwave Symposium Digest*, (San Francisco, CA, USA), pp. 246–249, IEEE, Jul. 2006. DOI: 10.1109/MWSYM.2006.249478.

[14] A. J. Hatch and W. H. Bartel, "The secondary electron resonance mechanism of low-pressure high-frequency gas breakdown," *Journal of Applied Physics*, vol. 25, no. 4, pp. 417–423, 1954. DOI: 10.1063/1.1721656.

[15] R. A. Kishek, "Multipactor discharge on metals and dielectrics: historical review and recent theories," *Physics of Plasmas*, vol. 5, pp. 2120–2126, May. 1998. DOI: 10.1063/1.872883.

[16] L. K. Ang, Y. Y. Lau, R. A. Kishek, , and M. Gilgenbach, "Power deposited on a dielectric by multipactor," *IEEE Transactions on Plasma Science*, vol. 26, pp. 290–295, Jun. 1998. DOI: 10.1109/27.7007561.

[17] A. Valfells, L. K. Ang, Y. Y. Lau, and R. M. Gilgenbach, "Effects of an external magnetic field, and of oblique radio-frequency electric fields on multipactor discharge on a dielectric," *Physical Review Letters*, vol. 92, pp. 750–757, Feb. 2000. DOI: 10.1063/1.873861.

[18] J. Power, W. Gai, S. H. Gold, A. K. Kinkead, R. Konecny, and C. Jing, "Observation of multipactor in an alumina-based dielectric-loaded accelerating structure," *Physics of Plasmas*, vol. 7, pp. 164801–1–164801–4, Apr. 2004. DOI: 10.1103/PhysRevLett.92.164801.

[19] G. Torregrosa, A. Coves, C. P. Vicente, A. M. Pérez, B. Gimeno, and V. E. Boria, "Time evolution of an electron discharge in a parallel-plate dielectric-loaded waveguide," *IEEE Transactions on Electron Devices*, vol. 27, pp. 619–621, Jul. 2006. DOI: 10.1109/LED.2006.877284.

[20] A. Coves, G. Torregrosa, C. P. Vicente, B. Gimeno, and V. E. Boria, "Multipactor discharges in parallel-plate dielectric-loaded waveguides including space-charge effects," *IEEE Transactions on Electron Devices*, vol. 55, pp. 2505–2511, Sep. 2008. DOI: 10.1109/TED.2008.927945.

[21] G. Torregrosa, A. Coves, B. Gimeno, I. Montero, C. Vicente, , and V. E. Boria, "Multipactor susceptibility charts of a parallel-plate dielectric-loaded waveguide," *IEEE Transactions on Electron Devices*, vol. 57, pp. 1160–1166, May. 2010. DOI: 10.1109/TED.2010.2043182.

[22] V. E. Semenov, E. I. Rakova, D. Anderson, M. Lisak, and J. Puech, "Multipactor in rectangular waveguides," *Physics of Plasmas*, vol. 14, pp. 033501–1–033501–8, Mar. 2007. DOI: 10.1063/1.2480678.

[23] L. S. Aguilera, *Supresión del efecto multipactor en instrumentación de RF en misiones en el espacio mediante superficies nano y microestructuradas*. Ph.D. thesis, Autonomous University of Madrid, 2014.

[24] G. Cheng and L. Liu, "Temporal evolution of multipactor electron discharge on a dielectric under excitation of high-power microwave," *IEEE Transactions on Plasma Science*, vol. 39, no. 4, pp. 1067–1074, 2011. DOI: 10.1109/TPS.2011.2106519.

[25] A. G. Sazontov, V. E. Nechaev, and N. K. Vdovicheva, "The susceptibility diagrams of a multipactor discharge on a dielectric: Effects of rf magnetic field," *Applied Physics Letters*, vol. 98, no. 16, p. 161503, 2011.

[26] H. Xiwei, S. Baipeng, and Z. Guanjun, "PIC-MCC simulation for HPM multipactor discharge on dielectric surface in vacuum," *Plasma Science and Technology*, vol. 13, pp. 682–688, Dec. 2011. DOI: 10.1088/1009-0630/13/6/09.

[27] R. A. Kishek and Y. Y. Lau, "Multipactor discharge on a dielectric," *Physical Review Letters*, vol. 80, pp. 193–196, Jan. 1998. DOI: 10.1103/PhysRevLett.80.193.

[28] A. Valfells, J. P. Verboncoeur, and Y. Y. Lau, "Space-charge effects on multipactor on a dielectric," *IEEE Transactions on Plasma Science*, vol. 28, pp. 529–536, Jun. 2000. DOI: 10.1103/PhysRevLett.80.193.

[29] G. Cheng, L. Liu, Y. Liu, and C. Yuan, "Monte carlo study of the single-surface multipactor electron discharge on a dielectric," *IEEE Transactions on Plasma Science*, vol. 37, no. 10, pp. 1968–1974, 2009. DOI: 10.1109/TPS.2009.2016967.

[30] J. G. Power, W. Gai, S. H. Gold, A. K. Kinkead, R. Konecny, C. Jing, W. Liu, and Z. Yusof, "Observation of multipactor in an alumina-based dielectric-loaded accelerating structure," *Physical Review Letters*, vol. 92, p. 164801, Apr. 2004. DOI: 10.1103/PhysRevLett.92.164801.

[31] O. V. Sinitsyn, G. S. Nusinovich, and T. M. Antonsen, "Self-consistent nonstationary two-dimensional model of multipactor in dielectric-loaded accelerator structures," *Physics of Plasmas*, vol. 16, no. 7, p. 073102, 2009. DOI: 10.1063/1.3160612.

[32] O. V. Sinitsyn, G. Nusinovich, and T. Antonsen, "Studies of multipactor in dielectric-loaded accelerator structures: Comparison of simulation results with experimental data," *AIP Conference Proceedings*, vol. 1299, no. 1, pp. 302–306, 2010. DOI: 10.1063/1.3520333.

[33] S. Riyopoulos, "Multipactor saturation due to space-charge-induced debunching," *Physics of Plasmas*, vol. 4, no. 5, pp. 1448–1462, 1997. DOI: 10.1063/1.872319.

[34] A. Sounas, *Modeling of long-term multipactor evolution in microwave components including dielectric layers*. Ph.D. thesis, École Polytechnique Fédérale de Lausanne, 2015.

[35] D. M. Pozar, *Microwave Engineering, 4th Edition*. Wiley, 2011.

[36] A. Coves, A. A. S. Blas, B. Gimeno, A. Díez, M. V. Andrés, , and V. E. Boria, "Two-dimensional photonic crystal microwave waveguide," *Microwave and Optical Technology Letters*, vol. 39, pp. 243–246, Aug. 2003. DOI: 10.1002/mop.11181.

[37] A. Coves, *Caracterización modal de sistemas guiadores inhomogéneos: análisis de superficies selectoras de frecuencias dieléctricas*. Ph.D. thesis, University of Valencia, 2004.

[38] L. D. Landau and E. M. Lifshitz, *The Classical Theory of Fields: Volume 2*. Course of theoretical physics, Elsevier Science, 1975.

[39] R. F. Harrington, *Time-Harmonic Electromagnetic Fields*. Wiley-IEEE Press, 2001.

[40] K. Zhang and D. Li, *Electromagnetic Theory for Microwaves and Optoelectronics*. Springer-Verlag Berlin Heidelberg, 2nd ed., 2008. DOI: 10.1007/978-3-540-74296-8.

[41] J. A. Monsoriu, A. Coves, B. Gimeno, M. V. Andrés, and E. Silvestre, "A robust and efficient method for obtaining the complex modes in inhomogeneously filled waveguides," *Microwave and Optical Technology Letters*, vol. 37, pp. 218–222, Mar. 2003. DOI: 10.1002/mop.10875.

[42] E. Silvestre, M. Abián, B. Gimeno, A. Ferrando, M. V. Andrés, and V. E. Boria, "Analysis of inhomogeneously filled waveguides using a bi-orthonormal-basis method," *IEEE Transactions on Microwave Theory and Techniques*, vol. 48, pp. 589–596, Apr. 2000. DOI: 10.1109/22.842031.

[43] A. Berenguer, A. Coves, F. Mesa, E. Bronchalo, B. Gimeno, and V. E. Boria, "Calculation of the electrostatic field in a dielectric-loaded waveguide due to an arbitrary charge distribution on the dielectric layer," in *2016 Progress in Electromagnetic Research Symposium (PIERS)*, (Shanghai, China), pp. 3251–3255, IEEE, Aug. 2016. DOI: 10.1109/PIERS.2016.7735274.

[44] A. Neuber, D. Hemmert, H. Krompholz, L. Hatfield, and M. Kristiansen, "Initiation of high power microwave dielectric interface breakdown," *Journal of Applied Physics*, vol. 86, pp. 1724–1728, Aug. 1999. DOI: 10.1063/1.370953.

[45] P. Ylä-Oijala and M. Ukkola, "Suppressing electron multipacting in ceramic windows by dc bias," *Nuclear Instruments and Methods in Physics Research Section A: Accelerators, Spectrometers, Detectors and Associated Equipment*, vol. 474, pp. 197–208, Dec. 2001. DOI: 10.1016/S0168-9002(01)00882-8.

[46] R. B. Anderson, W. D. Getty, M. L. Brake, Y. Y. Lau, R. M. Gilgenbach, and A. Valfells, "Multipactor experiment on a dielectric surface," *Review of Scientific Instruments*, vol. 72, pp. 3095–3099, Jul. 2001. DOI: 10.1063/1.1380687.

[47] S. Michizono and Y. Saito, "Surface discharge and surface potential on alumina rf windows," *Vacuum*, vol. 60, pp. 235–239, Jan. 2001. DOI: 10.1016/S0042-207X(00)00380-8.

[48] D. J. Griffiths, *Introduction to Electrodynamics*. Pearson, 3rd ed., 2008.

[49] J. D. Jackson, *Classical Electrodynamics*. John Wiley and Sons, 3rd ed., 1999.

[50] J. V. Bladel, *Electromagnetic Field*. IEEE Press, 2nd ed., 2007.

[51] A. Berenguer, L. Gandarias, and A. Arévalo, "Singular spectrum analysis for modelling the hard-to-model risk factors," *Risk Management*, vol. 22, pp. 178–191, Sep. 2020. DOI: 10.1057/s41283-020-00060-5.

[52] D. S. Broomhead and G. King, "Extracting qualitative dynamics from experimental data," *Physica D: Nonlinear Phenomena*, vol. 20, pp. 217–236, Jun.–Jul. 1986. DOI: 10.1016/0167-2789(86)90031-X.

[53] D. S. Broomhead and G. P. King, "On the qualitative analysis of experimental dynamical systems," in *Nonlinear Phenomena and Chaos* (S. Sarkar, ed.), pp. 113–144, Bristol: Adam Hilger, Jan. 1986.

[54] D. S. Broomhead, R. Jones, G. P. King, and E. R. Pike, "Singular system analysis with application to dynamical systems," in *Choas, Noise and Fractals. Malvern Physics Series* (E. Pike and L. Lugiato, eds.), Bristol: Adam Hilger, 1987.

[55] A. Agarwal, M. Jehangir, D. Shah, and D. Shen, "Model agnostic time series analysis via matrix estimation," *Proceedings of the ACM on Measurement and Analysis of Computing Systems*, vol. 2, Dec. 2018. DOI: 10.1145/3287319.

[56] V. Moskvina and K. M. Schmidt, "Approximate projectors in singular spectrum analysis," *SIAM Journal on Matrix Analysis and Applications*, vol. 24, no. 4, pp. 932–942, 2003. DOI: 10.4310/SII.2010.v3.n3.a11.

[57] M. Ghil, M. R. Allen, M. D. Dettinger, K. Ide, D. Kondrashov, M. E. Mann, A. W. Robertson, A. Saunders, Y. Tian, F. Varadi, and P. Yiou, "Advanced spectral methods for climatic time series," *Reviews of Geophysics*, vol. 40, pp. 3–1–3–41, Feb. 2002. DOI: 10.1029/2000RG000092.

[58] M. A. R. Khan and D. S. Poskitt, "Moment tests for window length selection in singular spectrum analysis of shortand long-memory processes," *Journal of Time Series Analysis*, vol. 34, pp. 141–155, Mar. 2013. DOI: 10.1111/j.1467-9892.2012.00820.x.

[59] Everything RF website. `https://www.everythingrf.com/`, (accessed September 13, 2020).

[60] L. Austin and H. Stark, "Ueber die reflexion der kathodenstrahlen und eine damit verbundene neue erscheinung secundärer emission," *Annalen der Physik*, vol. 314, no. 10, pp. 271–292, 1902. DOI: 10.1002/andp.19023141003.

[61] A. J. Dekker, "Secondary electron emission," in *Solid State Physics*, ch. 17, pp. 418–445, London: Macmillan Education UK, 1981.

[62] A. Berenguer, A. Coves, F. Mesa, E. Bronchalo, and B. Gimeno, "A new multipactor effect model for dielectric-loaded rectangular waveguides," in *2019 IEEE MTT-S International Conference on Numerical Electromagnetic and Multiphysics Modeling and Optimization (NEMO)*, pp. 1–4, 2019.

[63] A. Berenguer, A. Coves, E. Bronchalo, B. Gimeno, and V. E. Boria, "Analysis of multipactor effect in parallel-plate and rectangular waveguides," in *2015 Progress in Electromagnetic Research Symposium (PIERS)*, (Prague, Czech Republic), pp. 1564–1568, Jul. 2015.

[64] J. Hueso, *Analysis of wedge-shaped waveguides and design of multipactor-resistant microwave bandpass filters*. Ph.D. thesis, Polytechnic University of Valencia, 2013.

[65] I. Montero, L. Aguilera, M. E. Dávila, V. C. Nistor, L. A. González, L. Galán, D. Raboso, and R. Ferritto, "Secondary electron emission under electron bombardment from graphene nanoplatelets," *Applied Surface Science*, vol. 291, pp. 74–77, Feb. 2014. DOI: 10.1016/j.apsusc.2013.10.045.

[66] Y. Lin and D. C. Joy, "A new examination of secondary electron yield data," *Surface and Interface Analysis*, vol. 37, no. 11, pp. 895–900, 2005. DOI: 10.1002/sia.2107.

[67] K. Nishimurat, A. Itotani, and K. Ohya, "Influence of surface roughness on secondary electron emission and electron backscattering from metal surface," *Japanese Journal of Applied Physics*, vol. 33, pp. 4727–4734, Aug. 1994. DOI: 10.1143/jjap.33.4727.

[68] J. de Lara, F. Perez, M. Alfonseca, L. Galan, I. Montero, E. Roman, and D. R. Garcia-Baquero, "Multipactor prediction for on-board spacecraft rf equipment with the mest software tool," *IEEE Transactions on Plasma Science*, vol. 34, pp. 476–484, Apr. 2006. DOI: 10.1109/TPS.2006.872450.

[69] H. Seiler, "Secondary electron emission in the scanning electron microscope," *Journal of Applied Physics*, vol. 54, no. 11, pp. R1–R18, 1983. DOI: 10.1063/1.332840.

[70] N. Bundaleski, B. J. Shaw, A. G. Silva, A. M. C. Moutinho, and O. M. N. D. Teodoro, "Novel approach to the semi-empirical universal theory for secondary electron yield," *Scanning*, vol. 33, no. 4, pp. 266–269, 2011. DOI: 10.1002/sca.20257.

[71] J. J. Scholtz, D. Dijkkamp, , and R. Schmitz, "Secondary electron emission properties," *Philips Journal of Research*, vol. 50, no. 3–4, pp. 375–389, 1996. DOI: 10.1016/S0165-5817(97)84681-5.

[72] M. Ito, H. Kume, and K. Oba, "Computer analysis of the timing properties in micro channel plate photomultiplier tubes," *IEEE Transactions on Nuclear Science*, vol. 31, pp. 408–412, Feb. 1984. DOI: 10.1109/TNS.1984.4333288.

[73] R. Vaughan, "A new formula for secondary emission yield," *IEEE Transactions on Electron Devices*, vol. 36, pp. 1963–1967, Sep. 1989. DOI: 10.1109/16.34278.

[74] J. Vaughan, "Secondary emission formulas," *IEEE Transactions on Electron Devices*, vol. 40, p. 830, Apr. 1993. DOI: 10.1109/16.202798.

[75] C. Vicente, M. Mattes, D. Wolk, B. Mottet, H. L. Hartnagel, J. R. Mosig, and D. Raboso, "Multipactor breakdown prediction in rectangular waveguide based components," in *IEEE MTT-S International Microwave Symposium Digest*, (Long Beach, CA, USA), pp. 1055–1058, IEEE, Jun. 2005. DOI: 10.1109/MWSYM.2005.1516852.

[76] R. Seviour, "The role of elastic and inelastic electron reflection in multipactor discharges," *IEEE Transactions on Electron Devices*, vol. 52, pp. 1927–1930, Aug. 2005. DOI: 10.1109/TED.2005.851854.

[77] R. Cimino, I. R. Collins, M. A. Furman, M. Pivi, F. Ruggiero, G. Rumolo, and F. Zimmermann, "Can low-energy electrons affect high-energy physics accelerators?," *Physical Review Letters*, vol. 93, p. 014801, Feb. 2004. DOI: 10.1103/PhysRevLett.93.014801.

[78] E. Bronchalo, A. Coves, R. Mata, B. Gimeno, I. Montero, L. Galán, V. E. Boria, L. Mercadé, and E. Sanchís-Kilders, "Secondary electron emission of pt: Experimental study and comparison with models in the multipactor energy range," *IEEE Transactions on Electron Devices*, vol. 63, pp. 3270–3277, Aug. 2016. DOI: 10.1109/TED.2016.2580199.

[79] D. Gonzalez-Iglesias, A. M. Perez, S. Anza, J. Vague, B. Gimeno, V. E. Boria, D. Raboso, C. Vicente, J. Gil, F. Caspers, and L. Conde, "Multipactor in a coaxial line under the presence of an axial dc magnetic field," *IEEE Electron Device Letters*, vol. 33, no. 5, pp. 727–729, 2012. DOI: 10.1109/LED.2012.2186952.

[80] A. J. Hatch and H. B. Williams, "Multipacting modes of high-frequency gaseous breakdown," *Physical Review*, vol. 112, pp. 681–685, Nov 1958. DOI: 10.1103/PhysRev.112.681.

[81] J. Vaughan, "Multipactor," *IEEE Transactions on Electron Devices*, vol. 35, pp. 1172–1180, Jul. 1988. DOI: 10.1109/16.3387.

[82] R. A. Kishek and Y. Y. Lau, "Interaction of multipactor discharge and rf circuit," *Physical Review Letters*, vol. 75, pp. 1218–1221, Aug. 1995. DOI: 10.1103/PhysRevLett.75.1218.

[83] J. Sombrin, "Effect multipactor," Tech. Rep. 83/DRT/TIT/HY/119/T, CNES, 1983.

[84] Z. J. Ding, H. M. Li, R. Shimizu, and K. Goto, "On the energy distribution of secondary electrons emitted from metals," *Journal of Surface Analysis*, vol. 15, pp. 186–194, 2008. DOI: 10.1384/jsa.15.186.

[85] M. S. Chung and T. E. Everhart, "Simple calculation of energy distribution of low-energy secondary electrons emitted from metals under electron bombardment," *Journal of Applied Physics*, vol. 45, no. 2, pp. 707–709, 1974. DOI: 10.1063/1.1663306.

[86] S. M. Ross, *Simulation*. Elsevier, 4th ed., 2006.

[87] S. Ghahramani, *Fundamentals of Probability, with Stochastic Processes*. Prentice Hall, 3rd ed., 2004.

[88] S. Glen, "Acceptance-rejection sampling: Plain english definition / overview." `https://www.statisticshowto.com/acceptance-rejection-sampling/`, (accessed September 13, 2020).

[89] U. Dieter and J. Ahrens, "Acceptance-rejection techniques for sampling from the gamma and beta distributions," *Office of Naval Research Technical Report*, May. 1974.

[90] E. Somersalo, P. Yl-Oijala, D. Proch, , and J. Sarvas, "Computational methods for analyzing electron multipacting in rf structures," *Particle Accelerators*, vol. 59, pp. 107–141, 1998. DOI: 10.1063/1.2480678.

[91] J. Greenwood, "The correct and incorrect generation of a cosine distribution of scattered particles for monte-carlo modelling of vacuum systems," *Vacuum*, vol. 67, no. 2, pp. 217–222, 2002. DOI:10.1016/S0042-207X(02)00173-2.

[92] J. M. Lafferty, *Foundations of vacuum science and technology*. Wiley, 1998.

[93] Y. Suetsugu, "Application of the monte carlo method to pressure calculation," *Journal of Vacuum Science & Technology A*, vol. 14, no. 1, pp. 245–250, 1996. DOI: 10.1116/1.579927.

[94] R. L. Geng and H. S. Padamsee, "Exploring multipacting characteristics of a rectangular waveguide," in *Particle Accelerator Conference*, (New York, NY, USA, USA), pp. 429–431, IEEE, Mar.–Apr. 1999. DOI: 10.1109/PAC.1999.795724.

[95] E. Sorolla and M. Mattes, "Multipactor saturation in parallel-plate waveguides," *Physics of Plasmas*, vol. 19, p. 072304, Jul. 2012. DOI: 10.1063/1.4736852.

[96] A. Wood and J. Petit, "Investigations into multipactor breakdown in satellite microwave payloads," *ESA Journal*, vol. 14, pp. 467–478, Jan. 1990. Provided by the SAO/NASA Astrophysics Data System.

[97] A. Berenguer, A. Coves, E. Bronchalo, B. Gimeno, and V. E. Boria, "Comparison of multipactor effect in parallel-plate and rectangular waveguides: 1D and 2D-3D models," in *XXX Simposium Nacional de la Unión Científica Internacional de Radio*, (Pamplona, Spain), Sep. 2015.

[98] A. Berenguer, A. Coves, F. Mesa, E. Bronchalo, and B.Gimeno, "Analysis of multipactor effect in a partially dielectric-loaded rectangular waveguide," *IEEE Transactions on Plasma Science*, vol. 47, pp. 259–265, Jan. 2019. DOI: 10.1109/TPS.2018.2880652.

[99] G. Schmidt, *Physics of High Temperature Plasmas*. Academic Press, 2nd ed., 1979. DOI: 10.1016/B978-0-12-626660-3.X5001-9.

[100] Chemours, "Teflon© fep film properties bulletin k26941." `https://www.chemours.com/`.

[101] K. Nishimura, T. Itotani, and K. Ohya, "Influence of surface roughness on secondary electron emission and electron backscattering from metal surface," *Japanese Journal of Applied Physics*, vol. 33, pp. 4727–4734, Aug. 1994. DOI: 10.1143/jjap.33.4727.

[102] L. E. García-Castillo, D. Pardo, I. Gómez-Revuelto, and L. F. Demkowicz, "A two-dimensional self-adaptive hp finite element method for the characterization of waveguide discontinuities. part i: Energy-norm based automatic hp-adaptivity," *Computer Methods in Applied Mechanics and Engineering*, vol. 196, pp. 4823–4852, Nov. 2007. DOI: 10.1016/j.cma.2007.06.024.

[103] N. Marcuvitz, I. of Electrical Engineers, I. of Engineering, Technology, M. I. of Technology, P. P. Limited, M. I. of Technology. Radiation Laboratory, U. S. O. of Scientific Research, and D. N. D. R. Committee, *Waveguide Handbook*. IEEE electromagnetic waves series, McGraw-Hill, 1951.

[104] F. Ishihara and I. Shinichi, "Equivalent characteristic impedance formula of waveguide and its applications," *Electronics and Communications in Japan (Part II: Electronics)*, vol. 75, no. 5, pp. 54–66, 1992. DOI: 10.1002/ecjb.4420750506.

[105] C. Holm, "Simulation methods in physics 1." Institute for Computational Physics. University of Stuttgart, 2012–2013.

[106] W. C. Swope, H. C. Andersen, P. H. Berens, and K. R. Wilson, "A computer simulation method for the calculation of equilibrium constants for the formation of physical clusters of molecules: Application to small water clusters," *The Journal of Chemical Physics*, vol. 76, no. 1, pp. 637–649, 1982. DOI: 10.1063/1.442716.

[107] G. V. Milovanović and M. Stanić, "Numerical integration of highly oscillating functions," in *Analytic Number Theory, Approximation Theory, and Special Functions* (G. Milovanović and M. Rassias, eds.), pp. 613–649, Springer, New York, NY, 2014. DOI: 10.1007/978-1-4939-0258-3_23.

[108] L. N. G. Filon, "On a quadrature formula for trigonometric integrals," *Proceedings of the Royal Society of Edinburgh*, vol. 49, p. 38–47, 1930. DOI:10.1017/S0370164600026262.

[109] C. P. Robert and G. Casella, "Random variable generation," in *Monte Carlo Statistical Methods*, Springer Texts in Statistics, pp. 35–70, Springer, New York, NY, 1999. DOI: 10.1007/978-1-4757-3071-5_2.

[110] Agustinus Kristiadi's Blog. `https://wiseodd.github.io/techblog/2015/10/21/rejection-sampling/`, (accessed September 13, 2020).

[111] R. Mata, Apr. 2016. European High Power RF Space Laboratory (ESA - Consorcio Espacial Valenciano), Valencia, Spain.

[112] F. B. Hildebrand, *Introduction to Numerical Analysis*. McGraw-Hill, 2nd ed., 1974.

[113] A. V. Gaponov and M. A. Miller, "Potential wells for charged particles in high-frequency electromagnetic field," *Journal of Experimental and Theoretical Physics*, vol. 7, p. 168, Jul. 1958.

[114] L. Aguilera, I. Montero, J. L. Sacedon, L. Galán, V. Nistor, D. Wolk, U. Wochner, and D. Raboso, "Surface treatments for controlling the secondary electron emission of materials for anti-multipactor applications," in *Multipactor, Corona and Passive Intermodulation, MULCOPIM 08 (ESA)*, (Valencia, Spain), Sep. 2008.

Biographical sketch

Andrés Berenguer was born in Elche (Alicante), Spain. He received the Degree in Telecommunication Engineering with First-Class Honours from the Miguel Hernandez University of Elche, Alicante, Spain, in 2006, where he is pursuing the PhD degree. He is currently team director within the derivative valuations area of the Market Risk department in Santander Bank. Since 2009 he has been working on derivative valuations including besides other things, advising on the pricing models of exotic trades, XVA calculation or interest rate curves modelling (basis spreads, collateral, OIS discounting,...). Before working in banking, his experience was in space and communications engineering. He holds a MBA from the University of Valencia and a M.Sc. in Technologies, Systems and Communications Networks Engineering from the Polytechnic University of Valencia. His current research interests include the study of the multipactor effect in waveguides, as well as quantitative and risk analysis (stochastic calculus, numerical methods and data analysis).